



**PHOTOGRAMMETRIC MEASUREMENT OF RECESSION RATES OF LOW
TEMPERATURE ABLATORS SUBJECTED TO HIGH SPEED FLOW**

DISSERTATION

Major David W. Callaway, USAF, Retired

AFIT/DS/ENY/11-03

**DEPARTMENT OF THE AIR FORCE
AIR UNIVERSITY**

AIR FORCE INSTITUTE OF TECHNOLOGY

Wright-Patterson Air Force Base, Ohio

The views expressed in this thesis are those of the author and do not reflect the official policy or position of the United States Air Force, Department of Defense, or the United States Government. This material is declared a work of the U.S. Government and is not subject to copyright protection in the United States.

PHOTOGRAMMETRIC MEASUREMENT OF RECESSION RATES OF LOW
TEMPERATURE ABLATORS SUBJECTED TO HIGH SPEED FLOW

DISSERTATION

Presented to the Faculty

Graduate School of Engineering and Management

Air Force Institute of Technology

Air University

Air Education and Training Command

In Partial Fulfillment of the Requirements for the

Degree of Doctor of Philosophy

David W. Callaway, BS, MAE

Major, USAF, Retired

June 2011

APPROVED FOR PUBLIC RELEASE; DISTRIBUTION UNLIMITED.

PHOTOGRAMMETRIC MEASUREMENT OF RECESSION RATES OF LOW
TEMPERATURE ABLATORS SUBJECTED TO HIGH SPEED FLOW

DISSERTATION

David W. Callaway, BS,MAE

Major, USAF, Retired

Approved:

Mark F. Reeder, PhD (Chairman)

Date

Robert B. Greendyke, PhD (Member)

Date

Paul I. King, PhD (Member)

Date

David J. Bunker, PhD (Member)

Date

Accepted:

M. U. Thomas, PhD
Dean, Graduate School of
Engineering and Management

Date

Abstract

This research advances a technique to simulate high temperature/high speed effects in a high speed/low temperature environment and to capture recession of the test article in three-dimensions. A method of fabricating dry ice test articles was developed, and the AFIT Mach 3 pressure-vacuum wind tunnel was used in combination with the dry ice test articles to collect three-dimensional ablation data for models of different shapes at stagnation pressures ranging from approximately 0.4 atm to 3 atm and stagnation temperatures equivalent to room temperature. High speed Schlieren photography was used for visualization, and the three dimensional shape change was quantified with sub-millimeter accuracy using laser dot photogrammetry. Experimental results for multiple shapes were compared to those computed using a computational model called ACFD. The ACFD model employed a finite-volume approach to solving the (3-D) Navier-Stokes equations with the gas assumed to be at equilibrium while employing an implicit solver accounting for the material response. By and large, the computational approach was validated for the conditions tested herein. Measurement of ablation rates at the stagnation point yielded approximate values of convective heat transfer rate when conduction through the solid is assumed negligible. The results of this analysis compared favorably to a variety of extensions of the Fay-Riddell correlation given in the literature. Paths for further research were selected and discussed.

To my patient and supportive wife. She sacrificed much to see this research finished, and without her motivation and support, this dissertation would probably still be in draft form. I could not have done this without her. Thank-you

.

Acknowledgements

This dissertation would not have been possible without the guidance and support of my research advisor, Dr. Mark Reeder. Without his insight, support, and willingness to take on this daunting project, this research would not have come to fruition. His calm attitude and work ethic gave me inspiration and will continue to do so in my career. I'd also like to thank my committee for their support and patience: Dr. Robert Greendyke, Dr. Paul King, and Dr. David Bunker. Dr. Greendyke was especially helpful with his insight into computational modeling and humor throughout the project.

The experimental results of this research would not have been possible without the help of all of the laboratory support staff and the machine shop crew. Specifically, Brian Crabtree at the machine shop was a whiz when it came to modifying the wind tunnel and crafting "unique" work requests. Jay Anderson was invaluable as the single source for any information or lab equipment. John Hixenbaugh was the go-to guy for all things technical and tracking down hard to find parts. Chris Zickefoose was the resident expert on producing resin parts and molds as well as a guru of the high speed cameras.

This research was made financially possible by AFRL/RBAC. The primary point of contact was Dr. Ryan Gosse, who contributed many hours of his time and computational and analytical skills to furthering this research. Dr. Reid Melville, Mr. Jim Miller, and Dr. Peter Erbland played instrumental roles supporting the initiation of this project.

Table of Contents

Abstract	iv
Acknowledgements	vi
List of Figures.....	x
List of Tables.....	xix
List of Symbols.....	xxi
List of Abbreviations.....	xxvii
1 Introduction.....	1
1.1 Background and Motivation	1
1.2 Research Objectives	6
1.3 Original and Significant Contributions of Research.....	7
1.4 Material Selection	7
1.5 Organization of Dissertation.....	8
2 Literature Review	10
2.1 Hypersonic Flow Region	10
2.2 Thermal Protection Systems	17
2.2.1 Reusable Thermal Protection Systems.....	17
2.2.2 Ablating Thermal Protection Systems	19
2.3 Ablation Studies.....	20
2.4 Low Temperature Ablation Studies.....	22
2.5 Computational Modeling of Fluid Dynamics and Ablation.....	28
2.5.1 Flow Field.....	29
2.5.2 Surface Interactions.....	34
2.6 AFRL Use of the ACFD Code.....	37
2.7 Measurement Techniques.....	40
2.7.1 Photogrammetric Recession Measurement.....	40
2.7.2 Dot Projection Photogrammetry	42
2.7.3 Schlieren Imaging	43
2.8 Attributes of Solid Carbon Dioxide	44
3 Experiment Methodology.....	48
3.1 Experimental Facilities and Equipment	48
3.1.1 Wind Tunnel Equipment.....	48

3.1.2	Wind Tunnel Operations	53
3.1.3	Test Conditions.....	55
3.1.4	Cameras Used for Photogrammetry.....	57
3.1.5	Camera Test Set Up	59
3.1.6	Schlieren Imaging Setup	62
3.1.7	Laser Grids	63
3.1.8	Image Data Capture.....	66
3.2	Accuracy and Limitations.....	72
3.2.1	Image Capture	72
3.2.2	Image Processing.....	75
3.2.3	Index of Refraction	77
3.2.4	Tunnel Test Condition Continuity.....	80
3.3	Dry Ice Models.....	83
3.3.1	Fabrication of Dry ice.....	84
3.3.2	Dry ice Model Density	95
3.3.3	Molds and Model Shapes	97
3.4	The ACFD Code Set Up.....	101
4	Experimental Results.....	105
4.1	Proof of Concept.....	107
4.2	Spherically Blunted Cone at 0° Angle of Attack, $P_o = 6.1$ psia	111
4.3	Spherically Blunted Cone at 0° Angle of Attack, Multiple Pressures.....	120
4.4	Spherically Blunted Cylinder at 0 Angle of Attack Similarity Test	127
4.5	Spherically Blunted Cylinder at 0 Angle of Attack and Multiple Pressures	132
4.6	Elliptical-Nose Model at 0 Angle of Attack and Multiple Pressures.....	141
4.7	Multiple Shapes at $P_o \sim 20$ psia	148
4.8	5° Angle of Attack Experimental Results	155
4.8.1	Spherically Blunted Cone.....	156
4.8.2	Spherically Blunted Cylinder.....	160
4.9	10° Angle of Attack Experimental Results	165
4.9.1	Spherically Blunted Cone.....	165
4.9.2	Spherically Blunted Cylinder.....	171

4.9.3	Shock Interactions	176
5	Analysis of Results	178
5.1	Spherically Blunted Cone at 0 Angle of Attack	179
5.1.1	Spherically Blunted Cone at 0 Angle of Attack, $P_o = 6.1$ psia.....	179
5.1.2	Spherically Blunted Cone at 0 Angle of Attack, $P_o = 23.0$ psia.....	181
5.1.3	Spherically Blunted Cone at 0 Angle of Attack, Multiple Stagnation Pressures..	185
5.2	Spherically Blunted Cylinder at 0 Angle of Attack	187
5.2.1	Spherically Blunted Cylinder at 0 Angle of Attack, $P_o = 7.5$ psia	187
5.2.2	Spherically Blunted Cylinder at 0 Angle of Attack, $P_o = 19.5$ psia	189
5.2.3	Spherically Blunted Cylinder at 0 Angle of Attack, $P_o = 37.9$ psia	191
5.2.4	Spherically Blunted Cylinder at 0 Angle of Attack, Multiple Stagnation Pressures 193	
5.3	Relation to Real World Effects.....	195
5.3.1	Stagnation Point Heating.....	195
5.3.2	Recession Predictions	203
6	Summary and Conclusions	206
6.1	Motivation	206
6.2	Summary of Research.....	206
6.3	Conclusions and Contributions to the Hypersonics Community.....	208
6.4	Recommendations for Future Work.....	210
	APPENDIX A: Model Diagrams.....	212
	APPENDIX B: ACFD Input Parameters.....	219
	APPENDIX C: Master List of Tests	222
	APPENDIX D: 2 Jun Test 6 data at 0.5 second intervals.....	232
	APPENDIX E: Table Calculations of Constants for Section 5.2.4.....	248
	Works Cited	252

List of Figures

Figure 1: Teflon test article before and after exposure to rocket engine showing cross-hatching (Larson & Nachtsheim, 1970).....	4
Figure 2: Shuttle Orbiter tile locations (Day, 2003)	18
Figure 3: Shadowgraph Images taken at Arnold Engineering Development Center’s High Enthalpy Ablation Test Unit H1 (Sherrouse, Sheeley, Mansfield, & Rotach, 2003)	22
Figure 4: Fluorescence from laser dot projection onto gossamer structure (Pappa, Black, Blandino, Jones, Danehy, & Dorrington, 2003)	43
Figure 5: Three-dimensional surface by photogrammetry of gossamer structure in Figure 4 (Pappa, Black, Blandino, Jones, Danehy, & Dorrington, 2003)	43
Figure 6: Schlieren images of a resin cone model in nominal Mach 3 flow (Jung, Reeder, Maple, & Crafton, 2006).....	44
Figure 7: Carbon Dioxide phase diagram produced from CRC data (Lide & Haynes, CRC Handbook of Chemistry and Physics, 2009).....	47
Figure 8: AFIT blow down facility set up for a 10° angle of attack test.....	49
Figure 9: Wind tunnel viewed from the top with side labels visible; Sting is set up for a 15 degree angle of attack test.....	52
Figure 10: Spherically blunted cone model in the tunnel at 0 angle of attack.....	52
Figure 11: Four way liquid carbon dioxide connection unattached from wind tunnel....	53
Figure 12: X-Series high speed camera back panel	58
Figure 13: Motion Studio camera control panel with default settings.....	58
Figure 14: Raw images of dry-ice model in wind tunnel. Counter clockwise from top left: image of model in tunnel, image with lasers on, starboard side of model, top of model, port side of model	59
Figure 15: Camera set up for a zero angle of attack wind tunnel test.....	60
Figure 16: Top view diagram of camera set up for zero angle of attack test (image not to scale)	60
Figure 17: Wind tunnel setup for 5° angle of attack test viewed from the starboard of the model.....	61

Figure 18: Top view diagram of camera set up for five degree angle of attack test (image not to scale)	61
Figure 19: Camera setup for 10° angle of attack test viewed from the starboard of the model.....	62
Figure 20: Top view diagram of camera set up for 10° angle of attack test (image not to scale)	62
Figure 21: Schlieren lamp and first mirror in Schlieren set up.....	62
Figure 22: Schlieren camera with knife edge and second mirror	63
Figure 23: Laser grids projected onto a spherically blunted cone dry-ice model.....	64
Figure 24: Diagram of zero degree angle of attack test laser orientations as viewed from above	65
Figure 25: Diagram of five degree angle of attack test laser orientations as viewed from above	66
Figure 26: Diagram of ten degree angle of attack test laser orientations as viewed from above	66
Figure 27: Raw PhotoModeler® image captures of three camera angles for a spherically blunted cone at initial time (left images) and final time (right images).....	68
Figure 28: Three-dimensional referencing of point 1012 in a PhotoModeler® image ...	70
Figure 29: PhotoModeler® image of initial 3-D data (top) and final time position 3-D data (bottom)	71
Figure 30: Plastic resin model of a spherically blunted cylinder in model with two laser grids projected onto the surface	73
Figure 31: Average fluctuation during plastic resin model tests at varying pressures	74
Figure 32: A correctly referenced point in PhotoModeler® illustrating how a laser point can look different in each camera view	76
Figure 33: Index of refraction error diagram	78
Figure 34: Stagnation pressure, pressure at infinity, and stagnation temperature over the course of a $P_o = 38$ psia test	81
Figure 35: Multiple stagnation densities for the duration of each test.....	82
Figure 36: Liquid CO ₂ delivery set up	85

Figure 37: Solidworks® image of spherically blunted cone mold half	87
Figure 38: Resin mold for spherically blunted cylinder model and molds.....	87
Figure 39: Exterior test sting and liquid CO ₂ feed tube.....	88
Figure 40: Mold half on sting in wind tunnel	89
Figure 41: Early test article that failed upon removal from mold.....	89
Figure 42: Out of tunnel dry ice model fabrication set up	90
Figure 43: Density measurement set up.....	96
Figure 44: Mold halves for a spherically blunted cylinder, elliptical shape with wings, elliptical nose, and spherically blunted cone	97
Figure 45: Spherically blunted cylinder and cone resin test models	99
Figure 46: Resin test article models for (left to right) a spherically blunted cylinder, spherically blunted cone, elliptical nose and elliptical shape with wings.....	100
Figure 47: Dry ice model without an insulator in preliminary wind tunnel tests	108
Figure 48: Time progression of preliminary dry-ice ablation test at nominally Mach 3.110	
Figure 49: Schlieren imaging of a spherically blunted cone at 6.1 psia, Mach 2.94 at time = 0 (top) and time = 3 seconds (bottom).....	112
Figure 50: Spherically blunted cone at a stagnation pressure of 6.1 psia and time = 0.5 seconds	114
Figure 51: Spherically blunted cone at a stagnation pressure of 6.1 psia and time = 3.5 seconds	115
Figure 52: Spherically blunted cone at a stagnation pressure of 6.1 psia and time = 7.5 seconds	116
Figure 53: Comparison of trend lines for recession of a point near the nose for experimental tests 2 Jun Test 6, 2 Jun Test 7, 2 Jun Test 8, and 2 Jun Test 9 at ~6.1 psia stagnation pressures.....	119
Figure 54: Schlieren images of a spherically blunted cone at stagnation pressures of 6.1, 23.0, and 45.7 psia. The top row is at t = 0 sec, the second row at t = 1 sec, the third row at t = 2 sec, and the fourth row is at t = 3 sec.....	122
Figure 55: Comparison of 6.1, 23.0, and 45.7 psia stagnation pressure tests on spherically blunted cone model: top view of mesh surface	124

Figure 56: Comparison of 6.1, 23.0, and 45.7 psia stagnation pressure tests on spherically blunted cone model: top view of point cloud.....	124
Figure 57: Comparison of 6.1, 23.0, and 45.7 psia stagnation pressure tests on spherically blunted cone model: side view of point cloud.....	125
Figure 58: Comparison of 6.1, 23.0, and 45.7 psia stagnation pressure tests on spherically blunted cone model: front view of point cloud	125
Figure 59: Comparison of 6.1, 23.0, and 45.7 psia stagnation pressure test recession rates of a spherically blunted cone	126
Figure 60: Schlieren images of a spherically blunted cylinder tests 19 Jun Test 8 (left) and 19 Jun Test 9 (right) at $t = 0$ sec (top row) and $t = 3$ sec (bottom row)	128
Figure 61: Spherically blunted cylinder similarity tests 19 Jun Test 8 (top) and 19 Jun Test 9 (bottom) at 7.5 psia stagnation pressure after 8 seconds: top view of mesh surface plot.....	129
Figure 62: Spherically blunted cylinder similarity tests 19 Jun Test 8 (left) and 19 Jun Test 9 (right) at 7.5 psia stagnation pressure after 8 seconds: front view of the point cloud	130
Figure 63: Spherically blunted cylinder similarity tests 19 Jun Test 8 (top) and 19 Jun Test 9 (bottom) at 7.5 psia stagnation pressure after 8 seconds: side view of point cloud.....	130
Figure 64: Spherically blunted cylinder similarity tests 19 Jun Test 8 (top) and 19 Jun Test 9 (bottom) at 7.5 psia stagnation pressure after 8 seconds: top view of point cloud.....	131
Figure 65: Comparison of experimental nose recession results for a spherically blunted cylinder at 7.5 psia stagnation pressure	132
Figure 66: Schlieren images of spherically blunted cylinder at 7.5, 19.8, 27.9, and 37.9 psia stagnation pressures. The top row is at $t = 0$ sec, the second row at $t = 1$ sec, the third row at $t = 2$ sec, and the fourth row is at $t = 3$ sec.....	134
Figure 67: Comparison of experimental spherically blunted cylinders 7.5 (top left), 19.8 (top right), 27.9 (bottom left), and 37.9 psia (bottom right): top view of mesh surface	136
Figure 68: Comparison of experimental spherically blunted cylinders at time = 2.5 seconds 7.5 (top left), 19.8 (top right), 27.9 (bottom left), and 37.9 psia (bottom right): front view of point cloud.....	137

Figure 69: Comparison of experimental spherically blunted cylinders at time = 2.5 seconds 7.5 (top left), 19.8 (top right), 27.9 (bottom left), and 37.9 psia (bottom right): side profile view of point cloud	138
Figure 70: Comparison of experimental spherically blunted cylinders at time = 2.5 seconds 7.5 (top left), 19.8 (top right), 27.9 (bottom left), and 37.9 psia (bottom right): top view of point cloud	139
Figure 71: Comparison of experimental nose recession results for spherically blunted cylinder at 7.5, 19.54, 27.9, and 37.9 psia stagnation pressures.	140
Figure 72: Schlieren images of an elliptical nose model at stagnation pressures of 17.3 and 39.1 psia. The top row is at $t = 0$ sec, the second row at $t = 1$ sec, the third row at $t = 2$ sec, and the fourth row is at $t = 3$ sec	142
Figure 73: Comparison of experimental results for an elliptical nose shape at $P_o=17.3$ psia (left) and $P_o = 39.1$ psia(right): top view of mesh surface	144
Figure 74: Comparison of experimental results for an elliptical nose shape at $P_o=17.3$ psia (left) and $P_o = 39.1$ psia(right): side view of mesh surface	144
Figure 75: Comparison of experimental results for an elliptical nose shape at $P_o=17.3$ psia (left) and $P_o = 39.1$ psia(right): front view of point cloud.....	145
Figure 76: Comparison of experimental results for an elliptical nose shape at $P_o=17.3$ psia (left) and $P_o = 39.1$ psia(right): side view of point cloud	145
Figure 77: Comparison of experimental results for an elliptical nose shape at $P_o=17.3$ psia (left) and $P_o = 39.1$ psia(right): top view of point cloud	146
Figure 78: Comparison of experimental nose recession results for an elliptical nose at 17.3 and 39.1 psia stagnation pressures.	147
Figure 79: Comparison of zero angle attack, intermediate pressure runs from top to bottom: spherically blunted cone (23.0 psia), spherically blunted cylinder (19.5 psia), and horizontal oriented elliptical nose (17.3 psia): surface view from top after 3 seconds.....	150
Figure 80: Comparison of zero angle attack, intermediate pressure runs from top to bottom: spherically blunted cone (23.0 psia), spherically blunted cylinder (19.5 psia), and horizontal oriented elliptical nose (17.3 psia): point cloud view from top after 3 seconds	151
Figure 81: Comparison of zero angle attack, intermediate pressure runs from top to bottom: spherically blunted cone (23.0 psia), spherically blunted cylinder (19.5 psia), and horizontal oriented elliptical nose (17.3 psia): point cloud view from front after 3 seconds.....	152

Figure 82: Comparison of zero angle attack, intermediate pressure runs from top to bottom: spherically blunted cone (23.0 psia), spherically blunted cylinder (19.5 psia), and horizontal oriented elliptical nose (17.3 psia): point cloud view from side after 3 seconds	153
Figure 83: Comparison of experimental nose recession for a spherically blunted cone, spherically blunted cylinder and horizontal oriented elliptical nose near 20 psia	154
Figure 84: Comparison of 5° angle of attack, spherically blunted cone at 27.2 psia (left) and 39.9 psia (right): surface mesh viewed from above after 2.5 seconds	157
Figure 85: Comparison of 5° angle of attack, spherically blunted cone at 27.2 psia (left) and 39.9 psia (right): point cloud viewed from above after 2.5 seconds	158
Figure 86: Comparison of 5° angle of attack, spherically blunted cone at 27.2 psia (left) and 39.9 psia (right): point cloud viewed from the side after 2.5 seconds	159
Figure 87: Comparison of 5° angle of attack, spherically blunted cone at 27.2 psia (left) and 39.9 psia (right): point cloud viewed from the front after 2.5 seconds	159
Figure 88: Comparison of 5° angle of attack, spherically blunted cylinder at 20.8 psia (left) and 45.7 psia (right): surface mesh viewed from the front after 2 seconds	162
Figure 89: Comparison of 5° angle of attack, spherically blunted cylinder at 20.8 psia (left) and 45.7 psia (right) after 2 seconds: point cloud viewed from above (top) and side (bottom)	163
Figure 90: Comparison of 5° angle of attack, spherically blunted cylinder at 20.8 psia (left) and 45.7 psia (right) after 2 seconds: point cloud viewed from the front. 164	
Figure 91: Surface mesh as viewed from above of spherically blunted cone at 10° angle of attack after 2.5 seconds from top to bottom: 19.1 psia, 36.8 psia, and 42.8 psia	167
Figure 92: Point cloud of spherically blunted cone viewed from above (top) and the side (bottom) at 10° angle of attack after 2.5 seconds from left to right: 19.1 psia, 36.8 psia, and 42.8 psia	168
Figure 93: Point cloud of spherically blunted cone viewed from front at 10° angle of attack after 2.5 seconds from left to right: 19.1 psia, 36.8 psia, and 42.8 psia ...	169
Figure 94: Schlieren imaging of spherically blunted cone at 10° angle of attack at t = 0 s (top images) and t = 2.5 s (bottom images) from left to right: 19.1 psia, 30.8 psia, and 42.8 psia	170

Figure 95: Surface mesh as viewed from above (left) and side (right) of spherically blunted cylinder at 10° angle of attack after 2.5 seconds at $P_o = 19.2$ psia (top) and 36.7 psia (bottom)	172
Figure 96: Point cloud as viewed from above (left) and side (right) of spherically blunted cylinder at 10° angle of attack after 2.5 seconds at $P_o = 19.2$ psia.....	173
Figure 97: Point cloud as viewed from above (left) and side (right) of a spherically blunted cylinder at 10° angle of attack after 2.5 seconds at $P_o = 36.7$ psia.....	173
Figure 98: Point cloud as viewed from front of a spherically blunted cylinder at 10° angle of attack after 2.5 seconds at $P_o = 19.2$ psia (left) and 36.7 psia (right)	174
Figure 99: Schlieren imaging of spherically blunted cylinder at 10° angle of attack after 2.5 seconds at 19.2 psia (left) and 42.2 psia (right)	175
Figure 100: Schlieren imaging of a spherically blunted cylinder at 0°(left), 5°(center), and 10°(right) angles of attack at high stagnation pressures	177
Figure 101: Comparison of nose recession in ACFD and experimental tests of a spherically blunted cone at zero angle of attack and 6.1 psia stagnation pressure	181
Figure 102: Comparison of nose recession in ACFD and experimental tests of a spherically blunted cone at zero angle of attack and $P_o = 23.0$ psia stagnation pressure	182
Figure 103: Visual comparison of ACFD to experimental result for spherically blunted cone at 23.0 psia stagnation pressure after 6.5 seconds	184
Figure 104: Comparison of nose recession rates of ACFD experiments and experimental tests for a spherically blunted cone at zero angle of attack with $P_o = 6.1, 23.0,$ and 35.4 psia	186
Figure 105: Comparison of ACFD and experimental nose recession for a spherically blunted cylinder at $P_o = 7.5$ psia	188
Figure 106: Comparison of ACFD to experimental nose tip recession rates for a spherically blunted cylinder at $P_o = 19.54$ psia.....	190
Figure 107: Visual comparison of ACFD to experimental results for spherically blunted cylinder at 19.5 psia stagnation pressure after 3.5 seconds	191
Figure 108: Comparison of ACFD to experimental nose tip recession for a spherically blunted cylinder at $P_o = 37.9$ psia	192

Figure 109: Comparison of ACFD and experimental nose recession for a spherically blunted cylinder at $P_o = 7.5, 19.7, \text{ and } 37.9$ psia	193
Figure 110: Comparison of Scott, <i>et al</i> , and sublimation based heating rates for a spherically blunted cylinder	198
Figure 111: Comparison of Equation 26 to Experimental Projections of FIRE II conditions and FIRE II data points (Cauchon, 1967) (Scott, Ried, & Maraia, 1984)	200
Figure 112: Comparison of heating rates on a spherically blunted cylinder for Johnson, Scott, <i>et al</i> , and sublimation based equations	202
Figure 113: Comparison of heating rates on a spherically blunted cone for Johnson, Scott, <i>et al</i> , and sublimation based equations	202
Figure 114: 30 degree cone model on 0.60 inch base	213
Figure 115: Spherically blunted cylinder on 0.60 inch base	214
Figure 116: Spherically blunted cone on 0.60 inch base	215
Figure 117: Elliptical shape with wings on 0.60 inch base	216
Figure 118: Elliptical nose on 0.60 inch base	217
Figure 119: Example of mold for spherically blunted cylinder	218
Figure 120: Spherically blunted cone at a stagnation pressure of 6.1 psia and time = 0.5 seconds	233
Figure 121: Spherically blunted cone at a stagnation pressure of 6.1 psia and time = 1.0 seconds	234
Figure 122: Spherically blunted cone at a stagnation pressure of 6.1 psia and time = 1.5 seconds	235
Figure 123: Spherically blunted cone at a stagnation pressure of 6.1 psia and time = 2.0 seconds	236
Figure 124: Spherically blunted cone at a stagnation pressure of 6.1 psia and time = 2.5 seconds	237
Figure 125: Spherically blunted cone at a stagnation pressure of 6.1 psia and time = 3.0 seconds	238

Figure 126: Spherically blunted cone at a stagnation pressure of 6.1 psia and time = 3.5 seconds	239
Figure 127: Spherically blunted cone at a stagnation pressure of 6.1 psia and time = 4.0 seconds	240
Figure 128: Spherically blunted cone at a stagnation pressure of 6.1 psia and time = 4.5 seconds	241
Figure 129: Spherically blunted cone at a stagnation pressure of 6.1 psia and time = 5.0 seconds	242
Figure 130: Spherically blunted cone at a stagnation pressure of 6.1 psia and time = 5.5 seconds	243
Figure 131: Spherically blunted cone at a stagnation pressure of 6.1 psia and time = 6.0 seconds	244
Figure 132: Spherically blunted cone at a stagnation pressure of 6.1 psia and time = 6.5 seconds	245
Figure 133: Spherically blunted cone at a stagnation pressure of 6.1 psia and time = 7.0 seconds	246
Figure 134: Spherically blunted cone at a stagnation pressure of 6.1 psia and time = 7.5 seconds	247

List of Tables

Table 1: National Hypersonic Wind Tunnel Capabilities with Test Sections larger than 1 ft ² (Antón, et al., 2004)	3
Table 2: Conditions for dynamic viscosity Equation (25)	56
Table 3: Density and Reynolds number for P _o = 6.1 and 47.7 psia of conducted research tests	56
Table 4: High speed camera names, serial numbers and positions.....	57
Table 5: PhotoModeler® data export for point 1012 of test run 2 Jun Test 9	72
Table 6: Displacement of points during solid model runs at various pressures.....	75
Table 7: Error in position of point for a range of camera angles	79
Table 8: Average and standard deviations of stagnation pressures	83
Table 9: Dry ice densities	95
Table 10: Material properties of dry ice at test conditions required for ACFD solver..	104
Table 11: Experimental test results presentation sections arranged by common shape, angle of attack, and feature	106
Table 12: Test conditions for test 2 Jun Test 6	111
Table 13: Coordinate data for point 1035 near the nose tip of test 2 Jun Test 6	117
Table 14: Average rate of recession and percent differences of similar points near the nose of tests 2 Jun Test 6, 2 Jun Test 7, 2 Jun Test 8, and 2 Jun Test 9	120
Table 15: Test conditions of 2 Jun Test 6, 9 Jun Test 1, and 16 Jun Test 1	120
Table 16: Comparison of change in position over 2 seconds for a point near the nose of a spherically blunted cone	127
Table 17: Test conditions of 19 Jun Test 8 and 19 Jun Test 9.....	128
Table 18: Test conditions of 19 Jun Test 8, 19 Jun Test 6, 19 Jun Test 5 and 19 Jun Test 2.....	133
Table 19: Test conditions of 13 Jun Test 3 and 18 Jul Test 3.....	142

Table 20: Average recession rates calculated for a point near the nose of a horizontally oriented elliptical nose for $P_o = 17.3$ psia and $P_o = 39.1$ psia	148
Table 21: Test conditions for 9 Jun Test 1, 19 Jun Test 6, and 13 Jul Test 3	148
Table 22: Average recession rates calculated for spherically blunted cone, spherically blunted cylinder, and horizontal elliptical nose near 20 psia stagnation pressure	154
Table 23: Test conditions for 29 Aug Test 9 and 29 Aug Test 6	156
Table 24: Test conditions for 28 Aug Test 4 and 29 Aug Test 3	160
Table 25: Test conditions for 21 Aug Test 1, 26 Aug Test 4, and 24 Aug Test 3	165
Table 26: Test conditions for 21 Aug Test 3 and 26 Aug Test 6	171
Table 27: Comparison of nose recession in ACFD and experimental tests of a spherically blunted cone at zero angle of attack and 6.1 psia stagnation pressure	180
Table 28: Comparison of nose recession in ACFD and experimental tests of a spherically blunted cone at zero angle of attack and $P_o = 23.0$ psia	183
Table 29: Comparison of nose recession in ACFD and experimental tests of a spherically blunted cone at zero angle of attack and $P_o = 6.1, 23.0,$ and 35.4 psia	185
Table 30: Comparison of nose recession in ACFD and experimental tests of a spherically blunted cylinder at zero angle of attack and $P_o = 7.5$ psia	188
Table 31: Comparison of nose recession in ACFD and experimental tests of a spherically blunted cylinder at zero angle of attack and $P_o = 19.5$ psia	189
Table 32: Average difference comparison between experimental and ACFD results for a spherically blunted cylinder at $P_o = 37.9$ psia	192
Table 33: Comparison of nose recession in ACFD and experimental tests of a spherically blunted cylinder at zero angle of attack and $P_o = 7.5, 19.5, 27.9$ and 37.9 psia ..	194
Table 34: K constants calculated from results and from Sutton and Graves	197
Table 35: Test conditions for recession rate prediction of carbon based, camphor and dry ice at hypersonic velocities	205

List of Symbols

a	= speed of sound m/s
B'	= non dimensional mass transfer parameter
C	= gas species mass fraction
C_D	= drag coefficient
C_H	= Stanton Number
c_f	= local coefficient of friction
c_p	= gas mixture specific heat at constant pressure $J/(kg \cdot K)$
c_s	= species mass fraction
c_v	= gas mixture specific heat at constant volume $J/(kg \cdot K)$
D	= drag force N (Equation (8))
D	= diffusion coefficient m^2/s (Equation (18))
e_s	= internal energy per unit mass J/kg
e_v	= internal vibrational energy J
E	= total energy per unit volume J/m^3
E_v	= vibrational energy per unit volume J/m^3

F = axisymmetric flux vector

G = axisymmetric flux vector

H_{t2} = total enthalpy at stagnation point downstream of normal shock J/kg

h = specific enthalpy J/kg

$h_{w,t}$ = specific enthalpy at the wall at the stagnation point J/kg

K = Sutton and Graves constant _____

k = thermal conductivity $W/(m\ K)$

L = characteristic length (m)

M = Mach number

M = molecular weight (Equation (23))

= mass flow kg/s

n = axis normal to surface (Equations (21) and (22))

n, n' = index of refraction before and after shock respectively

n_s = number of chemical species

Pr = Prandtl number

p = pressure N/m^2

p_{1w} = partial pressure of sublimating species at wall N/m^2

= heat flux W/cm^2

R = universal gas constant $J/(kg \cdot K)$

Re = Reynolds number

Re_D = Reynolds number based on model diameter

Re_L = Reynolds number per characteristic length

Re_x = local Reynolds number

R_N = Nose radius m

r = recovery factor

s = entropy J/K (Equation 1)

S = surface area m^2

S = Sutherland's constant K (Equation (25))

T = temperature K

t = time s

u = velocity component (denoted by subscript) m/s

u, v = axisymmetric velocities (no subscript) m/s

U = vector of conserved quantities

V = velocity magnitude m/s

v_w	= vertical velocity component at wall m/s
W	= source vector
x, y	= axisymmetric coordinates m
α	= material density void ratio
γ	= ratio of specific heats —
δ	= boundary layer thickness m
δ_{ij}	= Kronecker delta
ε	= emissivity
ϕ, ϕ'	= angle of incidence <i>degrees</i>
κ	= thermal conductivity $W/(m \cdot K)$
	= thermal conductivity by the random walk method $W/(m \cdot K)$
μ	= dynamic viscosity $N \cdot s / m^2$
v_{sj}	= Fick's law diffusion flux $mol / (m^2 \cdot s)$
ρ	= density kg/m^3
σ	= Boltzmann Constant J/K
τ	= shear stress tensor component N/m^2

Subscripts:

c = gas species

e = edge of boundary layer

g = gas

ns = normal to surface

o = stagnation value upstream of shock

p = pyrolysis gas

s = denotes species value

s = solid material (Equations (20),(21), and (22))

sub = subliming material

i,j = coordinate direction components

t = denotes stagnation point value

t,ref = reference stagnation point value

t2 = condition at stagnation point downstream of shock

v = vibrational state

w = conditions at the wall

x,y = denotes derivative

∞ = denotes free stream value

1 = condition upstream of shock

2 = condition downstream of shock

Superscripts:

T = transpose

List of Abbreviations

3dFIAT	Three-dimensional Finite-volume alternating directional Implicit Ablation and Thermal response code
ACFD	Ablation Computational Fluid Design
AFIT	Air Force Institute of Technology
AFRL	Air Force Research Laboratory
CEA	Chemical Equilibrium Analysis
CFD	Computational Fluid Dynamics
DPLR	Data-Parallel Line-Relaxation
FIAT	Fully Implicit Ablation and Thermal response code
FRSI	Felt Reusable Surface Insulation
GIANTS	Gauss-Seidel Implicit Aero thermodynamic Navier-Stokes with Thermochemical Surface boundary conditions
HRSI	High-temperature Reusable Surface Insulation
LAURA	Aerothermodynamic Upwind Relaxation Algorithm
LRSI	Low-temperature Reusable Surface Insulation
NASA	National Aeronautics and Space Administration

PIV	Particle Image Velocimetry
PMV	PhotoModeler® Video module
PRM	Photogrammetric Recession Measurement
RBAC	Office symbol for Computational Sciences Branch, AFRL
RCC	Reinforced Carbon Carbon
STS	Shuttle Transport System
TITAN	Two-dimensional Implicit Thermal Response and Ablation
TPS	Thermal Protection System
US	United States

PHOTOGRAMMETRIC MEASUREMENT OF RECESSION RATES OF LOW TEMPERATURE ABLATORS SUBJECTED TO HIGH SPEED FLOW

1. Introduction

1.1 Background and Motivation

With the resurgence of interest in hypersonic flight vehicles, research into the behavior of ablative heat shields has likewise increased. Since the 1970's, heat shield research in the US Air Force and NASA has been primarily focused on the development of reusable technologies such as the ceramic tiles on shuttle. Now, NASA has revisited the capsule-like design in its latest Constellation vehicle. With the renewed focus on this design, NASA has also elected to return to an ablating heat shield instead of a fully reusable one. In a similar vein, the United States Air Force is investigating ablative heat shield material for hypersonic lifting bodies.

An ablative heat shield operates by absorbing energy from the flow and expending it in a phase change of the heat shield material. Operational carbon-based heat shields such as on Apollo sublime around 3600 K. The extreme conditions of atmospheric entry with very high Mach numbers and stagnation temperatures in the thousands of degrees are very difficult to produce and maintain in a test environment.

The most feasible way to simulate a heat shield's operational environment in a laboratory environment is to use an arc-jet set up. An arc-jet uses an electric arc in a wind tunnel to heat the test medium as it is expanded in a converging-diverging nozzle to

high supersonic speeds. Typical run times can vary from a few seconds to a few minutes depending on test conditions and particular tunnel capabilities. Recession rates in arc-jets have historically been collected using film with lighting provided by the self-luminance of the test article, which required a processing time of approximately 24 hours. Additionally, the tip of the test article is much brighter than downstream locations, and this extreme contrast makes images for comparison with calibration points difficult to obtain (Sherrouse, Sheeley, Mansfield, & Rotach, 2003).

One consideration when using an arc-jet is that mixing between the flow gas and the electric arc can make the free stream characteristics difficult to define (Bertin, 1994, p. 171). Other considerations for arc-jet facilities are the expense to operate and limited number of available facilities. In 2004, a RAND Corporation survey of hypersonic wind tunnels found eleven national and three private tunnels capable of speeds above Mach 5 with test cross-sectional areas of a square foot or greater. Of these, only ten tunnels have aero heating capabilities. The eleven national tunnels referenced in the RAND report are shown below in Table 1. The RAND report does not include commercially owned tunnels like those found at Lockheed and Boeing as those are not typically available for general research purposes. The study also determined that there were eighteen hypersonic tunnels available for research outside of the United States (Antón, et al., 2004).

A tunnel not included in this study exists at NASA Ames and is capable of Mach 5 with air, and Mach 8 and 14 with nitrogen (Beresh). According to these two reports, there are then thirty-five wind tunnels in the world capable of testing at hypersonic speeds, and time at these tunnels is limited and may be costly. Also, many of these

tunnels aim at a specific style of testing as well. For instance, the Langley tunnels are typically utilized for preliminary design where as the Arnold tunnels are operated for production testing (Antón, et al., 2004).

Table 1: National Hypersonic Wind Tunnel Capabilities with Test Sections larger than 1 ft² (Antón, et al., 2004)

Location	Tunnel Name	Mach Range
Langley	20-Inch CF4	6.0
	20-Inch Air	6.0
	31-Inch Air	10.0
Arnold EDC	VKF Tunnel A	1.5-5.6
	VKF Tunnel B	6 or 8
	VKF Tunnel C	10.0
	Hypervelocity Wind Tunnel 9	7,8,10,14,16.5
	Hypervelocity Range/Track G	24k fps
	Hypervelocity Impact Range S1	28k fps
Army/ CUBRC	LENS I	8.0-18.0
	LENS II	4.5-8.0
Ames	HWT	5,8,14

Limitations in the availability of facilities and their capabilities are not new, and from the beginning efforts were made to find more economical means of testing ablation. As early as the 1950s, research was under way using materials which undergo ablation at much lower temperatures and pressures than the actual ablative materials' environment (Anderson D. E., 1960).

Ablative heat shields ideally sublime directly from a solid to a gas to take advantage of the energy absorption of the phase change (Sutton G. W., 1982, p. 4). Therefore it is important in low temperature simulations that the material must sublime directly to a gas at the stagnation temperatures of the test. In this regard several efforts,

of varying degrees of success, were made using dry ice, paradichlorobenzene, naphthalene, camphor, and ammonium chloride (Kohlman & Richardson, 1969).

Except for dry ice, these materials require stagnation temperatures above room temperature to yield substantial material loss on the model and would therefore need the wind tunnel to be heated to observe sublimation. Camphor, for example, sublimates at $\sim 170^{\circ}\text{C}$. With the reestablished interest in expendable ablative heat shields, these past experiences have prompted a renewed interest in improving low temperature ablation simulation studies.

A further limitation on ablation data is the lack of three-dimensional data capture over time. Historically, most published data included either quantitative rates of a single location, typically the nose tip, or before and after comparison measurements. Other tests looked at surface patterns such as cross-hatching but were not focused on recession rates.

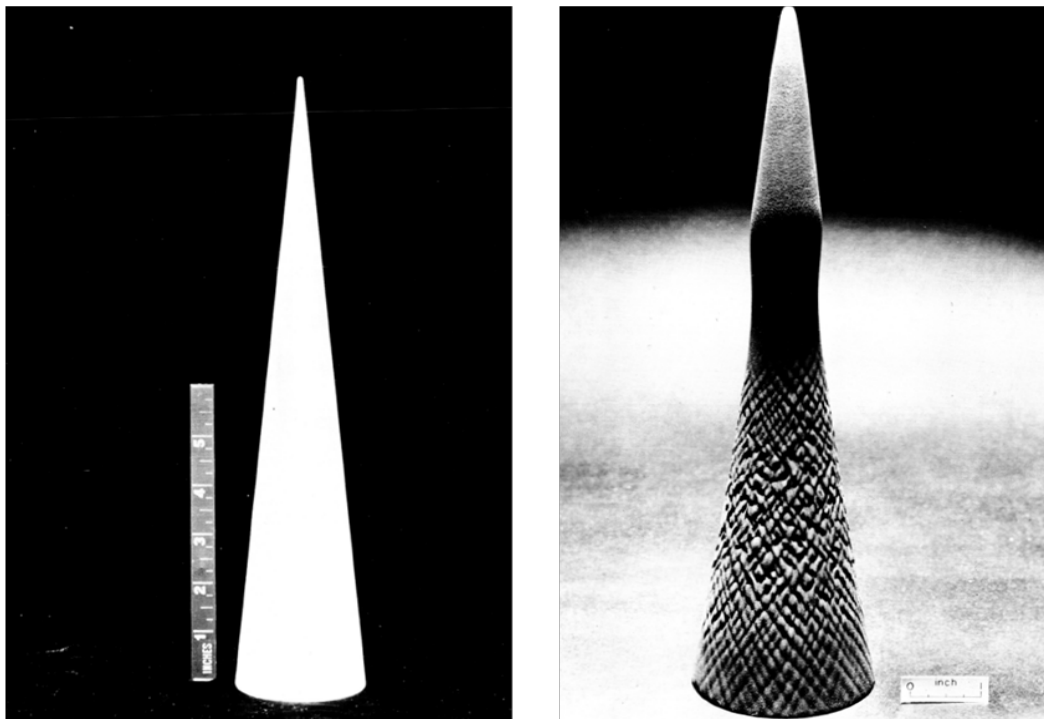


Figure 1: Teflon test article before and after exposure to rocket engine showing cross-hatching (Larson & Nachtsheim, 1970)

Examples of these before and after images are shown in Figure 1 and illustrate cross-hatching on a test vehicle as seen in NASA Ames research from 1970. These models were made of Teflon composites and were exposed to the thrust of a 4,000 lb rocket engine for 3.5 seconds to produce these results (Larson & Nachtsheim, 1970). Points of interest in these two images are not only the cross-hatching but also the blunting of the nose and necking down of the cone near the transition point. Typically in tests like this, data comes from measurements taken before and after tests by physically measuring the test article. Clearly, the shape change shown in Figure 1 is three-dimensional.

The capability to capture the ablation process in three-dimensions as it sublimates would add significant contributions to understanding the process that is occurring. This was recognized by Schairer and Heineck (2007) who developed a method they called Photogrammetric Recession Measurement (PRM). Photogrammetry is a widely accepted approach to determining three-dimensional locations of objects and has been used in a wide variety of applications including crime scene investigations and construction projects. The PRM process of Schairer and Heineck (2007) utilized two cameras recording images of the self luminescent surface of an ablating body in an arc-jet facility. The images taken from different viewing angles were then correlated using a processing technique, which the authors describe as similar to stereo particle image velocimetry, to establish a three-dimensional representation of the shape over time. Importantly, PRM depends upon distinguishable surface features which are generally absent in a smooth homogenous surface such as a dry ice model (Schairer & Heineck, 2007).

A different photogrammetry technique that does not require distinguishable features is laser dot projection. Laser dot projection has been successfully applied to three-dimensional surface mapping such as gossamer flight structures and micro air vehicles (Pappa, Black, Blandino, Jones, Danehy, & Dorrington, 2003) (Svanberg, Reeder, Curtis, & Cobb, 2009). A search of the literature suggests that this technique has not been applied to surface changes of an ablating body prior to this research.

1.2 Research Objectives

The purpose of this research project is to collect three-dimensional experimental ablation data under well-controlled conditions for the purpose of validating and improving a computational model currently used by AFRL/RBAC. A novel photogrammetric method was developed that combined PRM and laser dot projection and was applied to measure three-dimensional shape change of dry ice models exposed to Mach 3 free stream conditions. To facilitate the research, a method was developed which enabled a wide variety of models to be built in-situ. The research presented herein is categorized into four incremental research tasks:

1. Reliable and reproducible fabrication of test articles.
2. Capture of ablation recession in three dimensions.
3. Comparison with computational modeling performed by AFRL/RB, which incorporates shape change results.
4. Scaling or relating the data to real world conditions

1.3 Original and Significant Contributions of Research

As stated previously, published results marrying the two techniques of PRM and laser dot projection has not previously been accomplished for the use in recession of an ablating surface. The capability to capture three-dimensional ablation in real-time provides a significant research capability in the area of ablating bodies. This enabling technology was developed in the research herein to provide real-time measurements of ablation rates utilizing this technique and combining it with advanced imaging techniques. The results of this research provide researchers with a tool to further ablation studies in a wide array of conventional high speed wind tunnels while avoiding the limited availability and cost of high temperature, hypervelocity tunnels.

Additionally, the experimental results of this research provide much needed data points for validation of computational models with comparisons to AFRL's ACFD code. And unlike some computational models, experimental data does not become obsolete; therefore this data is available for future comparisons to even more advanced computational models.

1.4 Material Selection

When a material sublimates, the material undergoes a phase change from solid to gas with no intermediate liquid phase. In a closed wind tunnel system, such as a blow-down-to-vacuum wind tunnel, sometimes called a pressure-to-vacuum, like the AFIT high speed wind tunnel facility, this material may condense over time and foul the

vacuum chamber and pump. Dry ice, or solid carbon dioxide, has been chosen as the test material in part to avoid this issue. It has a low sublimation temperature and vapor pressure, and the byproduct of dry ice ablation is gaseous carbon dioxide, which is safe in the lab environment, does not risk damage to the wind tunnel and can be pumped out by the vacuum pump. Furthermore, the relatively high triple point of the carbon dioxide ensures that melting is avoided, greatly simplifying the analysis of the data. Also, dry ice is easy and inexpensive to manufacture or procure.

1.5 Organization of Dissertation

Chapter 2 presents a discussion of the hypersonic flow regime, basic governing equations, thermal protection systems, historical overview of low temperature ablation research, computational fluid dynamics, measurement techniques, and properties of dry ice. In chapter 3, the test facilities, test set up, test procedures, dry ice model fabrication technique, and accuracy and limitations are described in detail. Chapter 4 provides a discussion of the experimental data from tests involving a spherically blunted cone, spherically blunted cylinder, and elliptical nose at 0, 5, and 10 degree angles of attack. Chapter 5 compares the results presented in chapter 4 to the ACFD model, FIRE II data, theoretical stagnation heating trends, and a non dimensional analysis of the data. Chapter 6 concludes the discussion and suggests future studies for consideration.

Appendix A contains model diagrams for all of the test articles, and Appendix B contains the input parameters for ACFD. Appendix C presents the master list of the experimental tests' conditions and useable data frames. Appendix D contains an entire

output of data points for test 2 Jun Test 6 at half second intervals. Appendix E presents the spreadsheet to support the constants found in Section 5.3.

2. Literature Review

Chapter 2 presents a background review of the areas of interest and the history of low temperature ablation research. The hypersonic region and thermal protection systems are discussed; previous research on low temperature ablators is presented; computational models of note are discussed; and classical experimental techniques and properties of dry ice are explored.

2.1 Hypersonic Flow Region

Typically real world ablators operate at very high Mach numbers. The flow properties of this region of very high Mach numbers are described as the hypersonic flow region which is generally defined as flow above Mach 5. The hypersonic flow region is characterized by certain phenomena in the flow: thin shock layers, entropy layer, viscous interaction, and high temperature effects.

Thin shocks form as the Mach number increases, and the distance between the body and the shock wave becomes thin which can interact with a thickening boundary layer. Also as the Mach number of the flow increases, the stronger shocks lead to larger entropy increases. Strong entropy gradients are generated by curved shocks around a blunt nose and propagated downstream creating an entropy layer. The entropy layer leads to an area of strong vorticity interaction, demonstrated by Crocco's theorem. Due to this vorticity interaction, typical boundary layer calculations are faulty in a real flow

because the proper conditions at the outer edge of the boundary layer are uncertain (Anderson J. D., 2003, pp. 255, 550-552).

Hypersonic flow contains a large amount of kinetic energy which is partially transferred into internal energy through the process of viscous dispersion. This viscous interaction causes the temperature to increase, and as the temperature increases, the pressure normal to the body remains constant. The equation of state, shown in Equation (1), dictates that as the temperature increase and pressure remains constant, the density must decrease. The mass flow through the boundary layer, however, remains constant and so the boundary layer must grow larger.

(1)

The larger displacement thickness caused by the viscous dispersion displaces the inviscid flow outside the boundary layer causing the body to appear larger than it truly is. The changed inviscid flow field then in turn affects the growth of the boundary layer. This interaction between the inviscid and boundary layer is referred to as the viscous interaction and can affect the surface pressure distribution on a vehicle or body (Anderson J. D., 2003, pp. 552-553).

The increased thickness of the boundary layer for compressible laminar flow over a flat plate can be seen in Equation (2). Here δ is the boundary layer thickness, Re_x the local Reynolds number, and M_∞ is the free stream Mach number. From Equation (2) it can be seen that δ increases with Mach number squared and therefore will increase exponentially as Mach number increases for a specific x . If Mach number is held

constant, the boundary layer thickness will also increase with position x along the body (Anderson J. D., 2003, pp. 552-553).

$$\delta = \frac{5x}{\sqrt{Re_x}} \quad (2)$$

At hypersonic speeds the temperature increase caused by viscous dissipation can be large enough to cause dissociation and ionization of the gas. When dissociation occurs, the flow becomes a chemically reacting flow which among other things causes a high heat transfer rate to the surface of the vehicle. And if the shock layer temperature gets high enough, the gas will radiate energy which must be taken into account through the addition of a radiative flux. This can have a large impact at higher Mach numbers such as in the Apollo reentry which received 30% of its total heat transfer from radiative heating (Anderson J. D., 2003, pp. 550-555).

Convective heat transfer in a compressible flow is well-documented in many classic textbooks, though consideration of phase change is generally an advanced topic. Here an abbreviated overview is provided to document important variables to consider. When temperature varies within a flow field, the energy equation can be expressed using the Prandtl number, Pr , defined in Equation (3), where “ k ” is the thermal conductivity of the gas, μ is the viscosity, and c_p refers to the specific heat at constant pressure for the gas.

$$Pr = \frac{\mu c_p}{k} \quad (3)$$

For heat transfer to a surface, the local Stanton number, denoted C_H , is defined in Equation (4), where r is the recovery factor, the subscript “w” refers to wall conditions, and the subscript “e” refers to conditions at the edge of the boundary layer.

$$\frac{q_w}{\rho_e u_e (h_w - h_e)} = C_H (h_w - h_e) \quad (4)$$

The Reynolds analogy, discussed in (Anderson J. D., 2001) for example, leads to a relationship where the local Stanton number can be expressed in terms of the Prandtl number and local skin friction, c_f , defined in Equation (5).

$$C_H = \frac{c_f}{2 Pr} \quad (5)$$

The local skin friction is generally a function of Reynolds number, Re and Mach number. Thus, to characterize the local convective heat flux due to aerodynamic heating, each of these gas properties and conditions in the above discussion.

In practice, stagnation regions exposed to a hypersonic flow is subject to very high heating rates, and therefore, determining heating rates at the stagnation point is critical for design. A remarkable derivation of the heat flux at a stagnation point of a sphere subjected to a hypersonic flow was derived from first principles by Fay and Riddell, as documented, for example in (Bertin, 1994). They derived the formula which demonstrated that heat flux was inversely proportional to the square root of the sphere radius. According to (Anderson J. D., 2000), this result which many found to be counter-intuitive, was anticipated by Julian Allen, who had introduced the concept of using a blunt body for reentry as early as 1951.

When the surface of the aerodynamic body changes as a result of heat transfer to the body, the problem becomes even more challenging. Even for the relatively simple case of a solid body subliming into a gas, one must consider that the gas resulting from phase change enters the boundary layer initially at the same temperature as the solid. Despite leading to a more complicated problem for predicting the conditions, from a design perspective this is often considered beneficial as the subliming gas can assist in cooling the wall of the body at points downstream. The phase change from a solid to a gas also adds the complication that the shape of the aerodynamic body changes with time. Nonetheless, a pure subliming body does offer advantages in that the temperature at the surface is essentially constant once it reaches the phase change condition, as long as shape changes does not lead to differences in the phase change temperature due to pressure. The pure ablator is therefore considerably simpler to analyze than a body where the liquid phase is present or when chemical reactions occur. It is for this reason that pure ablators have been the subject of many idealized experimental studies in hypersonic flow environment.

The mass flow of ablative material leaving the surface is affected by the aforementioned heat transfer parameters and is additionally a function of the density of the solid, heat of sublimation of the solid, the heat capacity of the solid, the conductivity of the solid, and geometry. To deal with the introduction of gas from the surface, a mass addition parameter is generally introduced, as given in Equation (6). Here \dot{m} is the mass flow of ablative material sublimating from the wall; ρ_s and c_p are the density and

velocity at the edge of the boundary layer and C_H is the Stanton Number (Jumper G. Y., 1975, p. 10).

(6)

To establish the amount of gas introduced via phase change, consider that the portion of the heat flux to the body which yields phase change depends on the density of the solid and the heat of sublimation of the solid. Conceptually, heat transfer may also take place via conduction from the surface through the body. So, in general, the thermal conductivity and heat capacity of the solid would also need to be considered in the general problem. Furthermore, when the temperature is sufficiently high, one would generally have to account for radiative heat transfer as well. Any heat transferred away from the surface due to the conduction or radiation would reduce the blowing ratio. By contrast, heat transferred to the body via conduction or radiation would increase the blowing ratio. So in addition to the gas properties, the properties of the solid (density, heat of sublimation, thermal conductivity, and heat capacity) are also critical to include in a complete analysis of a pure ablator subjected to high speed flow.

An approximate relation of surface heating at the stagnation point is found in Equation (7), where it can be seen that the heat flux at the wall, q_w , increases with respect to velocity cubed, assuming the Stanton number, C_H , is held constant.

(7)

Equation (8) presents the drag, D , on the vehicle which increases with velocity squared, reference area, S , and coefficient of drag, C_D . Equation (7) and Equation (8) suggest that as the vehicle increases to higher Mach numbers, the surface heat transfer is increasing faster than the drag on the vehicle. For this reason, heat transfer is typically the dominating design factor for hypersonic vehicles (Anderson J. D., 2000, pp. 288-291).

$$\text{---} \tag{8}$$

These conditions, particularly the high temperatures, lead to the need for a protection system for the vehicle. Weight is a key design requirement of both spacecraft and aircraft; therefore their structures are typically made of a lightweight material. Aluminum is a common structural material in both types of vehicles but its melting point is only 700°F (644 K). For example, the internal frame of the space shuttle is primarily made out of aluminum, and with re-entry temperatures on the orbiter ranging from 600°F (589 K) to 2500°F (1644 K). In the case of the shuttle orbiter, the structure itself must be protected. Payload and personnel also need protection from the intense heat of reentry; therefore, a thermal protection system (TPS) is required to protect the vehicle from the external environment (Damon, 2001, pp. 145-150). Additional consideration of stagnation point heating is given in Chapter 5.

2.2 Thermal Protection Systems

Thermal protection systems (TPS) can be explained most simply as a system that reduces the heat transferred from the external thermal environment to a range within operational limits of the structure and payload. The two most common types of thermal protection systems in use for aerospace operations today are the reusable tiles on the space shuttle and ablative heat shields which were used, for example, on the Mercury, Gemini, and Apollo missions (NASA, 2000).

A third system mentioned is a heat sink which was most prominently used in the ballistic only Mercury missions. An ablation shield eventually won out due to safety concerns on performance and landing weight issues for the orbital missions (Swenson, Grimwood, & Alexander, 1989).

2.2.1 Reusable Thermal Protection Systems

NASA's Space Shuttle system has five different types of TPS in use. The three most obvious are the High-temperature Reusable Surface Insulation (HRSI) tiles which are black, Low-temperature Reusable Surface Insulation (LRSI) tiles which are white, and Reinforced Carbon-Carbon (RCC) tiles which are gray and found on the leading edges and nose cone. There are also Felt Reusable Surface Insulation (FRSI) blankets as well as two newer materials: Flexible Insulation Blankets and Fibrous Refractory Composite Insulation (NASA, 2000). A visual representation of the positions of each tile can be seen in Figure 2 (Day, 2003).

Each type of tile or blanket has a different thermal capability. For example, RCC can withstand up to 3000° F (~1922 K) while HRSI can only take 2300° F (~1533 K). While they have different capabilities, they all function on the same principle, which is to have a noncatalytic surface and a low internal thermal conductivity. The TPS material is such a poor conductor of heat that a tile can be handled while it is still red hot (NASA, 2000).

By their nature, TPS tiles are very easily damaged and as seen in the loss of Columbia, even a small amount of damage can lead to a catastrophic failure of the system. Another major drawback to this type of thermal protection system is the maintenance involved in its upkeep. In shuttle mission STS-85, the TPS required about

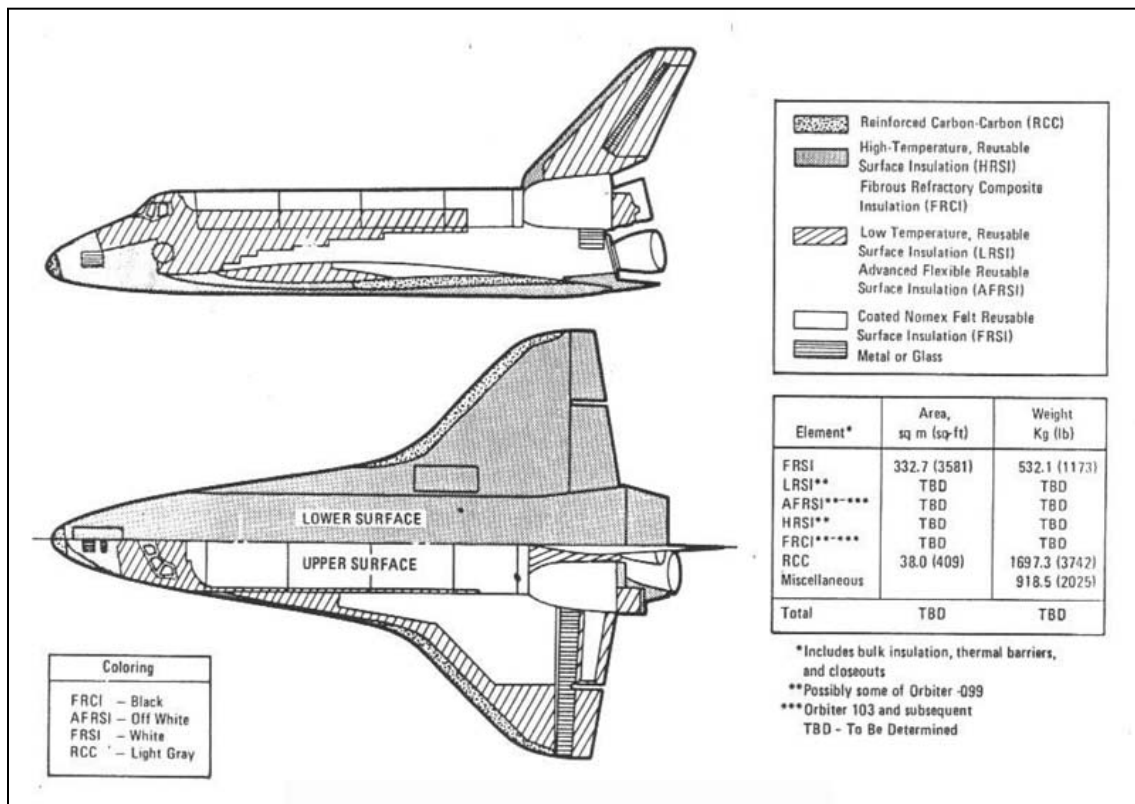


Figure 2: Shuttle Orbiter tile locations (Day, 2003)

37,000 man hours for preparation (Moster, Callaway, & Bhungalia, 2005). This maintenance requirement limits the operational tempo a vehicle can sustain and increases the budget requirements.

2.2.2 Ablating Thermal Protection Systems

Hankey defines ablation as a heat absorbing method that “results in a change of phase of the substance” (Hankey, 1988, p. 6). The concept of ablation is that an ablative surface absorbs energy through conduction until it reaches a temperature for degradation or pyrolysis of the substance to occur. The absorption of energy in this phase change process protects the underlying structure or vehicle. Ablation can be divided into two categories of interest for this research: sublimation and charring.

Subliming ablators transition directly from the solid to the gaseous state. In this process, the material absorbs energy until the sublimation temperature is reached at which point the solid material converts to gas with no liquid phase. The vehicle is protected through the energy absorption in the phase change and reduction in the convective heat flux by the transpiration effect from the subliming surface. Drawbacks to typical pure subliming ablators such as Teflon are brittleness and low resistance to thermal stresses (Sherman, 1968, pp. 5-7).

When the surface temperature of a carbon based ablator reaches a certain point, typically 500-800 K, the material begins to decompose or pyrolyze. As the surface goes through pyrolysis, the thermal energy absorbed by the ablating material breaks down the material and releases gas products, leaving behind a carbon residue that is referred to as char. This process needs no reagents, such as oxygen, and will penetrate into the material

as the thermal energy soaks through. The area undergoing this process is referred to as the pyrolysis zone. As the heating continues, the pyrolysis zone expands and a char layer of carbon will begin to form on the surface of the ablative material. This char layer acts as a heat sink until it too begins a process of oxidation or sublimation. A carbon char usually sublimates at temperatures near 3600 K. The surface temperature is then fairly constant at the vaporization or melting point of the ablating material until it is consumed. A thick char can be a good insulation barrier as it will radiate heat away from the surface. However most char layers are brittle and can be removed by shear and spallation leaving the underlying structure unprotected (Sherman, 1968, pp. 8-9). The char layer protects the ablation material underneath. As the char layer breaks down the process of forming a char layer starts again (Koo, Ho, & Ezekoye, 2006).

The Apollo program used a charring ablator named AVCO-5026-H/CG for the heat shield of the command module. This ablator material consisted of phenolic microballoons embedded in a Novolac resin. This was in turn formed in a phenolic honeycomb. These heat shields withstood temperatures approaching 5000° F (Williams, Curry, Bouslog, & Rochelle, 1993).

2.3 Ablation Studies

The most effective test is a real world test under true flight conditions and profiles. This is, however, very expensive and time consuming with most launches costing millions of dollars. It is also difficult to observe the test article during such tests.

A commonly referenced test is the FIRE II NASA test in 1965 part of which is presented for comparison in Chapter 5 (Cauchon, 1967).

In addition to measuring the start and ending body shape, some experiments used embedded sensors; however embedded sensors generally interfere with the article being tested. The next logical step is to simulate the flight profile; however, ablative heat shields operate in an environment near 3000 K and Mach 15-20 which is not easily reproduced in a laboratory.

Typically, wind tunnel ablation studies are performed in arc-jet facilities. These facilities use an electric arc to heat the flow to simulate the massive heating encountered at hypersonic speeds. The two most common measurement techniques of an ablating body in this flow are shadowgraph imaging and filming the test using the test article's self-luminance. Using self-luminance is time consuming and sometimes the brightness of the forward part of the model makes imaging the rest of the body difficult. The recession rates are backed out by manual evaluation of the images. The shadowgraph or Schlieren images, which yield views of areas of density change, are taken over time of the model to collect a side view of the change of shape in addition to the shock waves in the stream. The ablation rates are then backed out from the images using the known initial dimensions of the test article. An example of a shadowgraph is shown in Figure 3 (Sherrouse, Sheeley, Mansfield, & Rotach, 2003).

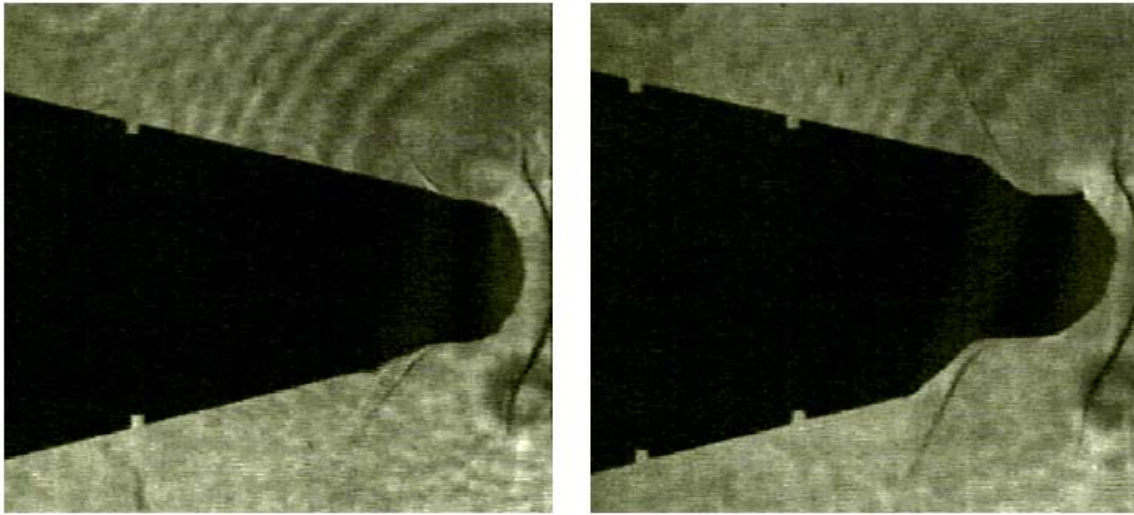


Figure 3: Shadowgraph Images taken at Arnold Engineering Development Center's High Enthalpy Ablation Test Unit H1 (Sherrouse, Sheeley, Mansfield, & Rotach, 2003)

2.4 Low Temperature Ablation Studies

This section provides a brief overview of research in low temperature ablation of interest presented by and large in chronological order. These are not the limit of available research, but are a reasonable representation of papers pertinent to the ongoing research.

An early study of low temperature ablation research dates to 1960 in a master's thesis by David E. Anderson at the California Institute of Technology. Anderson worked with Lester Lees and Toshi Kubota in an investigation of ablation modeling using dry ice (CO_2), water ice (H_2O), and camphor ice ($\text{C}_{10}\text{H}_{16}\text{O}$) (Anderson D. E., 1960).

Anderson's tests were performed at Mach 5.8 and 149 C stagnation temperature in a 5 x 5-in test section and at Mach 8.0, 482 C in a 7.1 x 7.3-in test section. Anderson's test articles were mostly hemisphere-cylinders with a diameter of 1-in with one model being produced for a state of constant heat transfer over the surface. The CO_2 models were made by compressing crushed dry ice in a mold. The camphor models were

produced similarly by compressing camphor granules under 8,000 pounds of hydraulic pressure. Anderson had difficulty in the preliminary tests involving the dry ice models with what he called flaking, where large portions of the models would come apart. This, coupled with the difficulty at the time of manufacturing and storing the dry ice models, led to no quantitative data being recorded for cases where CO₂ was used as the model material (Anderson D. E., 1960).

The water ice and camphor ice models proved more productive and recession rates were taken via time delayed silhouette photography. A 35 mm camera with a 135 mm telephoto lens was used to take photographs at specific times during the test runs which averaged 7 minutes long. The sublimation rates were then calculated, compared to theory, and found to be noticeably less than expected. The largest source of error was decided to be the low picture sharpness. This was determined to be caused by the tunnel plate glass windows coupled with oil films which developed from tunnel operation (Anderson D. E., 1960).

A journal paper by David Kohlman and Richard Richardson (Kohlman & Richardson, 1969) had important ramifications on the present research due to their successful work with dry ice models. The primary focus of their work was to develop a fabrication method for solidified CO₂ wind-tunnel models and to investigate the feasibility of using dry ice for studying ablation effects.

Kohlman and Richardson's (Kohlman & Richardson, 1969) wind tunnel tests were run at Mach 2.38 with a 2 x 3.5 in test section. Their tests were accomplished by drawing in air from the atmosphere through the nozzle and test section into a vacuum

tank system. They noted that dry ice sublimation temperatures range from -78°C to -130°C while its triple point (-59°C , 79 psia) is high allowing sublimation to occur without melting during model fabrication. Kohlman and Richardson also noted other reasons for selecting dry ice as their medium: the low temperature vapor pressure is of the same order as higher temperature ablators; the ablation products of CO_2 are simple and safe; dry ice has a low heat of sublimation (248 Btu/lb at 1 atm); and dry ice provides significant ablation over the duration of a run.

Kohlman and Richardson's (Kohlman & Richardson, 1969) thoroughly documented fabrication technique is feasible for the current test setup with some modifications. Their process involved a high pressure zinc mold and forming the model from liquid CO_2 around an insulated mandrel. Recession rates at the nose were measured using time delay photography with images acquired roughly at one-second intervals, and heat transfer was measured with imbedded thermocouples. The recession rates found were in good agreement with predicted values near the nose of the test article.

In 1971, Fred Lipfert and John Genovese (Lipfert & Genovese, 1971) conducted an investigation of dry ice and camphor models in an experimental study on boundary layers to model the ablation of Teflon during flight. For model fabrication, Lipfert and Genovese took commercially available dry ice bricks and cut the model out using a specially designed rotating cutting blade while camphor models were formed from casting. Both models were fitted with a steel nose cone to prevent nose tip ablation as the research was primarily devoted to the effect of mass addition into the boundary layer. The experiments were run at Mach 6 with 6-in diameter models.

In their experiments, Lipfert and Genovese (Lipfert & Genovese, 1971) investigated the use of several types of imaging techniques. All tests were recorded using a high-speed video camera as well as time delayed photography. The video was used for analyzing ablation patterns while the photographs were used for recession rate data. An attempt was made to use a laser follower to map the ablation; however, there were difficulties encountered with the surfaces becoming translucent. It was determined that the location of the effective optical reflecting surface was offset from the actual model surface and the detector had trouble with the image being weak and causing distortion.

A cross-hatched pattern developed on the surface of both the dry ice and the camphor ice, similar to that shown in Figure 1, which represents areas of local intense ablation. Lipfert and Genovese believed the phenomena could account for sublimation rates that were above expected theoretical values. Lipfert and Genovese concluded that the tests proved the feasibility of using low temperature ablators for the study of boundary layers and that limited test results indicated that the theory tended to underestimate the turbulent blowing rates and local ablation peaks (Lipfert & Genovese, 1971).

In 1978, Chen (Chen C. J., 1978) simulated entry into the atmosphere of Jupiter by developing extensive derivations of similarity equations for comparison between the low temperature and realistic entry conditions on Jupiter. To simulate the Jovian reentry, the author offered the combinations of dry ice-air, dry ice-helium, dry ice-steam, or camphor-nitrogen combinations. Based upon the ratio of viscosity-density product, the ratio of thermal conductivity, and two Prandtl numbers for a given temperature, pressure

and density, Chen chose to use dry ice in air for his simulation of a graphite heat shield in a hydrogen atmosphere.

Chen's simulation incorporated the idea of recreating the conditions behind the shock in a supersonic wind tunnel. Chen developed similarity parameters and used the balance of radiative energy flux to the rate of energy absorbed by sublimation to simulate the conditions. Of interest is Chen's intended use of heat lamps pointed at the model to simulate energy transferred from the shock to the vehicle (Chen C. J., 1978).

In a journal article published in 1988, Jumper and Hitchcock (Jumper & Hitchcock, 1988) investigated a pure subliming substance, dry ice, and a dry ice model imbedded with glass beads to represent the presence of a non ablating material. Jumper and Hitchcock's research was conducted at 0.1 Mach with a free jet and data was captured by superimposing images over time to graph the silhouette shape of the test article. They found that the pure subliming substance behaved as predicted by simple thermo chemical models; however, these equations predicted no change with addition of the glass beads while the experimental results found a reduced stagnation-point mass loss of 23%. This journal article was based upon an AFIT dissertation written by Jumper in 1975 (Jumper G. Y., 1975).

It is noted that there was a tendency for the level of published research activity in general and low temperature ablation research to slow down in the mid 1970's. This corresponds to the NASA decision to switch from ablatives to reusable tiles in space access vehicles. Other than some research on transpiring walls of solid rocket motors (Ma, Van Moorhem, & Shorthill, 1990) (Barron & Van Moorhem, 1998), low

temperature ablation studies were difficult to find in the literature until the turn of the century.

Around 2000, research was begun at the University of Texas at Austin into the effects of ablation onset caused by a forward facing cavity (Silton & Goldstein, Ablation Onset in Unsteady Hypersonic Flow About Nose Tip with Cavity, 2000). Computational modeling of the forward facing cavity was accomplished using INCA v2.5, COYOTE v2.5, and GRIDALL. In 2003, Silton and Goldstein published an experimental validation of their computational work (Silton & Goldstein, Optimization of an Axial Nose-Tip Cavity for Delaying Ablation Onset in Hypersonic Flow, 2003). They chose to use water ice for a low temperature ablator due to it being inexpensive, well-characterized, easily molded and very lab safe. Water ice also has a low sublimation temperature, but melts rather than sublimates at room temperature which complicates the analysis. Silton and Goldstein's test runs were performed at the Mach 5 blow-down wind tunnel at Austin's J.J. Pickle Research Center Wind Tunnel Laboratory. Test conditions were Mach 4.91, stagnation temperature of 370K, and stagnation pressure of 2.30MPa in a 15.24 x 17.78 cm test section. The models were made by using liquid N₂ to freeze water mixed with fiberglass threads for structural support. This process provided them with a model well below melting temperature for set up. A shroud was used to protect the model until test conditions were reached, at which point the shroud was released and allowed to progress downstream. Video cameras (Canon L1 Hi-8 and Canon GL1) were used to capture the test at 30 Hz. This was then used to calculate the onset of ablation. Silton and Goldstein's research was aimed at determining the onset point based on the size and shape of the

forward facing cavity and did not capture ablation rates. The video was analyzed to determine the time of ablation onset and track the onset with respect to the characteristics of the forward facing cavity (Silton & Goldstein, Optimization of an Axial Nose-Tip Cavity for Delaying Ablation Onset in Hypersonic Flow, 2003).

The limitations found in the early low temperature ablation research were primarily in data capture and model fabrication techniques. The research presented herein expands upon the Kohlman and Richardson (Kohlman & Richardson, 1969) fabrication technique to conduct rapid model fabrication and utilizes modern methods of image capture to gather recession rates across the test article with sub millimeter accuracy.

2.5 Computational Modeling of Fluid Dynamics and Ablation

Modeling of a vehicle undergoing ablation must incorporate several complex conditions. For the purpose of heat shields, ablation occurs at hypersonic speeds, and thus brings in to play the phenomena discussed previously that are associated with hypersonic flow: thin shock layer, strength of shock wave, merging of the boundary layer with the shock layer, and dissociation and ionization of the fluid (Anderson J. D., 2003, pp. 549-550). Modeling ablation must also take into account the link between heat transfer, phase change, chemical reaction, and gas dynamic sub-processes (Mullenix, Povitsky, & Goitonde, 2008).

At hypersonic speeds, the flow can no longer be assumed to be ideal and the various chemical reactions in the flow itself should be included. The boundary condition at the wall must also be carefully considered as two things of primary interest are happening, (1) the boundary is ablating and therefore changing shape, and (2) the products from that ablation are being added to the flow. Since, in general, these two processes are coupled; a full simulation requires both a flow field component and a material response component with a “hand off” of information between the two.

2.5.1 *Flow Field*

Even without accounting for the difficulties modeling the boundary of an ablating wall, it is very challenging to resolve the features of a hypersonic flow field. While the conventional models of the Navier-Stokes equations accurately describe the flow field for many situations, in a hypersonic flow temperatures become high enough that air begins to dissociate, and an accurate model for hypersonic flow must account for the chemical and thermal effects of this process. Closure relations, appropriate values for model parameters, and fidelity criteria are all areas of active research today. One factor is the lack of available flight data for comparison. There are however several well known real-gas Navier-Stokes solvers that have been developed and validated within the last fifteen years currently available that focus on the hypersonic flow regime (Reuther, Prabhu, Brown, Wright, & Saunders, 2004).

The basic governing equations for Navier-Stokes solvers of chemically reacting flow are seen in the Equations (9) through (15) below.

The global continuity equation:

$$\frac{\partial \rho}{\partial t} + \nabla \cdot (\rho \mathbf{u}) = 0 \quad (9)$$

The species specific continuity equation:

$$\frac{\partial \rho_i}{\partial t} + \nabla \cdot (\rho_i \mathbf{u}) = \dot{\omega}_i \quad (10)$$

Solving for the density of the species:

$$\rho_i = \frac{\dot{\omega}_i}{\dot{\omega}} \rho \quad (11)$$

Fick's law for diffusive transport:

$$\mathbf{j}_i = -D_{i,j} \nabla \rho_i \quad (12)$$

The momentum equation:

$$\rho \frac{D\mathbf{u}}{Dt} = -\nabla p + \nabla \cdot \boldsymbol{\tau} \quad (13)$$

The energy equation:

$$\frac{1}{\sqrt{\pi}} \int_{-\infty}^{\infty} \frac{e^{-t^2}}{t^2} dt = \frac{1}{\sqrt{\pi}} \left(-\frac{1}{t} + \int_{-\infty}^{\infty} \frac{e^{-t^2}}{t^2} dt \right) \quad (14)$$

Fourier law heat flux:

$$\frac{d}{dt} \left(\frac{\partial L}{\partial \dot{x}} \right) = \frac{\partial L}{\partial x} \quad (15)$$

The global continuity equation, Equation (9), and momentum equation, Equation (13), are not changed for a chemically reacting flow; however, the global density must be updated using the reacting species (subscript s) and the energy equation, Equation (14), is modified to include diffusion. (Anderson J. D., 2000)

These governing equations are integrated in time for chosen boundary conditions until steady state is reached. For non-ablating boundaries, the typical boundary conditions are no-slip wall and a zero pressure gradient normal to the wall.

For computational purposes, the governing equations are discretized. For two popular hypersonic codes, GASP and DPLR, discretization is accomplished using the finite volume method, and various time-marching schemes are available to reach a steady state solution. The various available hypersonic real-gas solvers differ in their time integration approaches as well as their inviscid flux numerical schemes. GASP and DPLR are examples of this, as GASP utilizes the van Leer flux-vector splitting scheme while DPLR uses a modified Steger-Warming flux-vector splitting scheme. Each of these schemes has intrinsic dampening that differs from one another, so the results are

different whether the gas is ideal or real (Reuther, Prabhu, Brown, Wright, & Saunders, 2004).

oAnother well known Navier-Stokes based code is the Langley Aerothermodynamic Upwind Relaxation Algorithm (LAURA). LAURA uses a finite-volume shock-capturing upwind approach to solve high speed viscous and inviscid flow problems. One unique feature of LAURA is the ability to adapt the grid during convergence processing. (Zoby, Thompson, & Wurster, 2004) LAURA utilizes point implicit or line implicit relaxation scheme and has shown successful application to multiple hypersonic vehicle and flight conditions. (Thompson & Gnoffo, 2008)

To determine gas composition and associated thermodynamic variables for many sources, either the NASA CEA (chemical equilibrium analysis) code, a code based upon it, or FIAT (Fully Implicit Ablation and Thermal response program) are called upon. The CEA code is available to the public through NASA's website and is capable of calculating product concentrations from a set of reactants. The code also yields thermodynamic and transport properties using a minimization-of-free-energy approach (Gordon & McBride, 1994).

To more closely model the flow field, the gaseous composition of the ablative product must be taken into consideration. With this addition to the flow and dissociation of the gases, the varying chemical reactions and mass addition from the ablating boundary must be incorporated into the flow field. All of the papers reviewed used either a "black box" code or Navier-Stokes equations modified to include conservation of mass

for the individual species as seen in the equations above. Some examples of recent applications are discussed here.

Chen and Milos (Chen & Milos, Navier–Stokes Solutions with Finite Rate Ablation, 2005) utilized a code referred to as GIANTS (Gauss-Seidel Implicit Aerothermodynamic Navier-Stokes with Thermochemical Surface boundary conditions) to simulate the hypersonic aero thermal heat distribution over a blunt body. The governing equations are discretized using the implicit flux-split finite-volume method and then solved using Gauss–Seidel line relaxation with alternating sweeps in backward and forward directions.

Keenan & Candler (Keenan & Candler, 1993) approached the problem slightly differently. They used two sets of governing equations. One handles the flow field region while another set of governing equations dealt with the ablator material. For the flow field portion they used the two dimensional axis-symmetric vector form:

$$\frac{dU}{dx} + \frac{F}{r} + \frac{G}{r} = W \quad (16)$$

In Equation (16) U is the conserved vector, F is the Flux vector, G is the radial flux vector, and W is the source vector for thermochemical nonequilibrium. The conserved vector, U, is presented below:

$$(17)$$

The subscript on ρ indicates the species of gas in the flow, E_v is the vibrational energy and E is the total energy per unit volume. The flux vector, F , is given as:

$$\begin{pmatrix} \rho u \\ \rho u^2 + p \\ \rho u v \\ \rho u E \end{pmatrix} \quad (18)$$

Candler and Keenan solved the flow field and the body regions and coupled these two at the boundary. Using a finite volume formulation, their flow field governing equations were solved using a modified form of Steger-Warming flux vector splitting with convective fluxes handled in an upwind manner while the diffusive terms are centrally differenced. To speed up convergence, an implicit scheme was used and solved with a Gauss-Seidel line relaxation method (Keenan & Candler, 1993).

2.5.2 Surface Interactions

CFD models which include surface interactions attempt to improve the accuracy by accounting for the processes going on at the ablating boundary. In all cases reviewed for this research, when ablation was modeled along with the flow field, two solvers were

run in parallel trading information at the surface boundary. The information transferred across this fixed surface boundary typically included heat transfer and pressure from the flow and mass addition from the wall; however, this interaction between the flow field and material surface regions is not as thoroughly explained in the published research as the flow field methods. Since the flow field requires information from the surface boundary, the processes occurring inside the solid must be understood as well. Presented here are several topics that involve the material solvers and their interactions with the flow field solvers.

In Ayasoufi, *et al*, (Ayasoufi, Rahmani, Cheng, Koomullil, & Neroorkar, 2006), an upwind differencing method, explicit with respect to temperature is used for the mass conservation equations. Ayasoufi, *et al*, coupled this approach with LAURA for the flow field heating terms.

Keenan and Candler (Keenan & Candler, 1993) solved the unsteady heat equation using a forward time, centered space scheme. The central difference method is used for the spatial terms due to the parabolic nature of the surface modeled. The material solver was coupled with a Navier-Stokes flow field solver they developed. This research was a precursor to the ACFD code, which produced the computational results presented herein.

Chen and Milos (Chen & Milos, Navier–Stokes Solutions with Finite Rate Ablation, 2005) investigated two surface kinetic models based on carbon heat shields: Park and Zhlukto. Park’s model calculated the mass flow of individual processes during ablation and sums them to arrive at the mass flow from the wall. The recession rate of

the wall can then be determined by dividing the total mass flow by the density at the surface. A general species mass conservation at the surface is used to determine the mass flow of the pyrolysis gas injection, which is the gas released by the decomposition of the heat shield. A total mass blowing equation, Equation (19), is then used for global balance.

(19)

In Equation (19), ρ is the density of the gas near the wall, u is the velocity of the gas at the wall, and \dot{m}_g and \dot{m}_p are the mass flow of the gas and pyrolysis gases respectively.

A second model investigated by Chen and Milos, Zhlukotov, sets up phase equilibrium constants for each chemical process, reaction rate constants, rates of species production, and solves iteratively for a steady-state flow solution. For the carbon heat shield used in the research, there were thirteen unknowns. This model assumes the pyrolysis gas is in equilibrium before it outgases into the flow. When coupled with a flow field simulation, the surface temperature and gas injection rates are obtained in a time-dependent global iteration (Chen & Milos, Navier–Stokes Solutions with Finite Rate Ablation, 2005).

Also in 2005, Chen and Milos (Chen & Milos, Three-Dimensional Ablation and Thermal Response Simulation System, 2005) investigated a method for three-dimensional thermal response and simulation of ablation to predict charring and shape change at hypersonic speeds. The code used, called the Three-dimensional Finite-volume

alternating directional Implicit Ablation and Thermal response code (3dFIAT), models ablation at the surface which is then updated with a commercially available finite element internal structure solver named MARC. With these two solvers integrated, they were used to predict surface recession and thermal response of a three-dimensional ablative thermal protection system and underlying structure with complicated geometry. This method was compared with the Two-dimensional Implicit Thermal Response and Ablation (TITAN) code for consistency and accuracy for a case at 0° angle of attack with an axis-symmetric solution. The results were a difference of less than 1%.

2.6 AFRL Use of the ACFD Code

The CFD code used in this research is referred to as the Ablation Computational Fluid Design code, or ACFD, and is being developed for AFRL with the specific goal of accounting for the coupling between the fluid dynamics and the material response. The code is Navier-Stokes based as well, so the governing equations are presented above in Equation (9) through Equation (15). ACFD discretizes the governing equations with a standard finite-volume formulation and uses a modified Steger-Warming flux vector splitting scheme to evaluate the fluxes at the control volume surfaces. This method was shown to be as accurate as the best approximate Riemann solvers. The code is relatively easy to linearize for implicit time integration methods and implements several second-order accurate upwind-biased extrapolations (Candler & Nompelis, 2007).

Integration in time is performed using the data-parallel line-relaxation (DPLR) method with standard second-order accurate upwind flux vector splitting methods. There

are several available choices in the code, but the authors recommended a TVD MUSCL approach in which the primitive variables are used for the extrapolation (Candler & Nompelis, 2007).

To find the state of the gas species in Equation (10), the ACFD solver minimizes the Gibbs and Helmholtz free energies to solve for the thermodynamic state of the fluid and the composition of the species. ACFD depends upon the NASA CEA code (Gordon & McBride, 1994) for the species thermodynamic data.

The ablation reaction of the surface is dependent on temperature and the thermal response of the ablator. ACFD uses a form of the solid-phase energy equation seen in Equation (20).

$$\rho_s \frac{dU_s}{dt} = -q''_{s,f} + \dot{m}''_{s,f} h_{f,s} \quad (20)$$

Here U_s is the internal energy per unit mass for the solid; ρ_s is the density of the solid; and the heat flux within the solid is $q''_{s,f}$. The boundary layer is controlled by the mass and energy balance equations seen in Equations (21) and (22) respectively.

$$\dot{m}''_{s,f} = \rho_s \frac{d\delta}{dt} \quad (21)$$

(22)

These equations are the standard for all equilibrium-gas ablation models and are taken from the CMA manual (Gosse, Callaway, Reeder, Nompelis, & Candler, 2009, pp. 2-3) (Moyer & Rindal, 1968).

The B-prime parameter as found in Equation (6) can also be found from partial pressures by using Equation (23):

(23)

In Equation (23), M is the molecular weight of the subliming material and the air; p_{1w} is the partial pressure of the subliming species at the wall; and p is the mixture pressure. When assuming a subliming species, the ablation rate can be determined with the equilibrium vapor pressure. If the vapor pressure is higher than the equilibrium pressure, the gas will revert to solid form, and if the partial pressure is lower than the equilibrium pressure, the ablative material will continue to sublime until the equilibrium state is reached (Jumper G. Y., 1975, p. 11). As the dry ice used in this research behaves thus, the carbon dioxide at the surface must be at equilibrium vapor pressure. And by solving Equation (23), Equation (6) can be solved for the expected mass flow given the flow conditions.

2.7 Measurement Techniques

The ability to track the rate at which a thermal protection system is ablating is vital to the design and the numerical modeling of the protection system. Measurements only taken before and after experiments provide average rates without specific ablation rates over time. An added concern with this technique is that the test article may change shape as it cools (Schairer & Heineck, 2007).

Another technique is to imbed sensors in the test material, usually to measure the isotherm at a given point. This provides real-time quantitative data, but an isotherm is only indicative of the recession rate. A compounding difficulty is that as the material ablates, the sensors are exposed to the flow and may ablate at a different rate, causing issues with the test accuracy (Schairer & Heineck, 2007).

2.7.1 Photogrammetric Recession Measurement

Photogrammetry generally involves a region of interest being marked clearly by targets on the test article, camera positions that are well known, and several common reference points in each image. The positions of the targets may then be determined. Photogrammetry has been used to measure deflection of flexible wings such as those on micro air vehicles (Black, Pitcher, Reeder, & Maple, 2010). Unlike photogrammetry applied to problems of simple solid motion, as one might encounter for aero-elasticity research, it is typically very difficult to place markers on the model in an ablation study due to continuous changes in the surface of the ablating model.

In a 2007, Schairer and Heineck (Schairer & Heineck, 2007) addressed the need for a non-intrusive, quantitative measurement of ablation rates using a photogrammetry technique. Their Photogrammetric Recession Measurements (PRM) is based upon what they describe as a combination of the techniques of photogrammetry and three-dimensional (stereo) Particle Image Velocimetry (PIV). The PIV technique involved two synchronized cameras capturing different views of the surface in stereo. With stereo PIV, the region of interest is illuminated by a pulsed laser sheet and seed particles suspended in the flow pass through the laser sheet. Two cameras at different angles to the sheet are synchronized to record images of particles illuminated by the laser pulses at closely spaced instants in time. The displacements of the particles in the images are determined using a two-dimensional cross correlation, and the velocities of the particles are evaluated by dividing by the time between images. Hundreds or thousands of image pairs from both cameras are typically collected and processed to compute flow statistics.

PRM harnesses the data processing approaches used in PIV to determine surface features of interest in multiple frames by projecting a grid into the image and choosing identifiable features on the surface of the ablative material visible in both images. It then tracks these surface features through the succeeding frames. Photogrammetry techniques are then used to calculate recession rates of the target points. The correlation between the two techniques and stereo imaging enables time-dependent tracking of points of interest on the ablative model, ultimately yielding ablation rates. Schairer and Heineck studied real ablators in an arc-jet facility and found that inhomogeneous materials led to better

measurements since surface features are easier to detect with cameras (Schairer & Heineck, 2007).

2.7.2 Dot Projection Photogrammetry

Another technique, which is being utilized and explored for the current research, is laser dot projection photogrammetry. Photogrammetry generally employs physical targets to measure object coordinates, but dot projection photogrammetry uses projected dots of lights as the targets of the technique. The use of the dot-projection photogrammetry is explained for gossamer space structures by (Pappa, Black, Blandino, Jones, Danehy, & Dorrington, 2003). A grid of dots is projected onto a structure and captured through a stereo photogrammetric process. This approach leads to the three-dimensional coordinates for the center of each dot in the grid for the imaged time step. For movement these points are tracked over time using video or multiple image captures.

Unlike an attached target, projected dots are not free to move directly with the structure. Instead, they move along the line of projection as the surface changes. While dot-projection photogrammetry can lead to correct measurements of the movement of each target dot, the path of each will always follow a direct path away from or towards the source projector. An example is shown of dot projection onto a surface in Figure 4 and a processed view captured using two cameras in Figure 5 (Pappa, Black, Blandino, Jones, Danehy, & Dorrington, 2003).

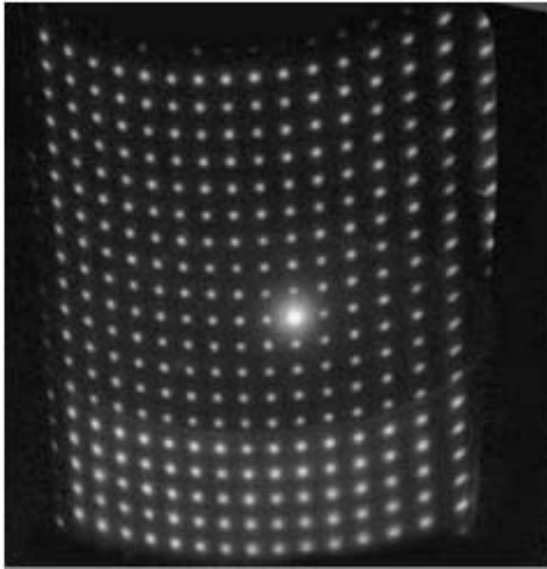


Figure 4: Fluorescence from laser dot projection onto gossamer structure (Pappa, Black, Blandino, Jones, Danehy, & Dorrington, 2003)

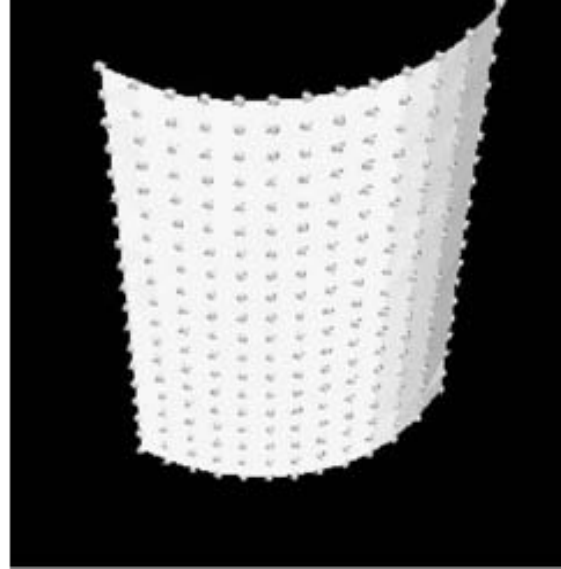


Figure 5: Three-dimensional surface by photogrammetry of gossamer structure in Figure 4 (Pappa, Black, Blandino, Jones, Danehy, & Dorrington, 2003)

2.7.3 Schlieren Imaging

The Schlieren method uses photography or video capture to observe shock waves by capturing varying density in the flow. While this approach is not typically used to quantify ablation rates, Schlieren photography has been used to track rates of nose tip ablation by backing out the shape change over several images (Anderson D. E., 1960) (Jumper & Hitchcock, 1988).

In Schlieren imaging, a collimated light source is used to illuminate the test section or object from behind. The beam of light is then focused down onto a knife edge which blocks about half of the light impacting the camera lens or image sheet. The density gradients in the flow change the refractive index which causes distortion of the light beam that can be visualized. This causes positive and negative fluid density gradients to appear lighter and darker respectively. Figure 6 is an example of Schlieren

images of supersonic flow past a cone taken from the work of (Jung, Reeder, Maple, & Crafton, 2006), which was performed in the same wind tunnel used in the current experiment.

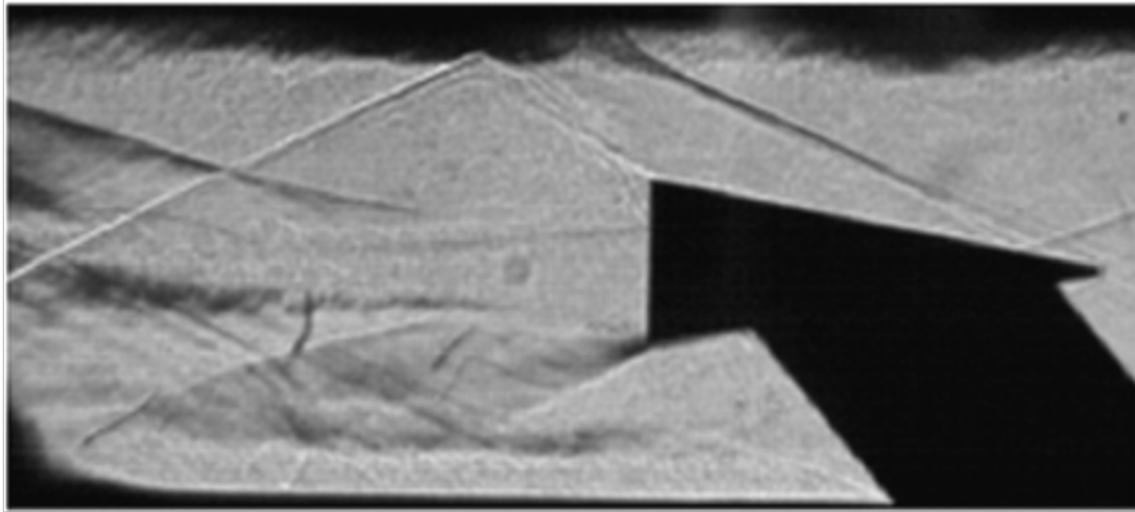


Figure 6: Schlieren images of a resin cone model in nominal Mach 3 flow (Jung, Reeder, Maple, & Crafton, 2006).

2.8 Attributes of Solid Carbon Dioxide

In 1823, Michael Faraday found that gases could be liquefied using experiments with bent glass tubes commonly referred to as retorts. This led to a large number of researchers investigating various liquids and their properties, and in 1834, a French chemist named Thilorier expanded this research using cast iron retorts and focused on liquid carbon dioxide. In one experiment, he removed the lid to watch the liquid carbon dioxide evaporate. Much to his surprise, he found a solid form. “When the solid is exposed to the air it disappears insensibly by slow evaporation, without melting” (Quinn & Jones, 1936, pp. 14-15).

For nearly one hundred years, the use of solid carbon dioxide was restricted to the realm of the laboratory. It would not be until 1924 that a practical commercial use was found for the substance. In New York City, a company that would come to be known as the Dry Ice Corporation of America began producing solid carbon dioxide. It was first marketed as a way to keep ice cream cold over long distances and to refrigerate railroad cars. The carbon dioxide ice had two benefits, it was more than twice as cold as water ice and it left no residue as it evaporated (Quinn & Jones, 1936, pp. 193-196). This sublimation directly to a gas led to the common household name of dry ice.

The process for making dry ice has not changed much in the years since. The general process starts with liquid carbon dioxide under pressure. The liquid is released into a capture tank which is at much lower pressure and much larger volume. As the pressure of the liquid drops drastically so does the temperature. Some of the liquid will evaporate into gas while the rest will cool below the sublimation temperature and solidify. These solid particles of carbon dioxide fall snow like into a capture tank until a predetermined weight is achieved. The carbon dioxide snow is then compacted into blocks of desired sizes with pressure plates (Quinn & Jones, 1936, pp. 205-208).

With current technology, the conversion of carbon dioxide gas to solid is about 46% by mass. The rest is either lost back to the atmosphere or is recaptured for reprocessing. The liquid carbon dioxide is held at 300 psi and the pressure in a modern press is typically about 270 psi. Some machines will produce up to a 220 pound block of ice and the denser the ice, the longer it will take to completely evaporate. Typical

densities reported for commercially available dry ice range from 1.2 to 1.6 g/cm³ (Ackerman & Ackerman, 2009).

A phase diagram of carbon dioxide can be seen in Figure 7. The more traditional phase diagrams are presented with pressures in atmospheres, but this diagram was created in pounds per square inch to correlate with the units used in this research. The sublimation and vapor pressure curves of this phase diagram were constructed based on data found in the CRC Handbook (Lide & Haynes, CRC Handbook of Chemistry and Physics, 2009, pp. 6-70, 6-102, 6-106, 6-107). The melting line of carbon dioxide was found by adding 50 atmospheres for each degree above the triple point. (Quinn & Jones, 1936, p. 60) The area outlined in red (or bold) in Figure 7 represents the range of stagnation pressures used in the experimental data presented herein and corresponds to a range of $T = 185\text{K}$ to 210K .

Carbon dioxide has a very low triple point temperature but high pressure, which is where all three phases of a substance may be present. As seen in Figure 7, the triple point of carbon dioxide is -56.6°C (216.6 K) at 5.11 atmospheres (75.1 psi). Obviously, this condition does not occur naturally on Earth. For the conditions at one atmosphere the sublimation point is -78.5°C (194.65 K). So at room temperature and one atmosphere pressure, the solid will attain a temperature of -78.5°C and, as heating continues, will sublime directly to a gas. The low sublimation temperature is a reason for exploring the use of dry ice in the simulation of higher temperature ablating materials. Carbon, by contrast, is used in many ablating heat shields and has a triple point of 4660 K at 168

atmospheres (2466 psi) and a sublimation temperature of around 3800 K at 1 atmosphere (Kerley & Chhabildas, 2001, pp. 6-8).

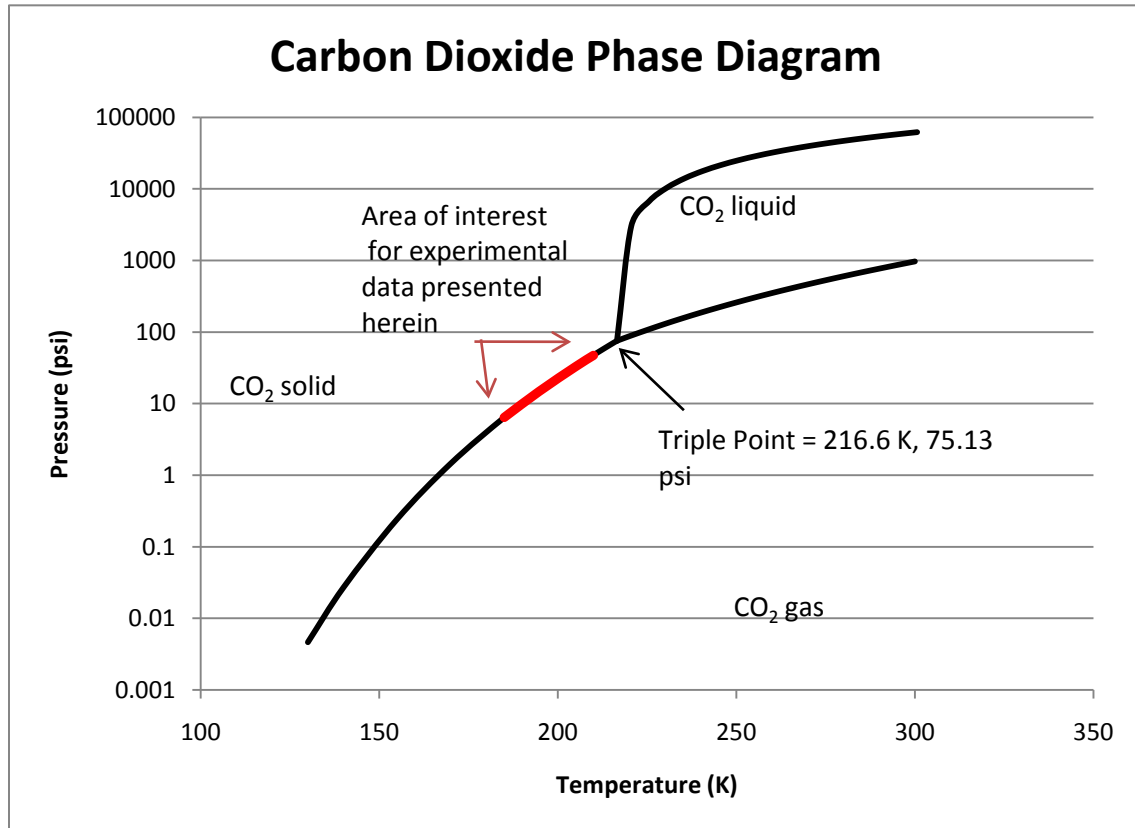


Figure 7: Carbon Dioxide phase diagram produced from CRC data (Lide & Haynes, CRC Handbook of Chemistry and Physics, 2009)

3. Experiment Methodology

The overarching goal of this research project is to collect experimental ablation data under well-controlled conditions for the purpose of validating and improving a computational model currently used by AFRL/RBAC. One byproduct of this research is the description of a process which may enable researchers to test ablation effects in other supersonic wind tunnels. This chapter provides descriptions of: (1) the methodology and set up of the research experiment in the AFIT high speed blow-down facility, (2) the set up and technique for collecting and processing three-dimensional recession rate data, (3) the process to reliably fabricate dry ice test articles, and (4) the parameters input into the ACFD computational code.

3.1 Experimental Facilities and Equipment

3.1.1 Wind Tunnel Equipment

The wind-tunnel used for this experiment, part of the AFIT blow-down facility, has been in use in its current configuration since the mid to late 1990's. The test section is 6.4 x 6.4 cm. There are currently two convergent-divergent nozzles capable of producing Mach 1.8 and nominally Mach 2.94 conditions in the test section. For the purposes of this research, only the Mach 2.94 nozzle was used. Pressure transducers are used to record the mean stagnation chamber pressure as well as the mean free stream pressure in the test section. In practice, Mach 2.94 flow can be produced for approximately 20 to 30 seconds (Bjorge, Reeder, Subramanian, Crafton, & Fonov, 2005).

Figure 8 illustrates the tunnel with the Mach 2.94 nozzle in place and the cameras' placement for a 10 degree angle of attack test. Viewed from this angle, the flow is left-to-right. Visible is the placement of the liquid carbon dioxide Dewar, the feed line, the three high speed cameras on the right side, and a thermal imaging camera in the foreground.



Figure 8: AFIT blow down facility set up for a 10° angle of attack test

The test section of the wind tunnel was specifically designed for this research. The redesign entailed lengthening the test section to a total length of 13 inches and adding a window on the roof of the test section for camera viewing angles. The attachment of the sides was designed using quick release clamps for easy access to the tunnel in order to minimize the time between model production and operation of the wind tunnel.

The quick release clamps' limit was 200 lbs per lock. The surface area of each side panel exposed to the tunnel flow was 32.5 in², giving a maximum safe internal

positive pressure of approximately 12.3 psig. This is well above operational pressures in the tunnel which are typically around 3 psia or less.

Being that the two side windows appear identical, the side windows were labeled A and B to maintain the configuration between tests. Side A was to the starboard side of the model, and side B the port side. These letters are used herein this dissertation to designate a side of the wind tunnel. Both the side labels and the quick access clamps can be seen in Figure 9, which displays the sting in the 15 degree angle of attack position as well as one of the laser grids projected onto the floor of the tunnel. Note that in conventional wind tunnel test terminology, the model would be considered to be at zero angle of attack and at a yaw of 15 degrees since only one angle is varied, angle of attack is the term used here.

A custom designed sting was fabricated for the tests and can be seen in both Figure 9 and Figure 10. A 0.25 inch outer diameter steel tube with a 0.125 inner diameter was bent to incorporate a 90 degree turn. The tube served as both the liquid carbon dioxide feed for model fabrication and as the sting. The end of the tube was threaded (1/4 – 28) to accommodate a nut and threaded plastic insulation piece. The insulator served to protect the dry ice model from thermal transference from the sting and worked with the nut to hold a filter in place. In Figure 10, the filter, plastic spacer, and nut are visible directly behind a spherically blunted cone dry ice model.

The sting enters the tunnel from below via a removable disk which also enables angle of attack experiments to be conducted. The disk and sting are controlled by a screw, accessible from below the tunnel, which allows the test article to be placed at

angles as high as 15 degrees angle of attack with respect to the flow. The test results presented here are limited to 10 degrees angle of attack as shock interference from the wall is inferred from the Schlieren imaging at 15 degrees for the test articles used herein.

The spherically blunted cone model shown in Figure 10 has a base diameter of 0.60 inches and this model is representative of the majority of test runs. Initially, some molds were produced with a 1.0 inch diameter base, but Schlieren imaging revealed that blockage prevented tunnel operation at supersonic speeds for test articles with a base diameter of 1 inch. After stepping down several sizes, it was found that for the blunt objects, 0.60 inch diameter bases were the largest base diameter the tunnel could conveniently accommodate. The sharper objects, such as the cone shape, could be accommodated at larger diameters, but in the interest of uniformity in the testing, a base of 0.60 inches was used for all of the tests described herein.

A four way connector, shown in Figure 11 and also partly visible in Figure 10, was placed below the tunnel test section. Figure 11 shows the bleed off valve, Swagelok ball valve, relief valve, and pressure gauge. The Swagelok ball valve was added early in the course of the research to prevent premature model failure due to pressure build up in the line. After a model is fabricated, the carbon dioxide tank was shut off and the line was vented through the relief valve to avoid high pressure build up. So during nominal operation the tunnel is at less than one psia but the feed line is open to room conditions, the model would often fail due to this internal pressure. A common problem caused by this was the test article disintegrating during the vacuum drawdown at the onset of tunnel operation. After the Swagelok ball valve was installed and engaged to seal the tube, the

problem of this model failure was eliminated. As a point of interest, some data that was taken prior to the installation of the Swagelok was kept but not processed or used in the research presented in this dissertation.

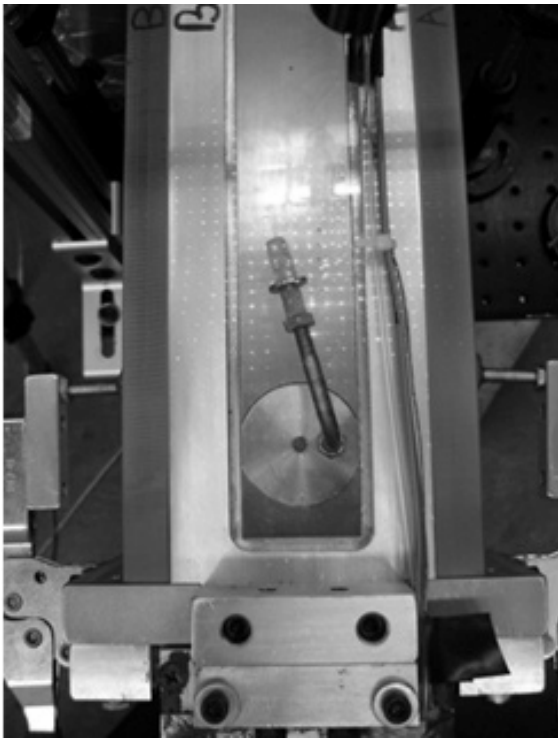


Figure 9: Wind tunnel viewed from the top with side labels visible; Sting is set up for a 15 degree angle of attack test

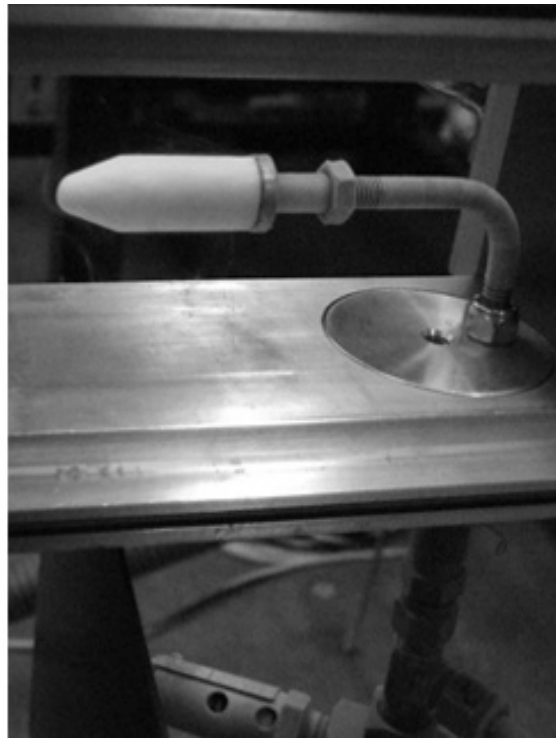


Figure 10: Spherically blunted cone model in the tunnel at 0 angle of attack

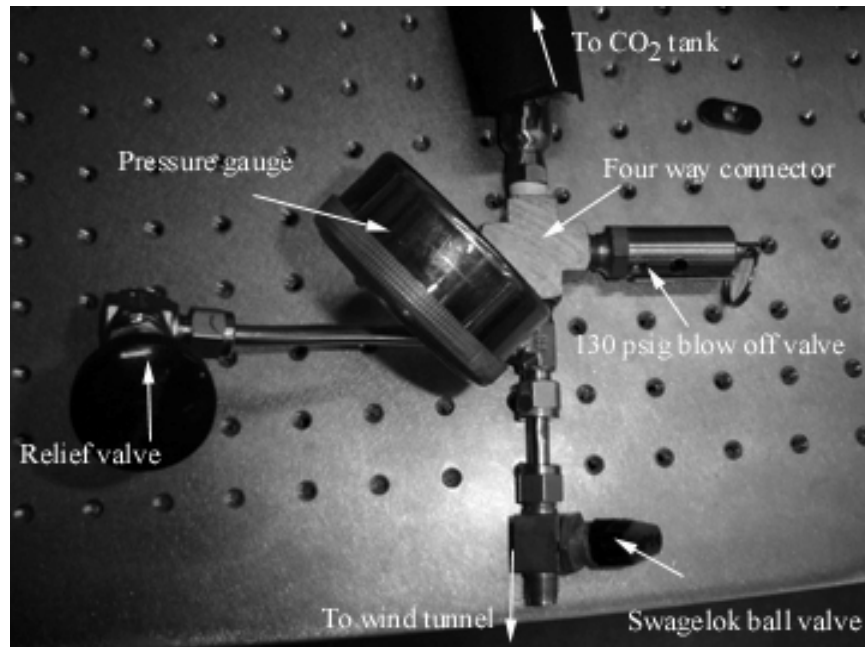


Figure 11: Four way liquid carbon dioxide connection unattached from wind tunnel.

3.1.2 Wind Tunnel Operations

The tunnel works as a pressure-vacuum blow down system. Upstream of the test section is a high pressure source tank and downstream is a vacuum tank. The source tank for the high pressure is a common pressure source for several facilities at AFIT. The vacuum tank is shared by only two facilities which rarely operate simultaneously. The pumps take approximately 10 minutes to pull the tank down from ambient pressure to approximately 0.1 psia. So long as the pressure ratio needed for Mach 2.94, approximately 33.33, is maintained between the stagnation chamber and the test section, the tunnel will continue to operate correctly. The lower the pressure in the vacuum tank, the longer the test can maintain that ratio. In practice, the tunnel was not operated unless the vacuum pressure was under 0.1 psia.

The wind tunnel is controlled via computer and is operated using National Instrument's LabView program. The development of the LabView program used to operate the wind tunnel is shown in great detail by LT Peltier in his thesis (Peltier III, 2007). The reader is directed to this reference for an in depth discussion of the LabView program for wind tunnel control. Peltier's program was only modified for this research in naming conventions and sampling rates. In his work, Peltier was using a particle image velocimetry (PIV) system which was triggered to record by the computer. The trigger was compatible with the cameras used in this research and was reused to trigger image capture.

When the tunnel is activated through the software, several things happen in sequence. First, the valve to the vacuum tank is opened. This causes the test section to draw down to equilibrium with the vacuum tank. Two and a half seconds after the vacuum valve is opened, the high pressure valve opens. There is a safety switch in the program that prevents the high pressure valve from opening if the vacuum valve is not open.

Once the pressure valve allows high pressure air to propagate down the tunnel, the tunnel is "on". However, the flow does not stabilize immediately. Schlieren imaging found that the flow approaches steady state between half a second and a second after the high pressure valve is opened. For this reason, the trigger to the high speed cameras was delayed one second from the time of the high pressure valve opening.

3.1.3 Test Conditions

Test conditions were at nominally Mach 2.94 with a stagnation chamber temperature of 293 K at static pressures ranging from 6 to 48 psia. Stagnation pressures under 0 psig were inferred from the test section pressures where an absolute pressure gauge was placed. Control of the stagnation pressure provided the ability to change the dynamic pressure and Reynolds numbers of the flow while maintaining a constant Mach number. Average static temperature in the test section for all tests presented herein was 109 K since the static temperature for all was 293 K.

The Reynolds number is given in Equation (24):

$$\text{Re} = \frac{\rho u L}{\mu} \quad (24)$$

In Equation (24), Re is Reynolds number, L is the characteristic length, u is velocity of the flow, ρ is the density and μ is the dynamic viscosity of the fluid. Since the temperature in the test section is far below room temperature, the Sutherland's formula relation in Equation (25) is used to determine μ .

$$\mu = \mu_0 \left(\frac{T}{T_0} \right)^{3/4} \left(\frac{S + T_0}{S + T} \right) \quad (25)$$

In Equation (25), μ is the dynamic viscosity at temperature T, μ_0 is the dynamic viscosity at reference temperature T_0 , and S is the Sutherland's constant of the gas. Using the information shown in Table 2, the dynamic viscosity found in the test section of the tunnel is $7.56\text{E-}6 \text{ N}\cdot\text{s}/\text{m}^2$. (White, Viscous Fluid Flow, 2nd Edition, 1991, pp. 28-29)

Table 2: Conditions for dynamic viscosity Equation (25)

T_o (K)	273
T (K)	109
S (K) for air	111
$(N*s/m^2)$	1.72E-5

Using the ideal gas law, Equation (1), a range of densities for the test conditions is found to be from 0.0397 kg/m^3 to 0.317 kg/m^3 . Then using Equation (26), the speed of sound, a , is determined to be 209.3 m/s and therefore Mach 2.94 yields the velocity $u = 615 \text{ m/s}$.

$$\frac{\mu}{\rho a} \quad (26)$$

Substituting these results into Equation (24) yields the results found in Table 3 which represent the low and high values for Reynolds numbers in the tests presented herein. The Reynolds number per unit length here is calculated as Re_L , with L being the unit length in meters, and Re_D based on diameter where D is the diameter of the test article in the tunnel.

Table 3: Density and Reynolds number for $P_o = 6.1$ and 47.7 psia of conducted research tests

Test Name	Stagnation Pressure (psia)	Test Section Static Pressure (psia)	Test Section Density (kg/m^3)	Test Section Re_L (Re/m)	Model Re_D (unitless)
2 Jun Test 8	6.1	0.18	4.09E-02	3.33E+06	5.07E+04
27 Aug Test 10	47.7	1.44	3.15E-01	2.56E+07	3.91E+05

3.1.4 Cameras Used for Photogrammetry

Three MotionPro X-stream XS-4 series high speed cameras with Nikkor 60 mm lenses were used in this research. The camera serial numbers and positions are displayed in Table 4. The cameras are referred to by name in the remainder of this document. The X-series are designed for use in industrial and research applications that involve motion evaluation. The cameras are connected to a computer via a USB 2.0 digital interface. The newest of the three is also capable of being used with a Gigabyte Ethernet, connection. The cameras have a resolution of 512x512 and a frame rate of 5000 frames per second, which is far faster than this research required (Integrated Design Tools, Inc, 2008).

Table 4: High speed camera names, serial numbers and positions

Camera Name	Camera Serial Number	Position
Camera A	1412050046	Tunnel Side A
Camera B	1406080507	Tunnel Side B
Camera C	1404050016	Above Tunnel / Center Camera

Figure 12 shows the back panel of one camera. When multiple cameras are used to image an object, one camera must be set to master and the others to slave. BNC cables were hooked from the SYNC OUT of the master camera to the SYNC IN on the slave cameras. This allowed the cameras to capture images at the same instant. A “T connector” was used for connecting the two slave cameras to the master. A trigger from the computer controlling the wind tunnel is also connected via BNC cables to the TRIG

IN connector on the back of each camera. All three cameras must receive the trigger in order to record images.

The MotionPro's Motion Studio software suite is used to control the cameras as well as record and manipulate images. In the Motion Studio recording menu one camera can be selected as the Master Camera. Once this option is selected, the other cameras' options grey out, and changing the master's options will change the slave cameras' properties.

Figure 13 shows the default settings of the software. For this research, the rate was set to 1000 Hz, the exposure 897 μ s, record mode was normal and the number of frames to record was the maximum the cameras would take, which was 8000 frames for full resolution frames. There is one box for each camera being used (Integrated Design Tools, Inc, 2008).



Figure 12: X-Series high speed camera back panel

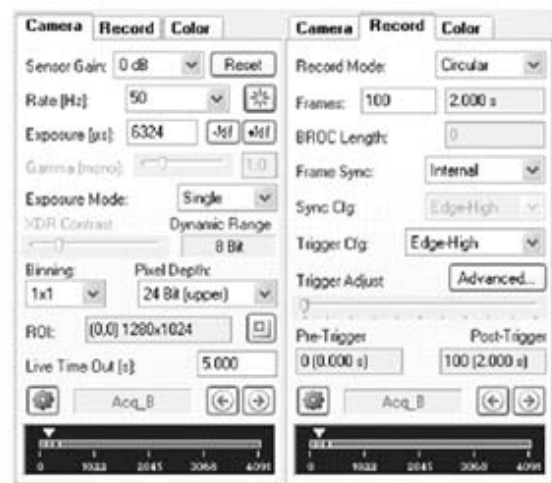


Figure 13: Motion Studio camera control panel with default settings

3.1.5 Camera Test Set Up

For the research presented here, the three cameras are connected to the wind tunnel's computer via USB 2.0 cables. A BNC cable connects the master camera, camera C as described in the previous section, which was chosen to be the center camera in the array of three cameras in all tests. Another BNC cable is used to bring the trigger from the wind tunnel computer, through the three cameras and to the Schlieren camera which is described in section 3.1.6.

The cameras were set to record at 1000 frames per second with an exposure of 897 microseconds and an f-stop of 8 on the Nikkor 60 mm lenses. This provides a sufficiently fast exposure time to capture the laser grids in good contrast as can be seen in Figure 14 where images from a point and shoot camera are shown on the top left with

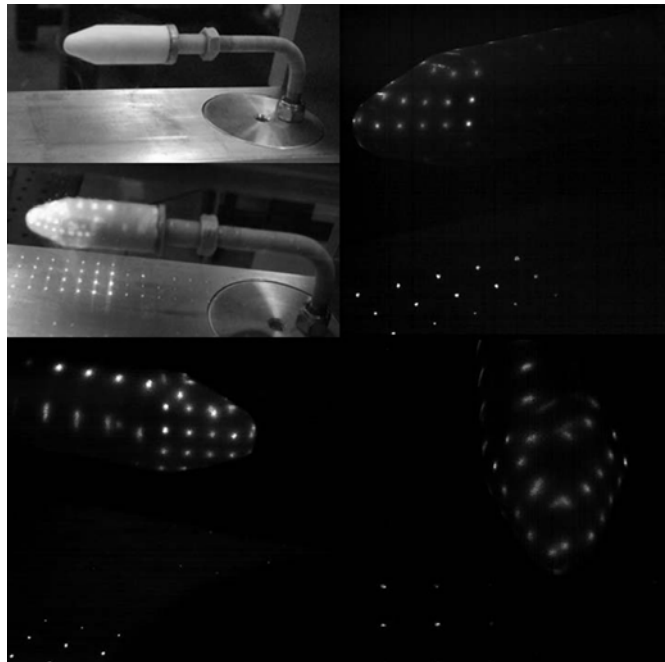


Figure 14: Raw images of dry-ice model in wind tunnel. Counter clockwise from top left: image of model in tunnel, image with lasers on, starboard side of model, top of model, port side of model

raw images from the Motion Studio capture.

For all tests, the cameras were placed between 9 and 11 inches from the test article for best resolution. The cameras were positioned to observe the model from different points of view and their angles were recorded. The angles are presented here as part of the set up but are not required for processing in PhotoModeler®.

For the zero angle of attack tests, Figure 15 presents the locations of the cameras: Camera A is on the right, Camera B is on the left side of the tunnel, and Camera C is in the center viewing down into the tunnel. Figure 16 is a top down diagram providing the camera orientations with respect to the tunnel: Camera A at an angle of 65° facing aft and an elevation of 25° , Camera B at an angle of 65° facing aft with an elevation of 35° , and Camera C down the center of the tunnel at an elevation of 45° . The elevations are not shown in the diagrams.

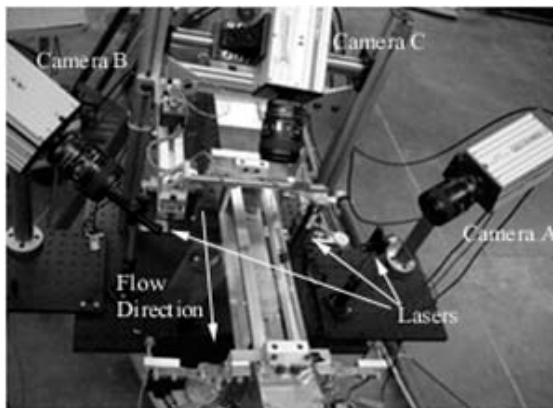


Figure 15: Camera set up for a zero angle of attack wind tunnel test

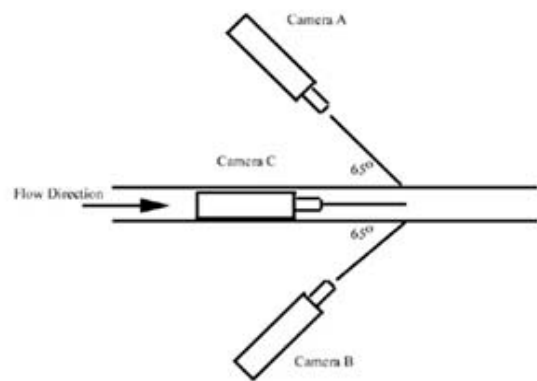


Figure 16: Top view diagram of camera set up for zero angle of attack test (image not to scale)

In the five and ten degree angle of attack tests, the cameras were repositioned to better view the test article and anchor points. The order of the cameras was kept consistent in all orientations: with Camera C in the center, Camera A to the side nearest tunnel side A, and Camera B to the position closest to tunnel side B.

For the 5 degree angle of attack tests, Figure 17 and Figure 18 present the locations of the cameras: Camera A was positioned aft of the model at an angle of 70° at an elevation of 30° ; Camera B remained on tunnel side B but was positioned to view the model at an angle of 40° at an elevation of 30° ; and Camera C was moved to tunnel side A, forward of the model, facing aft at 20° at an elevation of 20° .

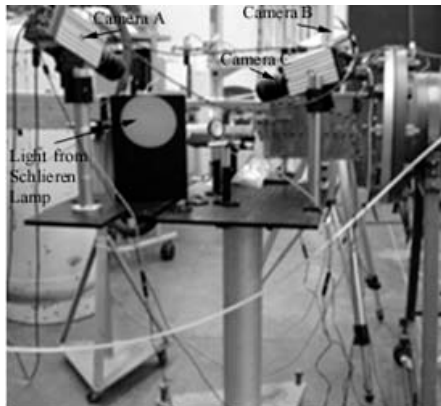


Figure 17: Wind tunnel setup for 5° angle of attack test viewed from the starboard of the model

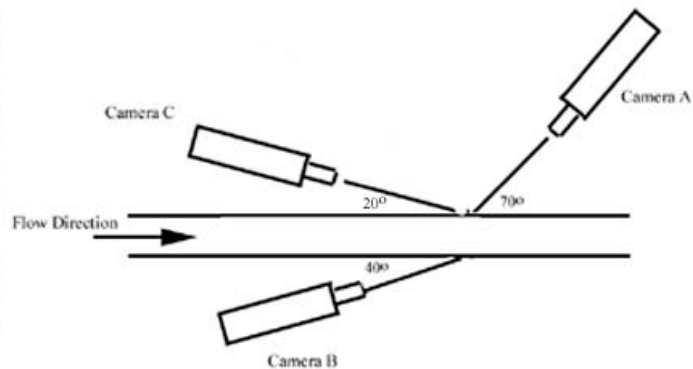


Figure 18: Top view diagram of camera set up for five degree angle of attack test (image not to scale)

For the 10 degree angle of attack tests, all of the cameras were moved to side A of the tunnel as seen the image seen in Figure 19 and in the top down layout diagram shown in Figure 20. Camera A is facing forward, 70° from aft, at an elevation angle of 29° . Camera B was on tunnel side A, forward of both cameras A and C, facing aft at 35° and

22° elevation. Camera C was in the center of cameras A and B facing aft at 68° at an elevation angle of 23°.

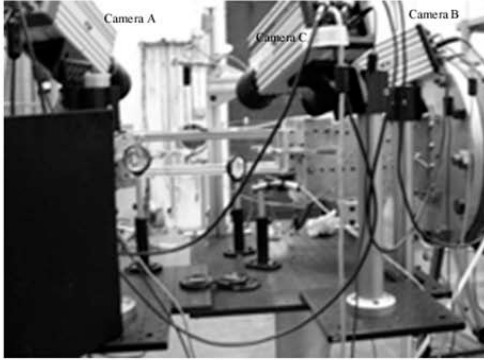


Figure 19: Camera setup for 10° angle of attack test viewed from the starboard of the model

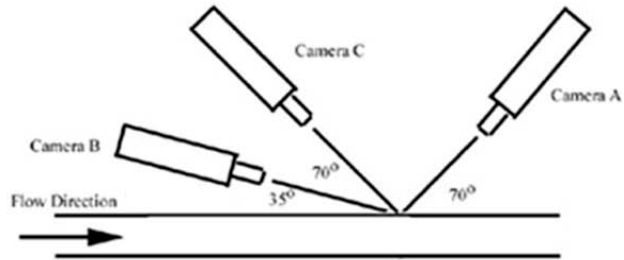


Figure 20: Top view diagram of camera set up for 10° angle of attack test (image not to scale)

3.1.6 Schlieren Imaging Setup

Schlieren imaging was set up using a Photron FASTCAM-X 1280 PCI camera with a 50 mm lens and the Photron software suit for image capture. Figure 21 represents the first half of the Schlieren set up, with the lamp on the right and the first mirror on the left. The second half of the Schlieren set up can be seen in Figure 22. If one refers back to Figure 17, the Schlieren light circle is visible on a back stop. The back stop allowed the operator to work in the tunnel without powering down the lamp between tests and prevented excess heating of the model prior to the wind tunnel operation. After passing

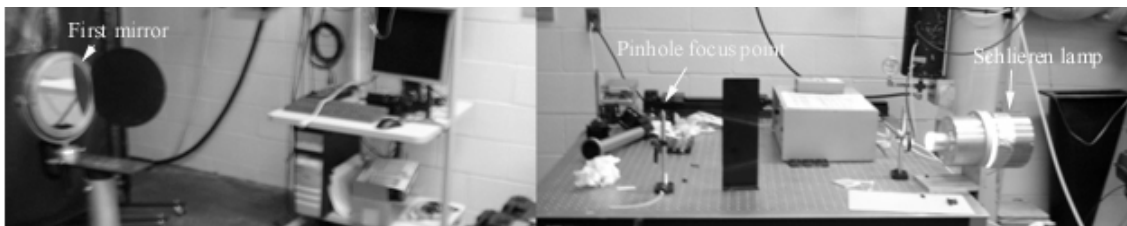


Figure 21: Schlieren lamp and first mirror in Schlieren set up

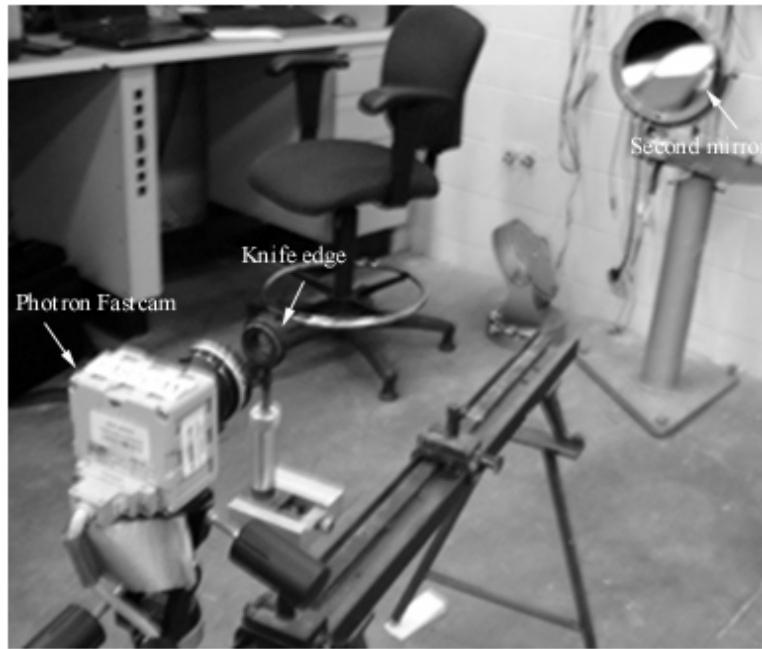


Figure 22: Schlieren camera with knife edge and second mirror

through the test section, the column of light reflects off of the second spherical mirror (Figure 22) and is focused down to a knife edge at the focal point of the mirror and into the camera lens. Schlieren images were recorded at 4000 frames per second with an exposure time of $1\text{E-}6$ seconds. The Schlieren system had a 4 second recording limit due to the camera's memory capacity. This technique was used as an alternate imaging source and a means to determine the state of the flow field in the tunnel.

3.1.7 Laser Grids

The lasers used in this research were Class IIIa and IIIb lasers in the 400-710 nm wavelength range. Three lasers were available for use: two red and one green laser. The difference in color had little if any effect on the data capture as the imaging was all in grayscale. Each of the lasers was fitted with a 7x7 dot matrix projector head which split the beam into a 7x7 grid. The two class IIIa lasers were projected from tunnel sides A and B and focused through 100 mm plano-convex lenses onto the nose of the test article.

Focus and placement on the surface were optimized to produce as many points visible on the test article as possible.

The Class IIIb laser was projected from above and did not use a focusing optic. Instead the 7x7 array was projected onto both the model and the floor surface of the wind tunnel. The projected points on the wind tunnel floor would later be used as non-moving anchor points for image processing and referencing. Figure 23 is an image taken from a point and shoot camera showing the laser grids being projected onto a typical spherically blunted cone dry ice model. In the image, the anchor points are visible below the model. Marks were made on the surface floor of the tunnel in order to maintain the anchor point positions after movement or refocusing of the lasers. The Class IIIb laser was maintained in the same orientation for all wind tunnel tests.

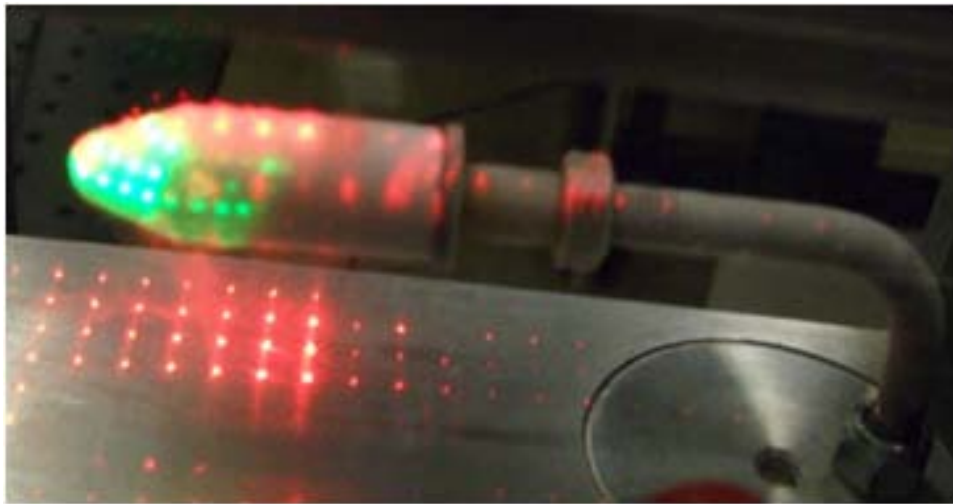


Figure 23: Laser grids projected onto a spherically blunted cone dry-ice model

The orientation of the lasers is provided here for tunnel set up preparations. The angles were not used in processing and were chosen to produce the highest concentration of laser dots on the areas of interest.

The laser orientation for the zero angle of attack tests is presented in the diagram of Figure 24: the laser on tunnel side A was at 0° elevation and a 50° angle with the wind tunnel facing aft, and the laser on side B was also at 0° elevation and 50° angle facing aft.

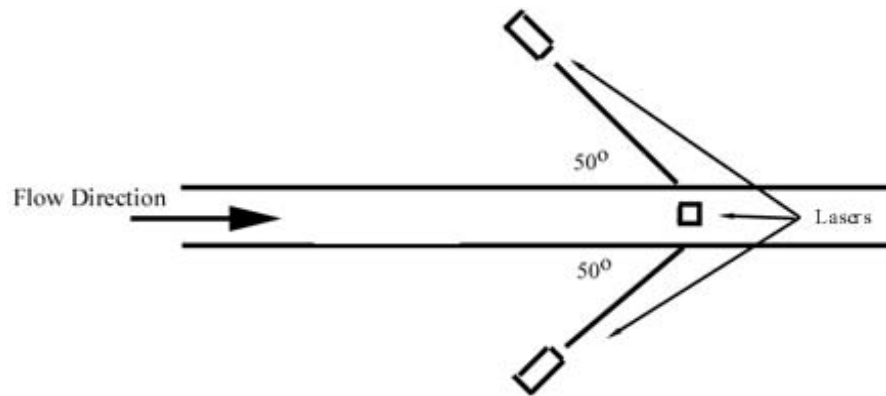


Figure 24: Diagram of zero degree angle of attack test laser orientations as viewed from above

The laser orientation for the five degree angle of attack tests is presented in the diagram of Figure 25. A fourth Class IIIa laser was acquired during the research and used for the five degree angle of attack. The lasers were oriented at 0° elevation. On tunnel side A, two lasers were positioned to project onto the surface. One was placed aft of the model, facing forward at an angle of 70° and another laser is forward of the test article facing rearward at a 45° . On tunnel side B, the laser was oriented at 40° facing aft.

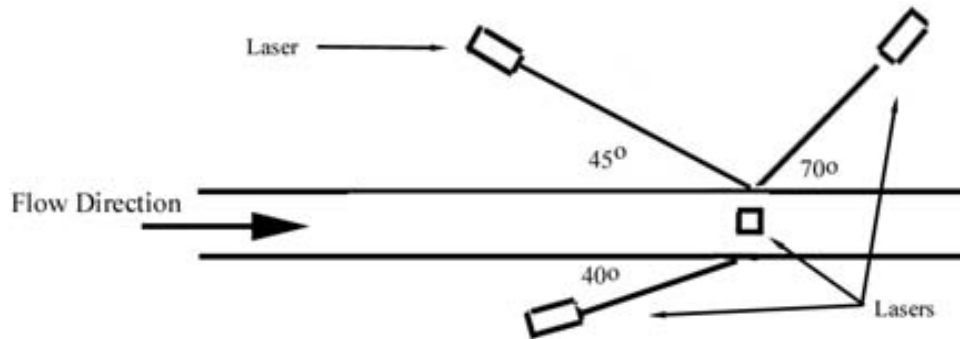


Figure 25: Diagram of five degree angle of attack test laser orientations as viewed from above

The laser orientation for the ten degree angle of attack tests is presented in Figure 26. Two class IIIa lasers were positioned on tunnel side A. The forward laser was at an 20° angle of elevation and a 70° angle with the tunnel facing aft. The rear laser was facing forward at a 70° angle at 0° elevation.

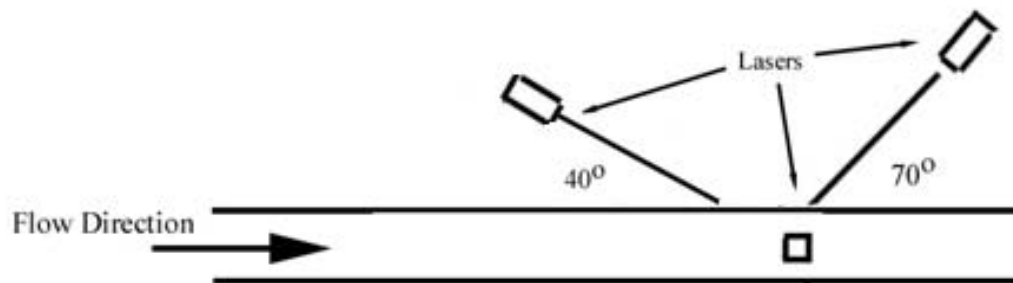


Figure 26: Diagram of ten degree angle of attack test laser orientations as viewed from above

3.1.8 Image Data Capture

The laser grids were projected onto the surface of the test article and captured through stereo-photography. These images were then processed using PhotoModeler®

software. PhotoModeler® is a commercially available software package designed to extract measurements and produce three-dimensional computer models from photographs. The software can be used with images from unknown sources, known camera specifications, or cameras that are calibrated by PhotoModeler® during imaging. For curved surfaces, three camera angles are preferred with as near to a 90° offset as possible between camera angles. According to the software developer, the program is designed for use in such areas as accident reconstruction, architecture, preservation, archeology, forensics, film, games, animation production, and modeling for engineering, industrial and experimental applications.

For capturing shape change of an object, the PMV (PhotoModeler® Video) module is needed. The PMV module provides the program the capability to load image sequences for analysis. The module also automatically tracks target points, for example laser grid points in this research, across the time frames, or time epochs, for maximum efficiency (Eos Systems Inc., 2007).

While the automation of the software is useful, each frame must still be manually inspected by the user to insure accuracy in point tracking. Results were captured for this research at 500 frames per second, but it was found that images acquired at every half second was sufficient to quantify the shape change. All data was, therefore, processed at half second intervals.

Three-dimensional coordinates of the points were extracted using PhotoModeler® over times which varied from as low as three seconds for high pressure experiments up to 16 seconds for low pressure experiments. An example of the raw PhotoModeler®

imported images can be seen in Figure 27 for an initial time and final time of a spherically blunted cone.

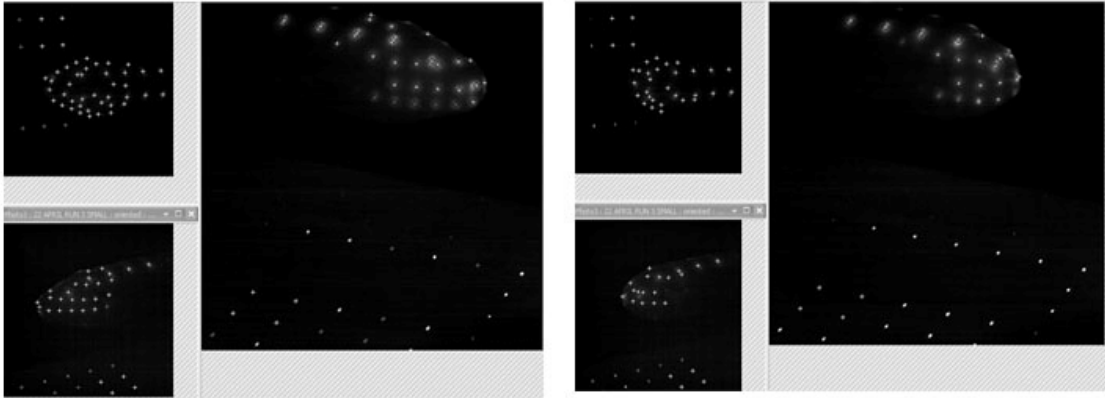


Figure 27: Raw PhotoModeler® image captures of three camera angles for a spherically blunted cone at initial time (left images) and final time (right images)

Once the images had been acquired, the three images in the initial frame used for analysis must be correlated. To do this, the PhotoModeler® needs points referenced in each image. The number of referenced points for correlation depends on the viewing angles as well as the number of points in each image. A poor correlation resulted in high residuals between points, and a possibly erroneous three-dimensional representation. The software would provide its own check of the quality of the correlation, but a inspection of the anchor points would quickly reveal the quality of the correlation. If the correlation were off, the floor of the tunnel would not be flat. Typically, ten points in all images were enough to get a good correlation. In some cases points were in two images, but not all three. The anchor points on the floor of the tunnel help fulfill the need for targets visible in all three image requirement, and provide a good in-situ calibration through the sequence as the laser dots on the floor do not move beyond the accepted tunnel noise (discussed in Section 3.2).

Once the images were correlated, the points in each image had to be manually linked or referenced to the counterpart points in the other images. PhotoModeler® aids in this by predicting the position of an expected target point. This prediction also provided guidance about the quality of the three-dimensional correlation. If the expected position is off by more than a few pixels, the correlation was either poor or points were incorrectly referenced. The sequence being processed would then need to be reprocessed.

Figure 28 displays a processed image from the same sequence given in Figure 27. At this point in the processing, three-dimensional correlation has been calculated between the initial points. The point labeled 1012 has been linked in the two images on the right and is now being referenced in the final image. The expected position is triangulated by the two lines in the left image. In the left image, the point has turned blue, indicating that it is within what PhotoModeler® allows with the expected range, given the default operating parameters of one residual pixel.

Once the initial image in the sequence has been completely referenced, the operator should check the residuals. The residual reflects the disagreement between the cameras detecting the point and provides a measurement of the accuracy of the project being processed. The residual in PhotoModeler® is found by projecting the previously calculated three-dimensional point onto the photo and calculating the difference between the expected position and marked position. Any residuals above 1 pixel width are considered poor accuracy. As can be seen in Figure 28, the laser grid points look different from each camera angle. The operator must evaluate any high residual points to

determine the correct position for the point to be placed. If the residual cannot be reduced, the point should be deleted from the processing.

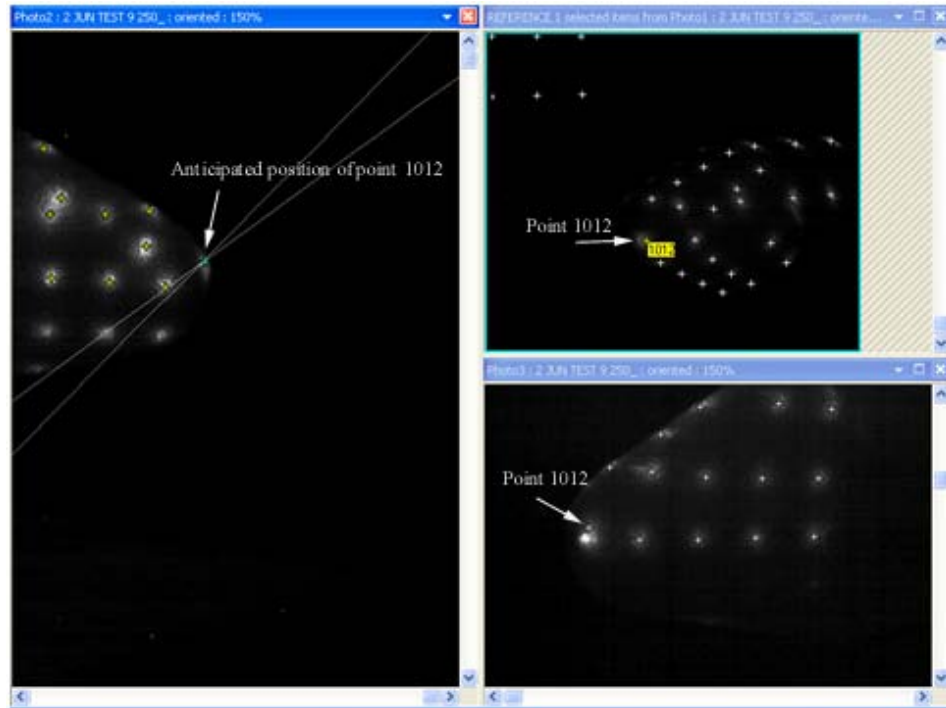


Figure 28: Three-dimensional referencing of point 1012 in a PhotoModeler® image

PhotoModeler® provides the operator with a tool for increasing the accuracy of the project. After the residuals have been reduced, PhotoModeler® can then propagate through the sequence of images. The operator must manually review each image in the sequence for incorrectly referenced points and high residuals. At any point during the correlation and referencing, the scale, units, and origin of the project can be selected. This is not necessary for processing, but aids in data processing by giving the export data proper units. The time epochs are selectable and in the research presented here were one half second apart.

Figure 29 shows an inverted rendering of the three-dimensional points resulting from processing in PhotoModeler® with a three dimensional representation of the grid points. These images can be rotated and viewed in all time epochs processed. The coordinates of the point cloud can be exported in a text file of three dimensional data points along with the residuals of each point. Table 5 is the data export of the three-dimensional coordinates for point 1012 as shown in Figure 28. The positions are relative to one of the anchor points on the floor of the wind tunnel.

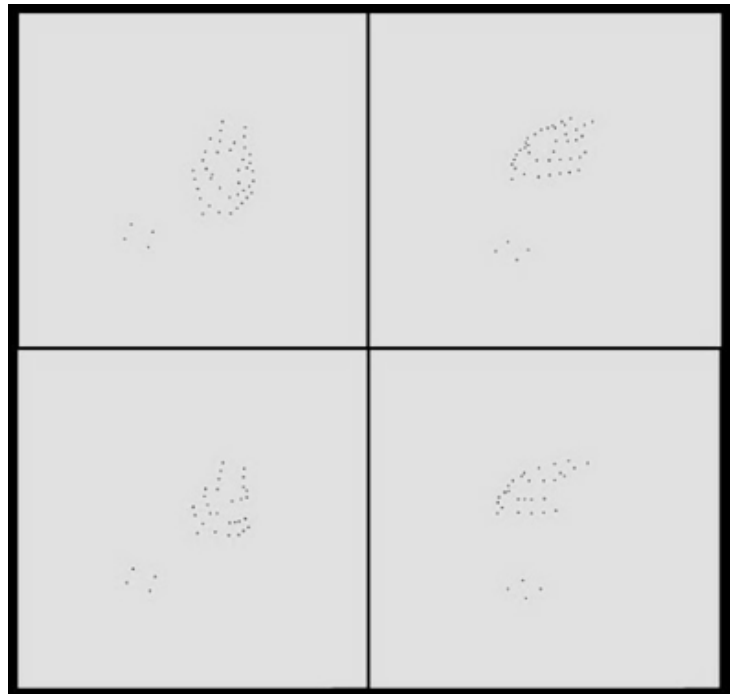


Figure 29: PhotoModeler® image of initial 3-D data (top) and final time position 3-D data (bottom)

PhotoModeler® software has been used in house at AFIT for several years. For example, Captain Nathan Pitcher used the PhotoModeler® software with the PMV module to capture three dimensional images of a flexible wing. That research used

physical targets on the surface which is challenging to apply to an ablating body such as in this research (Black, Pitcher, Reeder, & Maple, 2010).

Table 5: PhotoModeler® data export for point 1012 of test run 2 Jun Test 9

Point ID	Epoch	X position (mm)	Y position (mm)	Z position (mm)
1012	0	29.87	11.86	36.38
1012	1	29.80	11.89	36.39
1012	2	29.74	11.87	36.34
1012	3	29.69	11.82	36.44
1012	4	29.65	11.77	36.50
1012	5	29.57	11.71	36.45
1012	6	29.50	11.68	36.46
1012	7	29.43	11.66	36.39
1012	8	29.38	11.68	36.37
1012	9	29.31	11.76	36.40
1012	10	29.26	11.72	36.42
1012	11	29.20	11.63	36.40
1012	12	29.11	11.49	36.37
1012	13	29.07	11.51	36.36
1012	14	29.06	11.37	36.35
1012	15	29.01	11.37	36.35

3.2 Accuracy and Limitations

This section outlines and quantifies the sources of error involved in the experimental set up and data capture. Identified sources of error are shown for imaging through the shock, image capturing, image processing, and tunnel flow conditions.

3.2.1 Image Capture

To determine the accuracy of the analysis, images of plastic resin models were taken and processed at zero angle of attack. The image seen in Figure 30 was taken from

the location of Camera C and shows a spherically blunted cylinder plastic resin model with the two class IIIa laser grids projected onto its surface. The third laser, which would be projected from above, is not on in the image.

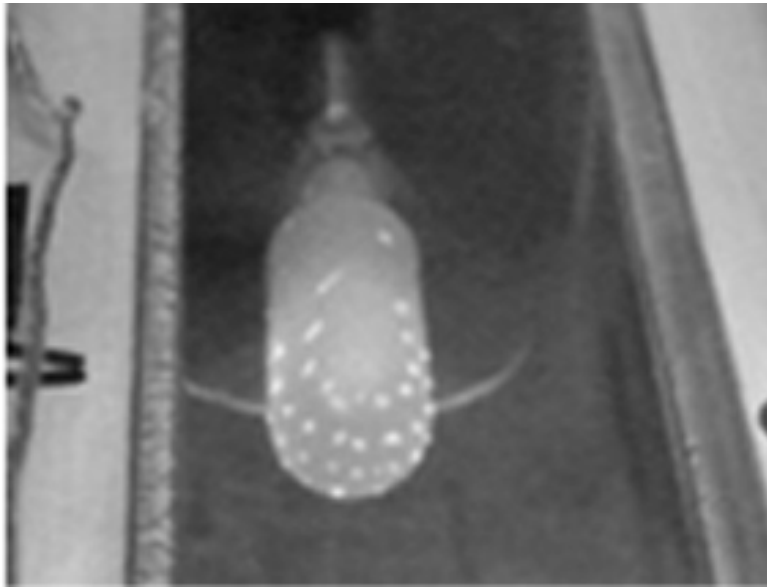


Figure 30: Plastic resin model of a spherically blunted cylinder in model with two laser grids projected onto the surface

With the set up and data capture used for all data captured in this research, the processed static shape data was compared with the known dimensions of the model. The error in diameter was found to be 0.07 mm error or about a 1% difference from the expected value.

In further test runs, the “noise” of the wind tunnel was found by following the change in grid position during a plastic resin model test. Since no ablation occurred, this was considered a control run reflecting wind tunnel noise, perhaps due to model vibration or deflection. The cameras and lasers do not touch the wind tunnel, but the tunnel operation can lead to vibrations in the room which can cause errors in the processing. The

noise in the data was also of interest in determining if the test article was moving in the flow or if the sting was allowing motion. The level of fluctuations was reasonably small. The average fluctuation of similarly placed points are graphed in Figure 31 and displayed in Table 6 for multiple pressures.

It should be noted that these points did not move over time but would oscillate in a location, and one might think of the average displacements as an error radius for each grid point. The largest was actually at the lower pressure test run. Even then, the error is comparable to the difference in the solid shape found during the accuracy test.

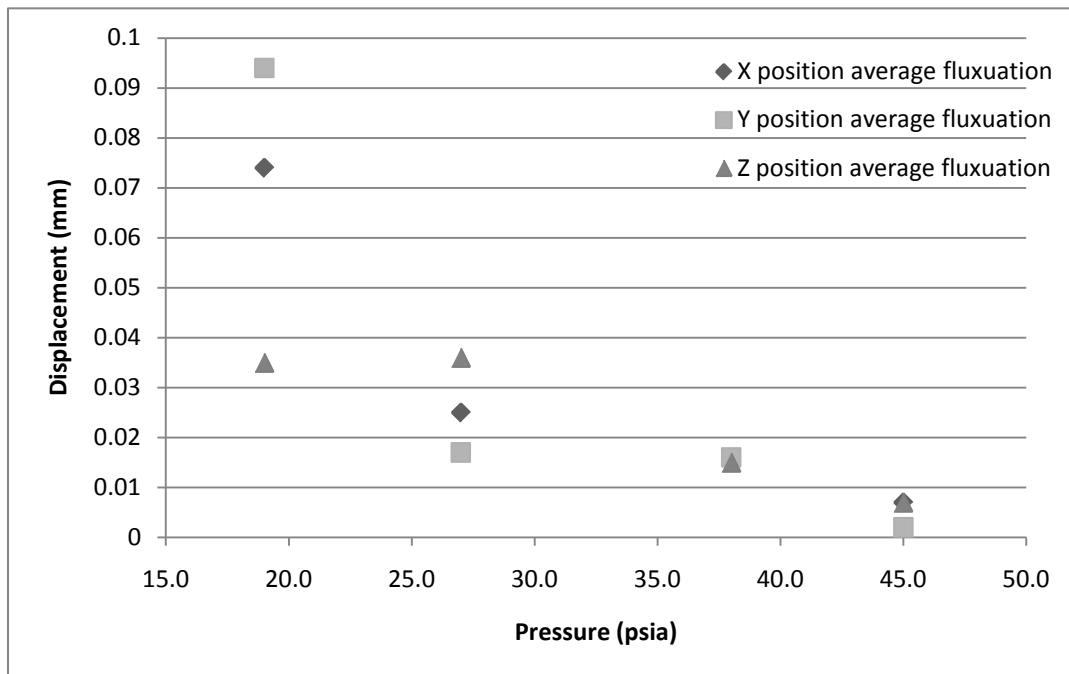


Figure 31: Average fluctuation during plastic resin model tests at varying pressures

Table 6: Displacement of points during solid model runs at various pressures.

Test Pressure	Axis	Average displacement (mm)	Standard Deviation
19 psia	X	0.07	0.012
	Y	0.09	0.018
	Z	0.04	0.012
27 psia	X	0.03	0.011
	Y	0.02	0.018
	Z	0.04	0.014
38 psia	X	0.02	0.012
	Y	0.02	0.008
	Z	0.02	0.013
45 psia	X	0.01	0.006
	Y	0.00	0.003
	Z	0.01	0.007

3.2.2 Image Processing

In this research, the laser grids are projected onto the dry ice models at an angle. Therefore as the model ablates, the laser grid moves across the surface. Thus, the data must be treated as a surface taken over time versus following a specific point. The same point on the surface can be used directly in some instances, such as a point from the center laser pointing down. If a particular position is desired, however, the point data can be determined using intensive user interaction with PhotoModeler®.

For example, in Figure 32, a single point of interest is highlighted in red and with arrows in each image. These two points are referenced across the three images and are very near the leading edge of the model. The left image is taken from tunnel side A, the top right is from Camera C looking down, and the bottom right image is from tunnel side B. Visible in the images, the laser point can look different in each view and it is up to the

operator to maintain as near the same place on each point over time. It is also obvious in Figure 32 that the point is much smaller than the laser dot. The size of the laser dot can cause problems with the automation of the PhotoModeler® software as the program only looks for center of each laser dot. The center may not be the same location within the laser dot on each photo, or the software may pick an incorrect laser dot in a time step and propagate the error in proceeding time steps. The laser dot shown in Figure 32 is approximately 1 mm in diameter. The change in position of a single laser dot is not important so long as the data point is considered in context with other points on the surface.

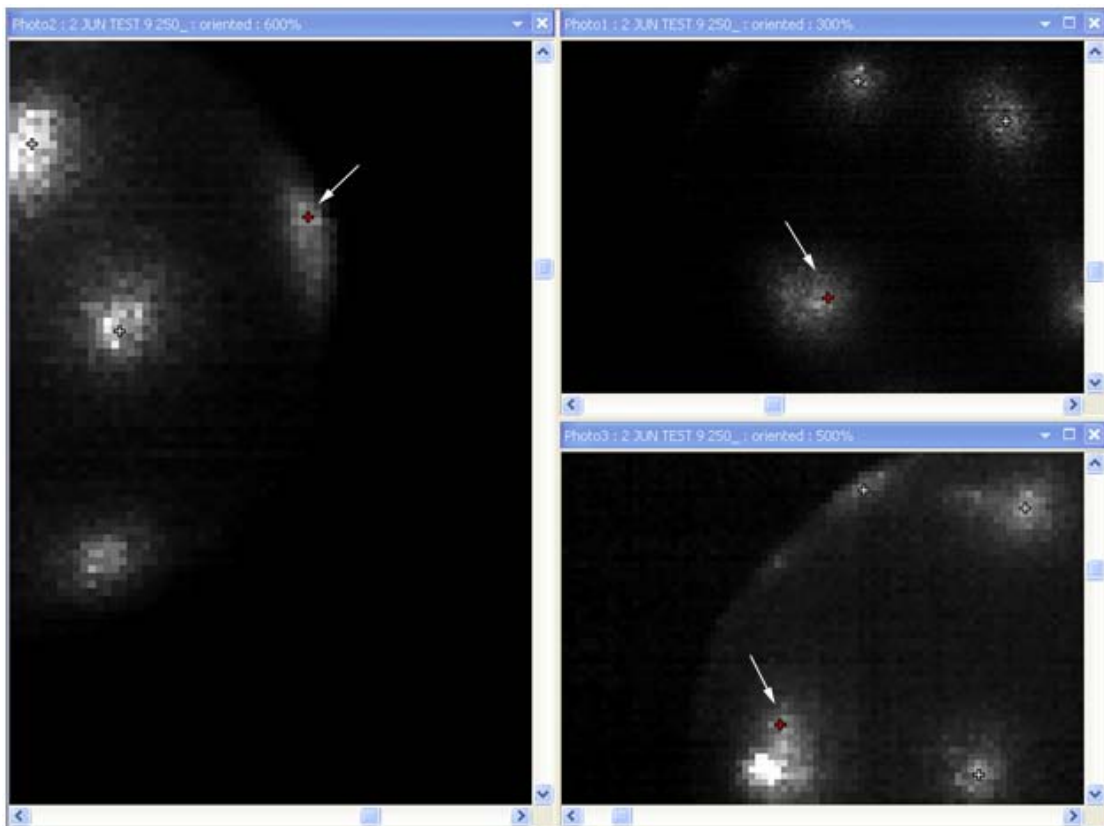


Figure 32: A correctly referenced point in PhotoModeler® illustrating how a laser point can look different in each camera view

Nose recession was determined by selecting points on or near the leading portion of the nose that have only small movements in the off body axis directions. Intensive operator input was used in these cases to maintain the correct position in the laser dot as the surface changed.

When tracking recession of the stagnation point, it would be preferable to have the laser points track from directly in front of the model, allowing for direct correlation between the x direction displacement and the laser grid points. However, this would require the laser projectors to be inside of the wind tunnel was simply not a viable option in the AFIT blow down facility.

The three sources of known measurement errors in the image projection, capture, and processing are all less than 0.1 mm. Data in this research is presented limited to the nearest 0.01 mm with the knowledge that there may be a small error in data of less than 0.1 mm.

3.2.3 Index of Refraction

Another source of error is introduced by the shock wave in the flow. Since the photogrammetry relies only on where the projected laser dots lie on the model, it does not matter that the beams refract as they pass through a shock wave. However, the fact that the shock wave is present between the imaged surface and the camera will affect the inferred location of the dots similar to looking into a pool of water.

The change in refractive index was clearly present given that it forms the basis for the Schlieren flow visualization. The visualization also indicated that the standoff

distance of the normal shock was small. To assess the order of magnitude of the error due to refractive index change, a near worst-case scenario is assumed. The density change across a normal shock, consistent with tunnel conditions, is assumed to lie 5 mm off the surface. In practice, the standoff distance is much smaller in the normal shock region. For this scenario, two cameras are assumed to view the point on the surface, and the error in the position normal to the shock is determined as demonstrated in Figure 33.

Here, the shock is treated as a boundary between two fluids and assumed infinitesimally thin. In Figure 33 a diagram of this exercise with the index of refraction designated n fore of the shock while the n' conditions are aft of the shock. Index of refraction, n , is the ratio of the speed of light in a vacuum to the speed of light in the subject medium. Although the index of refraction varies slightly with wavelength, the density of the gas is mainly responsible for the change. The error expected is also visually noted in Figure 33.

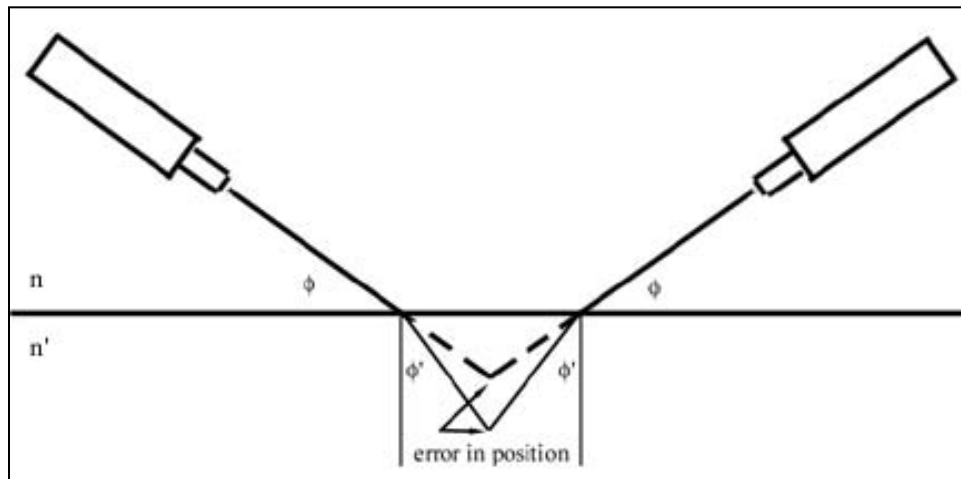


Figure 33: Index of refraction error diagram

Using Equation (27), the angles of incidence were calculated for a range of camera angles. Using the CRC tables (Lide, CRC Handbook of Chemistry and Physics, 2009, p. 10246), the index of refraction was found for air at the conditions fore and aft of the shock. Equation (27) was used to calculate the ϕ' , which is the angle of refraction, for the range of wavelengths of the lasers (400 and 710 nm) and for $P_o = 6$ and 46 psia. The error was then determined based on the difference of the viewing angle and the angle of refraction. The error difference between the two laser wavelengths was negligible. The error results found for the range of camera viewing angles are presented in Table 7.

(27)

Table 7: Error in position of point for a range of camera angles

	$P_o = 6$ psia		$P_o = 46$ psia	
n	1.00001		1.00007	
n'	1.00012		1.00086	
ϕ (degrees)	ϕ' (degrees)	error (mm)	ϕ' (degrees)	error (mm)
20	20.00	0.002	19.98	0.012
25	25.00	0.001	24.98	0.010
30	30.00	0.001	29.97	0.009
35	35.00	0.001	34.97	0.008
40	39.99	0.001	39.96	0.008
45	44.99	0.001	44.96	0.008
50	49.99	0.001	49.95	0.008
55	54.99	0.001	54.94	0.008
60	59.99	0.001	59.92	0.009
65	64.99	0.001	64.90	0.010
70	69.98	0.002	69.88	0.012

As seen in Table 7, the largest error found is 0.01 mm in the high pressure and mid range viewing angles. As was shown in the preceding sections, this is the smallest error source and is nearly negligible.

3.2.4 Tunnel Test Condition Continuity

As the AFIT wind tunnel system used for this research is a pressure blow down system, there is the possibility of the tunnel pressure tapering off over the course of the test due to the limited volume of the pressure tank. A drift in stagnation pressure or temperature would lead to difficulties in analyzing and characterizing the ablation rate data. In order to better capture the tunnel pressure characteristics, stagnation pressure, pressure at infinity and stagnation temperature were plotted starting at $t = 3.5$ seconds in Figure 34 for a 38 psia average stagnation pressure test. As per Section 3.1.2, $t = 0$ is the initialization of the wind tunnel and data acquisition began after the 2.5 second pause between vacuum and high pressure valve operation and an additional second for flow stabilization.

It is noted in Figure 34 that the temperature data starts high and drops rapidly. This behavior is due to the response time of the thermocouple probe in the tunnel stagnation chamber. The probe responds to the initial vacuum pull of the tunnel as a temperature increase and is slow to correct. It is also intuitive from the figure that while there is a variance in the pressures over the course of a run, the pressure at infinity is near constant and the stagnation pressure is not tapering off.

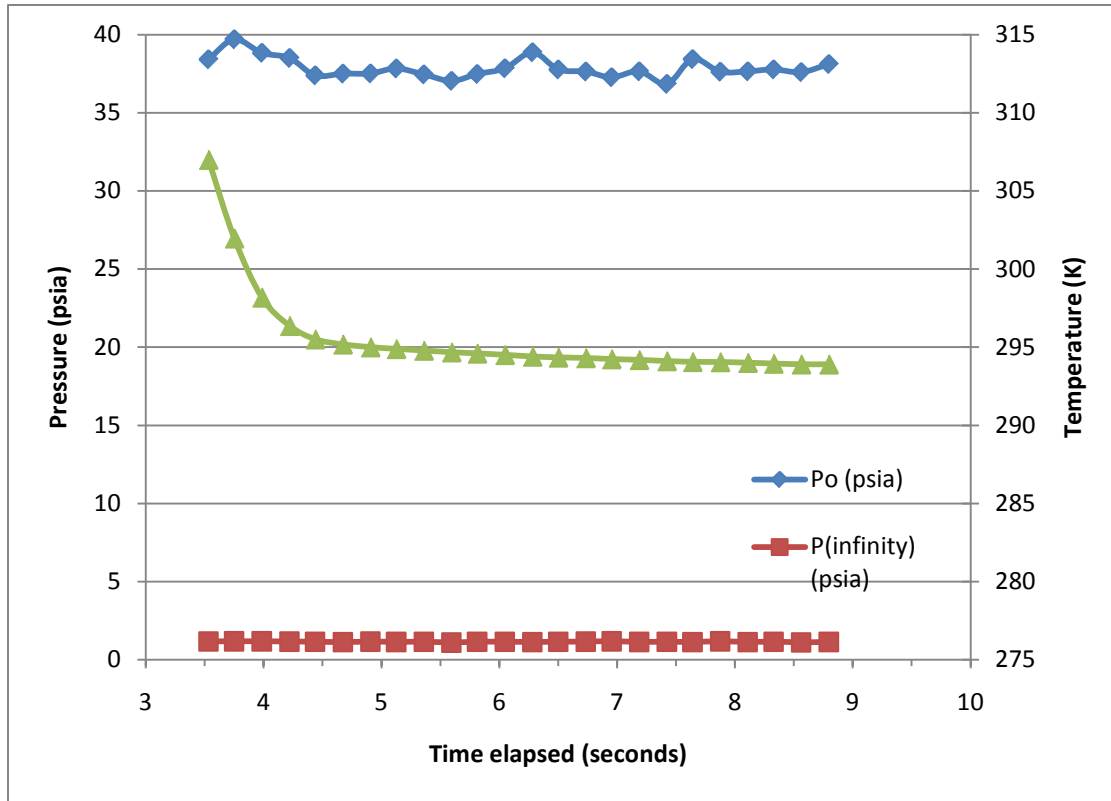


Figure 34: Stagnation pressure, pressure at infinity, and stagnation temperature over the course of a $P_o = 38$ psia test

Figure 35 presents a graphical representation of the stagnation density over time of multiple tests covering the range of stagnation pressures presented in this dissertation. The ending time of the pressure data is dictated by one of two things. Either the run was ended manually due to model failure or a predetermined test section pressure was reached, typically 3 psia. It is noted that for tests above 30 psia stagnation pressure, the assumption that the flow has stabilized by 1 second after flow initiation is off by approximately one second and the experimental results must be adjusted to take into account this lag time. Table 8 below gives the average stagnation pressures, stagnation densities and the stagnation density standard deviations of the individual runs.

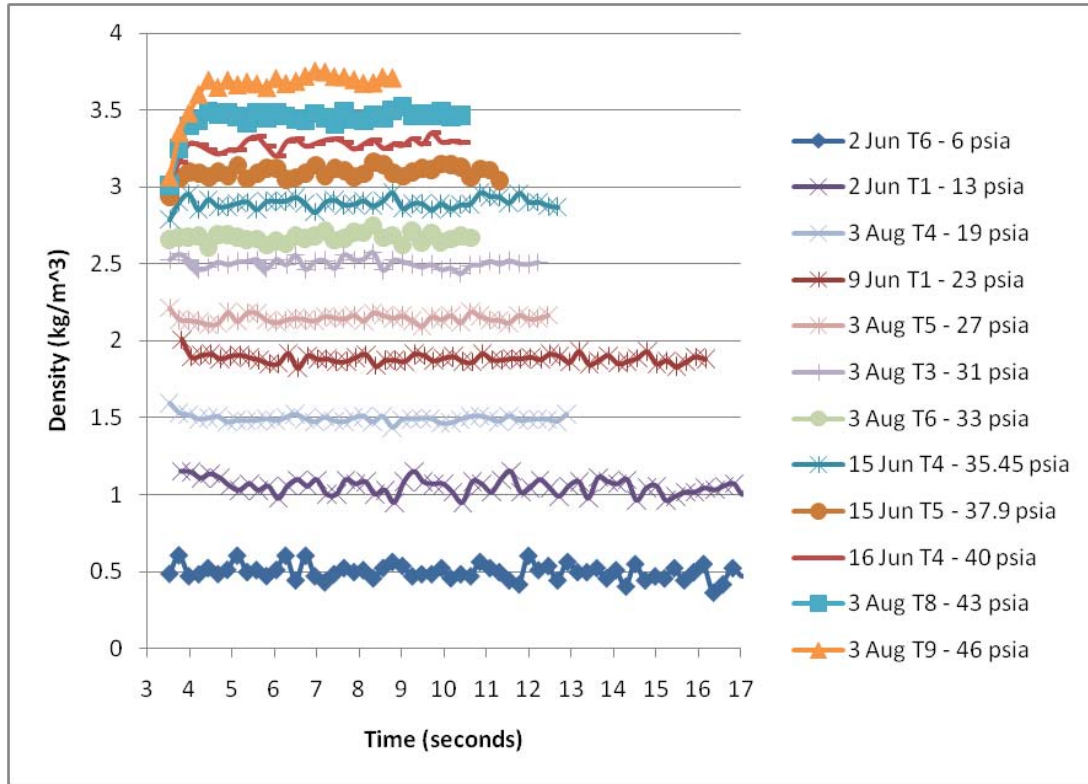


Figure 35: Multiple stagnation densities for the duration of each test

The averages presented in Table 8 include the first second of data ($t = 3.5$ to 4.5 seconds) which skews the higher pressure standard deviations. Overall, the standard deviation is low and the fluctuation in the tunnel conditions is low as well.

Table 8: Average and standard deviations of stagnation pressures

	Average Stagnation Pressure (psia)	Average Stagnation Density (kg/m ³)	Standard Deviation of Stagnation Density
2 Jun T6	6	0.50	0.05
2 Jun T1	13	1.05	0.05
3 Aug T4	19	1.49	0.02
9 Jun T1	23	1.88	0.03
3 Aug T5	27	2.15	0.03
3 Aug T3	31	2.51	0.03
3 Aug T6	33	2.67	0.03
15 Jun T4	35	2.90	0.03
15 Jun T5	38	3.09	0.04
16 Jun T4	40	3.27	0.06
3 Aug T8	43	3.44	0.09
3 Aug T9	47	3.80	0.15

3.3 Dry Ice Models

As noted in Chapter 1 solid carbon dioxide, commonly referred to as dry ice, has been manufactured for close to 200 years. It is most commonly used for refrigeration and special effects. With a sublimation temperature of 194.65 K at 1 atm, it also offers the possibility to be used as a low temperature ablation simulator.

The choice of dry ice as the principle model material was made after reviewing the available literature and the available test equipment at AFIT. Any solid material released in the wind tunnel must be removed to avoid damage to the vacuum pumps. Since dry ice sublimates directly to a gas at ambient conditions, there is no residue associated with the material being pulled into the vacuum chamber.

3.3.1 Fabrication of Dry ice

The fabrication method developed for this research was based upon the process developed by Kohlman and Richardson (Kohlman & Richardson, 1969), who formed the models directly from liquid carbon dioxide in molds of the prescribed shape. The general principle, similar to those described previously, takes liquid carbon dioxide under 350psig and drops the pressure to room conditions, thereby flash freezing some of the liquid into solid.

A commercially available dry ice maker, the Frigimat Cub Dry-ice Maker, was initially purchased for the purpose of studying the formation of dry ice. When in operation, a brick of dry ice is produced in the Cub's reservoir. Designed to operate at less than 10 psig with a pressure relief valve and a pressure gauge for safety, the Cub Dry-ice Maker can be hooked up to any carbon dioxide tank with a liquid tap.

Initial investigations yielded two points of interest. First, the dry ice produced had the consistency of snow and was therefore not dense enough for model usage. Second, filters were used to allow outgassing. There is a need to allow both air and excess carbon dioxide gas to evacuate the mold area as the dry ice is formed. Preventing the out gassing can cause a void in the formed solid or a dangerous build up of pressure inside the mold, neither of which is desirable.

From the lessons learned in the use of the Cub Dry-ice Maker, a method was developed to proceed with model fabrication. Generally speaking, liquid carbon dioxide flowed out of a siphon tube of the tank through a flexible, insulated metallic hose, and formed dry ice in a mold of a predetermined shape. An image of this set up is presented in Figure 36. A four way connector that came with the Cub was used to support a 10 psi pressure release valve and a pressure gauge for monitoring. The connector was eventually modified to include a relief valve, 130 psi pressure release valve, 500 psi pressure gauge, and a Swagelok® ball valve. The connector can be seen in Figure 11 on page 53. A 300-350 psig carbon dioxide Dewar tank, seen in Figure 36, was chosen as the liquid carbon dioxide reservoir over the smaller 800 psig tank because it provided longer duration model production and allowed the production of more models from a

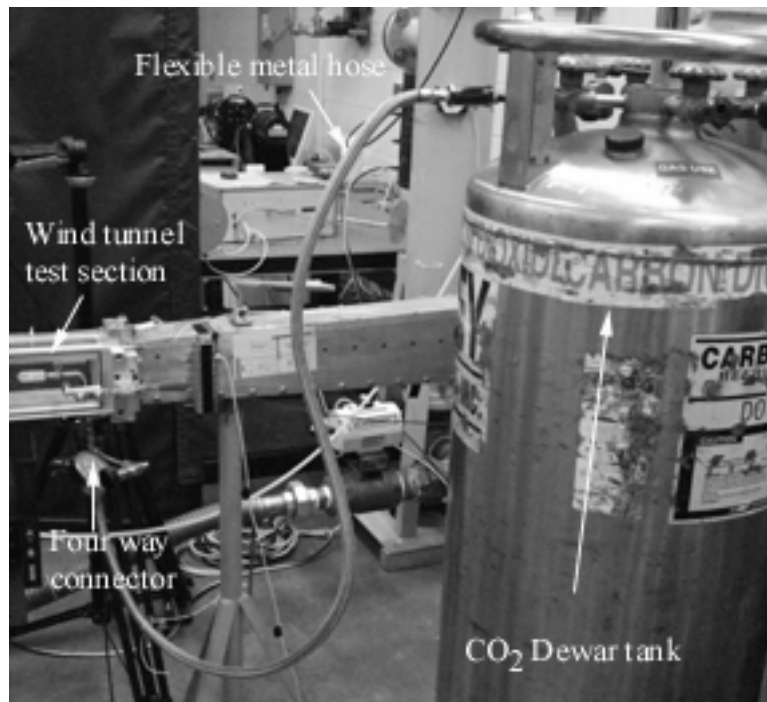


Figure 36: Liquid CO₂ delivery set up

single tank. Also since the molds were made of resin, the lower pressure of the Dewar relieved potential safety concerns. The Dewar tanks worked reasonably well, so the higher pressure cylinders were not used. Under normal circumstances, a Dewar produced approximately 40 models per full tank.

With the liquid carbon dioxide source and delivery system selected, the design of the mold was considered. From literature reviews such as Kohlman and Richardson's (Kohlman & Richardson, 1969) work and experience with the Cub Dry-ice Maker, it was obvious that some type of filter needed to be included for outgassing. Since it was desired from the beginning to fabricate the models in the tunnel, it was realized early on that the filter would need to be connected to the sting and left in the tunnel during operation. The type of filter used in the Cub Dry-ice Maker was found to have a consistency and strength similar to Styrofoam. It is unknown whether this material could withstand the conditions inside the test section of the wind tunnel, and with the only feasible way to determine that being a live test, an alternative was sought.

A porous metallic filter produced by Mott Corporation out of 316L stainless steel was found that met the needs of this research. The filters can be machined and cut and are hydrophobic, so the liquid carbon dioxide is trapped but the filter allows outgassing. The filters come in a variety of porosity from 0.1 to 100 microns. The research presented here used a 20 micron filter unless otherwise stipulated; 10, 40, and 100 microns were also investigated. Tests were performed to investigate if the porosity had an effect on the density of the model and those results are presented later in this section.

After the choice of a metallic filter, a Solidworks® split mold model was produced. Figure 37 shows half of a mold as viewed in Solidworks® for a spherically blunted cone mold. The Solidworks® model was exported as an IGS file and used to produce a rapid prototype resin mold model on an Eden 500V rapid prototype machine. An example of the end result is seen in the spherically blunted cylinder model and mold shown in Figure 38. The material handled repeated cycling between room temperature and -80° C while being subjected to 300 psi with no signs of wear. The molds were made in two pieces and held together by four screws. The only problem encountered with resin pieces was a tendency for the insulator to break when manipulated at cold temperatures.

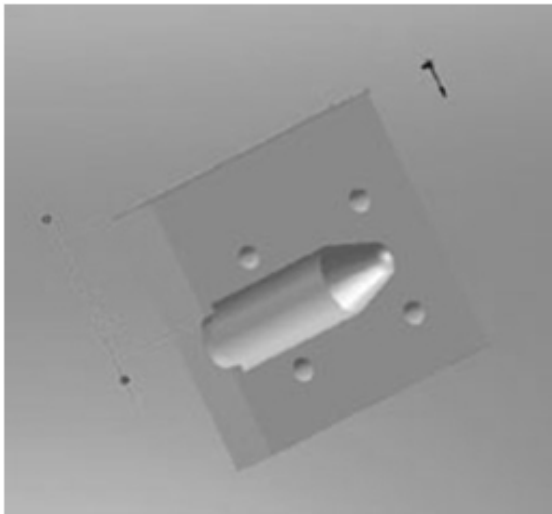


Figure 37: Solidworks® image of spherically blunted cone mold half

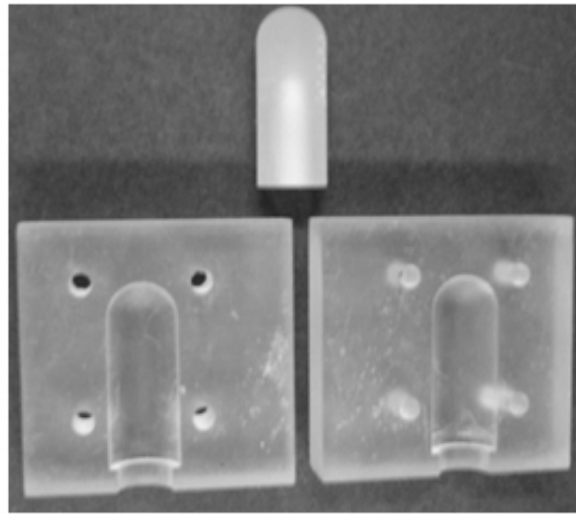


Figure 38: Resin mold for spherically blunted cylinder model and molds

Initial models had a one inch diameter base and were of the basic shapes of a cone or a spherically blunted cylinder. Due to difficulty with starting the wind tunnel using models of this size, the diameter of the models was scaled down to a 0.6 inch base.

Unless otherwise noted, the models discussed are those with a 0.6 inch diameter base. Lengths varied from shape to shape but fell into a range of approximately 1.5 to 2.5 inches. Detailed drawings of the shapes are provided in Appendix A.

Initial model fabrication experiments were done outside the wind tunnel. A stainless steel tube took the place of a conventional wind tunnel sting and was made of 0.25 inch outer diameter steel tubing with an inner diameter of 0.12 inches. These dimensions were the same as the tube used in the wind tunnel. Larger inner diameter tubes were considered for flow characteristics. However, the outside of the tube had to be threaded for the insulator and due to concerns about the thickness of the pipe wall, the AFIT Machine shop advised against attempting to thread a thinner walled pipe.

A resin insulator also designed in Solidworks®, was placed on the sting forward of the filter to minimize heat exchange between the steel tube and the dry ice model. Once the models were reduced to the 0.6 inch base, the nut would not fit within the opening in the mold and a resin spacer was placed between the filter and the securing nut to accommodate the nut and allow outgassing. An image of the exterior test sting with the insulator, filter, spacer, and nut can be found in Figure 39. Figure 40 shows half of a mold on the sting in the wind tunnel as would be set up for a test and provides a visual reference of the mold and sting configuration.



Figure 39: Exterior test sting and liquid CO₂ feed tube

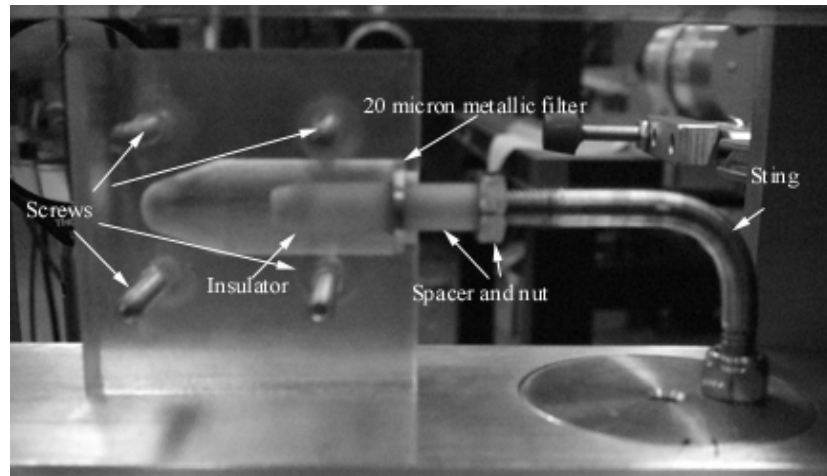


Figure 40: Mold half on sting in wind tunnel

Once the mold, filter, and sting were ready, research was conducted outside of the wind tunnel. Initial fabrication attempts were performed with a 100 micron filter and the 10 psig relief valve included in the Cub Dry-ice Maker. These attempts produced models that did not survive removal from the mold, as seen in Figure 41.



Figure 41: Early test article that failed upon removal from mold

It was observed that the initial models had a low density similar to that produced by the Cub Dry-ice Maker. After consulting the manufacturers of the Cub Dry-ice Maker, it was determined that a higher pressure relief valve was required to produce denser models.

It was quickly obvious that the addition of a 60 psig relief valve did in fact produce a denser model; however, the model was still not structurally sound enough for wind tunnel use. A 130 psig pressure relief valve was ordered and installed. This produced even denser models. A higher pressure gauge was also installed that provided monitoring up to 500 psig. The higher pressure also required the clamping of the mold in place as the relief valve now had more than enough pressure to move the assembly at high velocity. Figure 42 shows set up and the restraints for external model fabrication.

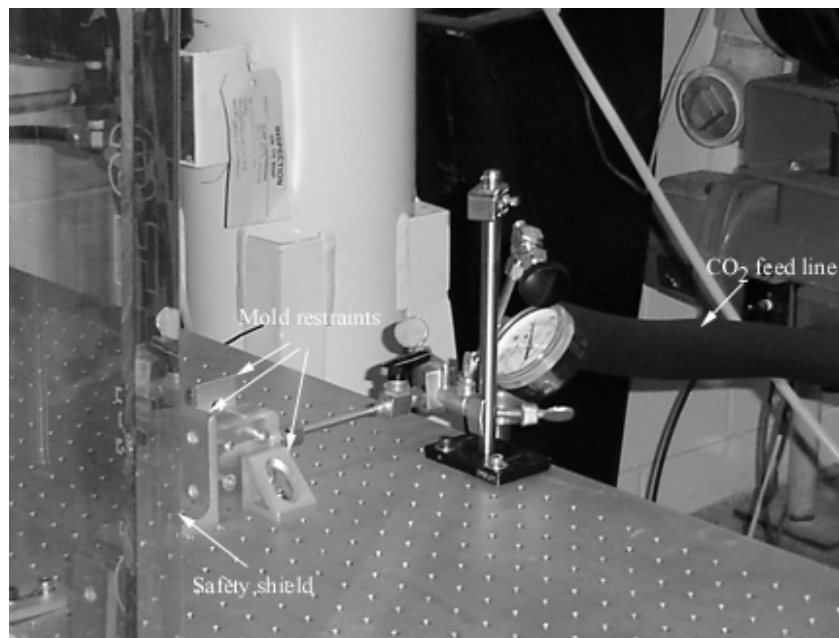


Figure 42: Out of tunnel dry ice model fabrication set up

Even with the 130 psig relief valve, the articles were not entirely satisfactory in that the surfaces were not smooth. It was obvious during formation that solid particles were exiting the mold through the filter. So the 100 micron filter was changed to a 40 micron filter. This produced far better models that were strong enough to withstand handling. To check the model integrity, the model was struck with a screwdriver. Surfaces of these models were also generally smoother. Typical success rate of model formation with the 40 micron filter was one in three attempts for the spherically blunted cylinder model.

A successful model build was considered one that was satisfactory for tunnel use. This meant that there were no large defects in the ice such as cracking or holes. Pin-sized small holes located at least a half inch from the nose of the test article were allowed, and were somewhat common.

Since the drop from a 100 to a 40 micron filter was successful, the filter was replaced again with a 20 micron version. This produced a visibly better model with about the same success rate. Visual observation suggested that the 20 micron filter produced a denser model than the 40 micron. This observation was investigated and confirmed during density measurements as documented at the end of this section.

A 10 micron filter was also investigated and worked well in the one inch diameter models; however, when the models were refined to a 0.6 inch diameter base the 10 micron filter produced defective models. The most common error was that some large regions did not fill with dry ice. The success rate for the 10 micron filter was closer to one in five models attempted, and was therefore not investigated further. The five micron

filter continued this trend with larger voids believed to be from trapped gas. For these reasons, none of the filters with porosities smaller than 10 microns were investigated further and the research was conducted using the 20 micron filter. It is possible that some of these findings are model specific, and future work might lead to more robust filter configurations.

To actually produce the dry ice, the mold with its pressure gauge and relief valve was attached to the carbon dioxide Dewar's liquid tap via a flexible metal hose. On later runs, this hose was wrapped in a rubber insulator to minimize heat transfer and to protect the operator from the cold metal sheath. The hose was secured with a safety line in the event of a fitting release, and the mold was clamped to the table.

The most productive technique found for model fabrication was as follows:

- 1) The liquid tap on the Dewar was turned until the pressure relief valve began blowing off. The first several seconds of flow are gaseous as the liquid flows through the siphon.
- 2) Once liquid was flowing, which was visible as a large cloud of condensation exiting the mold or relief valve, the valve was opened another full turn.
- 3) The semi-transparent resin allowed for the model to be observed for fullness, and the pressure gauge was monitored for back pressure build up. As the models were refined over the research, the molds were built on a glossy setting which produced a more transparent material to allow for easier viewing during model

fabrication. Once the mold was full or the pressure spiked to 300 psig, the tank valve was closed and the Swagelok® ball valve was closed.

4) The mold was opened and the model inspected for defects.

The combination of a 20 micron filter, a 130 psig relief valve, and this technique produced a success rate of approximately two out of three attempts. It should be noted that not all carbon dioxide is solidified. If the pressure is under the relief valve safety pressure (130 psig), the line is still pressurized. A manual relief valve was installed near the pressure gauge to relieve pressure prior to mold and model removal. All safety equipment should be worn until the pressure gauge reads atmospheric conditions.

If the flow from the tank is not increased soon after the liquid carbon dioxide is flowing into the mold, the pressure relief valve can potentially freeze up, causing the mold to be exposed to the full 300-350 psig of the tank. Also, the tank must have at least 300 psi reading on the gauge because lower values did not generally produce viable models. A pressure reading of 350 psi is preferred but is not always sustainable. Care must be taken in rapidly repeating model builds. Times of five minutes or less between model fabrications can quickly freeze the flexible hose. A frozen hose typically took fifteen minutes or more to thaw unaided. Producing more than five models in less than twenty minutes can overdraw the Dewar. In this scenario, the liquid is siphoned off so quickly that the tank contents may partially solidify. A frozen over tank takes more than a day to completely thaw and cannot be used until thawed.

Also of note, the production of dry ice appeared to be dependent upon the relative humidity present in the room. Observation showed that if the measured relative humidity inside the building was greater than 70%, then the success rate of models dropped by 50% or more regardless of shape.

The Swagelok ball valve was installed in the carbon dioxide feed line below the tunnel on June 2, 2009. Nearly 100 test runs were performed before the installation date and more than 170 test runs were performed afterwards. In an effort to compare similar test conditions, only the tests conducted after the installation of the Swagelok ball valve are included herein. All processed results correspond to runs performed with the 20 micron filter.

Of the 172 runs of interest, 58 test results were not processed. The most common reason to exclude a test was the premature failure of a dry ice model as any test that did not last a minimum of two seconds was not processed. These premature failures typically occurred in high pressure tests. Another common reason for discarding a test run was the discovery of obvious defects in the model made visible after exposure to the wind tunnel flow. A rapid development of voids near the nose was the most common sign of this condition. It is believed this might be improved if vents were located at various points in the mold to facilitate the expulsion of trapped gasses.

Six test runs were excluded from processing due to a lack of anchor points used for image processing or poor three-dimensional correlation. The lack of anchor points was usually caught during testing and immediate review of the test run. At least three stationary anchor points are required for camera orientation, though more points are

preferred. If these points are not available and visible in all three images, the PhotoModeler® software can not accurately align the images to resolve the spatial location of points.

3.3.2 *Dry ice Model Density*

Once the technique for fabricating models reached a satisfactory point, density measurements were made and averages are given in Table 9. The set up for this part of the experiment is shown in Figure 43.

To generate the density measurements, the volume of the mold was first determined using distilled water at room temperature. A syringe was used to inject it into the mold. The mold and pipe were filled and the mass of the water taken. Eleven measurements were taken and the average mass of water was found to be 6.1 g. Using the relationship of the mass of water that $1 \text{ g} = 1 \text{ mL} = 1 \text{ cm}^3$, the volume of the model and the pipe tube is 6.1 cm^3 .

Table 9: Dry ice densities

	Average (g/cm ³)	Range (g/cm ³)
Density (20 Micron)	1.01	0.976-1.042
Density (40 Micron)	0.94	0.912-0.958

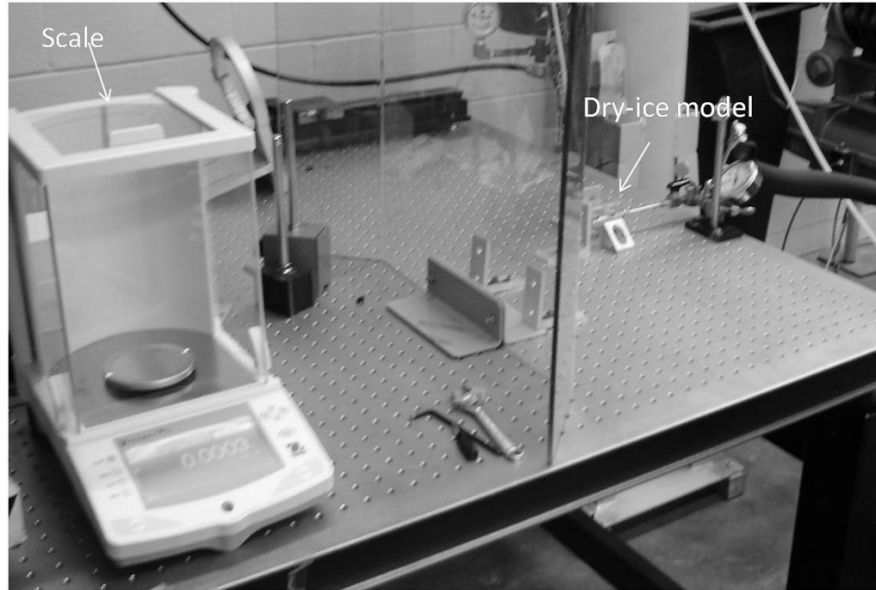


Figure 43: Density measurement set up

Dry ice models were then fabricated and measured to find the mass of the ice. The scale was re-zeroed before every measurement on the dry weight of the mold and pipe. Eight visibly flawless models were used to determine the mass of the models with a 20 micron filter and four samples of flawless models with the 40 micron filter. This proves that the visually suggested difference in densities was true, with a 7.5% increase in density for the 20 micron filter. It is also noteworthy that commercial grade dry ice is approximately 1.5 g/cm^3 , so the fabricated ice is about 30% less dense. Differences in densities are likely attributable to small voids present in the dry ice, which will in turn affect the thermal conductivity. The modified thermal conductivity is discussed in Section 3.4 with the set up of the ACFD code.

3.3.3 *Molds and Model Shapes*

Several test article shapes were investigated in this research, and full page diagrams of the models can be found in Appendix A. The process to make the models and molds began with a drawing of a model in Solidworks®. Once the male model was drawn, it was used to cut the shape out of a blank block. The block was then cut in half after adding an opening for the feed pipe, filter, and screw holes. An image of a Solidworks® mold half for a spherically blunted cone was presented previously in Figure 37. Later versions of the molds are shown in Figure 44 along with the out-of-tunnel test mount.

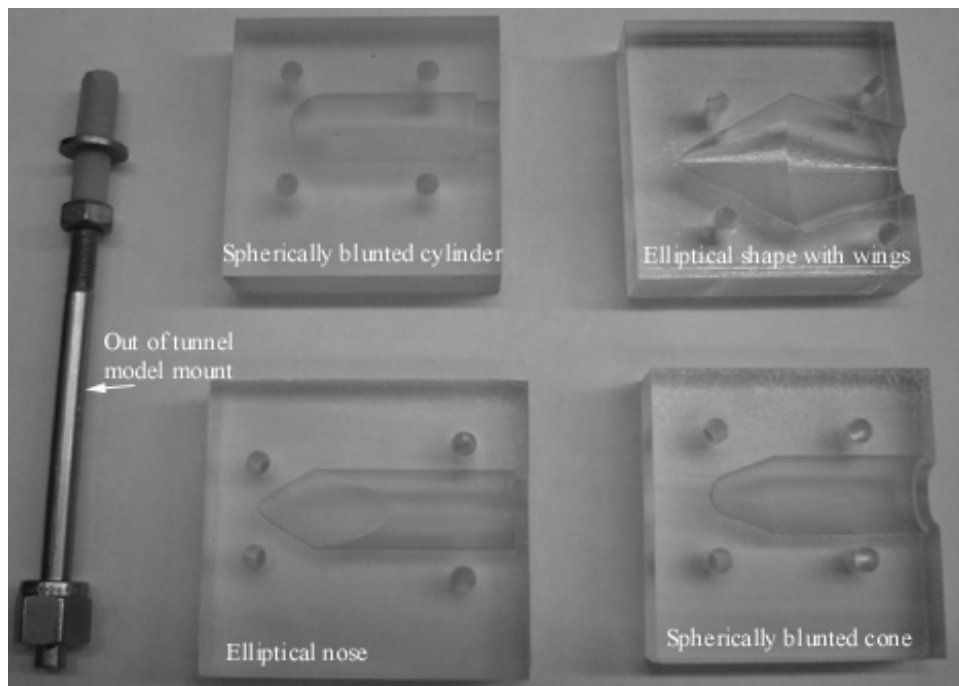


Figure 44: Mold halves for a spherically blunted cylinder, elliptical shape with wings, elliptical nose, and spherically blunted cone

The first two shapes chosen were basic shapes: a cone and a spherically blunted cylinder. These two shapes were investigated outside of the wind tunnel. The first cone shaped model had a 1 inch base and a cone half-angle of 15 degrees. The cone was of interest for the sharp leading edge, but was abandoned during fabrication as the ACFD cases were more conducive to spherically blunted cone and spherically blunted cylinder geometries. A secondary issue with the cone was structural instability. The sharp nose was not well supported by the dry ice due to the small diameter of the model overall and often broke upon removal from the mold. If a model could be made with a large enough diameter this problem might be able to be overcome.

Initially, a spherically blunted cylinder with a 1 inch diameter base and a nose radius of 0.5 inches was investigated and had good results in model building. After the initial out-of-tunnel experiments, plastic resin models were placed in the tunnel for shock observation. It was determined that the model size had to be reduced, and the models were stepped down until the tunnel operated properly which corresponded to a spherically blunted cylinder with a base diameter of 0.6 inches. The step down in size is visualized in Figure 45 for the cone and spherically blunted cylinder. The spherically blunted cylinder was reduced to a diameter of 0.6 inches with a nose radius of 0.3 inches. It yielded satisfactory models at approximately a two out of three success rate.

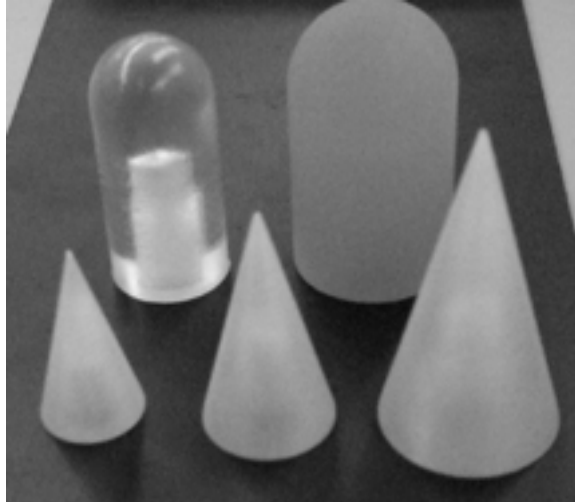


Figure 45: Spherically blunted cylinder and cone resin test models

After the initial two shapes were studied, a spherically blunted cone was developed as a conical shape to replace the failed cone model. A 20 degree cone half-angle with a rounded nose was placed on the front of a 0.6 inch diameter cylinder. The rounded nose was produced by tangentially rounding the cone, with the result a blunted cone with approximately a 0.15 inch radius nose. The spherically blunted cone was mounted on the front of a cylinder for two reasons: desired length of the model, and to prevent defects in the forward portion of the model. This model is presented as the second model from the left in Figure 46. This was the most successful of the models for fabrication with a typical success rate of three out of four.

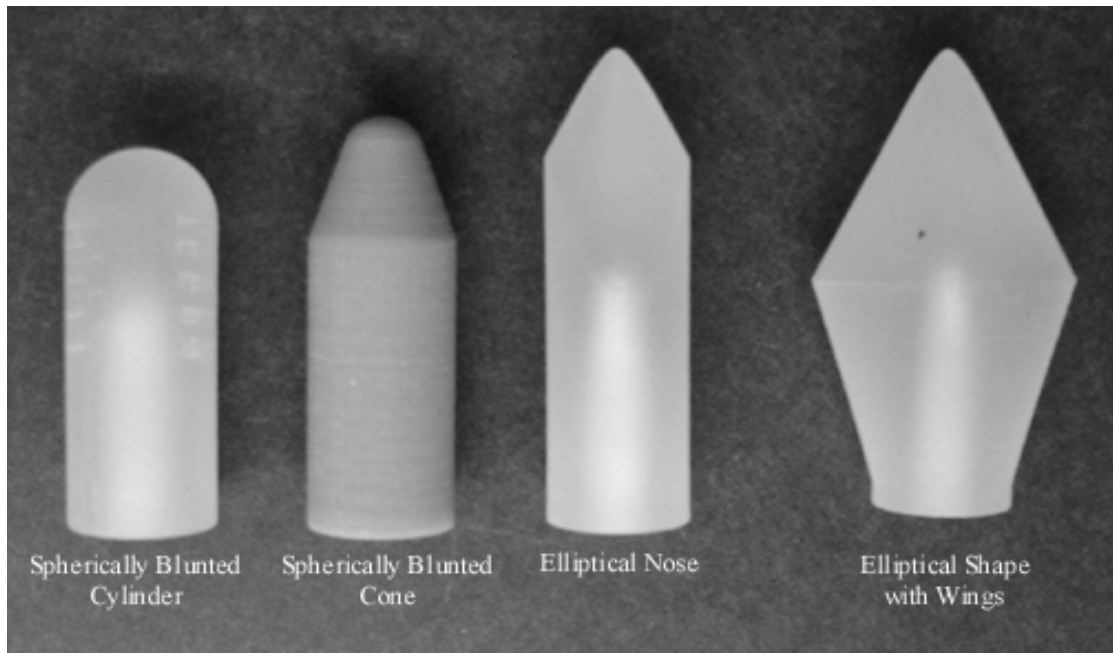


Figure 46: Resin test article models for (left to right) a spherically blunted cylinder, spherically blunted cone, elliptical nose and elliptical shape with wings

The next model investigated was a generic elliptical design requested and provided by the sponsor at AFRL/RBAC. Two versions of this model were made: an elliptical nose on a cylinder and an elliptical shape with wings. The nose areas of these two are identical with one truncated down to a cylinder base. Resin models of these two shapes can be seen as the right two models in Figure 46.

The elliptical nose on a cylinder, seen second from the right in Figure 46, was tested in a vertical orientation (shown) and a horizontal orientation, rotated 90°. The horizontal orientation worked well in zero angle of attack tests but was difficult to image in angle of attack tests. The vertical orientation produced good data in both zero angle of attack and ten degree angle of attack runs. Typical fabrication success of the elliptical nose on a cylinder model was approximately one in three attempts.

The far right model in Figure 46 is the elliptical shape with wings and is wider than the other models. Several zero angle of attack runs were made with this version in a horizontal orientation, and the common place for defects was out on the end of the wings. In all model shapes, the typical location for the defects was horizontally aligned with the end of the feed tube. The winged model had the added problem of the tips being far from the filter opening and thus the defects were larger. This shape in a horizontal orientation was difficult to image in angle of attack tests as the predominant shape change was along the thin leading edge and the coarseness and angle of the laser grids precluded accurate shape change imaging.

The elliptical shape with wings model was turned into a vertical orientation for angle of attack runs. The defects which had been out on the wing tips were here typically in the large flat surface area which was directly exposed to the tunnel flow by the angle of attack. These defects would grow rapidly and cause the models to fail prematurely. Because of this, the model with wings was not used apart from a few qualitative test runs. The elliptical shape with wings model had a fabrication success rate of approximately one in five attempts.

3.4 The ACFD Code Set Up

A primary goal of this research is to produce data using a repeatable technique to gather three-dimensional sublimation rates of an ablating body. A real world interest in this capability is to provide data for ACFD validation, as is the case with the sponsor of this research, AFRL/RBAC. A computational code being developed for AFRL to model

ablation of hypersonic vehicles is referred to as Ablation CFD or ACFD. The fundamental properties of ACFD and the underlying equations are described in Section 2.6. Presented in this section is the preparations and set up for the research presented herein.

Certain characteristic settings in the code were modified to enable a direct comparison to the experimental data. The tunnel operates at Mach 2.94 and stagnation temperature of 290K, which is not a high enough velocity to stimulate chemical reactions in the flow itself, so these chemical reactions had to be turned off in the flow solver. The solver assumes a chemical equilibrium fluid, with gas properties called from the NASA CEA code. ACFD stores an extensive list of molecules which can be added if a species of gas is found to be missing. The NASA CEA code was limited to gas fits above 300 K which made it ill suited for use with a dry ice simulation. To correct this problem, a hard sphere model that idealized molecules was used to give thermal data of the air and carbon dioxide molecules. The results of this idealized model were found to give similar answers to that of a perfect air assumption. Using the perfect gas model allowed for a much greater CFL number and faster solution convergence with ACFD, hence the calculations done for the simulations presented in this dissertation used the perfect gas model.

The ACFD code uses Blottner curve fits used for the carbon ablation analysis which were out of their data range just like the NASA CEA data. Sutherland's law was used to model the viscosity since it is valid for temperatures between $0 < T < 555 \text{ K}$ with an error less than 10% for pressures below 3.45MPa.

The solid properties for the dry ice were taken from Quinn (Quinn & Jones, 1936) and Sumarokov (Sumarokov, Stachowiak, & Jezowski, 2007) where a thermal conductivity of $W/(m^2 K)$ is reported for commercially produced dry ice. The solver utilizes the density, conductivity, specific heat, enthalpy, and entropy of the ablating material. Since, the density of the dry ice produced in this research was lower than commercial dry ice, it was assumed that there are small voids present and the conductivity will be lower as well. The voids (α) were assumed to be spherical in shape and uniformly spaced through the material and the effective thermal conductivity, k_{eff} , was estimated by the random walk method developed by Potter, *et al*, (Potter & Grossman, 1971) and shown in Equation (28).

(28)

The voids (α) were found to be the ratio of the density of experimentally produced dry ice to that of the industrial dry ice. The variation in the experimentally produced dry ice density was less than 7% and was incorporated into the ACFD test runs. Inputs for the solver included the static pressure and temperature in the test section and the carbon dioxide properties listed in Table 10: specific heat (C_p), enthalpy of the solid (H), heat of sublimation (H_{sub}), entropy (S), and the thermal conductivity (k) (Gosse, Callaway, Reeder, Nompelis, & Candler, 2009). The input parameter variables which are accessible to the user are presented in Appendix B.

While this experiment does not provide validation for the full capabilities of the solver, it does provide a very important step toward full validation of the code.

Table 10: Material properties of dry ice at test conditions required for ACFD solver

Dry Ice Material Properties at Test Conditions	Value
C_p (J/kg K)	3.5
H (J/K)	1043.7
ΔH_{sub} (J/kg)	558200
S (J/K)	3.1
$(W/m^2 K)$	0.11
$(W/m^2 K)$	0.03

4. Experimental Results

This chapter is devoted to the presentation and discussion of the experimental results found in this research. A total of 114 tests were considered complete and usable, and these were processed for images collected at 0.5 second intervals until either the tunnel preset pressures were reached or defects in the dry ice model appeared. The higher pressure runs were typically only a few seconds long, while some of the lower pressure tests survived for more than 16 seconds, which composed the limit imposed by the cameras' memory capacity.

A master list of all tests performed is provided in Appendix C with model type, run length, and pressures. The results of these experiments are described with varying levels of detail herein. The proof of concept test is presented first. Then, the test cases are grouped by common shape and by similar stagnation pressures. In Table 11, a legend is provided that gives the section numbers where various experimental results are discussed.

For processing, the data from PhotoModeler® was exported as a table of points for a time sequence. This point cloud was then manipulated in MatLab to create visible surfaces for comparisons. The data from the other test runs are available in digital formats from AFIT/ENY.

In all tests, the following axis naming scheme is used: the X-axis is aligned with the stream wise direction of the flow of the wind tunnel, positive being upstream. The Y-axis is aligned horizontally across the tunnel, positive to the port side of the model, and the Z-axis is the elevation, positive in the upward direction. This is consistent with a

body axis convention when the angle of attack of the model is zero. The origin in each frame was taken to be the aft most visible anchor point closest to the model. Thus the position of the origin varied slightly, particularly when angle of attack and camera orientation were altered. Unless otherwise noted, the coordinate systems should not be compared directly. The scale, however, is the same from test to test, and the Z position may be compared from run to run since the origin reference point was always on the floor of the tunnel.

Table 11: Experimental test results presentation sections arranged by common shape, angle of attack, and feature

Test Shape	Angle of Attack (degrees)	Repeatability	3-D Time Progression	3-D at One Time Step	Varied Stagnation Pressure	Schlieren Images
Spherically Blunted Cone	0	4.2	4.2, App. D	4.2,4.3	4.3	4.2, 4.3
Spherically Blunted Cylinder	0	4.4	--	4.4, 4.5	4.5	4.4, 4.5
Elliptical Nose	0	--	--	4.6	4.6	4.6
All Three Shapes	0	--	--	4.7	--	4.7
Spherically Blunted Cone	5	--	--	4.8.14.8	4.8.1	--
Spherically Blunted Cylinder	5	--	--	4.8.2	4.8.2	--
Spherically Blunted Cone	10	--	--	4.9.1	4.9.1	4.9.1
Spherically Blunted Cylinder	10	--	--	4.9.2	4.9.2	4.9.2

The tests are named for the day they were performed. For example, 2 Jun Test 6 was the 6th test on 2 Jun. They are also described by the stagnation pressure of the test run which was found by averaging the measured stagnation pressures over the run. The exception to this are the low pressure tests ($P_o < 14$ psia). The probe in the stagnation chamber measured in psig and could not record below 0 psig. For tests in this case, the stagnation pressure was calculated using the isentropic flow properties based upon Mach 2.94 and the test section pressure (p_∞).

4.1 Proof of Concept

An initial proof of concept test was performed prior to laying out the full scope of this research. The findings of this preliminary investigation were presented in a conference paper at the 15th AIAA International Space Planes and Hypersonic Systems and Technologies Conference in Dayton, OH (Callaway, Reeder, & Greendyke, 2008).

For these tests, commercial dry ice was purchased and cut into a wedge shape with a band saw. This allowed for some early experimentation with the wind tunnel set up. The models were approximately three inches long and an inch wide. Several difficulties arose from this technique of making the models. Producing the desired shape consistently was difficult, as was the risk of damage to the cutting equipment.

The models were then mounted to a conventional wind tunnel sting. As shown in Figure 47, it became quickly evident that an insulator was needed between the threads of the sting and the dry ice as it very quickly sublimed away from the metal, originally at room temperature, since the metal sting acted as a fin. Plastic wall screw anchors were temporarily used as an insulator. A drill was used to produce the necessary hole in the back of the model and the plastic wall anchor was inserted. Then, the sting was threaded into the anchor.

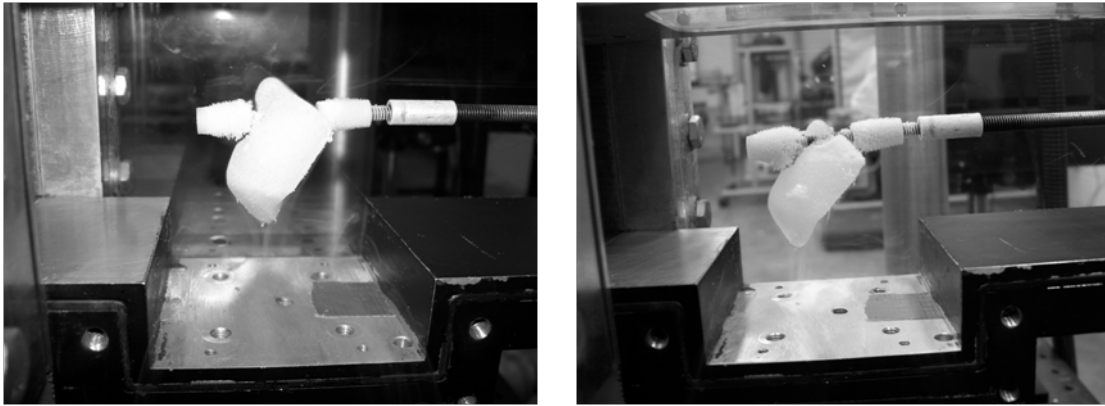


Figure 47: Dry ice model without an insulator in preliminary wind tunnel tests

After the first model, of arbitrary shape was attached to the sting, the sting and model were inserted into the test section and the tunnel test section was evacuated by opening the valve between the vacuum tank and the test section. The valve to the vacuum was then closed and room air slowly leaked back into the test section. After repeating this procedure several times to view stability of the model, the decision was made to proceed with a full test.

A shop light had been added to illuminate the test for imaging purposes. The light was placed near the test section which supplied a heat source to the test section and caused sublimation of the model between the vacuum tests. This heating contributed to eventual cracking of the model, and the first model disintegrated during one of the vacuum tests prior to operating the tunnel. Subsequently the light was removed until tunnel operation.

No problems were apparent in the downstream section of the tunnel or the vacuum tank after the first model released. A new model was produced in the same fashion and placed on the sting. The tunnel was operated by opening both the valves, and images were taken with a Photron FASTCAM-X 1280 PCI camera at 500 frames per second.

Figure 48 presents a time progression of this preliminary test and shows the sublimation of the model over six seconds. In Figure 48, image (a) shows the model mounted on the sting in the wind tunnel prior to the test. The model of arbitrary shape was oversized for the sting support and was deflected downward toward the tunnel floor within the first 0.35 seconds from when the flow was initiated. However, between 0.35 seconds and 1.0 seconds, it was clear by visual observation that the model was ablating.

Though rudimentary, this test provided a reasonable proof of concept: observable ablation was feasible using dry ice models in the AFIT pressure-vacuum wind tunnel operated at, nominally, Mach 3. With a reasonable proof of concept and a repeatable technique to fabricate the dry ice models, the decision was made to proceed with tunnel tests. Work then began with the spherically blunted cone.

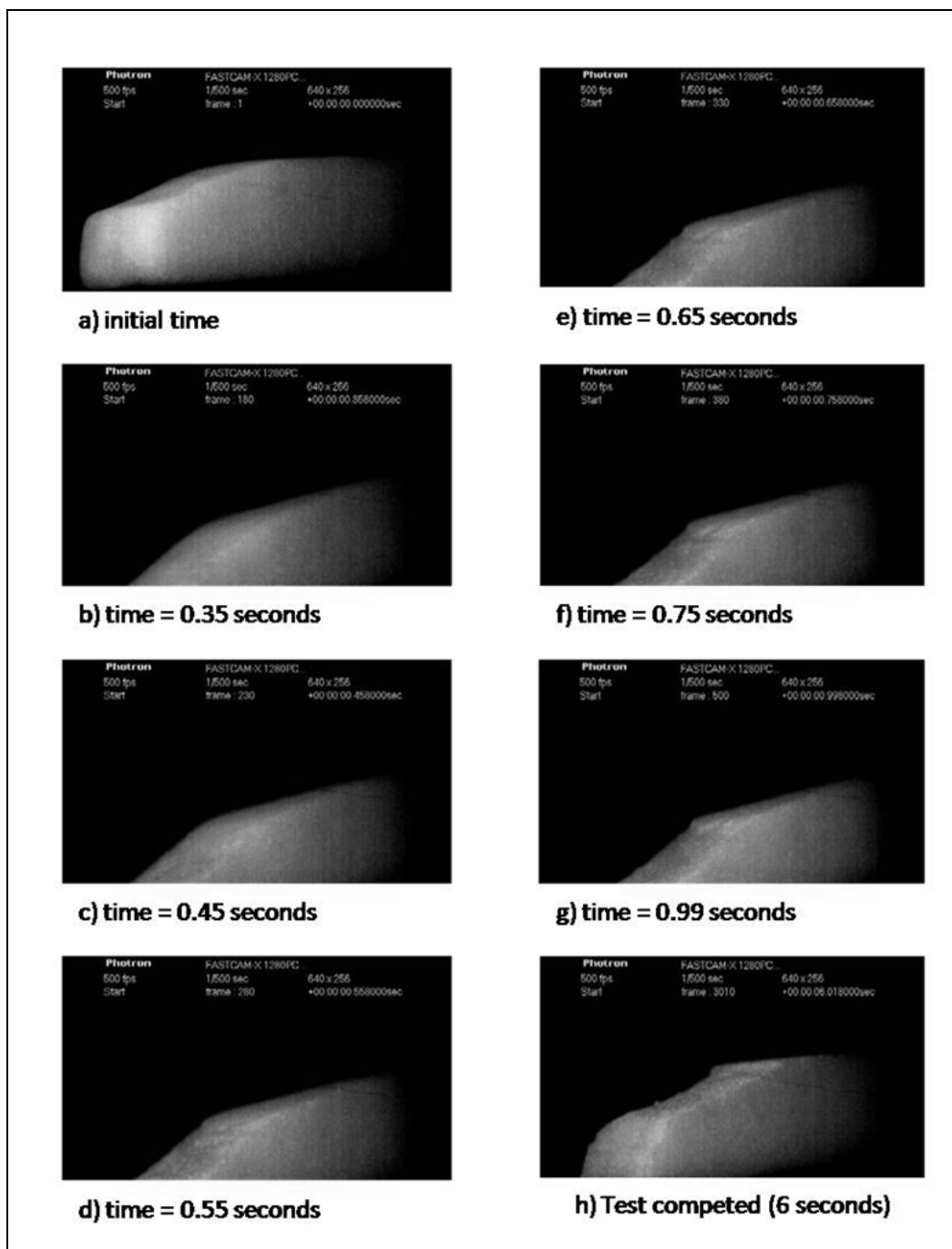


Figure 48: Time progression of preliminary dry-ice ablation test at nominally Mach 3

4.2 Spherically Blunted Cone at 0° Angle of Attack, $P_o = 6.1$ psia

With successful models being made approximately three out of four times, the spherically blunted cone shape was the most repeatable to build and had the most successful test runs. As shown in Appendix A, the spherically blunted cone is a spherically rounded 20° half-angle cone joined to a 0.60 inch diameter, 1.2 inch long cylinder. Presented in this section is the experiment labeled 2 Jun Test 6, which was conducted at an average 6.1 psia stagnation pressure and Mach 2.94. Table 12 gives the basic test conditions for the test case presented in this section.

Table 12: Test conditions for test 2 Jun Test 6

Test Name	(psia)	(psia)	(kg/m ³)	Re/x (1/m)
2 Jun Test 6	6.1	0.18	0.041	3.33E+06

Figure 49 presents Schlieren images of this test at time = 0 (top image) and time = 3 seconds (bottom image). The flow direction in Figure 49 is right to left. The bow shock can be seen clearly about the nose of the model and the shock reflections off the ceiling and floor approximately correspond to the stream wise base of the dry ice model. As such, there is no significant interference due to the reflected shocks. In the center of these images, one can detect a small gap between the filter disk and the dry ice model. The spacer can be seen downstream of (that is, to the left of) the disk. These two images are part of a 4 second sequence taken at 4000 Hz. In viewing of the video sequence, ablation is apparent.

Schlieren visualization provided valuable insight in real-time during the experiment. However, it must be borne in mind that one pixel width in the Schlieren images corresponds to approximately 0.43 mm. In the case of the 6.1 psia stagnation pressure, the difference over three seconds was approximately one pixel, so photogrammetry is needed to quantify the ablation rate with sufficient accuracy.

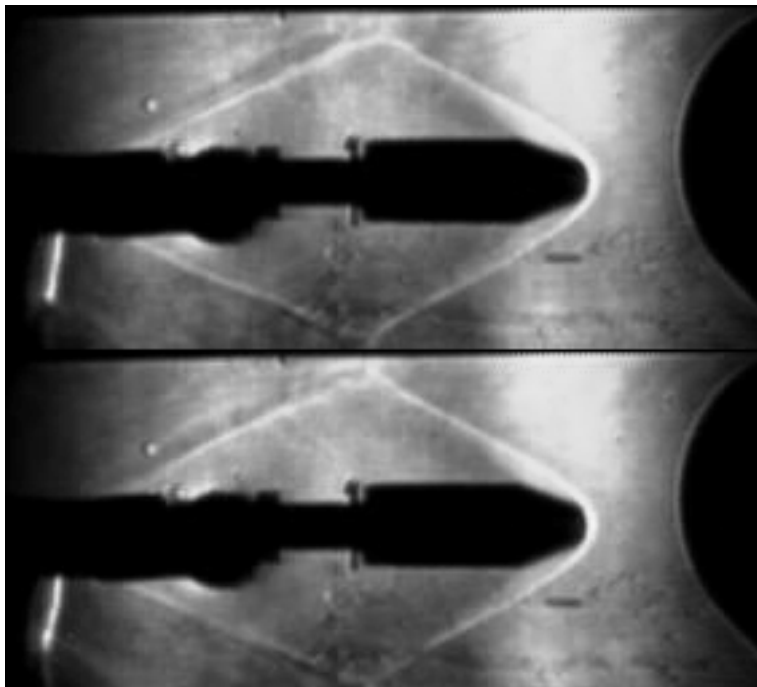


Figure 49: Schlieren imaging of a spherically blunted cone at 6.1 psia, Mach 2.94 at time = 0 (top) and time = 3 seconds (bottom)

It should also be noted that due to the placement of the optical windows and the limitation of using three high speed cameras only half of the model can be imaged in a test run. In the zero angle of attack tests, this was the top half of the model. The images can be rotated by the software to view from practically any angle, but the three viewpoints presented here were chosen to give the reader a sense of the three-

dimensional nature of the data point cloud and to maintain consistency in the comparisons.

The results of the photogrammetry for the spherically blunted cone at $P_o = 6.1$ psia are shown in Figure 50 for $t = 0.5$ seconds, Figure 51 at $t = 3.5$ seconds, and Figure 52 at $t = 7.5$ seconds. The set of test results is presented in half second intervals in Appendix C. The images presented here and in the appendix are correlated from the three high speed camera views. There are four images in each figure: Image (a), top left, displays a side view of the point cloud; Image (b), top right, is a front view of the point cloud while image (c), bottom left, is a top view of the point cloud; Image (d), bottom right, shows a surface mesh of the model created from the point cloud with MatLab and illustrates the surface changes over time.

In all, 30 points on the surface of the ablating model are tracked during this single run. In images a, b, and c, the initial point locations are represented as black circles, while the points in the presented time frame are shown by red 'x's.

In the surface mesh image, the black silhouette is the original shape and the red silhouette is the shape at the indicated time. There is a brownish region in the surface images that represents an overlap between the two fields. Ideally, the mesh should overlap at all points except the area of shape change, but the coarseness of the grid limits the surface continuity that the MatLab routine can display.

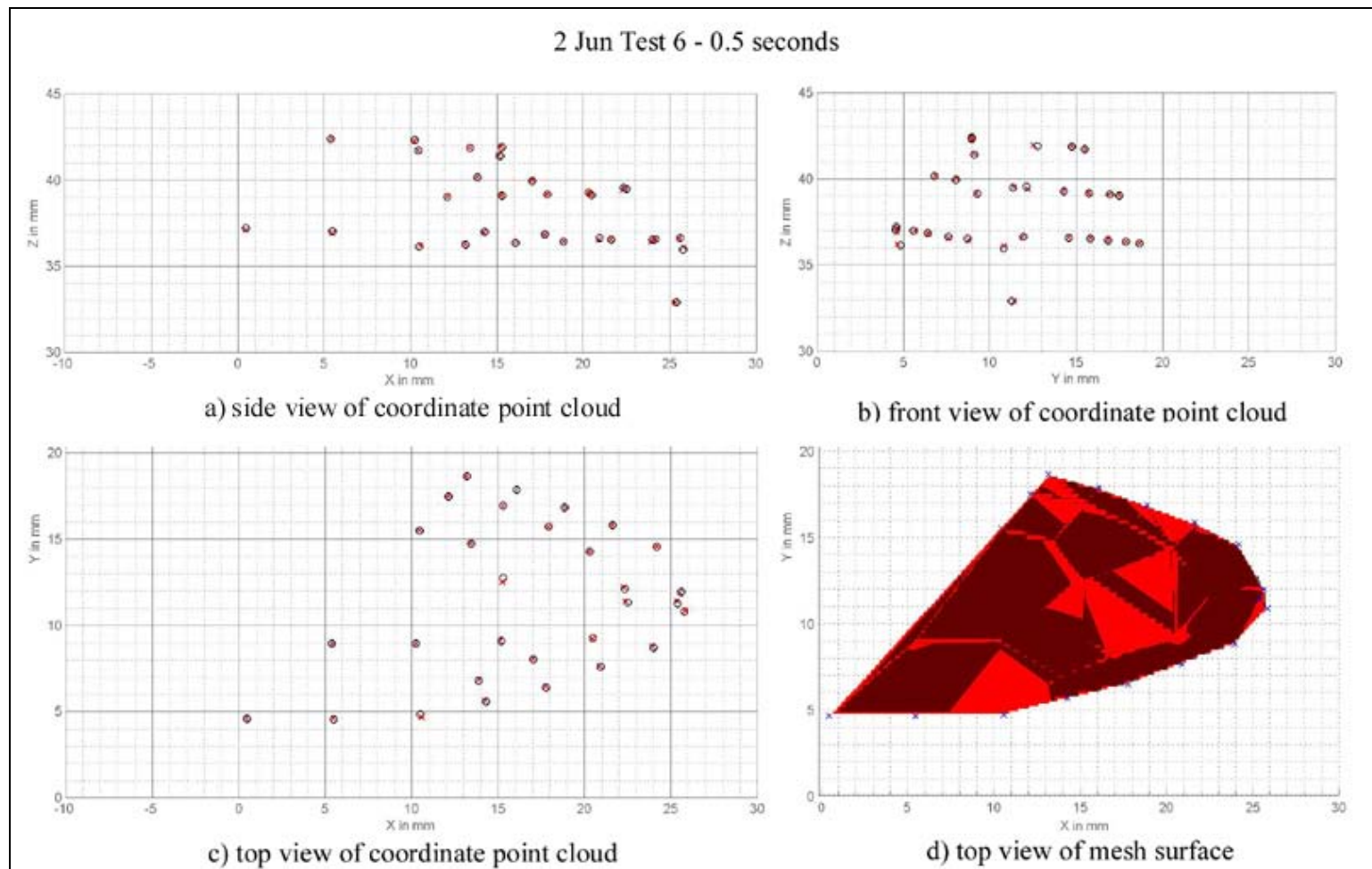


Figure 50: Spherically blunted cone at a stagnation pressure of 6.1 psia and time = 0.5 seconds

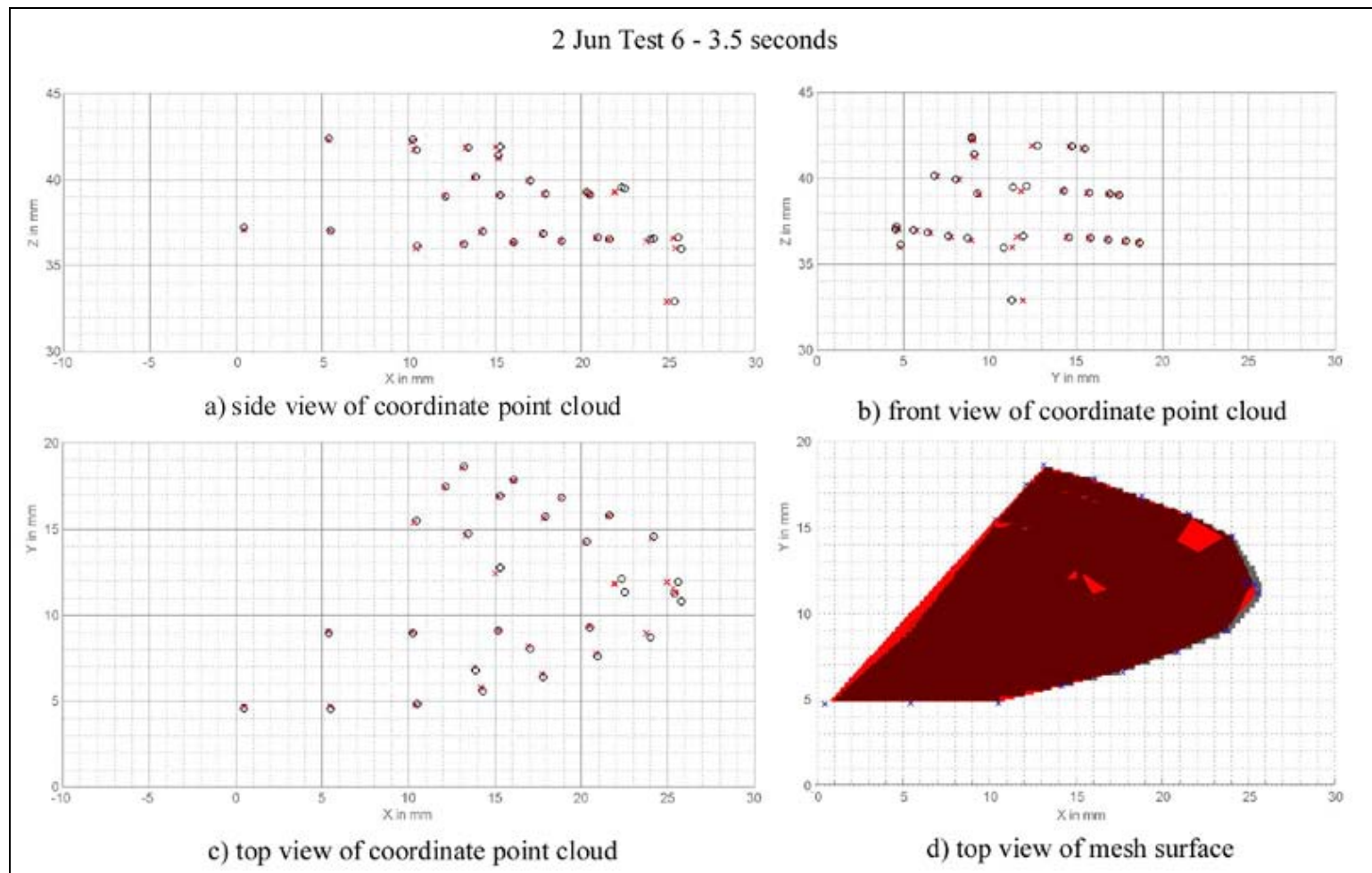


Figure 51: Spherically blunted cone at a stagnation pressure of 6.1 psia and time = 3.5 seconds

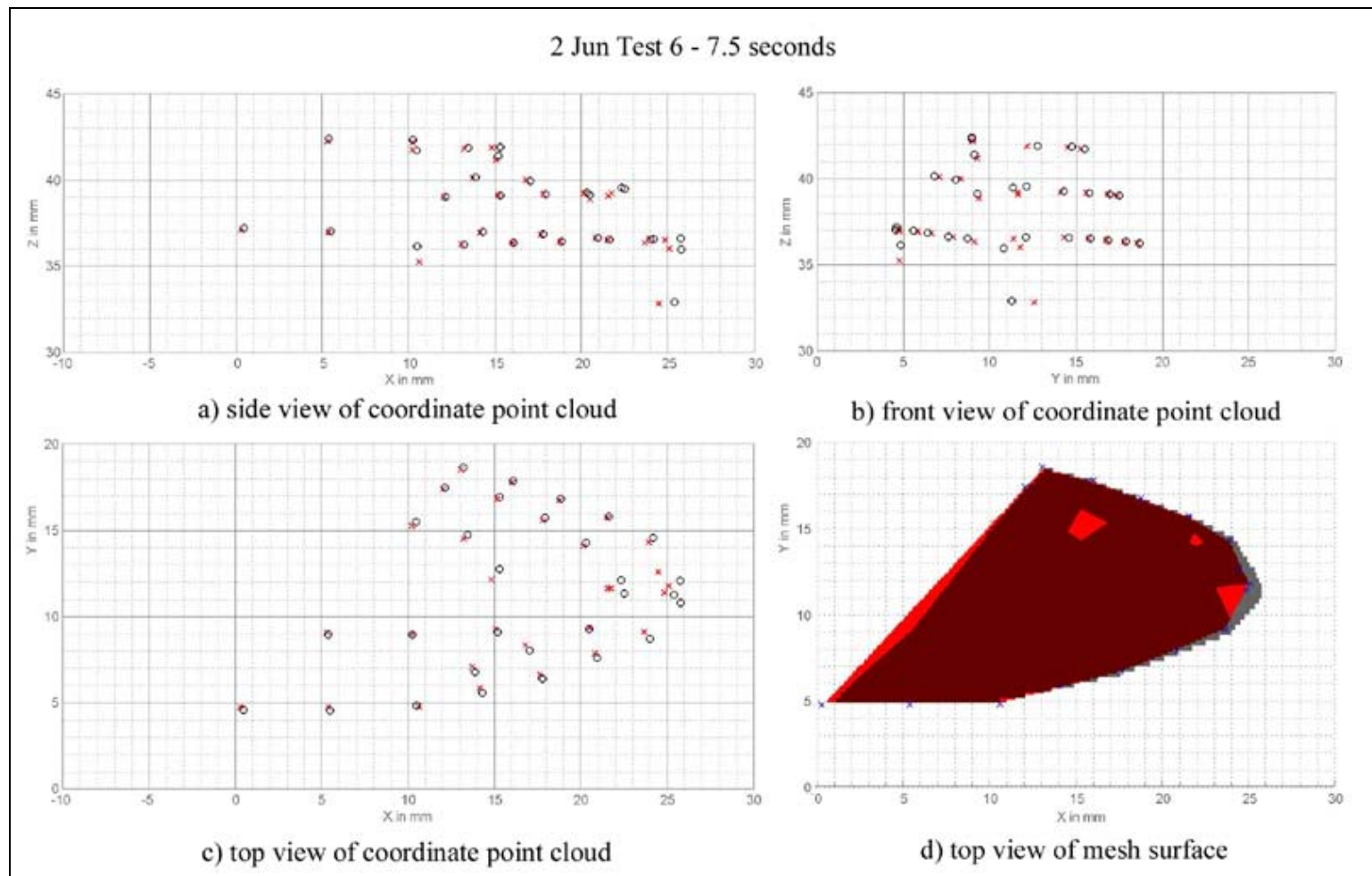


Figure 52: Spherically blunted cone at a stagnation pressure of 6.1 psia and time = 7.5 seconds

Point 1035, which has an original three-dimensional location of (25.7, 12.1, 36.6) in these charts based on the origin marked by a reference point, is located near the nose of the test article in the preceding figures. The three-dimensional change in position over time of point 1035 is tracked in Table 13. The point was normalized by assigning the origin of the coordinate to the point at time equals zero. Normalizing the recession data allows for more efficient comparison between runs as the origin can vary between tests for a variety of reasons.

Table 13: Coordinate data for point 1035 near the nose tip of test 2 Jun Test 6

Time (s)	X position (mm)	Y position (mm)	Z position (mm)	Residual (mm)
0.0	0.00	0.00	0.00	0.10
0.5	-0.10	-0.11	0.04	0.14
1.0	-0.16	-0.20	0.03	0.06
1.5	-0.22	-0.17	0.07	0.01
2.0	-0.26	-0.23	-0.05	0.02
2.5	-0.32	-0.36	0.05	0.09
3.0	-0.34	-0.36	0.04	0.07
3.5	-0.37	-0.44	0.03	0.08
4.0	-0.44	-0.50	-0.03	0.06
4.5	-0.52	-0.54	-0.06	0.04
5.0	-0.55	-0.64	-0.01	0.05
5.5	-0.62	-0.56	-0.04	0.04
6.0	-0.65	-0.61	-0.05	0.01
6.5	-0.75	-0.71	-0.10	0.04
7.0	-0.80	-0.72	-0.13	0.02
7.5	-0.89	-0.69	-0.10	0.10

As a point of interest, at the beginning of this section, the Schlieren imaging from Figure 49 indicated a one pixel, approximately 0.43 mm, recession at the nose after 3 seconds. Point 1035 shows a 0.34 mm recession after 3 seconds or slightly less than one pixel which presents a good comparison between the two measurement techniques given the lack of resolution of the camera used for Schlieren visualization.

Also presented in Table 13 are the residuals of the points. The residuals are a measurement of the disagreement as to where the camera calibration indicates the point lies and were discussed in Section 3.1.8. The residuals in the PhotoModeler® window are given in pixels, where one pixel is approximately 0.1 mm. However, in exporting the data, the residuals are converted into the project units, in the case of this research, millimeters. The operator can manipulate this residual by manually adjusting the placement of the point in PhotoModeler® to gain agreement among camera views. The largest residual for this test was 0.1 mm while the average residual is 0.06 mm.

An important aspect of this research is establishing the repeatability of multiple tests. A total of four tests were performed at similar stagnation pressures: 2 Jun Test 6 ($P_o = 6.1$ psia), 2 Jun Test 7 ($P_o = 6.1$ psia), 2 Jun Test 8 ($P_o = 6.1$ psia), and 6 Jun Test 9 ($P_o = 6.2$ psia). Figure 53 shows a comparison of similar points in these four tests. The points chosen were as close to the stagnation area and in the same location on each test model as possible. The 2 Jun Test 7 and Test 8 test models had their structural integrity compromised earlier than Tests 6 and 9; however, the measured ablation rates prior to the loss of the model's integrity were comparable to the two longer runs.

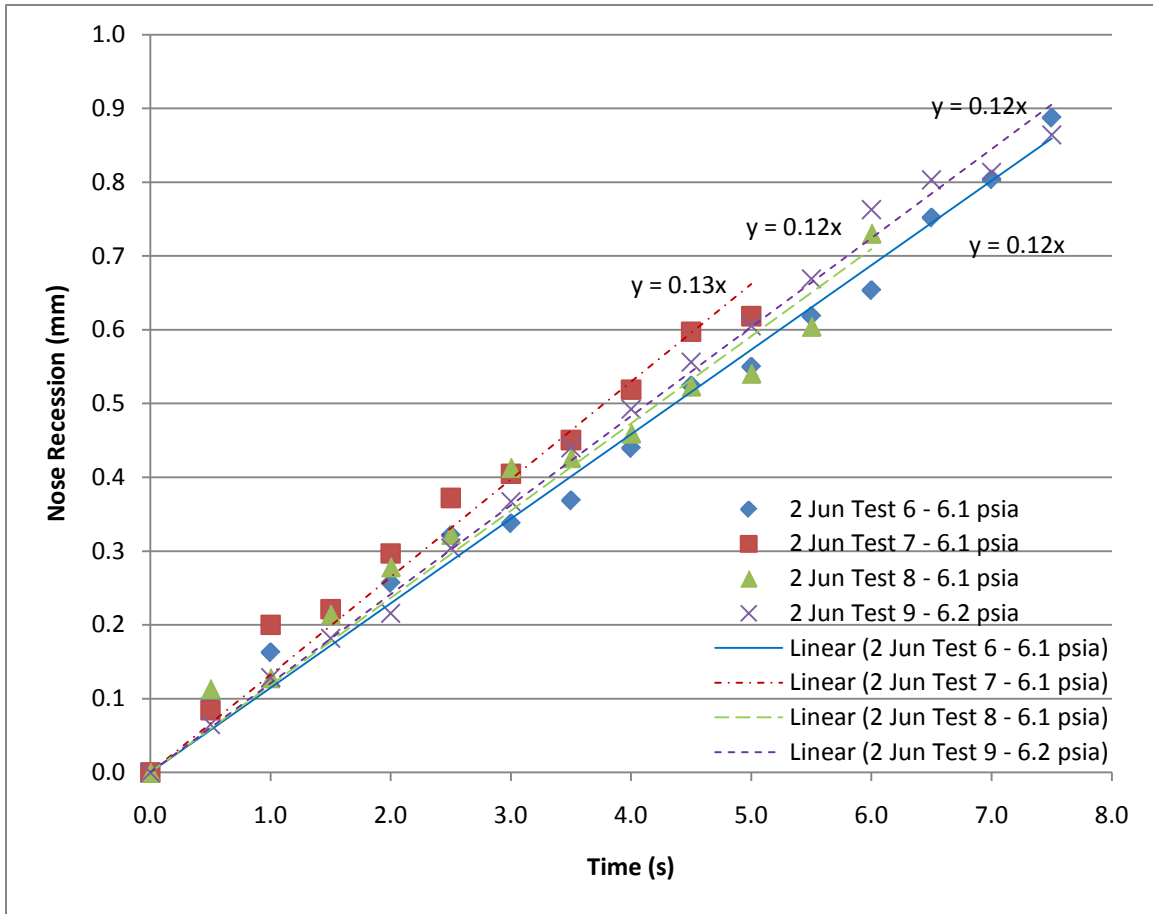


Figure 53: Comparison of trend lines for recession of a point near the nose for experimental tests 2 Jun Test 6, 2 Jun Test 7, 2 Jun Test 8, and 2 Jun Test 9 at ~6.1 psia stagnation pressures

The average rates of recession of each of the four tests are displayed in Table 14. These rates were computed using a least squares method to develop the average rate of the recession of the chosen points. These average rates are compared in Table 14 along with the percent difference calculated with respect to 2 Jun Test 6 which yields an average of 7.5% difference.

Table 14: Average rate of recession and percent differences of similar points near the nose of tests 2 Jun Test 6, 2 Jun Test 7, 2 Jun Test 8, and 2 Jun Test 9

Test Name	Average Rate of Recession (mm/s)	Percent Difference from 2 Jun Test 6
2 Jun Test 6	0.121	-.-
2 Jun Test 7	0.132	14.8
2 Jun Test 8	0.118	2.6
2 Jun Test 9	0.115	5.2

4.3 Spherically Blunted Cone at 0° Angle of Attack, Multiple Pressures

Having established that similar test conditions can yield repeatable results, the next step was to compare the effect of stagnation pressure on the same shape. Since stagnation temperature and Mach number were held throughout all experiments, changing the stagnation pressure was tantamount to varying the free stream density. Three tests were chosen for a representative sampling at low, medium, and high stagnation pressures, and are presented in this section. These tests are shown in Table 15 with the pressures, density and Reynolds numbers called out.

Table 15: Test conditions of 2 Jun Test 6, 9 Jun Test 1, and 16 Jun Test 1

Test Name	(psia)	(psia)	(kg/m ³)	Re/x (1/m)
2 Jun Test 6	6.1	0.18	0.041	3.33E+06
9 Jun Test 1	23.0	0.67	0.150	1.22E+07
16 Jun Test 1	45.7	1.42	0.317	2.58E+07

First, Schlieren images were used to compare the runs of varying pressure, as seen in Figure 54. This flow visualization provided valuable insight in real-time during the experiment. Simply by observation of the video, it was clear that the higher stagnation pressures generally yielded a higher ablation rate at the nose of the model. However, as stated previously, the Schlieren imaging in this research is limited to the width of a pixel, which corresponds to 0.43 mm. This limits the accuracy of any efforts to quantify ablation using the flow visualization alone. Nevertheless, over two seconds there is enough change to see that the nose tip for the low pressure run recesses about 1 pixel. The medium pressure run leads to a recession of approximately 1 or 2 pixels while the high pressure run yields between 2 and 3 pixels. This aligned with the expectation that a higher stagnation pressure would lead to higher ablation rates in the wind tunnel. Note that the set of images in Figure 54 shows 3 seconds of data starting from the top and stepping 1 second in each image down. The 16 Jun Test 1 ($P_o = 45.7$ psia) nose area was structurally compromised at 2.5 seconds. So, while the Schlieren image is shown in Figure 54, the high resolution coordinate data is unavailable after 2 seconds for comparison.

Also evident in Figure 54 are the shock waves generated by the different stagnation pressures. Schlieren imaging is used foremost for imaging density variants including shock waves, and it is visibly obvious in the image that as the pressure was increased the shock waves grew more distinct.

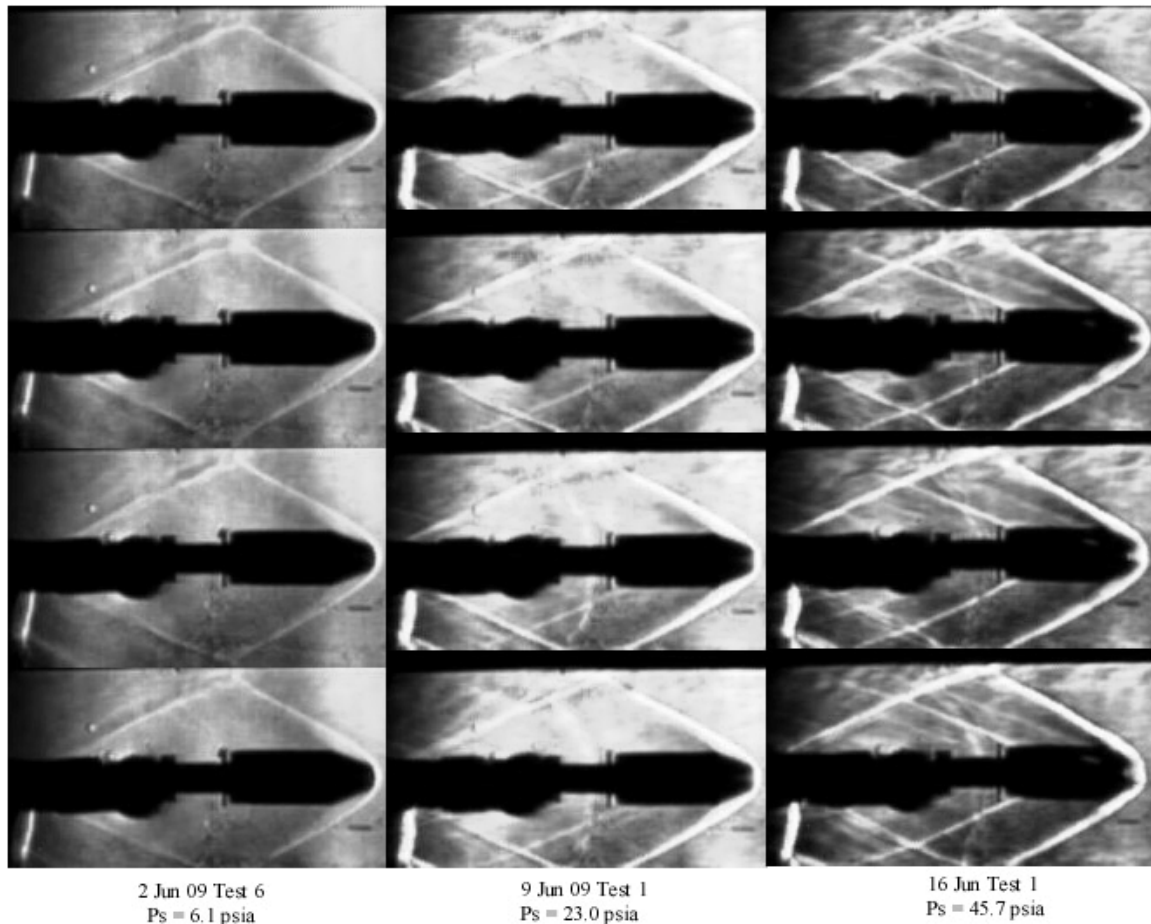


Figure 54: Schlieren images of a spherically blunted cone at stagnation pressures of 6.1, 23.0, and 45.7 psia. The top row is at $t = 0$ sec, the second row at $t = 1$ sec, the third row at $t = 2$ sec, and the fourth row is at $t = 3$ sec

These three wind tunnel tests were processed in PhotoModeler® and compared in the much higher resolution images. The results are presented differently in this section from the previous one to provide a comparison of the same view for each pressure. The results are also truncated to a 2 second elapsed time in order to compare all pressures with the shortest test, 16 Jun Test 1.

Figure 55 presents the mesh surface shape of the test articles rotated to view from above. As previously, the original shape is a black silhouette and the surface after 2 seconds is shown in red. Figure 56 presents the point cloud viewed from above at the

same angle orientation as Figure 55. Figure 57 and Figure 58 present the side profile and forward cross section views, respectively. Again, the circles are the initial positions of the laser grids and the red 'x's are the surface at the current time step, $t = 2$ seconds.

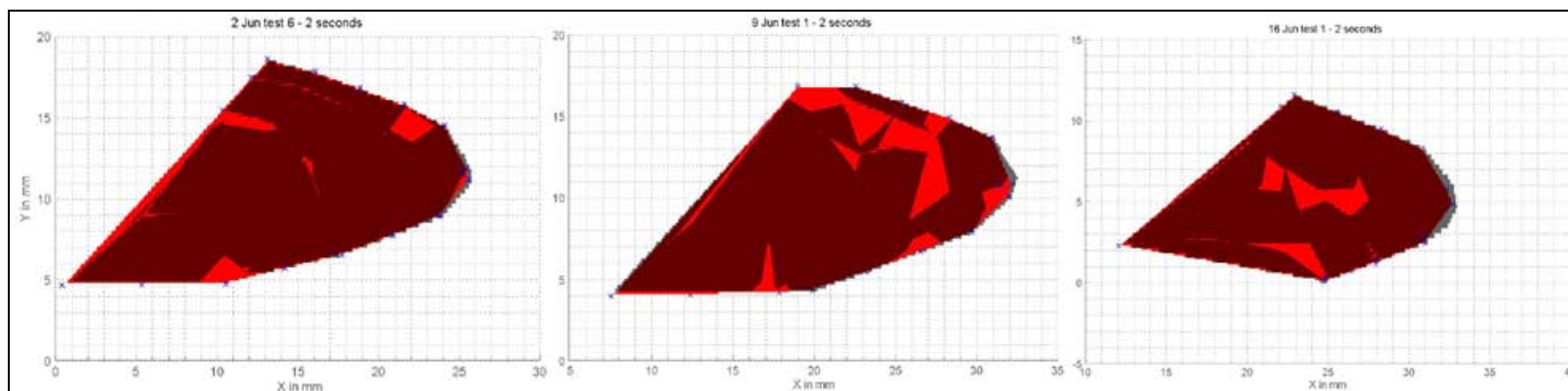


Figure 55: Comparison of 6.1, 23.0, and 45.7 psia stagnation pressure tests on spherically blunted cone model: top view of mesh surface

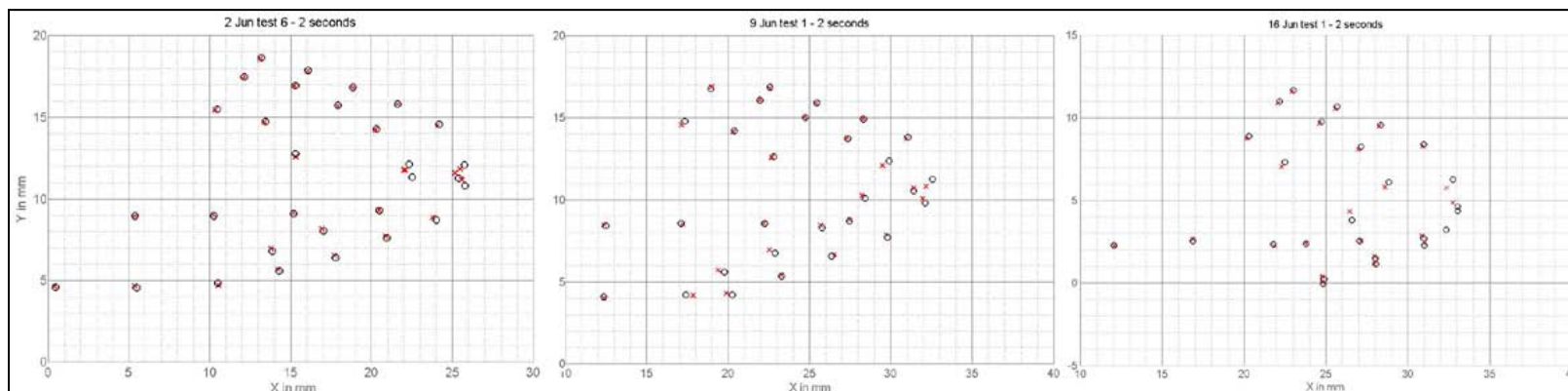


Figure 56: Comparison of 6.1, 23.0, and 45.7 psia stagnation pressure tests on spherically blunted cone model: top view of point cloud

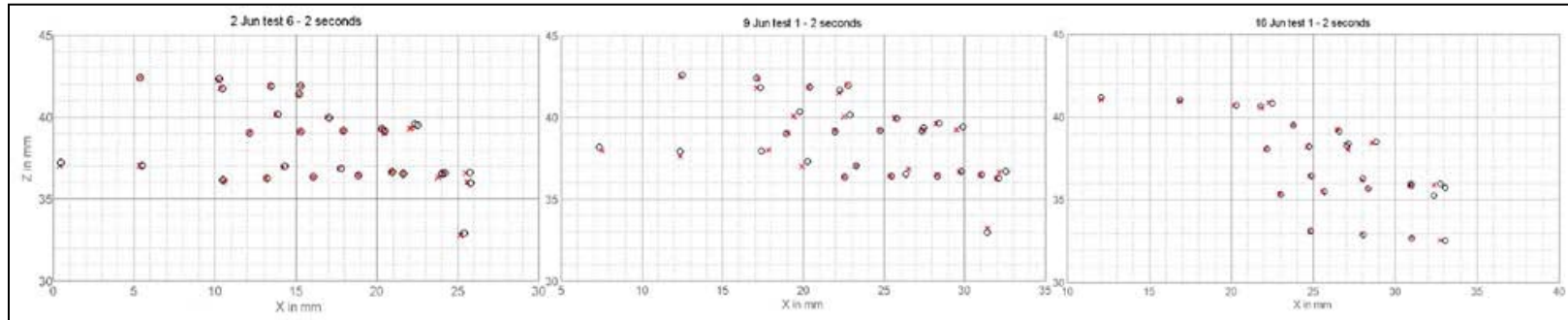


Figure 57: Comparison of 6.1, 23.0, and 45.7 psia stagnation pressure tests on spherically blunted cone model: side view of point cloud

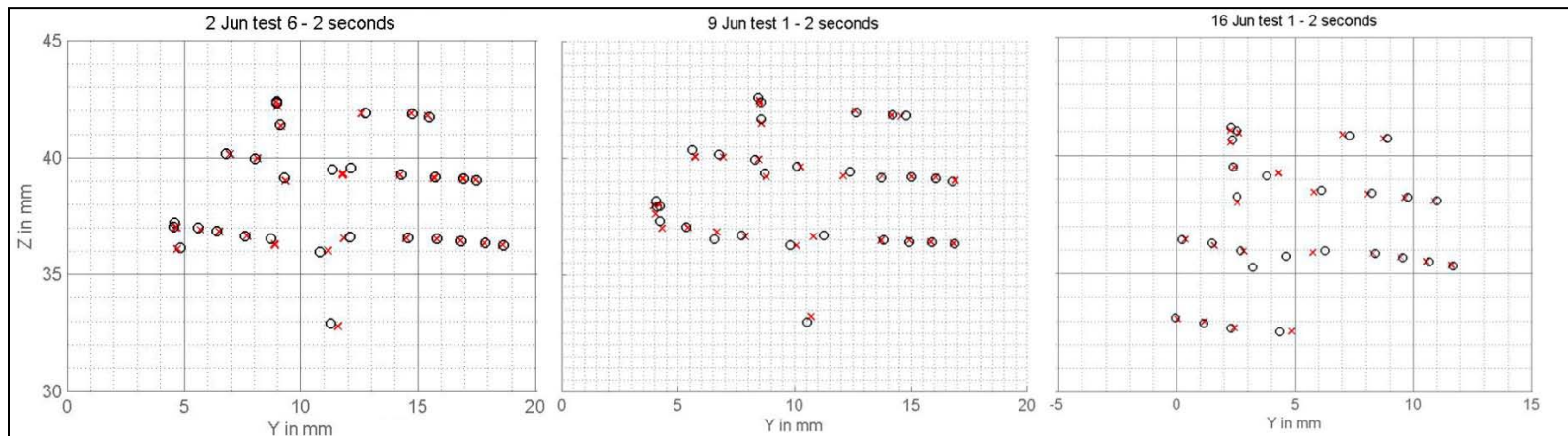


Figure 58: Comparison of 6.1, 23.0, and 45.7 psia stagnation pressure tests on spherically blunted cone model: front view of point cloud

In Figure 59, a graphical comparison of the nose recession is given for comparison with the trend lines of each test. As anticipated, higher stagnation pressures lead to a faster recession rate as is depicted in Table 16 where values for the tracking point closest to the nose are shown. It should be noted that the primary change of the point of interest is in the x direction as this reflects recession the flow direction. The changes in the y-direction and z-direction are mainly due to laser grid movement across the surface of the model. As stated in chapter 3, the laser grids are being projected at an angle to the surface and the wind tunnel flow. So as the surface recedes, the laser grid shifts across the surface.

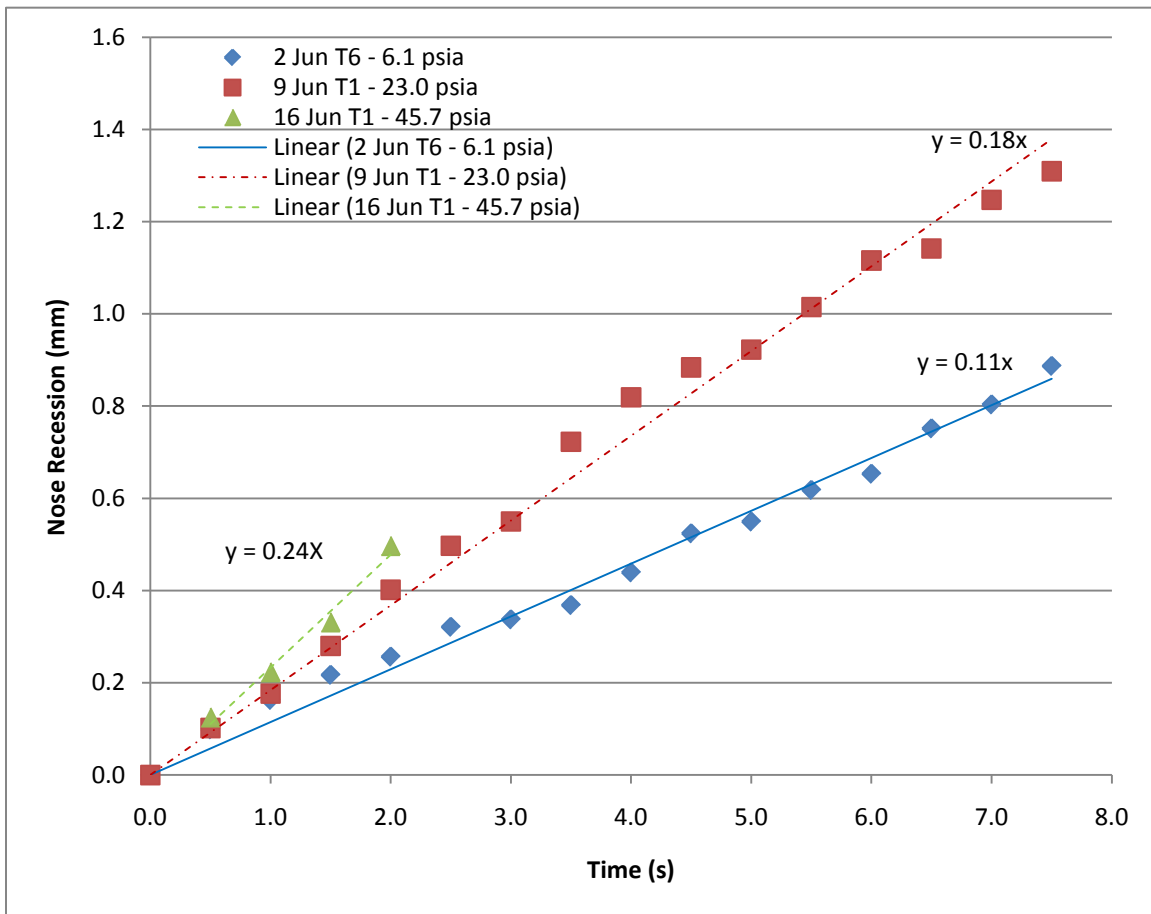


Figure 59: Comparison of 6.1, 23.0, and 45.7 psia stagnation pressure test recession rates of a spherically blunted cone

Table 16: Comparison of change in position over 2 seconds for a point near the nose of a spherically blunted cone

Stagnation Pressures (psia)	6.1	23.0	45.7
$\Delta x(\text{mm})$	0.26	0.40	0.50
$\Delta y(\text{mm})$	0.04	0.44	0.75
$\Delta z(\text{mm})$	0.23	0.04	0.02
Average Residual of point (mm)	0.06	0.04	0.05
Average Recession Rate	0.12	0.18	0.24

As previously stated, at 2 seconds, the Schlieren image showed a 1, 1-to-2, and 2-to-3 pixel nose tip recession for the $P_o = 6.1, 23.0,$ and 45.7 psia cases respectively. At one pixel equal to 0.4 mm, the test cases are predicted at $0.4, 0.4\text{-}0.8,$ and $0.8\text{-}1.2$ mm after two seconds. Comparing these to the data presented in Table 16 confirms that the data is indeed within these limits; however, this also proves that while the Schlieren is very valuable in this research, it is more qualitative than quantitative.

4.4 Spherically Blunted Cylinder at 0 Angle of Attack Similarity Test

A second important basic geometry tested is a spherically blunted cylinder. As previously discussed, and as shown in Appendix A, the spherically blunted cylinder is a 0.6 inch diameter cylinder with a 0.3 inch radius nose. Presented in this section is a comparison of two tests, 19 Jun Test 8 and 19 Jun Test 9, of a spherically blunted

cylinder at 7.5 psia stagnation pressure, which is a comparatively low value. The basic test conditions of these two tests are presented in Table 17.

Table 17: Test conditions of 19 Jun Test 8 and 19 Jun Test 9

Test Name	(psia)	(psia)	(kg/m ³)	Re/x (1/m)
19 Jun Test 8	7.5	0.225	0.0504	4.10E+06
19 Jun Test 9	7.5	0.226	0.0505	4.11E+06

Figure 60 presents Schlieren images of the test at time = 0 on the top and time = 3 seconds on the bottom of test 19 Jun Test 8 (left) and 19 Jun Test 9 (right). In the case of the spherically blunted cylinder at 7.5 psia stagnation pressure, the difference over three seconds was approximately one pixel, so again photogrammetry is needed to quantify the ablation rate with sufficient accuracy.

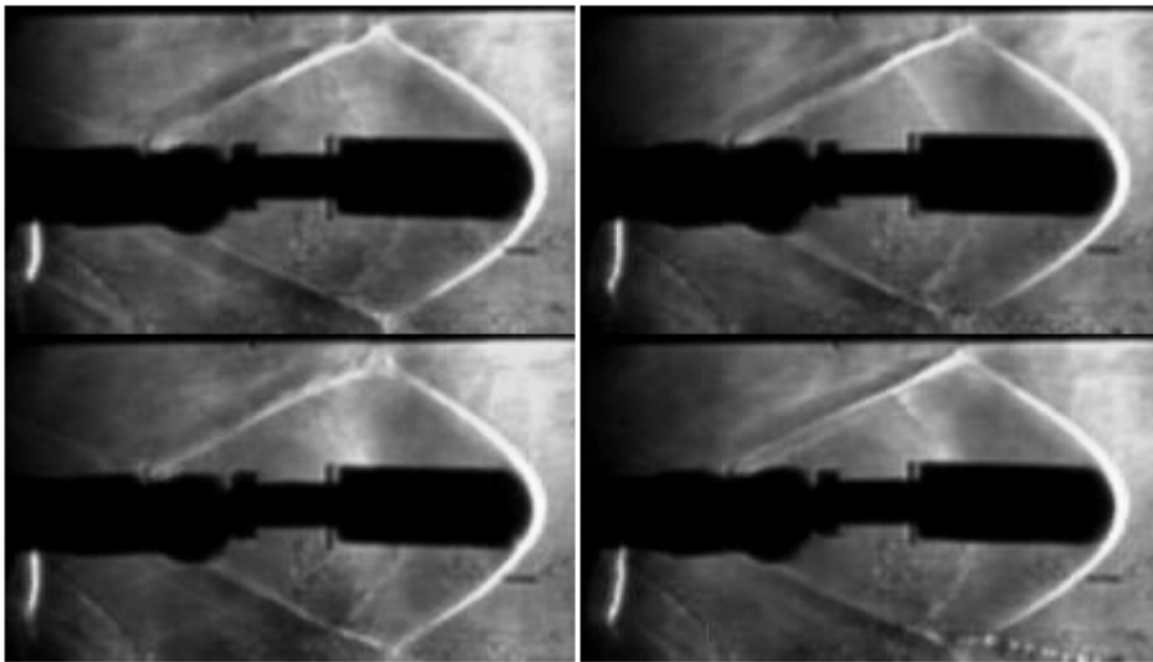


Figure 60: Schlieren images of a spherically blunted cylinder tests 19 Jun Test 8 (left) and 19 Jun Test 9 (right) at t = 0 sec (top row) and t = 3 sec (bottom row)

The PhotoModeler® processed position data of these two tests are presented here for comparison to one other at $t = 8$ seconds. Figure 61 shows a top view of the mesh surface of the two shapes. As previously, the original surface is a black silhouette and the red silhouette is the surface at time $t = 8$ seconds. Figure 62 presents the front view of the point cloud and Figure 63 presents the side profile view. Figure 64 shows the point cloud from the top view, which corresponds to the surface mesh seen in Figure 61. The original points are again represented as black circles, while the points in the presented time frame, $t = 8$ seconds, are shown by red 'x's. This is a low stagnation pressure run, and as such, the model remained intact for eight seconds, the longest amount of time the cameras can record.

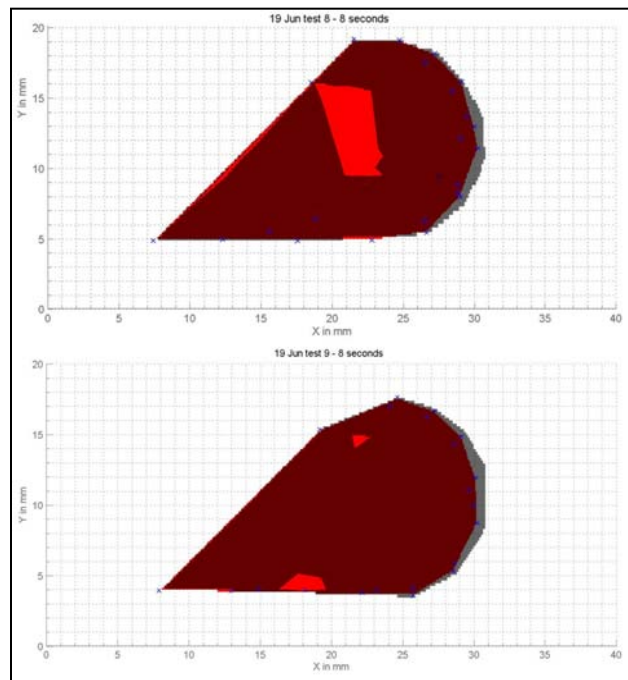


Figure 61: Spherically blunted cylinder similarity tests 19 Jun Test 8 (top) and 19 Jun Test 9 (bottom) at 7.5 psia stagnation pressure after 8 seconds: top view of mesh surface plot

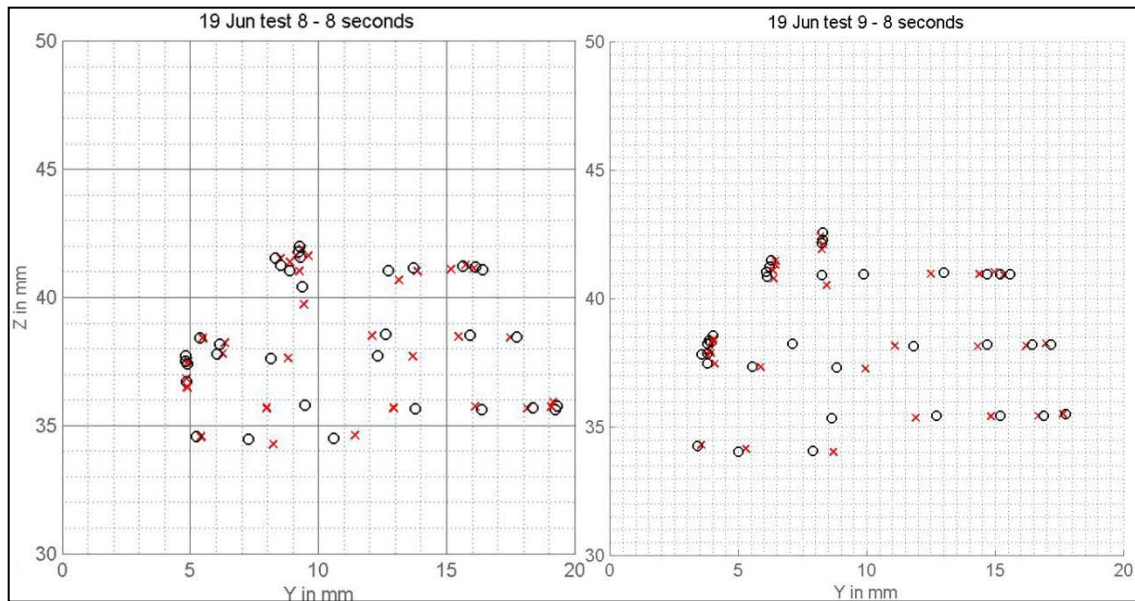


Figure 62: Spherically blunted cylinder similarity tests 19 Jun Test 8 (left) and 19 Jun Test 9 (right) at 7.5 psia stagnation pressure after 8 seconds: front view of the point cloud

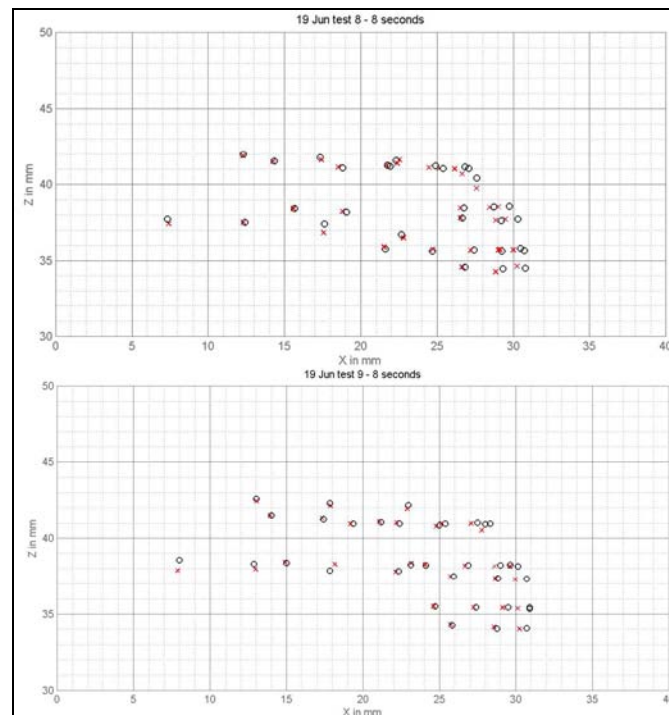


Figure 63: Spherically blunted cylinder similarity tests 19 Jun Test 8 (top) and 19 Jun Test 9 (bottom) at 7.5 psia stagnation pressure after 8 seconds: side view of point cloud

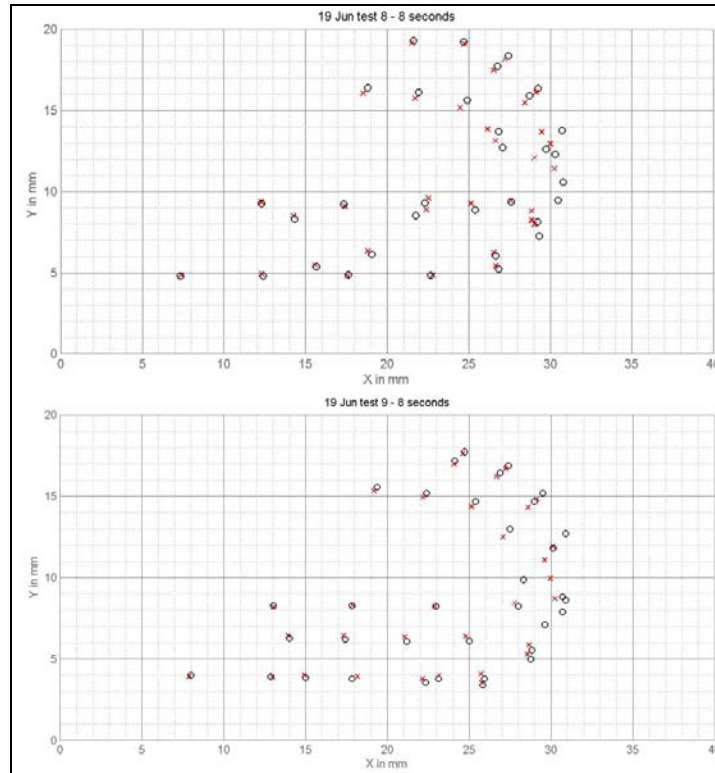


Figure 64: Spherically blunted cylinder similarity tests 19 Jun Test 8 (top) and 19 Jun Test 9 (bottom) at 7.5 psia stagnation pressure after 8 seconds: top view of point cloud

Only two tests were conducted at nominally $P_o = 7.5$ psia, and these two tests are used here to establish repeatability for this model geometry. Figure 65 shows a comparison of the recession of a point on the nose in these two tests with their respective least squares determined average recession rate. The trend line for 19 Jun Test 8 had an average recession rate of 0.094 mm/s and 19 Jun Test 9 had an average recession rate of 0.088 mm/s. This yields a difference of 7.2% or a ratio of 1.07. This is comparable to the 7.5% average difference in the spherically blunted cone at a similar stagnation pressure. While the average rates were similar, at any given time, the difference between the two points of each test averaged out to about 10-15%.

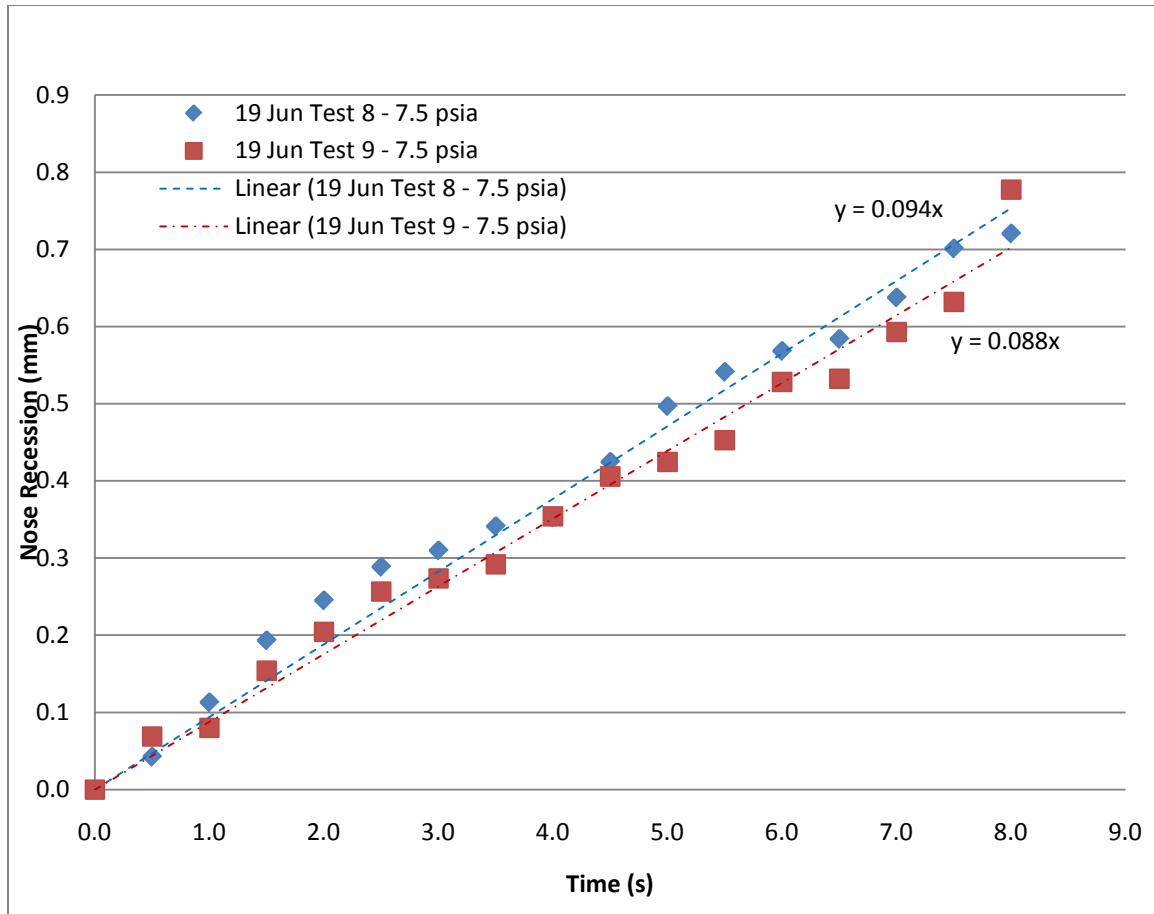


Figure 65: Comparison of experimental nose recession results for a spherically blunted cylinder at 7.5 psia stagnation pressure

4.5 Spherically Blunted Cylinder at 0 Angle of Attack and Multiple Pressures

With repeatability established, the next step was to compare the results for different stagnation pressure on the spherically blunted cylinder shape. For the spherically blunted cylinder, four different stagnation pressure runs were processed in

PhotoModeler®: 19 Jun Test 8 ($P_o = 7.5$ psia), 19 Jun Test 6 ($P_o = 19.8$ psia), 19 Jun Test 5 ($P_o = 27.9$ psia), and 19 Jun Test 2 ($P_o = 37.9$ psia). The test conditions for these four tests are shown in Table 18.

Table 18: Test conditions of 19 Jun Test 8, 19 Jun Test 6, 19 Jun Test 5 and 19 Jun Test 2

Test Name	(psia)	(psia)	(kg/m ³)	Re/x (1/m)
19 Jun Test 8	7.5	0.225	4.10E+06	4.10E+06
19 Jun Test 6	19.8	0.563	10.2E+06	10.2E+06
19 Jun Test 5	27.9	0.832	15.1E+06	15.1E+06
19 Jun Test 2	37.9	1.150	20.8E+06	20.8E+06

Schlieren images were used during the tests to compare runs of varying pressure, as seen in Figure 66. The images are ordered lower pressure to higher pressure from left to right, and at one second time steps vertically from top ($t = 0$ sec) to bottom ($t = 3$ sec). In general, visual observation of the model during wind tunnel tests suggested that more shape change was happening for the higher pressure cases. The Schlieren images presented in Figure 66 project a 1 or less pixel loss for the $P_o = 7.5$ psia test, a 1 to 2 pixel loss for the $P_o = 19.8$ and 27.9 psia tests, and 2 to 3 pixels for the $P_o = 37.9$ psia test. The results of the Schlieren are again limited to a 0.43 mm pixel measurement.

Evident in Figure 66, the 19 Jun Test 5 case has a defect in the cylindrical portion of the model. A defect in this location was fairly common but fortunately it was typically present in the cylindrical portion of the model, away from the stagnation region. Upon tunnel operation, if the defect appeared with no apparent effect on the nose area and the integrity of the model was maintained, then the data was processed nonetheless.

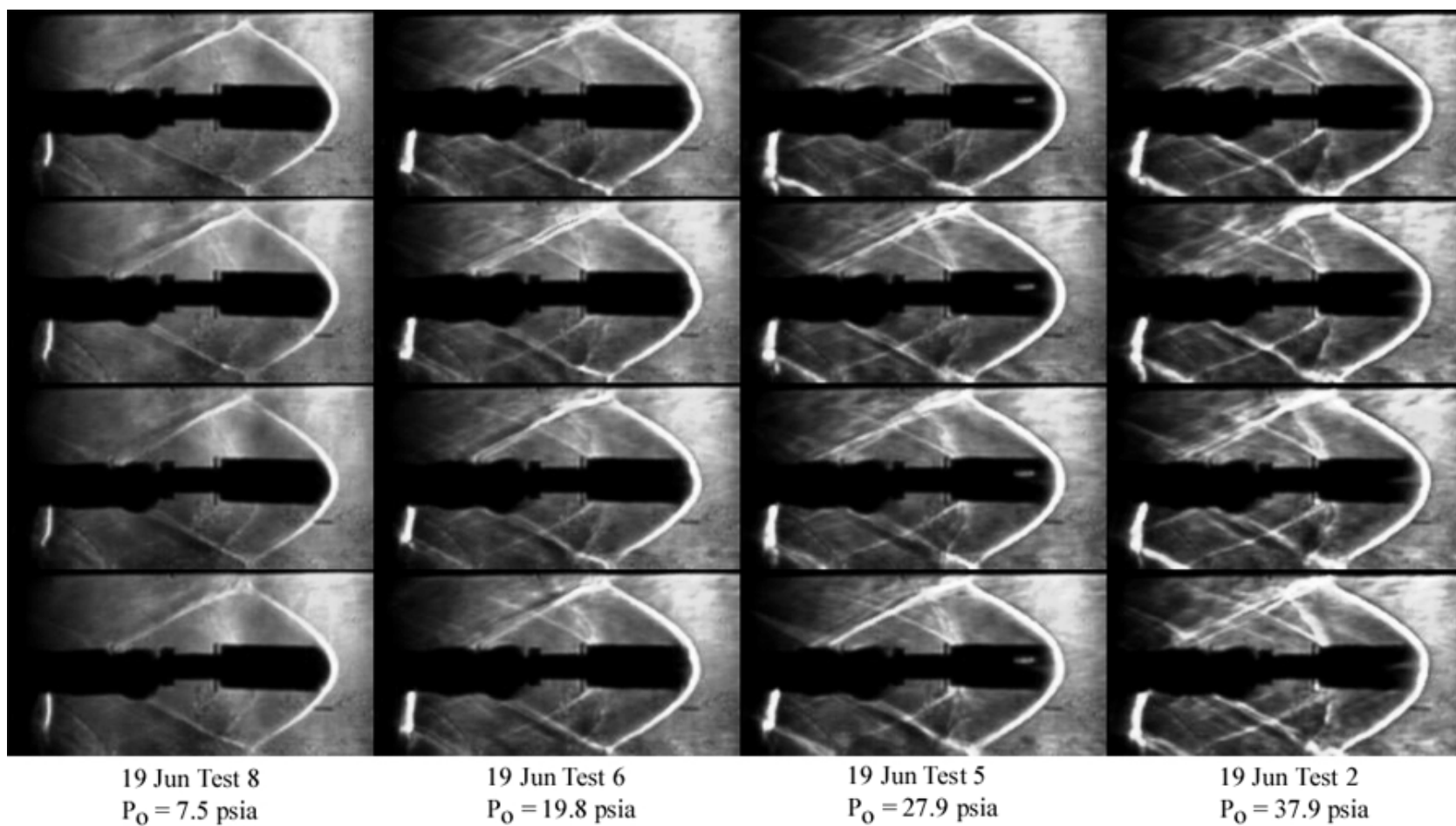


Figure 66: Schlieren images of spherically blunted cylinder at 7.5, 19.8, 27.9, and 37.9 psia stagnation pressures. The top row is at $t = 0$ sec, the second row at $t = 1$ sec, the third row at $t = 2$ sec, and the fourth row is at $t = 3$ sec

The four tests are compared at time $t = 2.5$ seconds in Figure 67 through Figure 69. In these images, 19 Jun Test 8 ($P_o = 7.5$ psia) is presented in the top left of the image; 19 Jun Test 6 ($P_o = 19.8$ psia) is presented in the top right; 19 Jun Test 5 ($P_o = 27.9$ psia) is in the bottom left; and 19 Jun Test 2 ($P_o = 37.9$ psia) is in the bottom right image.

Figure 67 provides the top down view of the mesh surface of the four models. As previously, the black silhouette is the original shape and the red surface is the surface at the indicated time step. Figure 67 also provides an overall comparison of the surface change at the various pressures. As anticipated, increasing stagnation pressure yields more recession. The image of 19 Jun Test 2 is representative of the shape that is expected in these tests.

The surface representation in 19 Jun Test 6 and 19 Jun Test 5 are misleading. In the representation of 19 Jun Test 6, a line of points shifted out of view on the port side of the model and MatLab constructed the surface with a large missing piece on that side of the model image. This is a result of the coarse grid and not a model defect. In 19 Jun Test 5, the missing portion on the farthest aft portion of the starboard side of the model is due to the lack of a visible point in the presented time step, and the nose is recessing as expected if only in the center. The MatLab surface rendering is a tool for visualizing the shape of the model, however the point cloud is more useful for gathering specific information.

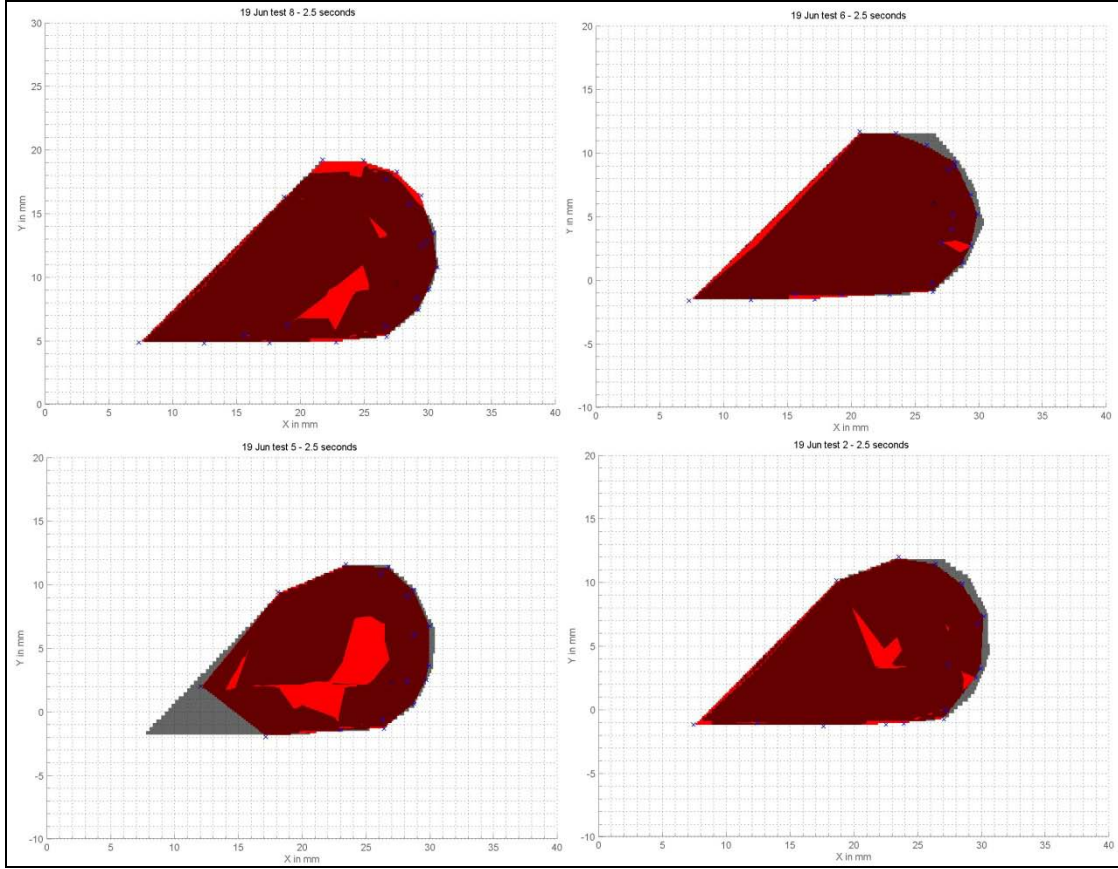


Figure 67: Comparison of experimental spherically blunted cylinders 7.5 (top left), 19.8 (top right), 27.9 (bottom left), and 37.9 psia (bottom right): top view of mesh surface

Figure 68 displays the front view of the point cloud for each of these four tests at time = 2.5 seconds. Figure 69 illustrates the side profile view of the point cloud, and Figure 70 presents the top down view of the point cloud in the same orientation as the surfaces of Figure 67. Again, the circles are the original position of the points and the red 'x's are the location of the points at the indicated time step.

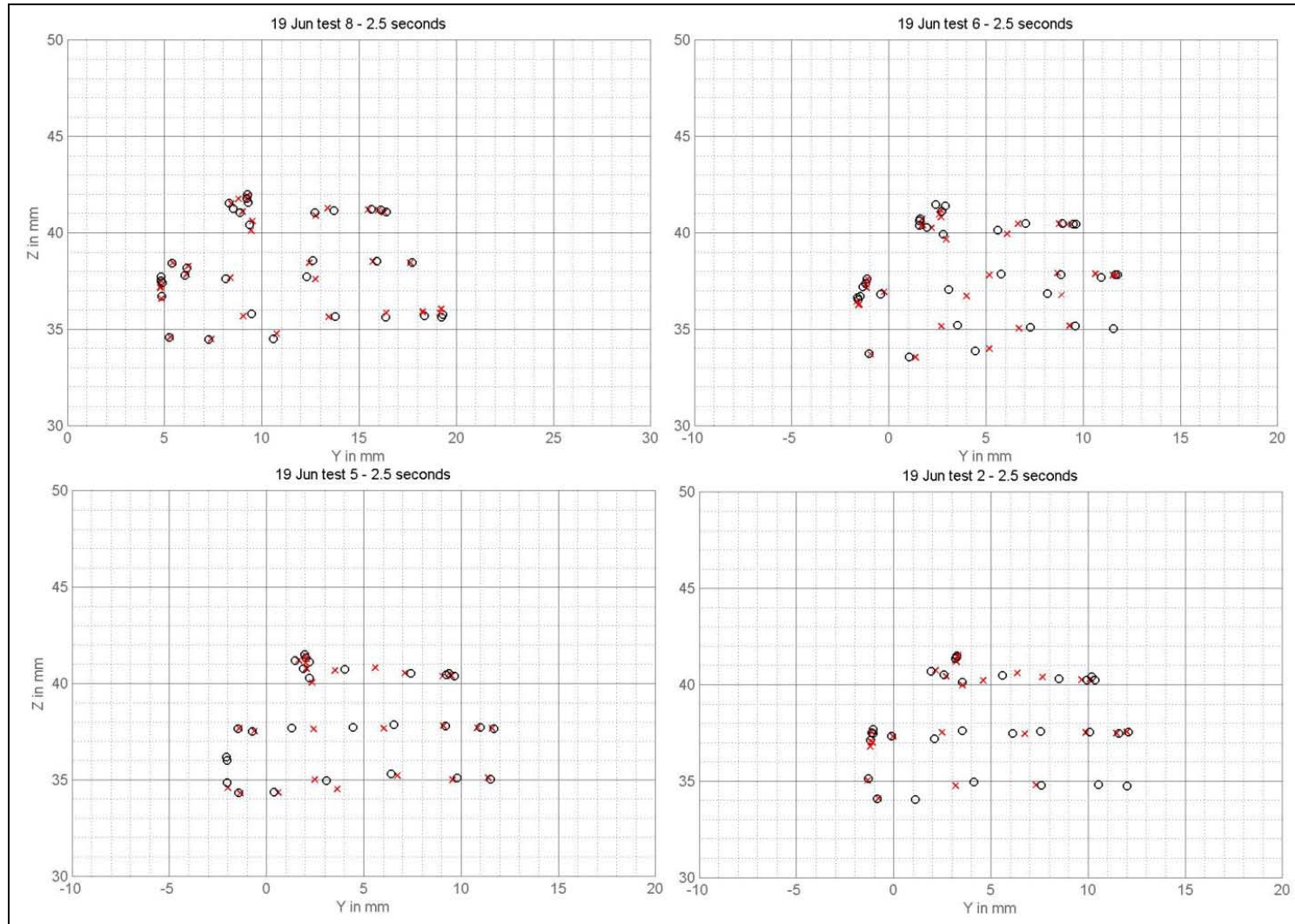


Figure 68: Comparison of experimental spherically blunted cylinders at time = 2.5 seconds 7.5 (top left), 19.8 (top right), 27.9 (bottom left), and 37.9 psia (bottom right): front view of point cloud

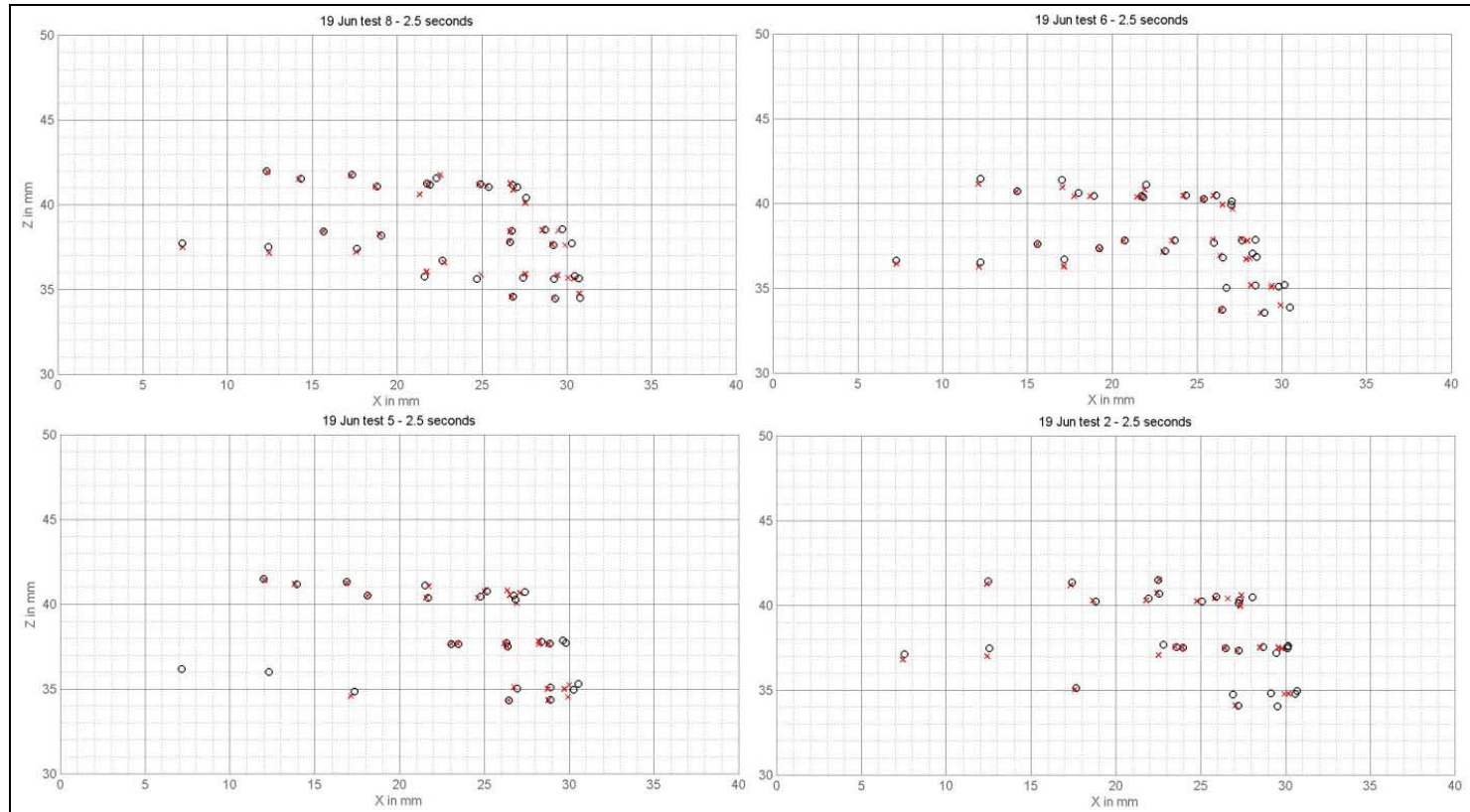


Figure 69: Comparison of experimental spherically blunted cylinders at time = 2.5 seconds 7.5 (top left), 19.8 (top right), 27.9 (bottom left), and 37.9 psia (bottom right): side profile view of point cloud

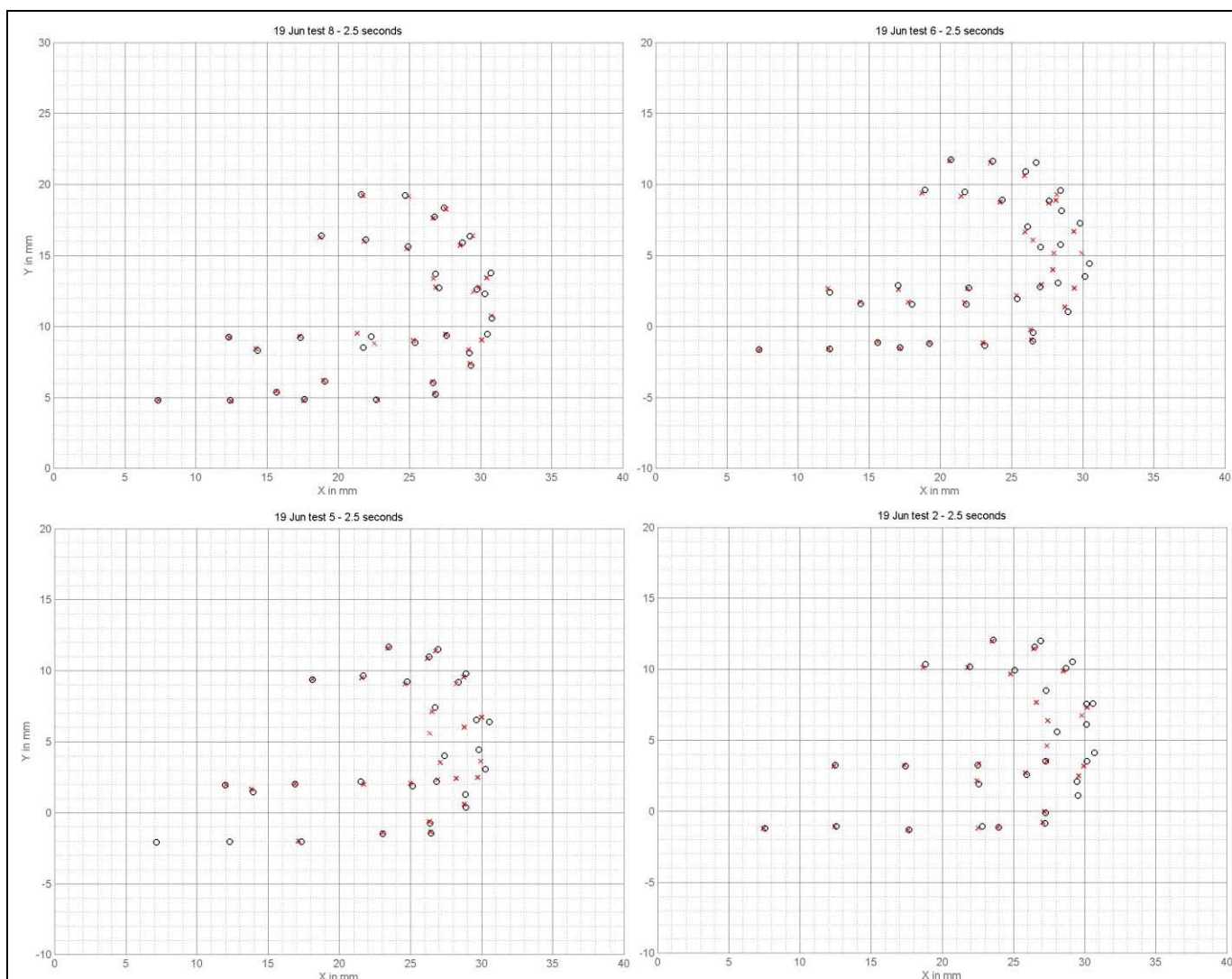


Figure 70: Comparison of experimental spherically blunted cylinders at time = 2.5 seconds 7.5 (top left), 19.8 (top right), 27.9 (bottom left), and 37.9 psia (bottom right): top view of point cloud

In Figure 71, a graphical comparison of the recession of the points near the nose is given for comparison along with their average trend lines. The results for the lower two stagnation pressures fall in line with expectations. Up to $t = 1.5$ seconds, tests 19 Jun Test 5 ($P_o = 27.9$ psia) and 19 Jun Test 2 ($P_o = 37.9$ psia) also show the expected trend toward increased ablation rates. However, after 1.5 seconds, the recession rates of the 19 Jun Test 2 ($P_o = 37.9$ psia) falls below that of the 19 Jun Test 5 ($P_o = 27.9$ psia) recession rate, which was unexpected. The $P_o = 37.9$ psia run developed a large concave opening in the nose and therefore the data past 2.5 seconds was unusable. It is conceivable that this contributed to the anomalous data or that a longer run may have shown an overall higher recession rate. This anomaly is discussed further in Section 5.1.3.

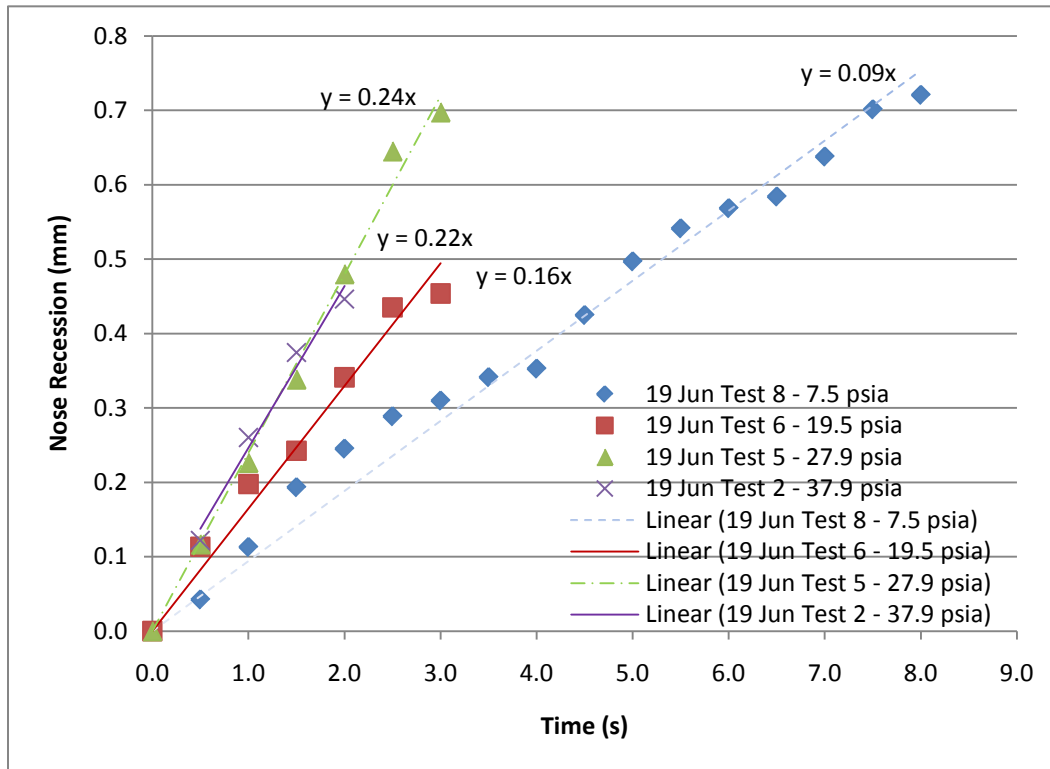


Figure 71: Comparison of experimental nose recession results for spherically blunted cylinder at 7.5, 19.5, 27.9, and 37.9 psia stagnation pressures.

With reference to Figure 66, at 2 seconds, the Schlieren images showed a nose tip recession of 1 pixel for 19 Jun Test 8, 1 to 2 pixels for 19 Jun Test 6, 1 to 2 pixels for 19 Jun Test 5, and 2 to 3 pixels for 19 Jun Test 2. At one pixel equal to approximately 0.43 mm, comparing these to the data presented in Figure 71, tests 19 Jun Test 8 and 19 Jun Test 6 should be within one pixel, while tests 19 Jun Test 5 and 19 Jun Test 2 will be less than two pixels. As previously, the Schlieren imaging is valuable for showing changes in the flow field but it is very limited in terms of yielding a quantitative recession rate.

4.6 Elliptical-Nose Model at 0 Angle of Attack and Multiple Pressures

The elliptical-nose model was produced with the assistance of AFRL/RBAC and molded onto a 0.6 inch diameter cylinder for the wind tunnel models as shown in Appendix A. The elliptical-nose had a success rate of approximately one in three attempts.

This section provides a comparison of the recession results for the elliptical-nose model in a horizontal configuration at two stagnation pressures, presented in Table 19. While this shape had a decent success rate in model fabrication, it failed rapidly in wind tunnel tests, likely due to the thinness of the model. Schlieren images were used during the tests to compare runs of varying pressure, as seen in Figure 72. As with the other model shapes, during the wind tunnel tests, the sense was that more shape change was happening for the higher stagnation pressure runs.

Table 19: Test conditions of 13 Jun Test 3 and 18 Jul Test 3

Test Name	(psia)	(psia)	(kg/m ³)	Re/x (1/m)
13 Jul Test 3	17.3	0.479	0.107	8.68E+06
18 Jul Test 3	39.1	1.18	0.244	19.8E+06

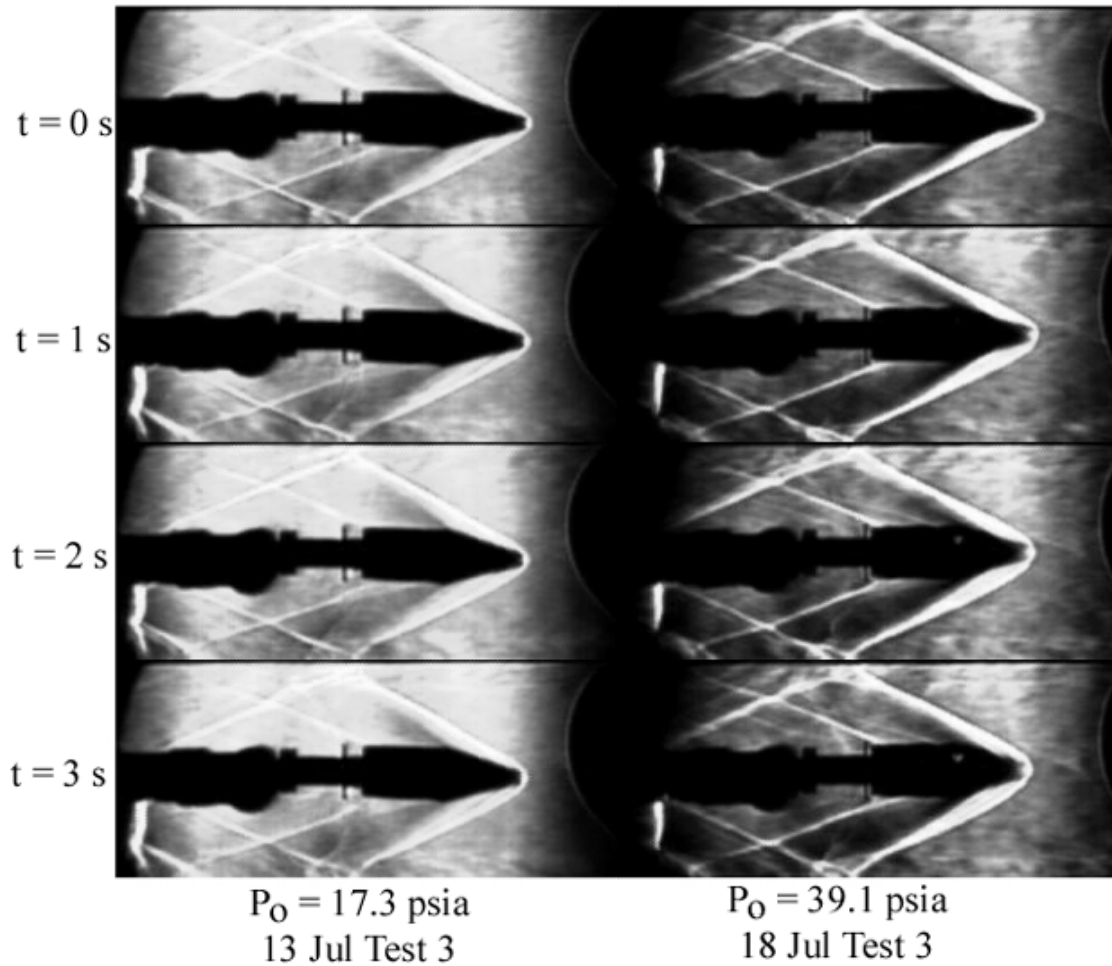


Figure 72: Schlieren images of an elliptical nose model at stagnation pressures of 17.3 and 39.1 psia. The top row is at $t = 0$ sec, the second row at $t = 1$ sec, the third row at $t = 2$ sec, and the fourth row is at $t = 3$ sec

The Schlieren images project an approximate 3 pixel loss for the 13 Jul Test 3 ($P_o = 17.3$ psia) and a 7 pixel loss for the 18 Jul Test 3 ($P_o = 39.1$ psia) test over 3 seconds of the test run. The results of the Schlieren visualization are again limited to the 0.43 mm pixel measurement. Evident in Figure 72, the 18 Jul Test 3 case has a defect that appears in the cylindrical portion of the model at the 2 second mark. This was a fairly common defect, but given the distance of the defect from the nose, the data was processed nonetheless.

Tests 13 Jul Test 3 and 18 Jul Test 3 are compared in Figure 73 through Figure 77 which shows each of these two tests at time = 2.5 seconds. Figure 73 provides the top down view of the mesh surface created from the point cloud. As previously, the black silhouette is the original shape and the red surface is the surface at the indicated time step. As this shape is highly elliptical and unlike the spherically blunted cone and spherically blunted cylinder the elliptical nose model is not axi-symmetric, a new viewing angle for this comparison is provided: the mesh surface viewed from the side in Figure 74.

Figure 75 displays the front view of the point cloud for the two tests at time = 2.5 seconds. Figure 76 presents the side profile view of the point cloud which is the same viewing angle as that of the new mesh surface seen in Figure 74. Figure 77 illustrates the top down view of the point cloud for each test case which corresponds to the top down mesh surface view in Figure 73. The circles are the original position of the points and the red 'x's are the location of the points at the indicated time step.

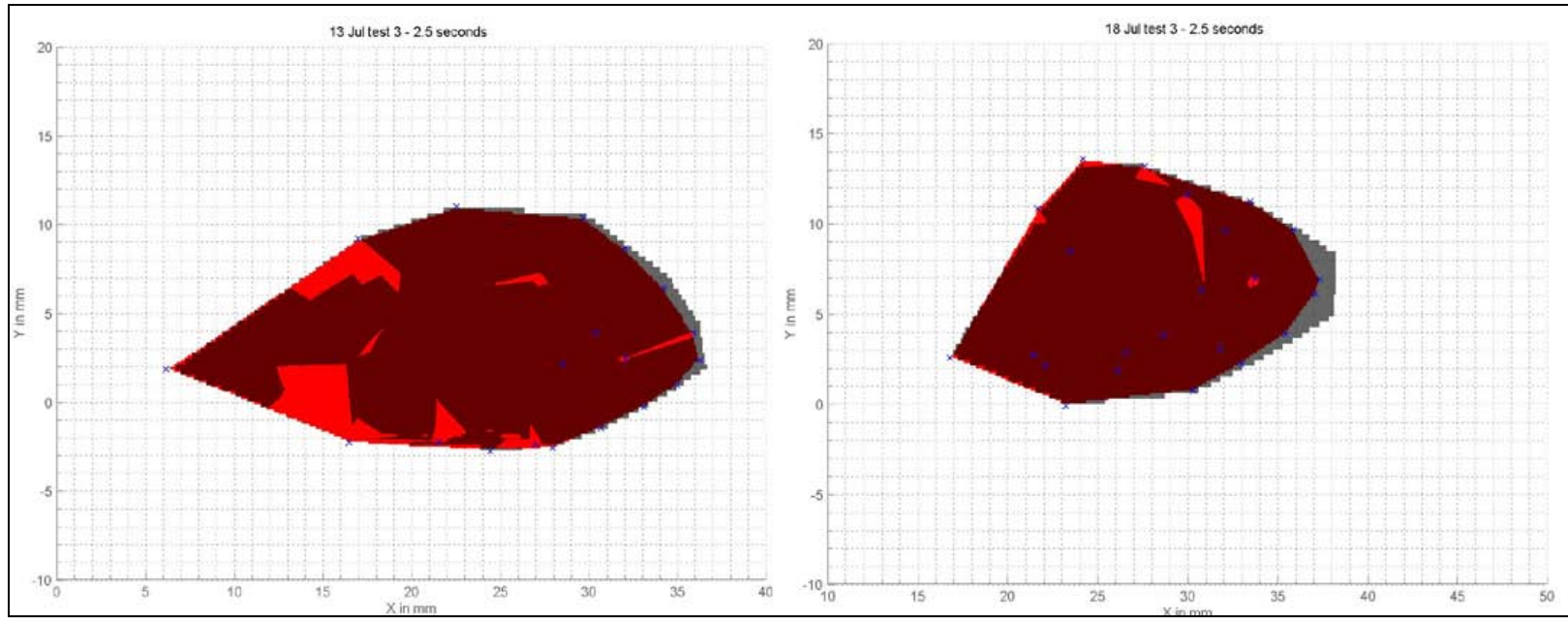


Figure 73: Comparison of experimental results for an elliptical nose shape at $P_0=17.3$ psia (left) and $P_0 = 39.1$ psia(right): top view of mesh surface

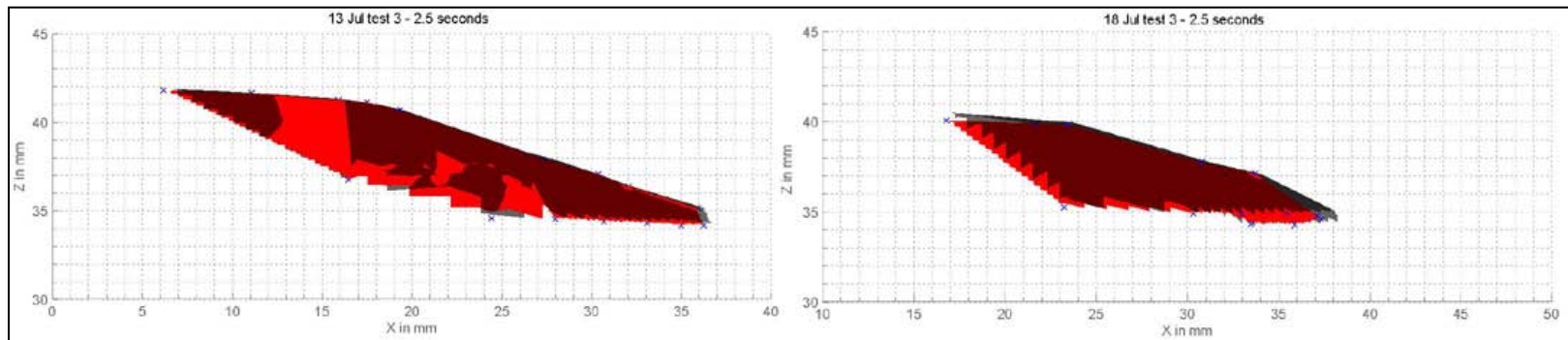


Figure 74: Comparison of experimental results for an elliptical nose shape at $P_0=17.3$ psia (left) and $P_0 = 39.1$ psia(right): side view of mesh surface

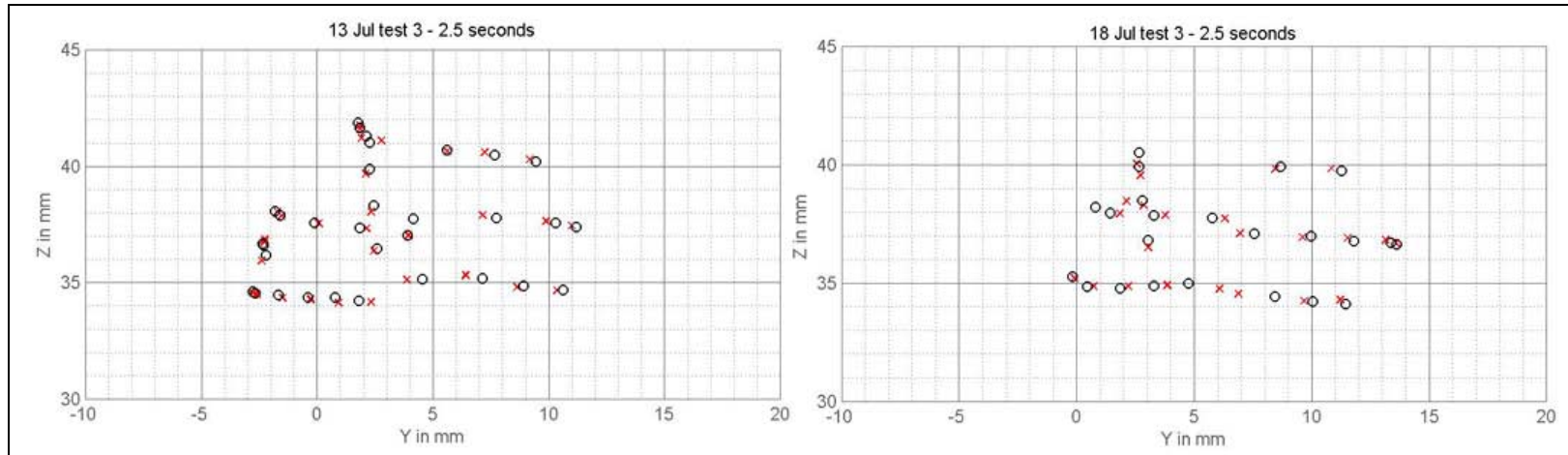


Figure 75: Comparison of experimental results for an elliptical nose shape at $P_0=17.3$ psia (left) and $P_0 = 39.1$ psia(right): front view of point cloud

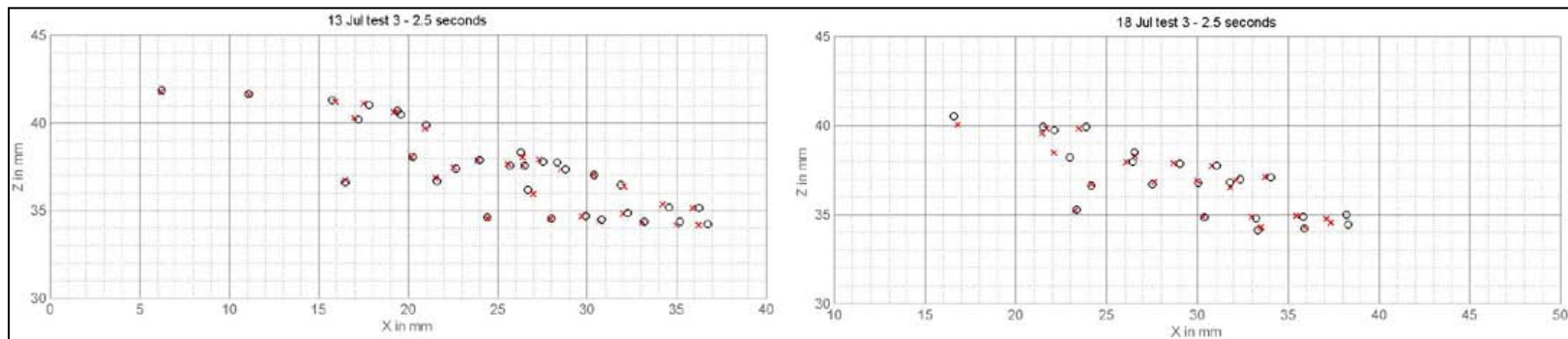


Figure 76: Comparison of experimental results for an elliptical nose shape at $P_0=17.3$ psia (left) and $P_0 = 39.1$ psia(right): side view of point cloud

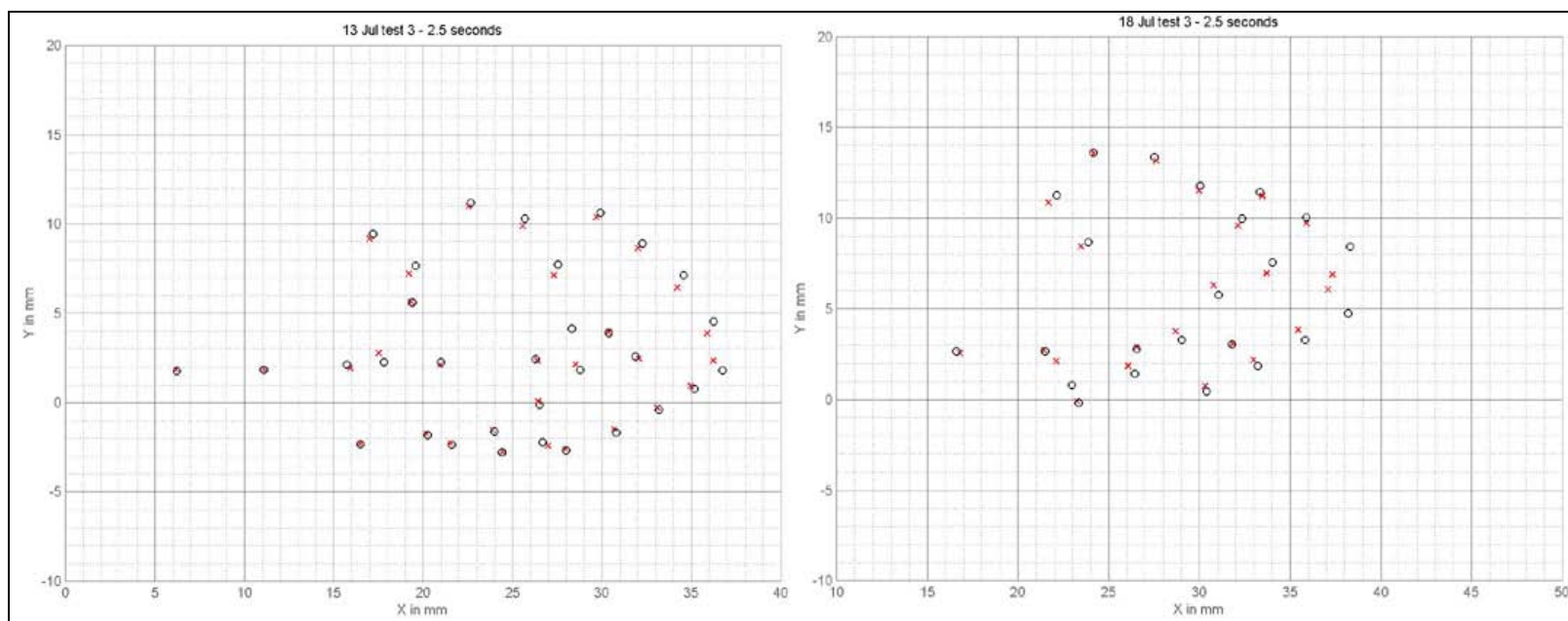


Figure 77: Comparison of experimental results for an elliptical nose shape at $P_o=17.3$ psia (left) and $P_o = 39.1$ psia(right): top view of point cloud

In Figure 78, a graphical comparison of the recession of the points near the nose is given with their average trend lines. The results for 13 Jul Test 3 ($P_o = 17.3$ psia) and 18 Jul Test 3 ($P_o = 39.1$ psia) are also include in Table 20 and behave as expected and similar to other results found in this research.

With reference to Figure 72, at 2 seconds, the Schlieren images showed a nose tip recession of 2 pixels for $P_o = 17.3$ psia (13 Jul Test 3) and 4 pixels for $P_o = 39.1$ psia (18 Jul Test 3). At one pixel equal to approximately 0.4 mm, comparing these to the data presented in Figure 78 after 2 seconds, tests 13 Jul Test 3 would be recessed approximately 1 pixel and 18 Jul Test 3 would have receded approximately 1.5 pixels.

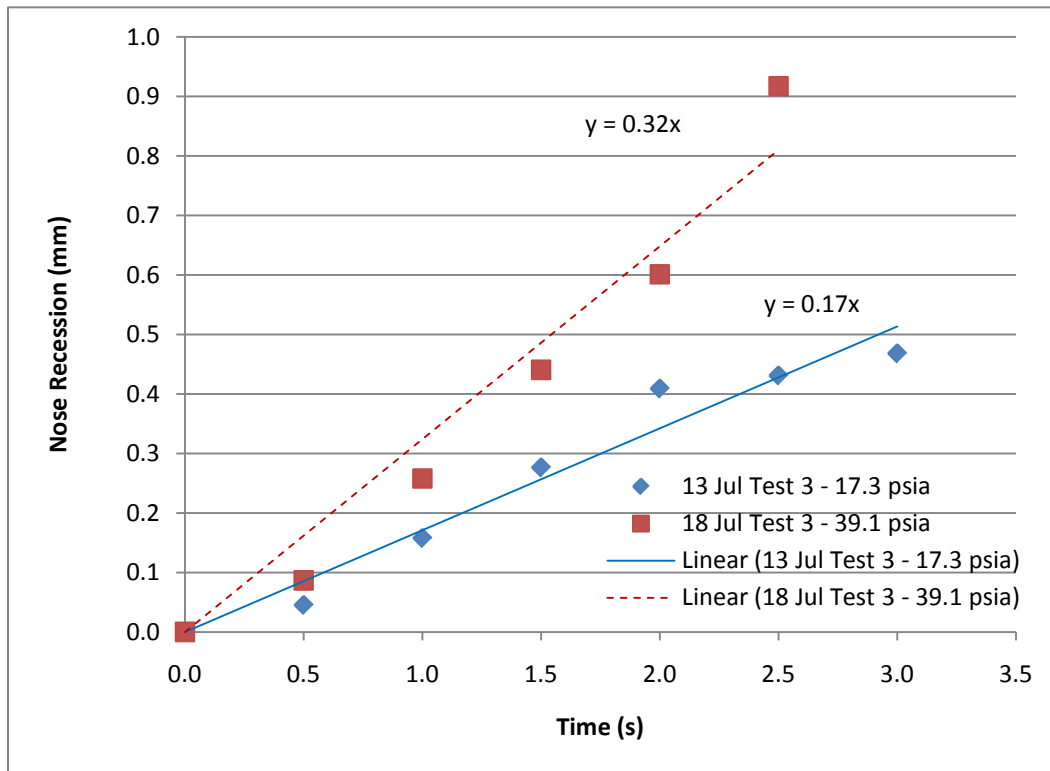


Figure 78: Comparison of experimental nose recession results for an elliptical nose at 17.3 and 39.1 psia stagnation pressures.

Table 20: Average recession rates calculated for a point near the nose of a horizontally oriented elliptical nose for $P_o = 17.3$ psia and $P_o = 39.1$ psia

Test	Average Recession Rate (mm/s)
13 Jul Test 3 (17.3 psia)	0.171
18 Jul Test 3 (39.1psia)	0.324

4.7 Multiple Shapes at $P_o \sim 20$ psia

In this section, a comparison of three different model shapes is made of similar stagnation pressures. A spherically blunted cone is presented from test 9 Jun Test 1 at 23.0 psia stagnation pressure. A spherically blunted cylinder is presented from test 19 Jun Test 6 at 19.5 psia and a horizontally oriented elliptical-nose is presented in 13 Jul Test 3 at 17.3 psia stagnation pressure. The conditions for each test are shown in Table 21. The expected result for this comparison is that the smaller nose radius should typically recede faster than the blunter nose.

Table 21: Test conditions for 9 Jun Test 1, 19 Jun Test 6, and 13 Jul Test 3

Test Name	Shape	(psia)	(psia)	(kg/m ³)	Re/x (1/m)
9 Jun Test 1	Spherically Blunted Cone	23.0	0.67	0.150	12.2E+06
19 Jun Test 6	Spherically Blunted Cylinder	19.8	0.56	0.126	10.2E+06
13 Jul Test 3	Elliptical-Nose	17.3	0.48	0.107	8.68E+06

Figure 79 presents the top down mesh surface view of the three models. As discussed in the previous section, the missing portion on the port side of the model in the mesh surface view of the spherically blunted cylinder, 19 Jun Test 6, is due to coarseness of the grid. The asymmetric missing surface of the elliptical nose, 13 Jul Test 3, is a

combination of the grid coarseness and a sharp leading edge. As previously, the black silhouette is the original shape and the red surface is the surface at the indicated time step.

Figure 80 displays the top view of the point cloud, which corresponds to the surfaces rendered in Figure 79. Figure 81 presents the front cross section view of the point cloud, and Figure 82 provides a side profile view of the point cloud coordinates of the three test cases. The original position of the points are marked by circles and the red 'x's are the location of the points at the current time step, $t = 3$ seconds.

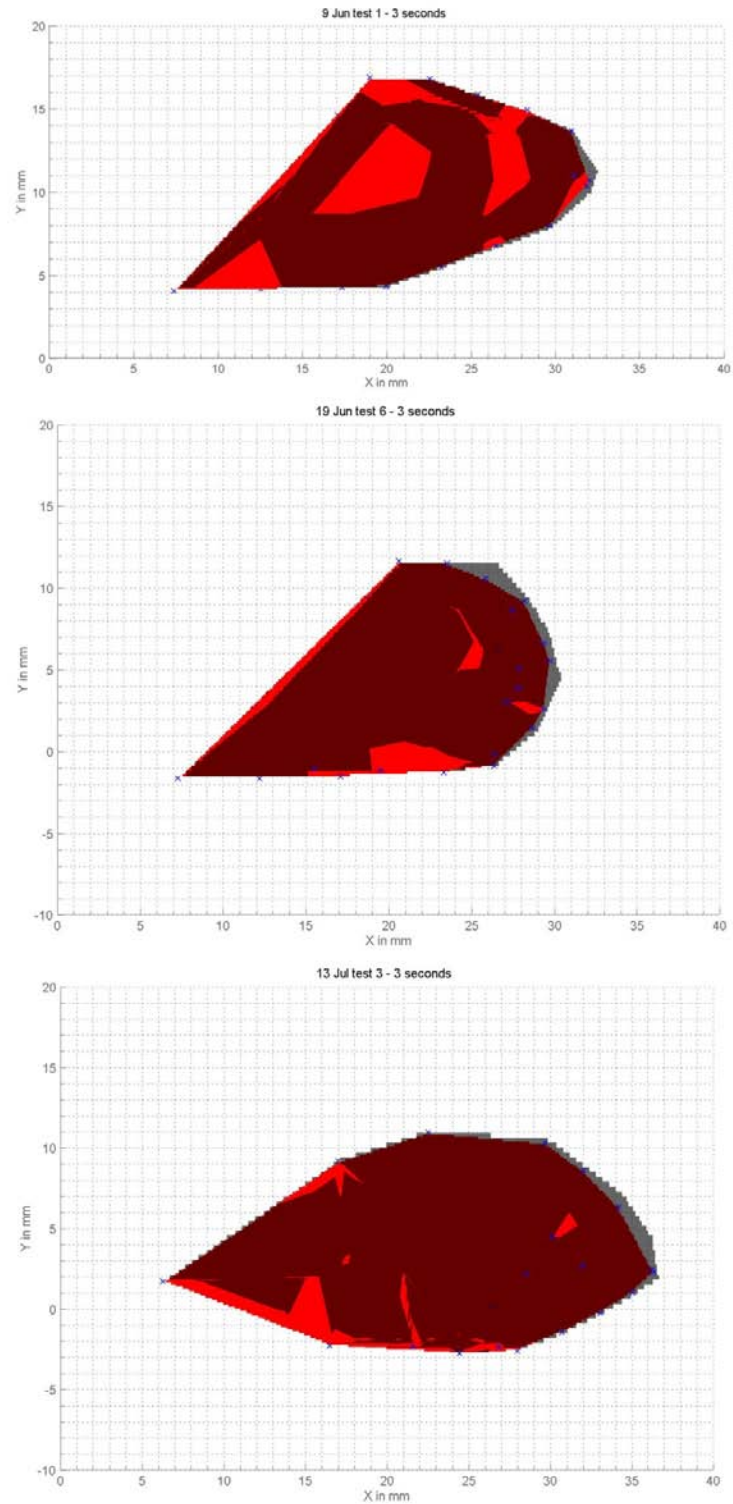


Figure 79: Comparison of zero angle attack, intermediate pressure runs from top to bottom: spherically blunted cone (23.0 psia), spherically blunted cylinder (19.5 psia), and horizontal oriented elliptical nose (17.3 psia): surface view from top after 3 seconds

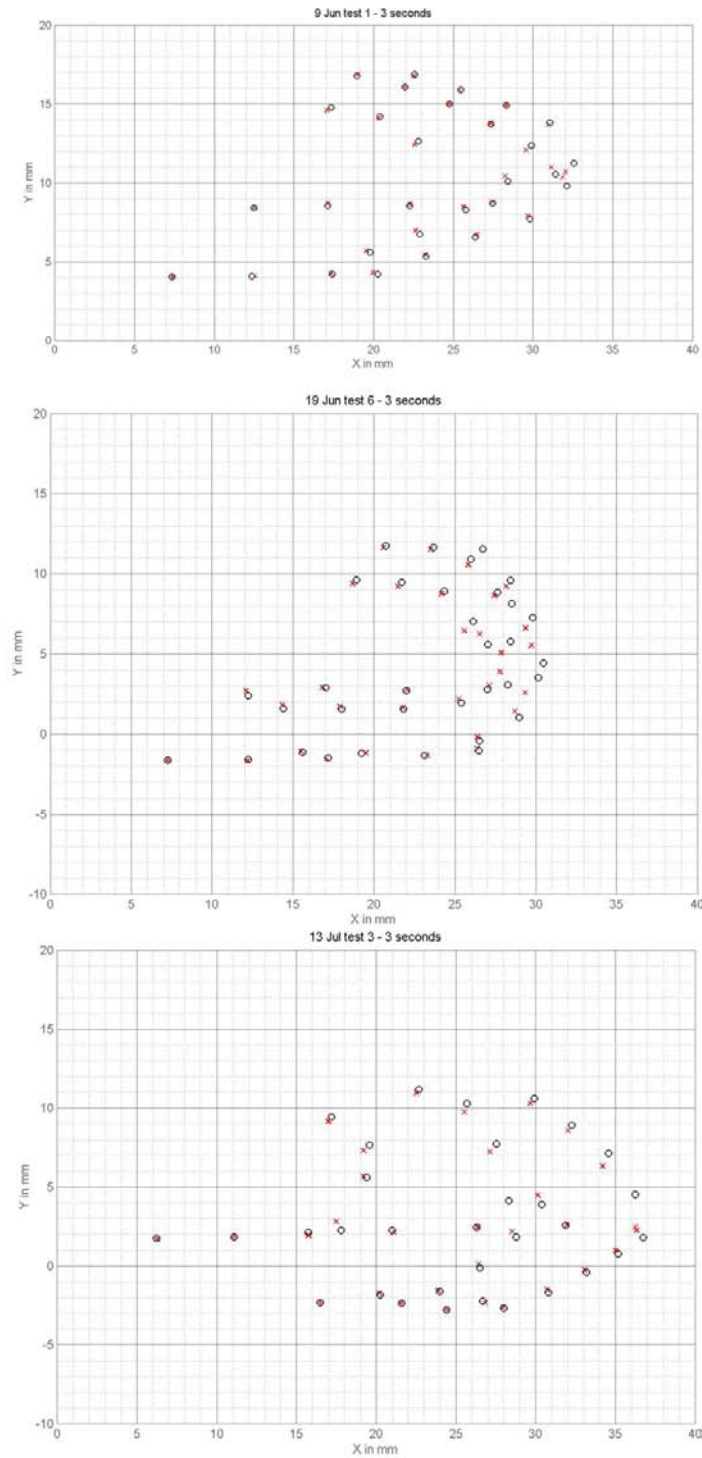


Figure 80: Comparison of zero angle attack, intermediate pressure runs from top to bottom: spherically blunted cone (23.0 psia), spherically blunted cylinder (19.5 psia), and horizontal oriented elliptical nose (17.3 psia): point cloud view from top after 3 seconds

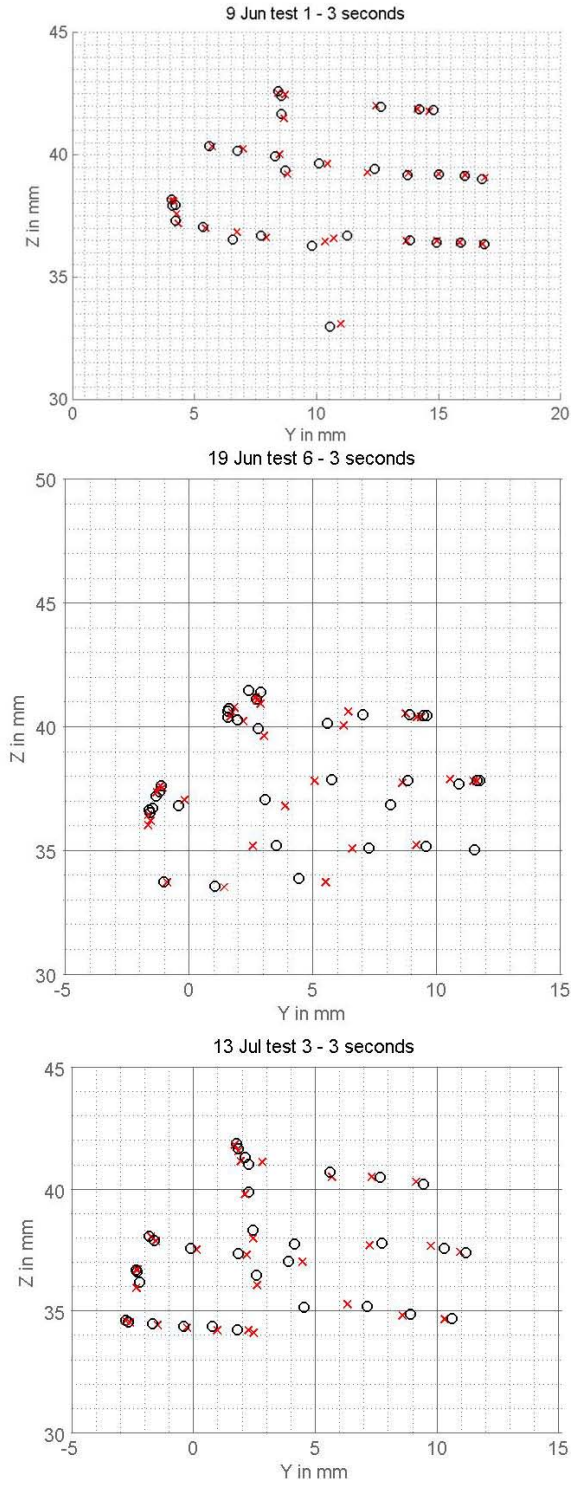


Figure 81: Comparison of zero angle attack, intermediate pressure runs from top to bottom: spherically blunted cone (23.0 psia), spherically blunted cylinder (19.5 psia), and horizontal oriented elliptical nose (17.3 psia): point cloud view from front after 3 seconds

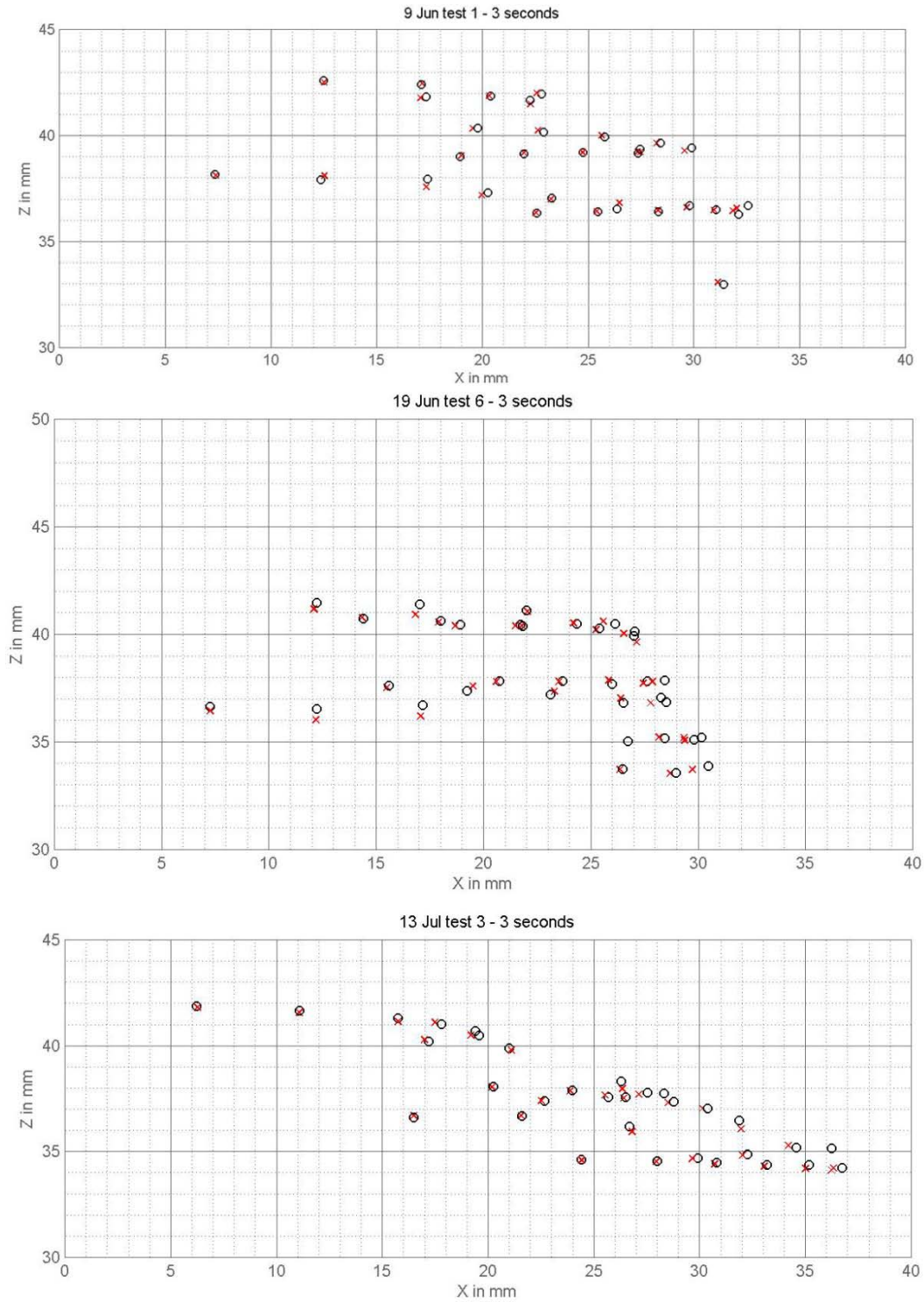


Figure 82: Comparison of zero angle attack, intermediate pressure runs from top to bottom: spherically blunted cone (23.0 psia), spherically blunted cylinder (19.5 psia), and horizontal oriented elliptical nose (17.3 psia): point cloud view from side after 3 seconds

The comparison of the nose tip recession of the three model shapes is shown in Figure 83 and provides some interesting insights into the shape characteristics. The average recession rates are also provided in table form in Table 22. The three shapes yielded similar nose tip recession rates for the indicated pressures. As anticipated, the blunt nosed test, 19 Jun Test 6, had the lowest recession rate followed by the elliptical nose and the spherically blunted cone.

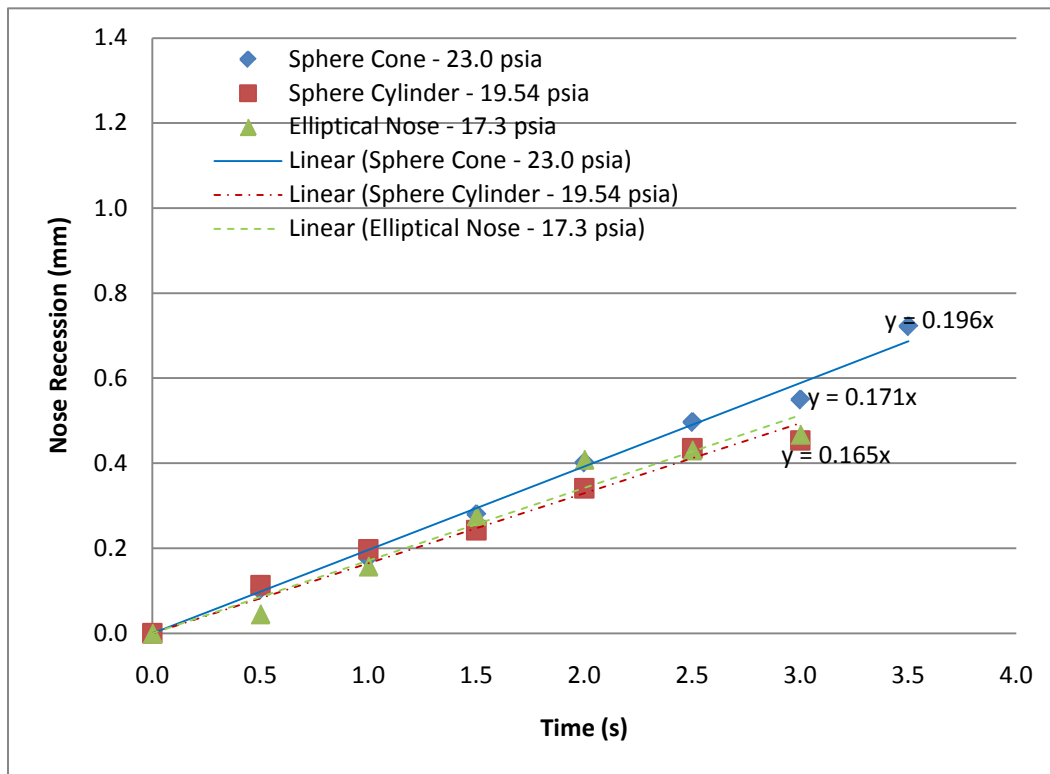


Figure 83: Comparison of experimental nose recession for a spherically blunted cone, spherically blunted cylinder and horizontal oriented elliptical nose near 20 psia

Table 22: Average recession rates calculated for spherically blunted cone, spherically blunted cylinder, and horizontal elliptical nose near 20 psia stagnation pressure

Test	Average Recession Rate (mm/s)
Spherically blunted cone – 23.0 psia (9 Jun Test 1)	0.196
Spherically blunted cylinder – 19.5 psia (19 Jun Test 6)	0.165
Elliptical nose – 17.3 psia (13 Jul Test 3)	0.171

It is noted that the pressures are not identical, and therefore not an ideal comparison for comparing the effect of nose radius. The difference in stagnation pressure accounts for part of the low recession rate for the elliptic-nose model used for comparison. The difference in the average recession rate of test 9 Jun Test 1 shown here and in section 4.3 is due to the different length of time used for the comparisons. These results are more rigorously compared to theory in chapter 5.

4.8 5° Angle of Attack Experimental Results

One of the key advantages of photogrammetry is that the ablation is captured in three dimensions. It was of great interest to show the capability to collect data for a test article at an angle of attack. For this reason, the tunnel test section was designed with the intent of performing angle of attack runs. Using a template to control the angle, the sting could be manipulated to an angle within +/- 1 degree. The angle of attack was increased in five degree increments. It should be emphasized that the angle of attack is viewed from above the wind tunnel and that the visibility of the leeward side of the models, port side in these tests, is limited due to camera angles.

In general, the expected results are an asymmetric distribution with increased ablation on the windward side of the model. Presented in this section are comparisons of a spherically blunted cone and a spherically blunted cylinder at an angle of attack of five degrees to the flow.

4.8.1 Spherically Blunted Cone

For the spherically blunted cone, tests 29 Aug Test 9 at $P_o = 27.2$ psia and 29 Aug Test 6 at $P_o = 39.9$ psia, shown in Table 23, were chosen for comparison. Figure 84, Figure 85, Figure 86, and Figure 87 show the comparisons side by side after 2.5 second elapsed time. The test at lower stagnation pressure, 29 Aug Test 9 at 27.2 psia, is presented on the left while the 39.9 psia stagnation test, 29 Aug Test 6, is presented on the right in each of the images.

Table 23: Test conditions for 29 Aug Test 9 and 29 Aug Test 6

Test Name	(psia)	(psia)	(kg/m ³)	Re/x (1/m)
29 Aug Test 9	27.2	0.81	0.177	1.44E+07
29 Aug Test 6	39.9	1.19	0.262	2.13E+07

Figure 84 presents surface mesh images of the spherically blunted cone viewed from above for comparison. As in previous images, the red shading represents the surface at the present time step while the black silhouette is the original shape. Arrows have been added to Figure 84 and Figure 85 to illustrate the actual position of the nose-tip as well as the orientation of the model. For all test orientations, the X axis points upstream.

Figure 85 presents the top down view of the three dimensional point cloud which corresponds to the surfaces in Figure 84. Figure 86 presents the point cloud as viewed from the side and Figure 87 presents the point cloud as viewed from the front. Again, the circles are the original position of the points and the red 'x's are the locations of the points at the indicated time step.

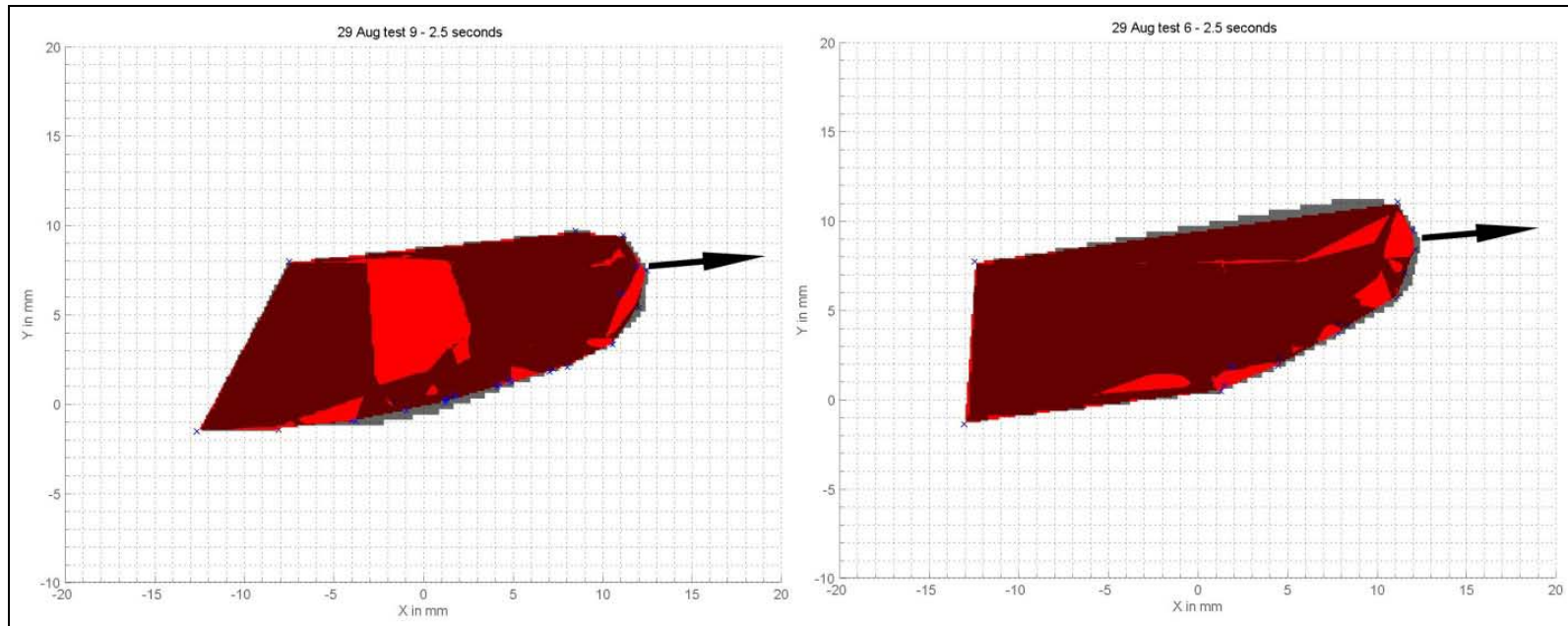


Figure 84: Comparison of 5° angle of attack, spherically blunted cone at 27.2 psia (left) and 39.9 psia (right): surface mesh viewed from above after 2.5 seconds

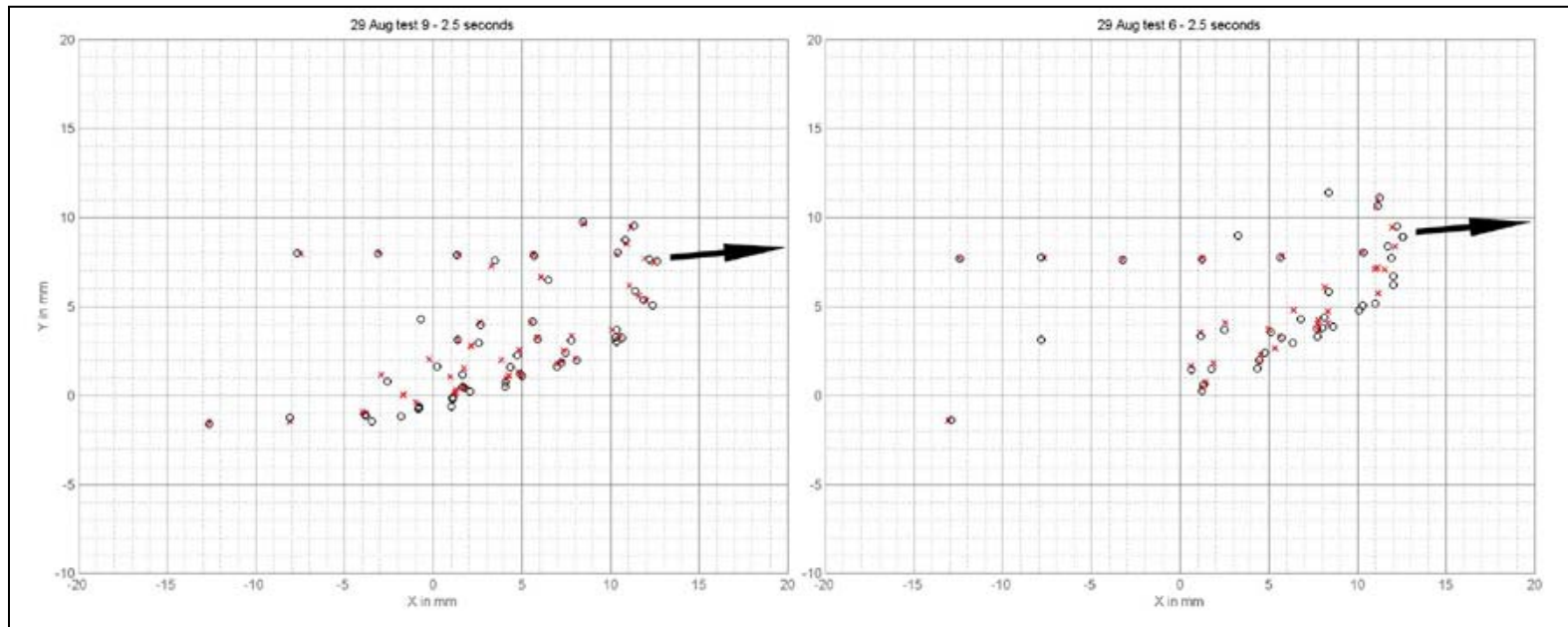


Figure 85: Comparison of 5° angle of attack, spherically blunted cone at 27.2 psia (left) and 39.9 psia (right): point cloud viewed from above after 2.5 seconds

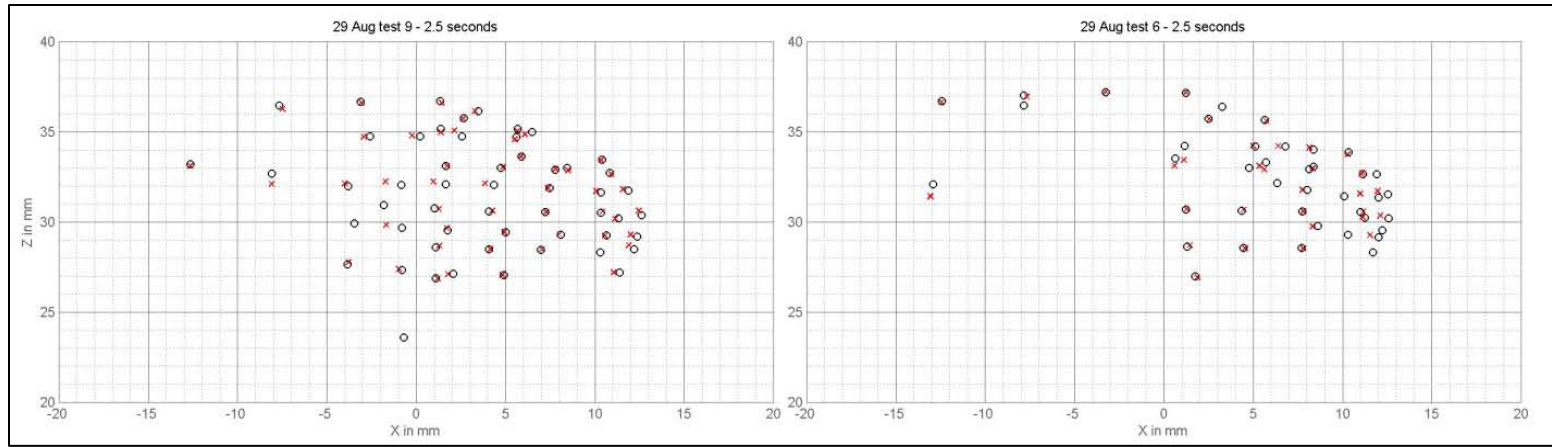


Figure 86: Comparison of 5° angle of attack, spherically blunted cone at 27.2 psia (left) and 39.9 psia (right): point cloud viewed from the side after 2.5 seconds

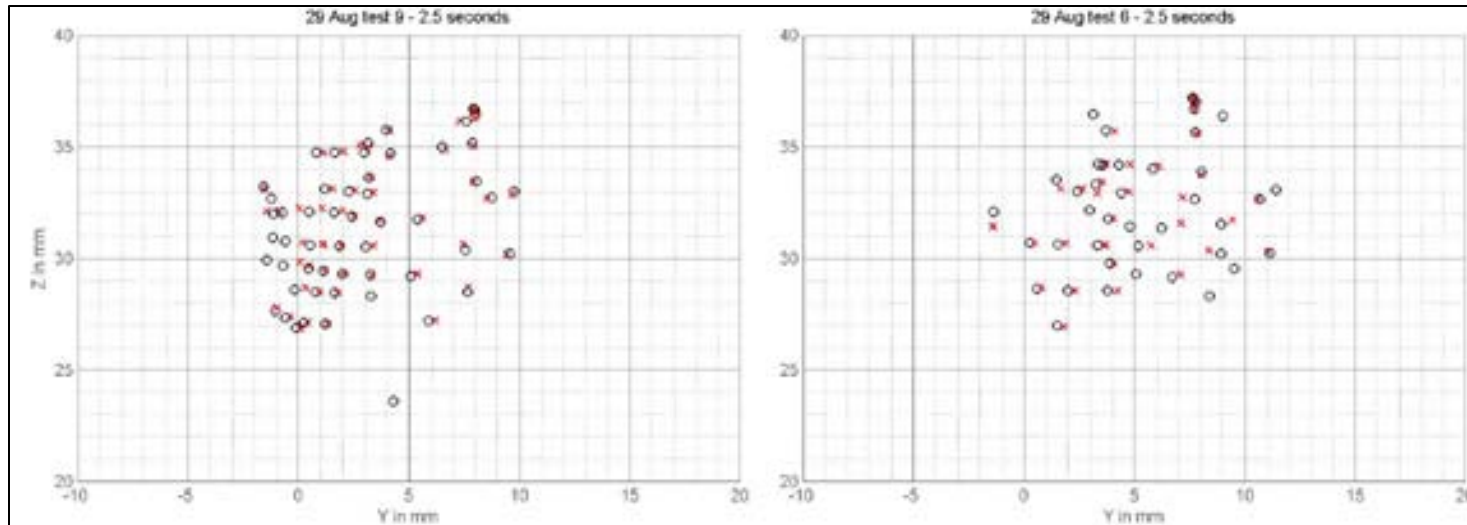


Figure 87: Comparison of 5° angle of attack, spherically blunted cone at 27.2 psia (left) and 39.9 psia (right): point cloud viewed from the front after 2.5 seconds

Figure 87 gives the front view of the point distribution. The center of the nose tip is located at approximately $Y = 7.5$ mm for the 29 Aug Test 9 case and at $Y = 9$ mm for the 29 Aug Test 6 test. A vast majority of the points tracked are on the windward side of both models due to camera angles.

4.8.2 Spherically Blunted Cylinder

For the spherically blunted cylinder at 5° angle of attack, tests 28 Aug Test 4 at $P_o = 20.8$ psia and 29 Aug Test 3 at $P_o = 45.7$ psia, as seen in Table 24, were chosen for comparison. Figure 88, Figure 89 and Figure 90 show the comparisons side by side after 2 second elapsed time. The test at lower stagnation pressure, 28 Aug Test 4, is presented on the left of the figures while 29 Aug Test 3 is presented on the right in each of the images.

Table 24: Test conditions for 28 Aug Test 4 and 29 Aug Test 3

Test Name	(psia)	(psia)	(kg/m ³)	Re/x (1/m)
28 Aug Test 4	20.8	0.57	0.126	1.03E+07
29 Aug Test 3	45.7	1.40	0.308	2.51E+07

Figure 88 presents surface mesh images from a top down view for comparison. As in previous images, the black silhouette represents the original shape and the red surface presents the mesh surface at the current time step. Arrows have been added to Figure 88 and Figure 89 to illustrate the actual position of the center of the blunt nose as well as the body axis of the model.

Note, in Figure 88, that significant recession is apparent aft of the nose on the windward side of the model. This is more evident at the higher pressure. To be clear, the portion missing from the representation of the front of 29 Aug Test 3 in Figure 88 is not due to grid coarseness but to shape change. This can be best discerned from the point clouds.

Figure 89 presents views of the three dimensional point clouds as seen from above and the side. The top two images correspond to the surfaces in Figure 88. Figure 90 shows the forward cross section of the three dimensional point cloud. Again, the circles are the original position of the points and the red 'x's are the locations of the points at the indicated time step.

Visible in Figure 88 and Figure 89, the images suggest asymmetric shape change on the models' noses. For example, referencing Figure 89, recession generally appears to be higher near $(X,Y) = (8 \text{ mm}, 4 \text{ mm})$ than that near $(8 \text{ mm}, 9 \text{ mm})$.

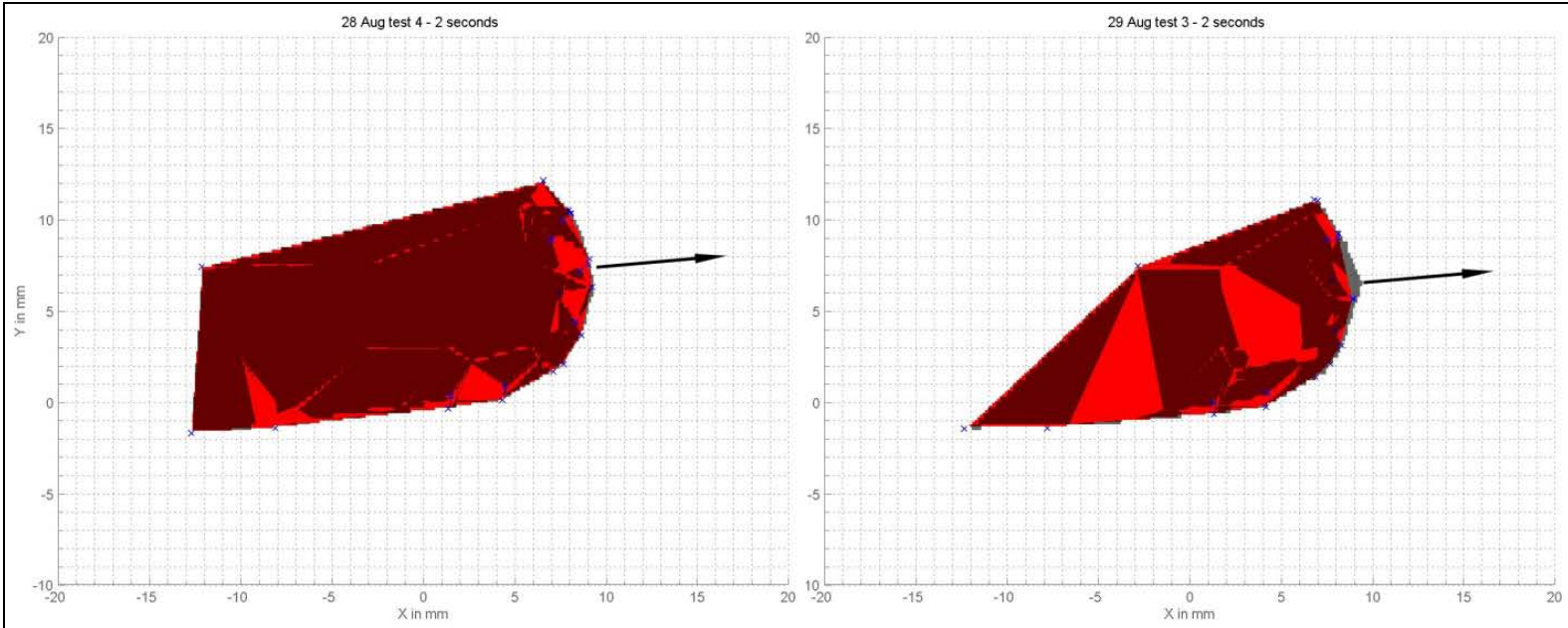


Figure 88: Comparison of 5° angle of attack, spherically blunted cylinder at 20.8 psia (left) and 45.7 psia (right): surface mesh viewed from the front after 2 seconds

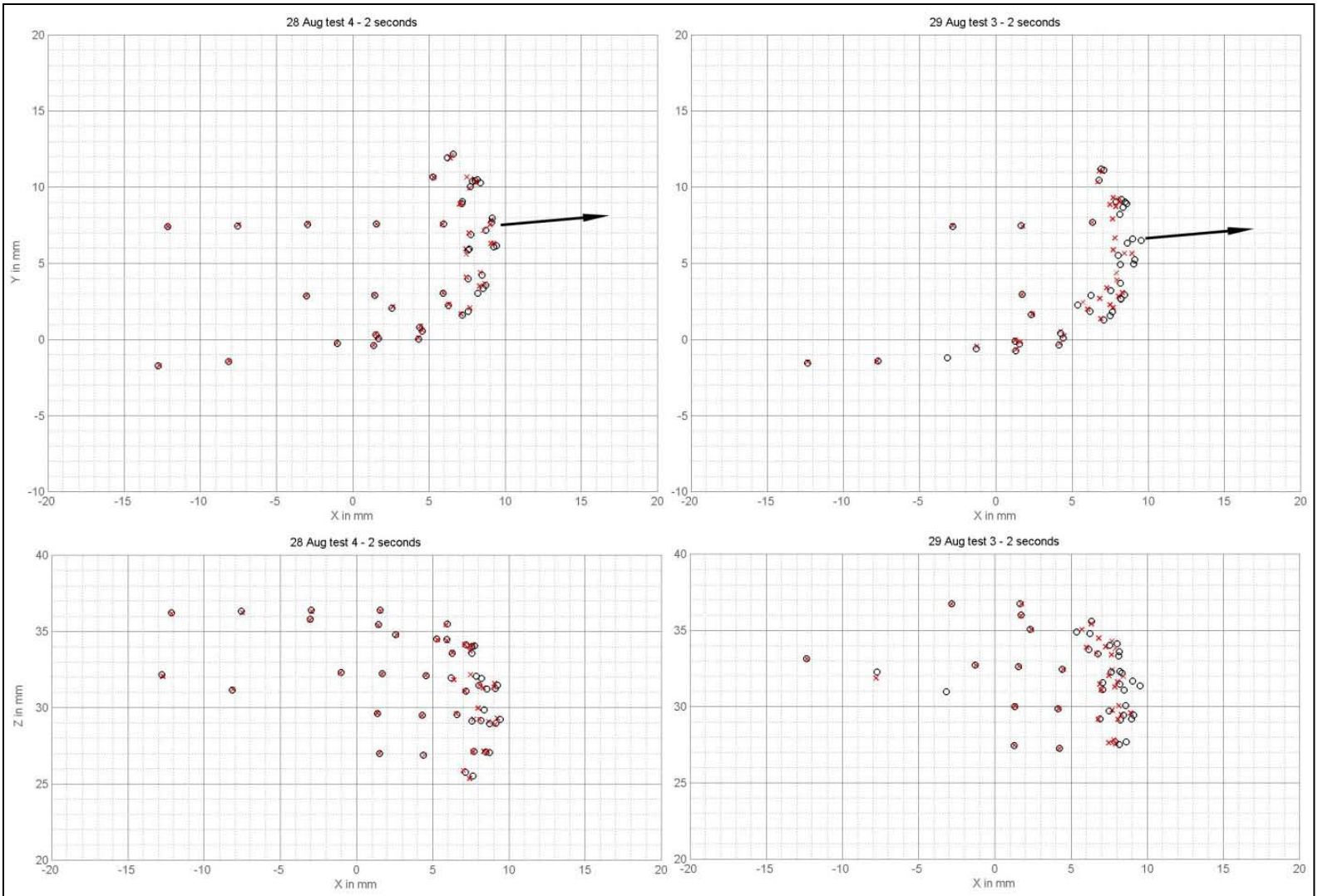


Figure 89: Comparison of 5° angle of attack, spherically blunted cylinder at 20.8 psia (left) and 45.7 psia (right) after 2 seconds: point cloud viewed from above (top) and side (bottom)

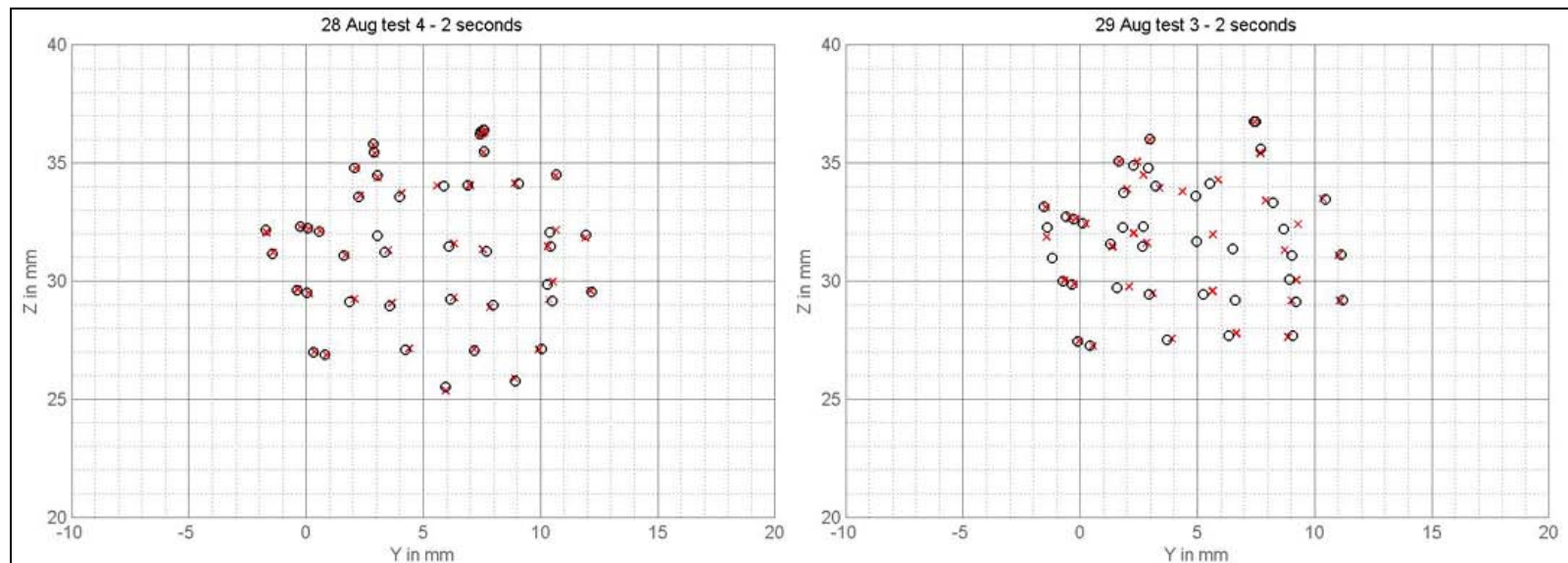


Figure 90: Comparison of 5° angle of attack, spherically blunted cylinder at 20.8 psia (left) and 45.7 psia (right) after 2 seconds: point cloud viewed from the front

4.9 10° Angle of Attack Experimental Results

For the 10° angle of attack tests, the sting was rotated to 10°, and the cameras and lasers were moved to tunnel side A to capture all of the windward side of the model. Due to the higher angle of attack, it was difficult to capture any of the ablation on the leeward side of the spherically blunted cone with only three cameras. Presented here are comparisons of a spherically blunted cone and spherically blunted cylinder at various stagnation pressures.

4.9.1 Spherically Blunted Cone

First, the spherically blunted cone at 10° angle of attack is represented by 21 Aug Test 1 ($P_o = 19.1$ psia), 26 Aug Test 4 ($P_o = 36.8$ psia), and 24 Aug Test 3 ($P_o = 42.8$ psia). These three tests are presented in Table 25.

Figure 91, Figure 92, Figure 93, and Figure 94 show the comparisons vertically side by side after 2.5 second elapsed time. In Figure 91, the test at the lowest stagnation pressure, 21 Aug Test 1, is presented on the top, 26 Aug Test 4 is presented in the middle, and 24 Aug Test 3 is presented in the bottom image. In Figure 92, Figure 93, and Figure 94, the tests are presented in the same order but horizontally left to right.

Table 25: Test conditions for 21 Aug Test 1, 26 Aug Test 4, and 24 Aug Test 3

Test Name	(psia)	(psia)	(kg/m ³)	Re/x (1/m)
21 Aug Test 1	19.1	0.53	0.119	9.71E+06
26 Aug Test 4	36.8	1.09	0.239	19.4E+06
24 Aug Test 3	42.8	1.28	0.279	22.7E+06

Figure 91 presents the surface mesh of the three spherically blunted cone test cases at 10° angle of attack. Notably, the missing tip of the nose in the high pressure ($p_o = 42.8$ psia) result of Figure 91 is not due to grid coarseness but rather is due to model failure and is physically missing. As in previous images, the red shading represents the surface at the present time step while the black surface is the original shape. From the standpoint of ablation rate measurement, though the high pressure (42.8 psia) experiment is not usable, it does provide an example of the photogrammetry. Also as in the 5° angle of attack cases, arrows have been added to the figures to illustrate the actual position of the nose as well as the orientation of the model. For all test orientations, the flow of the wind tunnel is oriented to the X axis and flows in the negative direction.

Figure 92 presents a top down view of the three-dimensional point clouds viewed from above (top images), which corresponds to the mesh surfaces in Figure 91, and a side profile view (bottom images) of the three spherically blunted cones. Figure 93 presents the same three-dimensional point clouds in a forward cross section orientation. In the point cloud images, the circles are the original position of the points and the red 'x's are the locations of the points at the indicated time step.

Figure 94 provides the Schlieren images at time = 0 (top) and 2.5 second (bottom) elapsed time of a spherically blunted cone at $P_o = 19.1$ psia, 36.8 psia, and 42.8 psia stagnation pressures for visual comparisons. It should be noted that the angle of rotation is normal to the image plane, and due to the failure of the lamp bulb, Schlieren imaging was unavailable for the day of the 26 August tests which in this situation affects the $p_o =$

36.8 psia cases. Test case 27 Aug Test 5 is included in Figure 94 as visualization for a test in the 30 psia stagnation pressure range.

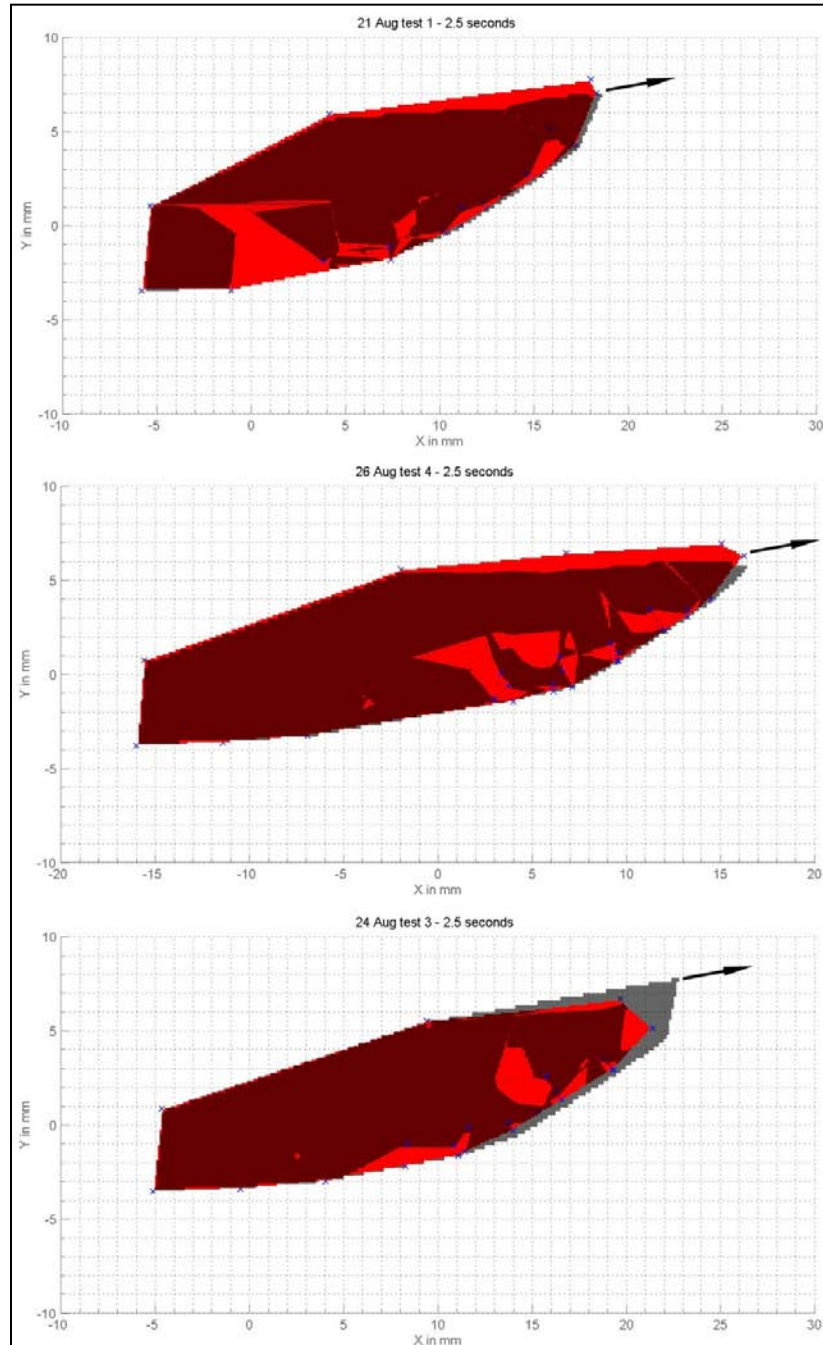


Figure 91: Surface mesh as viewed from above of spherically blunted cone at 10° angle of attack after 2.5 seconds from top to bottom: 19.1 nsia. 36.8 nsia. and 42.8 nsia

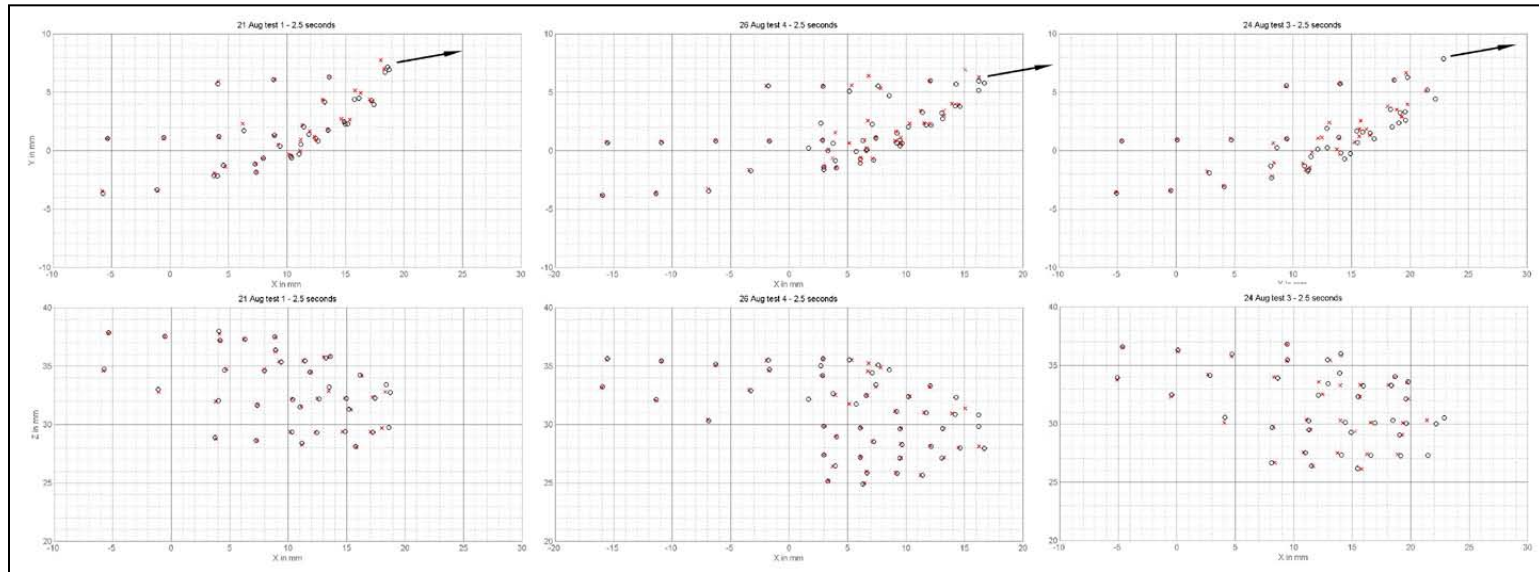


Figure 92: Point cloud of spherically blunted cone viewed from above (top) and the side (bottom) at 10° angle of attack after 2.5 seconds from left to right: 19.1 psia, 36.8 psia, and 42.8 psia

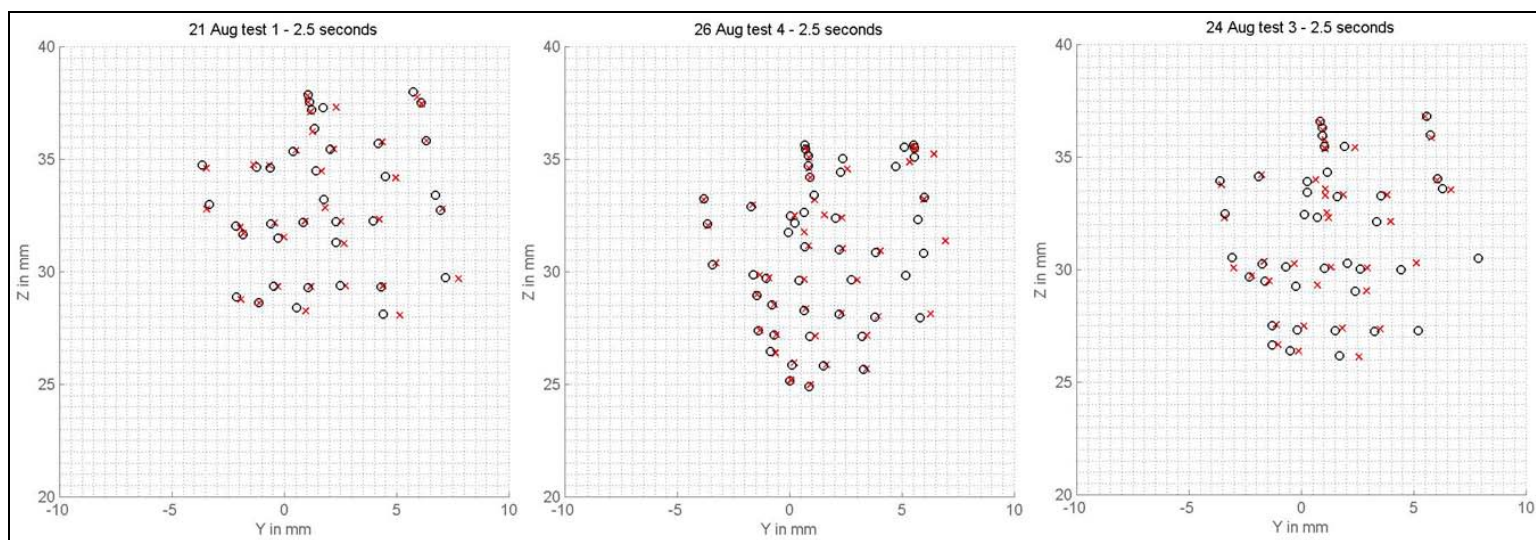


Figure 93: Point cloud of spherically blunted cone viewed from front at 10° angle of attack after 2.5 seconds from left to right: 19.1 psia, 36.8 psia, and 42.8 psia

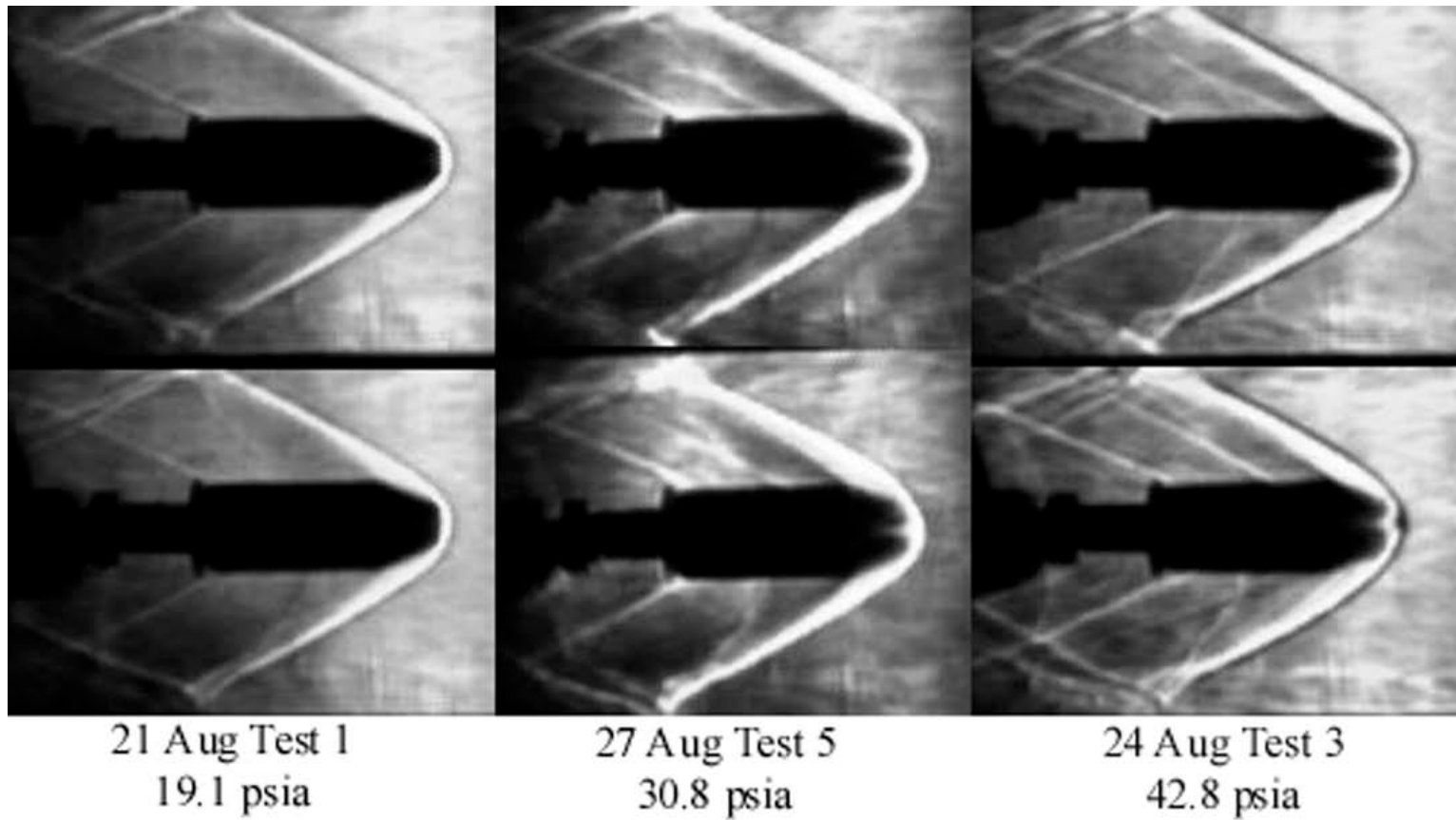


Figure 94: Schlieren imaging of spherically blunted cone at 10° angle of attack at $t = 0$ s (top images) and $t = 2.5$ s (bottom images) from left to right: 19.1 psia, 30.8 psia, and 42.8 psia

4.9.2 Spherically Blunted Cylinder

The next test case was the spherically blunted cylinder at 10° angle of attack represented in tests 21 Aug Test 3 ($P_o = 19.2$ psia) and 26 Aug Test 6 ($P_o = 36.7$ psia). Test conditions for these tests are shown in Table 26.

Table 26: Test conditions for 21 Aug Test 3 and 26 Aug Test 6

Test Name	(psia)	(psia)	(kg/m ³)	Re/x (1/m)
21 Aug Test 3	19.2	0.53	0.116	9.47E+06
26 Aug Test 6	36.7	1.09	0.239	19.4E+06

Figure 95 presents a surface rendering of the top down view (left) and side profile view (right) of the two tests. As with previous images, the red shading represents the surface at the present time step ($t = 2.5$ s) while the black surface is the original shape. Also as with previous figures, arrows have been added to the figures to illustrate the actual position of the nose as well as the body axis. The top images show the lower pressure test, 21 Aug Test 3, and illustrate the ablation. Surface rendering of the higher pressure run is difficult due to the limited data collection of the port side of the nose area which created false anomalies in the surface rendering, especially for the side view.

Figure 96 presents the three-dimensional point cloud in a top down view (left images) and the side profile view (right images) of 21 Aug Test 3, and Figure 97 presents the same for 26 Aug Test 6. Each image has arrows marking the center of the nose and the body axis. Figure 98 presents the forward cross section views of the spherically blunted cylinder tests at $P_o = 19.2$ psia (left image) and $P_o = 36.7$ psia (right image). Again, the circles mark the original position of the points and the red 'x's mark the locations of the points at the indicated time step.

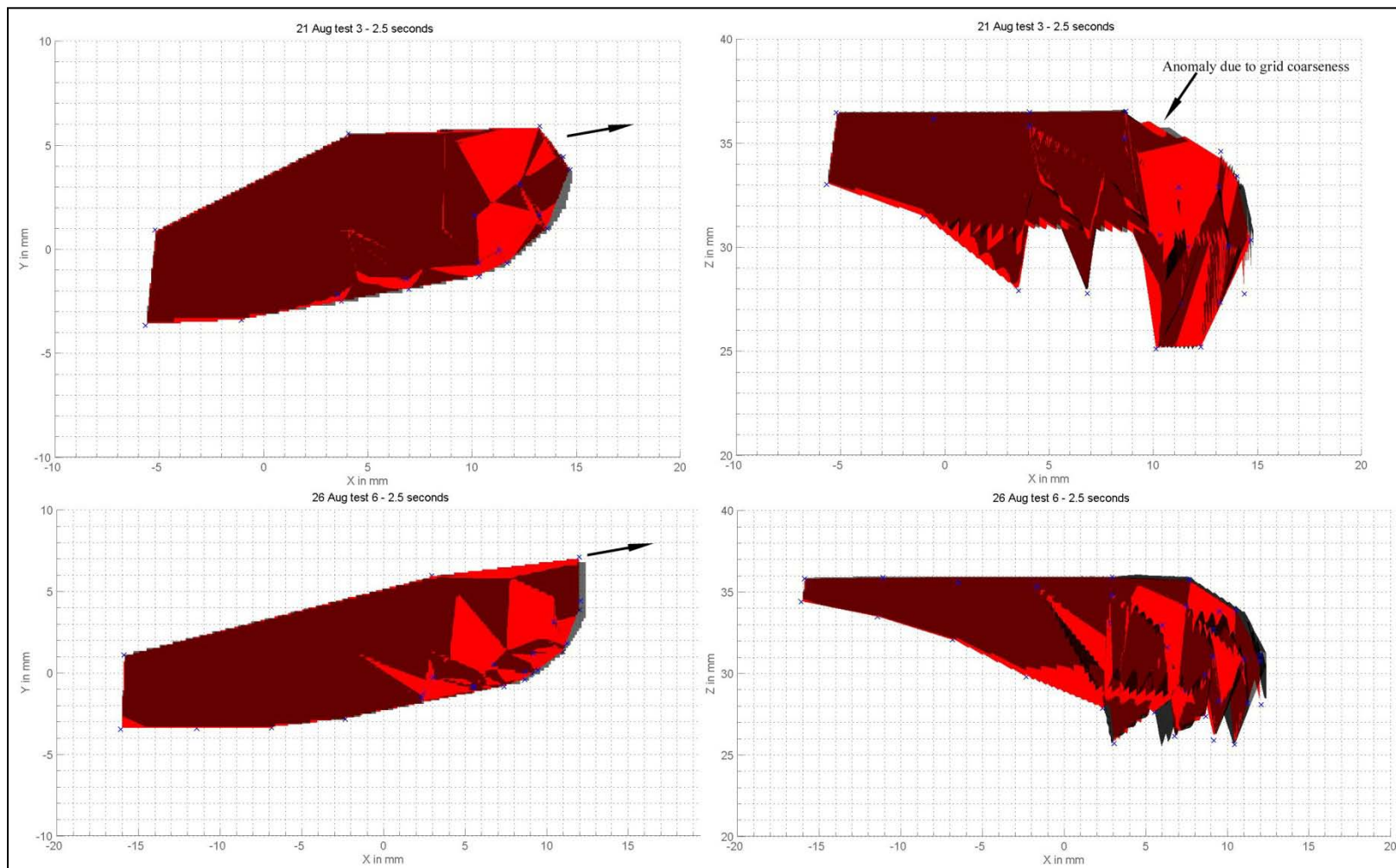


Figure 95: Surface mesh as viewed from above (left) and side (right) of spherically blunted cylinder at 10° angle of attack after 2.5 seconds at $P_0 = 19.2$ psia (top) and 36.7 psia (bottom)

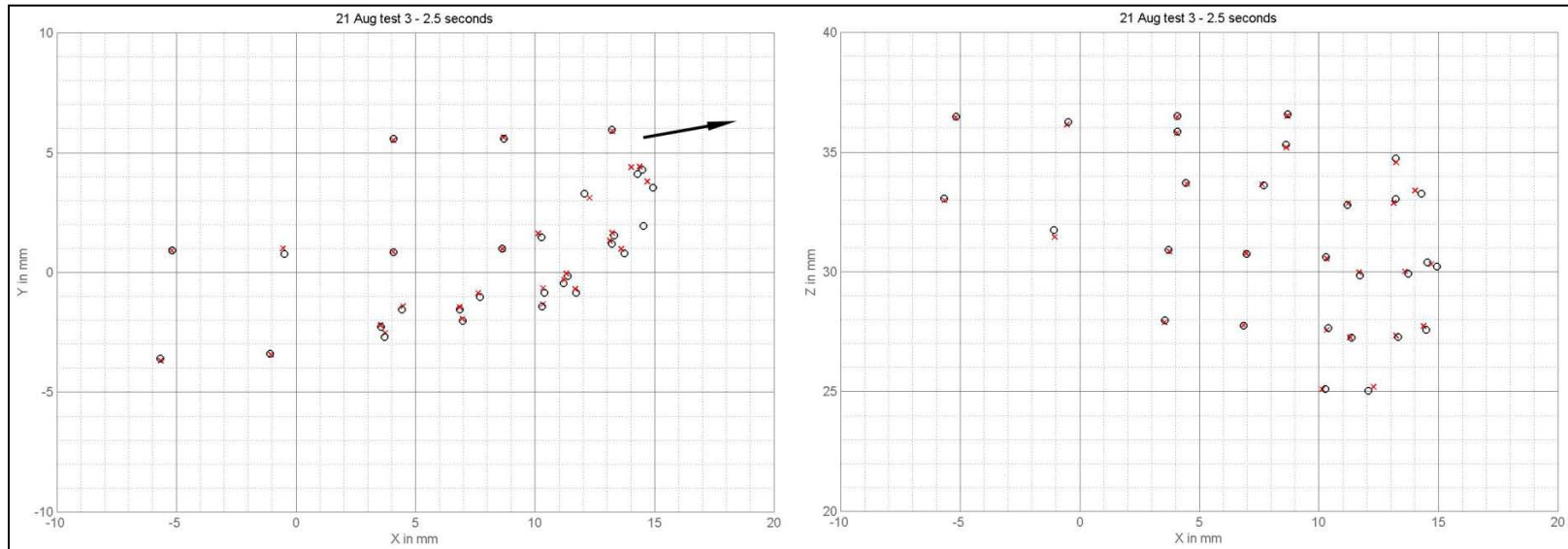


Figure 96: Point cloud as viewed from above (left) and side (right) of spherically blunted cylinder at 10° angle of attack after 2.5 seconds at $P_o = 19.2$ psia

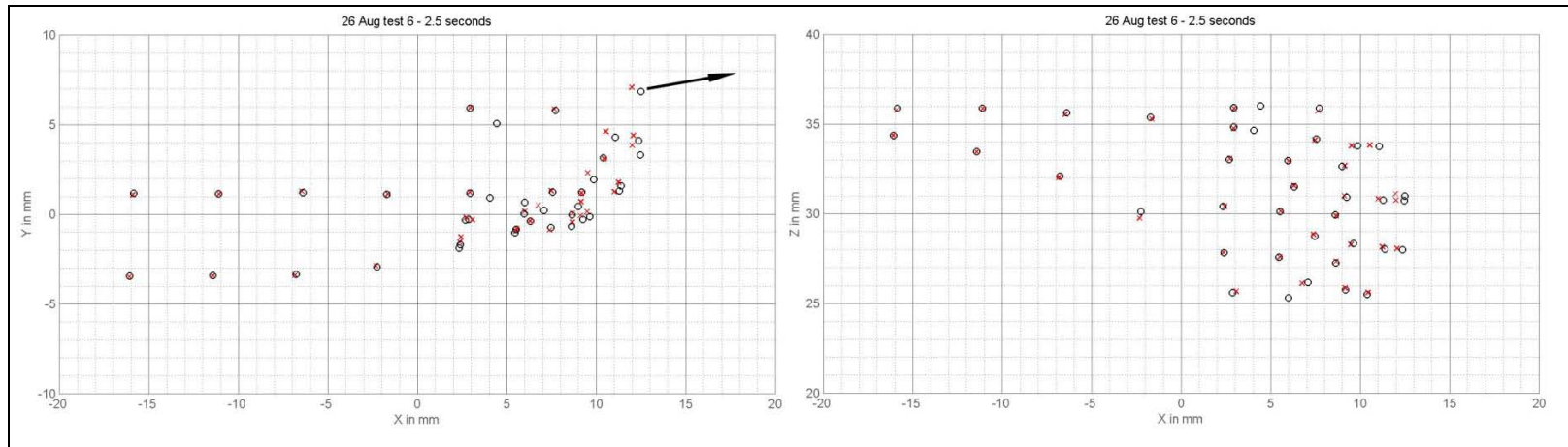


Figure 97: Point cloud as viewed from above (left) and side (right) of a spherically blunted cylinder at 10° angle of attack after 2.5 seconds at $P_o = 36.7$ psia

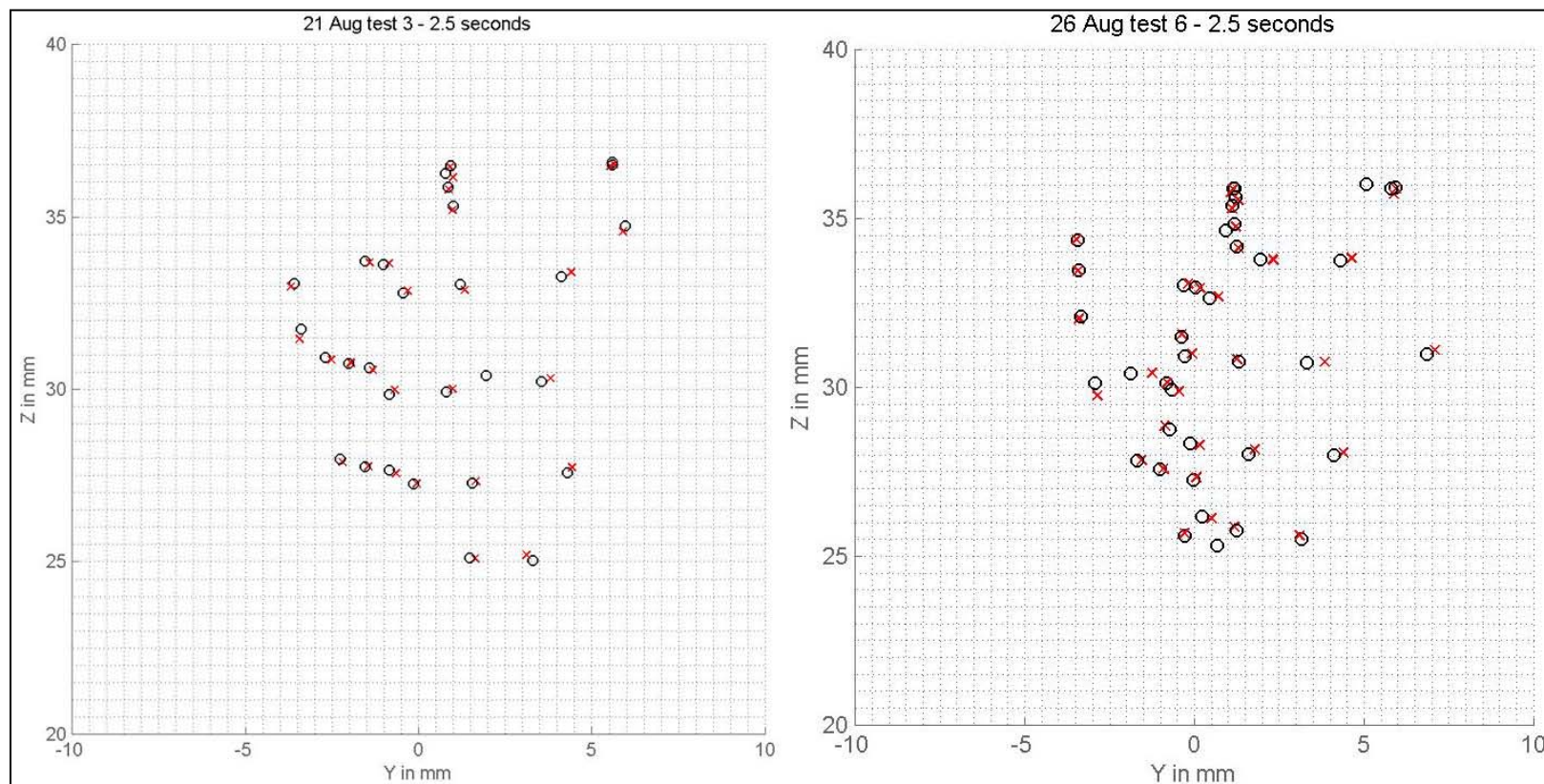


Figure 98: Point cloud as viewed from front of a spherically blunted cylinder at 10° angle of attack after 2.5 seconds at $P_0 = 19.2$ psia (left) and 36.7 psia (right)

Figure 99 provides the Schlieren images at $t = 0$ seconds (top) and $t = 2.5$ seconds (bottom) of the spherically blunted cylinder tests 21 Aug Test 3 and 24 Aug Test 1 for visual comparisons. Again, it should be noted that the angle of rotation is normal to the image plane. As the case with the 10° spherically blunted cone, Schlieren imaging was unavailable for 26 August tests. 24 Aug Test 1 is included in Figure 99 as visualization for a test in a higher stagnation pressure range.

Both the spherically blunted cone and the spherically blunted cylinder data sets at 10° AOA show signs of higher ablation rates on the windward side of the model. While a more thorough analysis of the effects of AOA is desirable, this demonstrates the value of the technique developed for this research.

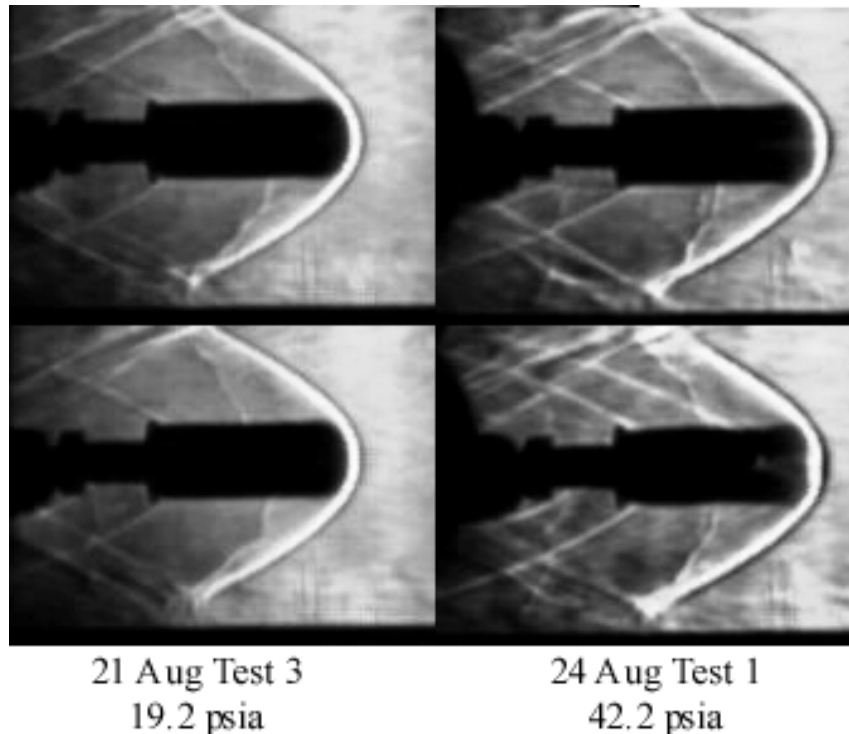


Figure 99: Schlieren imaging of spherically blunted cylinder at 10° angle of attack after 2.5 seconds at 19.2 psia (left) and 42.2 psia (right)

4.9.3 Shock Interactions

Included in this section is a comparison of the shock interactions from the side wall in the wind tunnel test section at the various angles of attack. Figure 100 presents the comparison of Schlieren images for a spherically blunted cylinder at 0° , 5° , and 10° angles of attack presented left to right at similar high stagnation pressures with the angle of rotation normal to the image plane. A white arrow has been inserted to highlight the reflected shock from the wind tunnel wall.

As the angle of attack increased, the reflected shock moved forward in the tunnel as would be expected. At the 15° angle of attack position (not shown), the reflected shock visibly interacted with the rear of the spherically blunted cylinder models. This interaction led to rapid structural failure of the models, so this research focused exclusively on the 0, 5, and 10 degree cases.

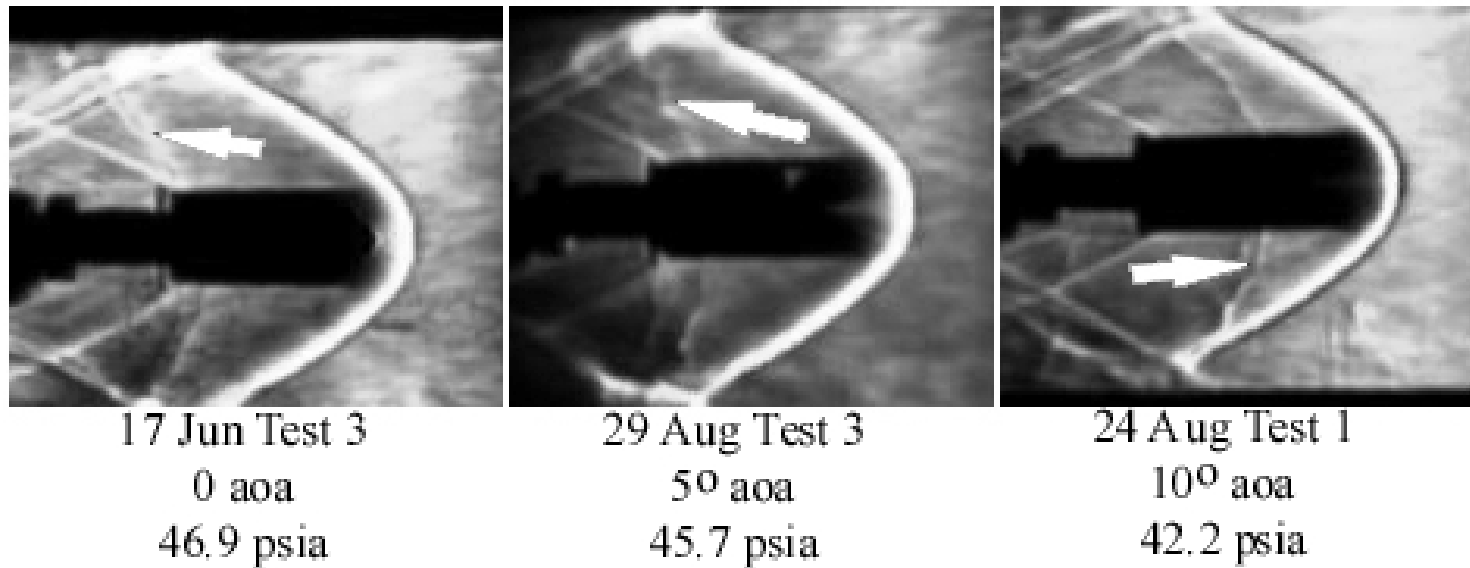


Figure 100: Schlieren imaging of a spherically blunted cylinder at 0°(left), 5°(center), and 10°(right) angles of attack at high stagnation pressures

5. Analysis of Results

A key interest of the hypersonic research community is the correlation between the experimental data and computational models. The sponsor of this research, AFRL/RBAC, is specifically interested in assessing the performance of a commercial code that combines an ablative and flow field solver. This code is referred to as ACFD. One goal of this research was to validate the performance of the code for a low temperature, nominally Mach 3 environment.

ACFD is described in Sections 2.6 and 3.4. This software is licensed and operated by AFRL/RBAC. The author of this dissertation provided the input conditions to Dr. Ryan Gosse at AFRL/RBAC. Dr. Gosse arranged the operating conditions of the wind tunnel and the characteristics of solid dry ice into input decks, built the grid, executed the code and provided the author with the outputs of ACFD. The author was trained on how the software operated and on the form and content of the input deck but did not directly execute the code.

Initial data did not match the ACFD results, as documented in (Gosse, Callaway, Reeder, Nompelis, & Candler, 2009). After repeatability was established in the experimental results, the computational method was reviewed, and modifications were made to the input settings for the code in order to improve boundary layer calculations and material solver properties to produce the results presented here. The most important issue, which was resolved, was that the influence of the gaseous CO₂ sublimation product on the behavior of the near wall fluid was not properly taken into account in these initial

computational runs. These changes in the settings were overseen by Dr. Ryan Gosse after consultation with Professor Graham Candler, who co-authored the ACFD code.

All comparisons are performed for Mach 2.94 and $T_o = 292$ K while stagnation pressure was varied. In order to compare the results of experimental tests to the ACFD results, the experimental test conditions were used as the input conditions for the ACFD solver. In this chapter, the spherically blunted cone and spherically blunted cylinder experimental results for zero angle of attack are compared to the ACFD output. Computations involving these and other shapes at angle of attack are planned to be performed in the near future.

In the literature, quantitative recession data is generally confined to the stagnation region of the test article. To stay in this theme, the quantitative comparisons made in this chapter are primarily for points near the nose of the test article.

5.1 Spherically Blunted Cone at 0 Angle of Attack

Presented in this section is a comparison of the results of the ACFD code and experimental results for a spherically blunted cone at zero angle of attack. The model shape is a spherically rounded 20° half-angle cone merged to the end of a 0.6 inch diameter, 1.2 inch long cylinder.

5.1.1 Spherically Blunted Cone at 0 Angle of Attack, $P_o = 6.1$ psia

A comparison of the ACFD and experimental nose recession rates for a spherically blunted cone at zero angle of attack and nominally 6.1 psia stagnation

pressure is compared in Figure 101. The ACFD result is shown in red, and the experimental results, presented earlier in Figure 53, are represented by tests 2 Jun Test 6, 2 Jun Test 7, 2 Jun Test 8, and 2 Jun Test 9.

Figure 101 illustrates the ACFD predicted recession rates of a point near the nose with the experimental results of four tests near 6.1 psia stagnation pressures, and all the cases match up well. The average recession rate of each test was determined by a least squares best fit curve and is compared with the ACFD projected result in Table 27. The largest difference between experimental and computational in these four cases at 6.1 psia stagnation pressure was 7.3% in test 2 Jun Test 7, while the closest results were within 1.6% of agreement in test 2 Jun Test 9. For comparing experimental results with theoretical predictions for such a complex problem, these relations are in excellent agreement.

Table 27: Comparison of nose recession in ACFD and experimental tests of a spherically blunted cone at zero angle of attack and 6.1 psia stagnation pressure

Test Name	Average Recession Rate (mm/s)	Comparison with ACFD (% Difference)
2 Jun Test 6	0.115	6.5
2 Jun Test 7	0.132	7.3
2 Jun Test 8	0.118	4.1
2 Jun Test 9	0.121	1.6
CFD - 6.1 psia	0.123	--

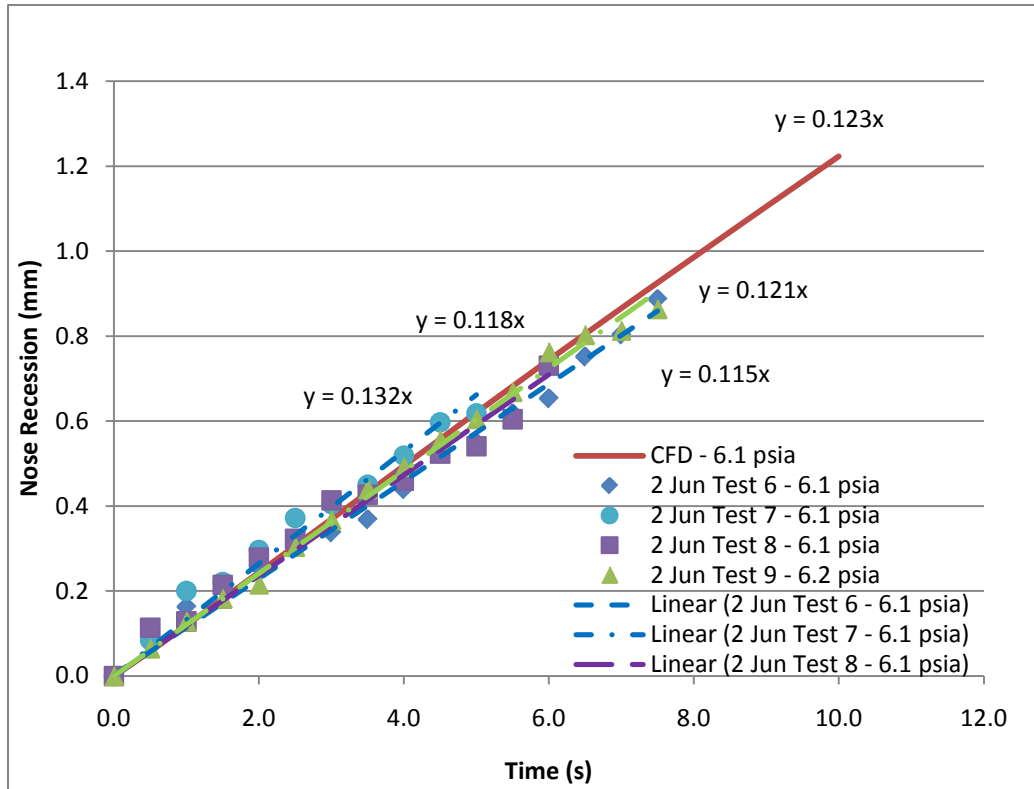


Figure 101: Comparison of nose recession in ACFD and experimental tests of a spherically blunted cone at zero angle of attack and 6.1 psia stagnation pressure

5.1.2 Spherically Blunted Cone at 0 Angle of Attack, $P_o = 23.0$ psia

A comparison of the ACFD and experimental recession rates at the nose of a spherically blunted cone at zero angle of attack and nominally 23.0 psia stagnation pressure is compared in Figure 102. The ACFD result is shown in red, and the experimental results are represented by tests 9 Jun Test 1 and 9 Jun Test 2.

Visual inspection shows that the 9 Jun Test 1 case matches the ACFD predictions closely while the test case 9 Jun Test 2 deviates slightly in the first second of the test, but the recession rate appears to parallel the ACFD predictions after the first second. The average recession rate of each test was determined by a least squares best fit curve and is

compared with the ACFD results in Table 28. The average recession rate for the 9 Jun Test 2 case proved higher than predicted, so a second trend line was created for 9 Jun Test 2 after the first second of the test. This trend line is shown in yellow in Figure 102 and is included in Table 28.

The full 9 Jun Test 2 case has the largest difference between experimental and ACFD results at 24.3%; however, when just taking into account data acquired after one second, the difference is only 1.7%. As was discussed previously in Section 3.2.4, the higher pressure tests showed some lag to reaching steady state conditions, and this variance may be attested to that observation. The 9 Jun Test 1 case only produced a difference of 4% from the computations.

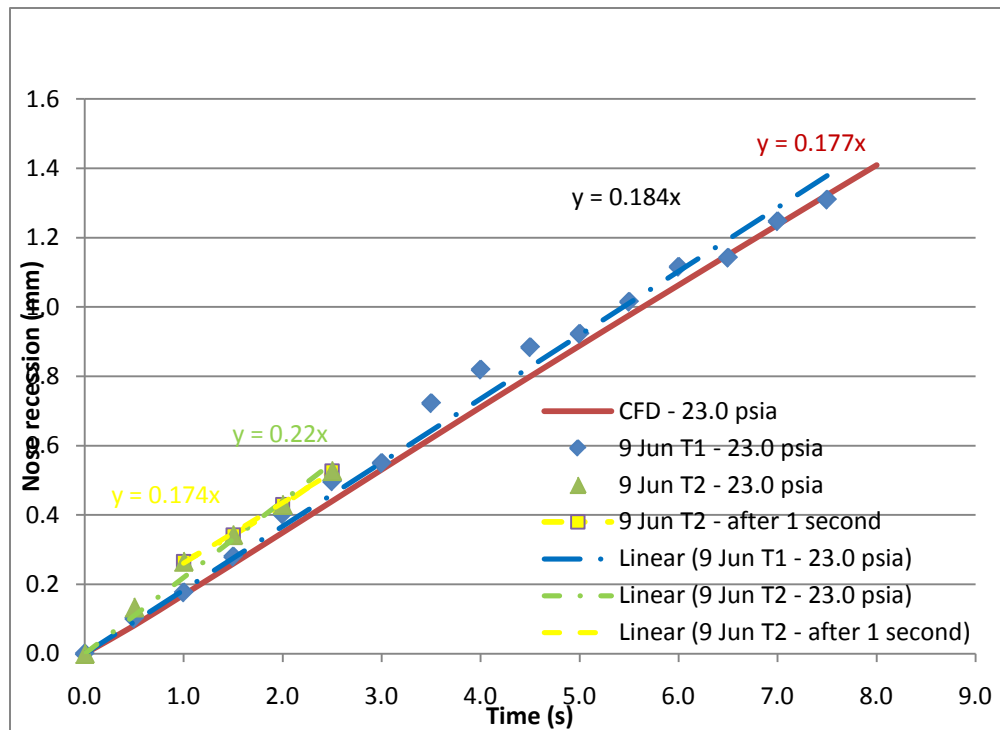


Figure 102: Comparison of nose recession in ACFD and experimental tests of a spherically blunted cone at zero angle of attack and $P_o = 23.0$ psia stagnation pressure

Table 28: Comparison of nose recession in ACFD and experimental tests of a spherically blunted cone at zero angle of attack and $P_o = 23.0$ psia

Test Name	Average Recession Rate (mm/s)	Comparison with ACFD (% Difference)
9 Jun Test 1	0.184	4.0
9 Jun Test 2	0.220	24.3
9 Jun Test 2 (after 1 second)	0.174	1.7
CFD – 23.0 psia	0.177	--

The 23.0 psia stagnation case also provides an excellent example of the ability to model and capture more than just the stagnation point using the photogrammetric technique. Figure 103 illustrates a visual comparison of ACFD and experimental results at 6.5 seconds into the test. The image is a surface mesh image of the test 9 Jun Test 1 as viewed from above with an ACFD cross section overlaid onto the top portion of the figure for comparison. Due to symmetry, for this zero angle of attack experiment, one would expect the top and bottom of the model to mirror images of one another. As in previous representations, the black shaded area is the original surface position and the red area is the surface after 6.5 seconds. The ACFD image provides two lines, the outer being the original modeled surface, and the inner being the surface position at 6.5 seconds. Indeed, the profiles of the computed and measured ablated surface are closely aligned.

It is worth pointing out the ‘necking down’ result seen in the ACFD output at the transition point from the blunted nose to the cone (labeled in Figure 103). This feature is difficult to see but present in raw images, and as in previous results, the grid is too coarse to pick up the feature. If a denser grid is used in future work, this feature may be captured.

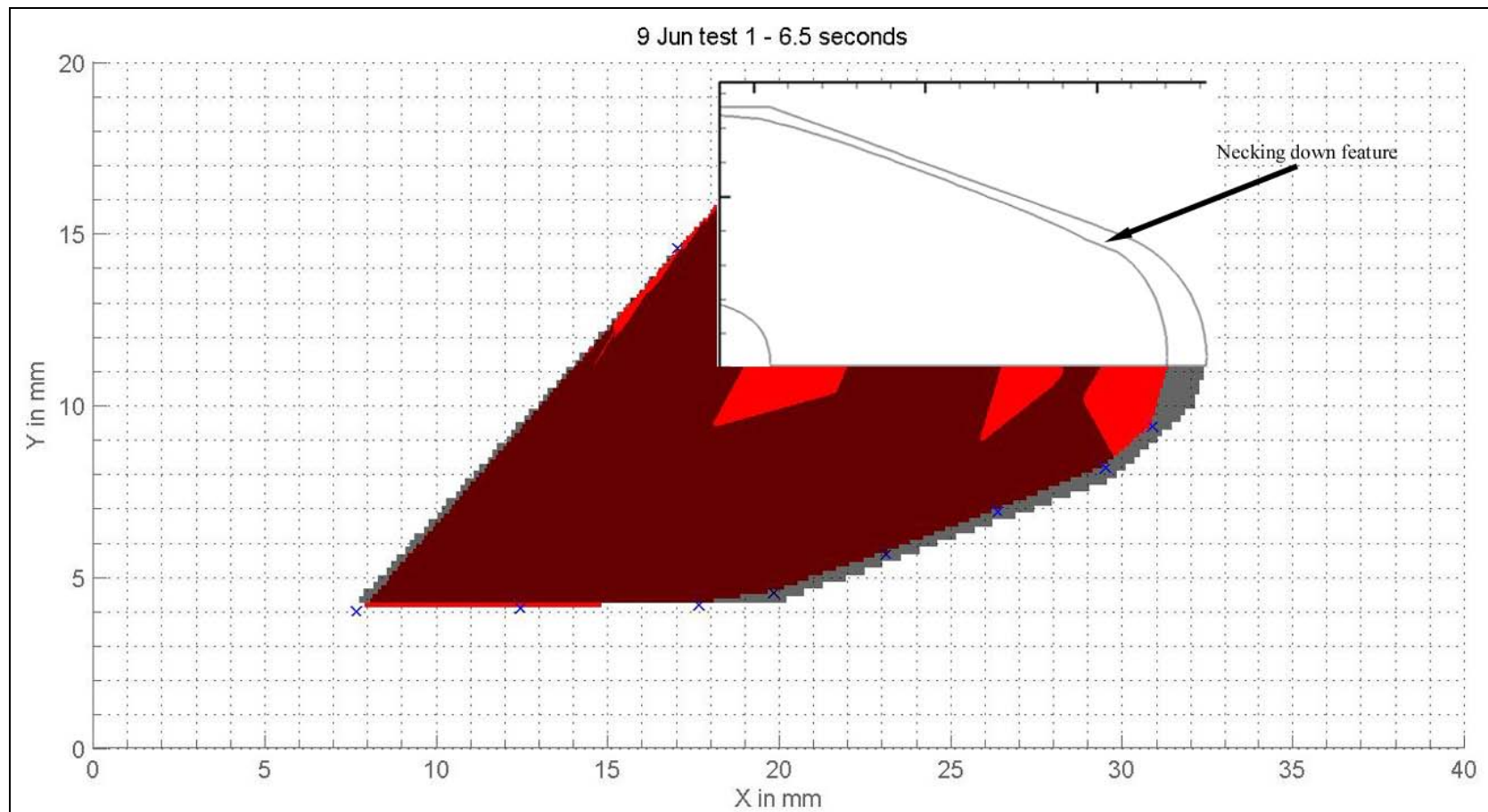


Figure 103: Visual comparison of ACFD to experimental result for spherically blunted cone at 23.0 psia stagnation pressure after 6.5 seconds

5.1.3 Spherically Blunted Cone at 0 Angle of Attack, Multiple Stagnation Pressures

For comparison of a spherically blunted cone at zero angle of attack, the ACFD test conditions were matched to the experimental test conditions of tests 2 Jun Test 9 ($P_o = 6.1$ psia), 9 Jun Test 1 ($P_o = 23.0$ psia), and 15 Jun Test 4 ($P_o = 35.4$ psia). The experimental results of these tests were combined with the computational results and graphed in Figure 104. Visual inspection shows that all the cases match up well. The average recession rate of each test was determined by a least squares best fit curve and is compared with the ACFD projected result in Table 29. A linear trend for recession at the stagnation point is typical, as documented by (Charwat, 1968) among others.

Table 29: Comparison of nose recession in ACFD and experimental tests of a spherically blunted cone at zero angle of attack and $P_o = 6.1, 23.0$, and 35.4 psia

Test Name	Average Recession Rate (mm/s)	CFD Recession Rate (mm/s)	Comparison with ACFD (% Difference)
2 Jun Test 9 – 6.1 psia	0.121	0.123	1.6
9 Jun Test 1 – 23.0 psia	0.184	0.177	4.0
15 Jun Test 4 – 35.4 psia	0.182	0.192	5.2

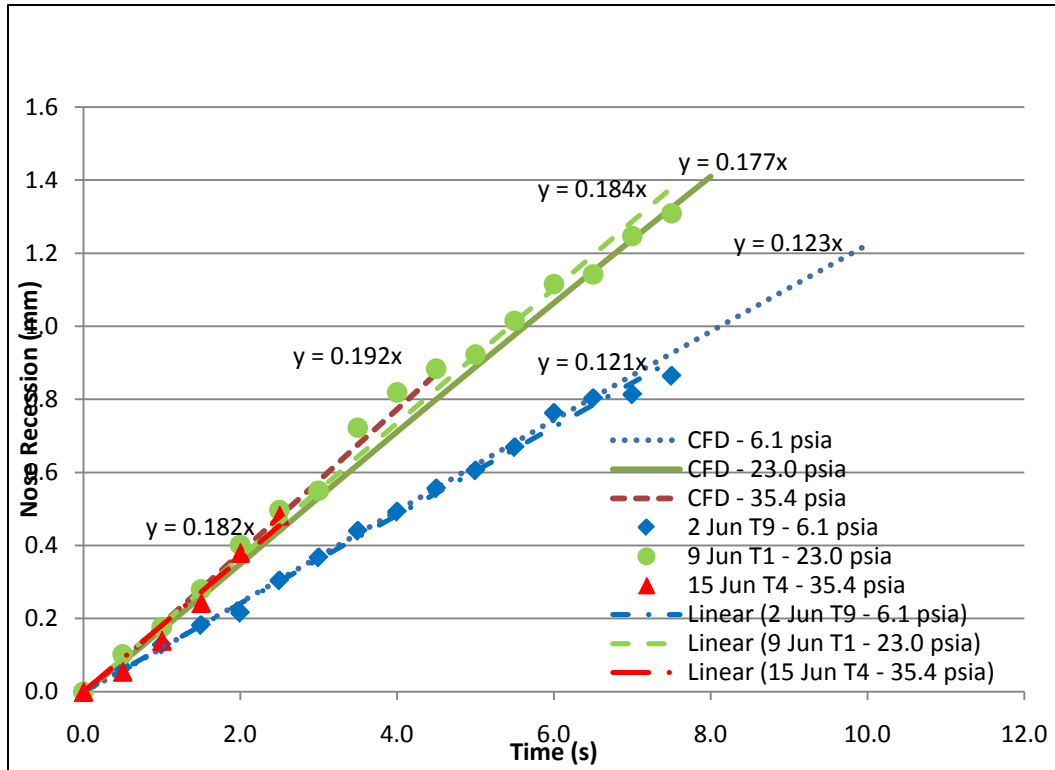


Figure 104: Comparison of nose recession rates of ACFD experiments and experimental tests for a spherically blunted cone at zero angle of attack with $P_o = 6.1, 23.0,$ and 35.4 psia

The 2 Jun Test 9 ($P_o = 6.1$ psia) was within 1.6% of agreement with the ACFD prediction, and the 9 Jun Test 1 ($P_o = 23.0$ psia) was only different by 4%. 15 Jun Test 4 ($P_o = 35.4$ psia) had the largest difference of 5.2% to ACFD results.

It is noted that the experimental results for the 9 Jun Test 1 ($P_o = 23.0$ psia) case indicate a slightly higher average recession rate than the 15 Jun Test 4 ($P_o = 35.4$ psia) case. There are at least two possible reasons for this anomaly. First, the 9 Jun Test 1 case is 4% greater than predicted values, while the 15 Jun Test 4 psia case is 5.2% below theoretical values so experimental imprecision could be the culprit. A second possible reason can be seen upon close inspection of the $P_o = 35.4$ psia data near $t = 0$ s. If one only considers the rate for $t > 0.5$ seconds, the recession rate would be 0.219 mm/s.

Even these experimental results agree quite well with the computational predictions. While the level of the agreement is quite good, one might ask whether this holds true for repeated experiments. To this end, the individual conditions listed above are separated and grouped as multiple runs at similar test conditions.

5.2 Spherically Blunted Cylinder at 0 Angle of Attack

This section presents a comparison of the spherically blunted cylinder experimental and ACFD results at zero angle of attack and nominal Mach 2.94. The model shape is a 0.3 inch radius half sphere mated onto a 0.6 inch diameter, 1.2 inch long cylinder shown in Appendix A. Due to instabilities in the grid, the ACFD solver diverged for this shape at approximately eight seconds. The experimental results and the first six seconds of the computation are presented here for comparison.

5.2.1 Spherically Blunted Cylinder at 0 Angle of Attack, $P_o = 7.5$ psia

A comparison of the ACFD and experimental nose recession rates for a spherically blunted cylinder at zero angle of attack and nominally 7.5 psia stagnation pressure is compared in Figure 105. The ACFD result is shown with the solid red line, and the experimental results are represented by tests 19 Jun Test 8 and 19 Jun Test 9. The average recession rate for each test was determined by a linear least squares best fit and is compared with the ACFD projected result in Table 30.

The linear best fit does not match up particularly well with the ACFD prediction. However, on inspecting the experimental data of both cases, the data appears to follow the ACFD portion for the first 2.5 seconds. The average recession rate for the entire 19 Jun Test 8 case had a difference of 18.3% when compared to ACFD results, and test case 19 Jun Test 9 had a difference of 26.7%. Of note is that both cases are over-predicted by the ACFD results and that the two experimental tests follow a similar pattern.

Table 30: Comparison of nose recession in ACFD and experimental tests of a spherically blunted cylinder at zero angle of attack and $P_o = 7.5$ psia

Test Name	Average Recession Rate (mm/s)	CFD Recession Rate (mm/s)	Comparison with ACFD (% Difference)
19 Jun Test 8	0.098	0.120	18.3
19 Jun Test 9	0.088	0.120	26.7

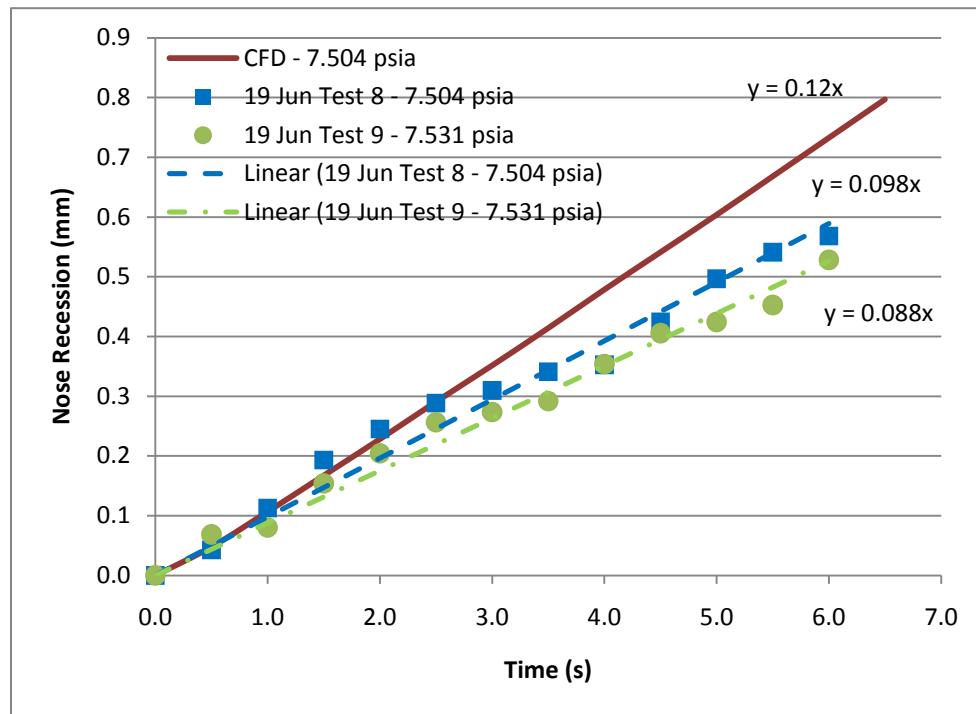


Figure 105: Comparison of ACFD and experimental nose recession for a spherically blunted cylinder at $P_o = 7.5$ psia

5.2.2 Spherically Blunted Cylinder at 0 Angle of Attack, $P_o = 19.5$ psia

A comparison of the ACFD and experimental nose recession rates for a spherically blunted cylinder at zero angle of attack and nominally 19.5 psia stagnation pressure is compared in Figure 106. The ACFD result is shown in red, and the experimental results are represented by tests 19 Jun Test 6 and 19 Jun Test 7.

Figure 106 illustrates the ACFD predicted recession rates of a point near the nose with the experimental results of two experimental test cases at 19.5 psia stagnation pressures. The average recession rate of each test was determined by a least squares best fit curve and is compared with the ACFD projected result in Table 31.

The largest difference between experimental and ACFD predicted results in these test cases at $P_o = 19.5$ psia was 11.5% in test 19 Jun Test 7, while the 19 Jun Test 6 case average recession was within 5.2% of agreement with ACFD results, suggesting good agreement.

Table 31: Comparison of nose recession in ACFD and experimental tests of a spherically blunted cylinder at zero angle of attack and $P_o = 19.5$ psia

Test Name	Average Recession Rate (mm/s)	CFD Recession Rate (mm/s)	Comparison with ACFD (% Difference)
19 Jun Test 6	0.165	0.174	5.2
19 Jun Test 7	0.154	0.174	11.5

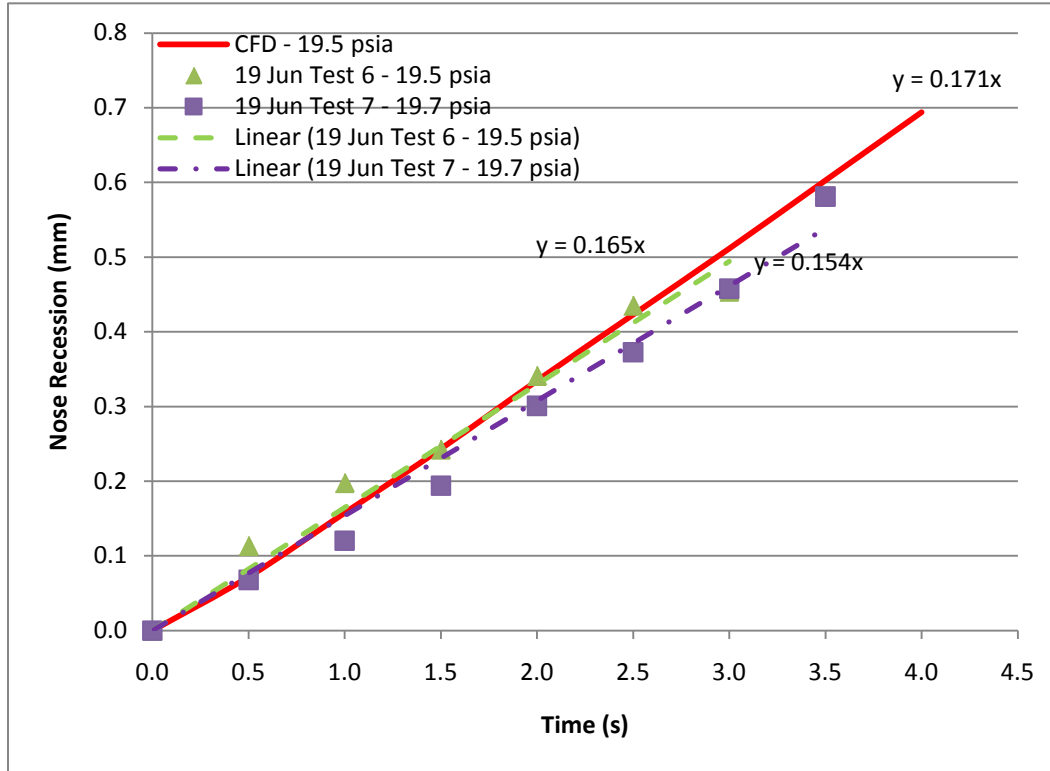


Figure 106: Comparison of ACFD to experimental nose tip recession rates for a spherically blunted cylinder at $P_o = 19.54$ psia

Similarly to the 23.0 psia stagnation case for spherically blunted cone, the 19.5 psia stagnation case was chosen to illustrate a visual comparison of the ACFD and experimental results for a spherically blunted cylinder at 3.5 seconds into the test. The image presented in Figure 107 is a surface mesh image of the test 19 Jun Test 7 as viewed from above with an ACFD cross section overlaid onto the top portion of the figure for comparison. Due to symmetry, for this zero angle of attack experiment, one would expect the top and bottom of the model to mirror images of one another. As in previous representations, the black shaded area is the original surface position and the red area is the surface at $t = 3.5$ seconds. The ACFD image provides two lines, the outer being the

original modeled surface, and the inner being the surface position at 3.5 seconds. Indeed, the profiles of the computed and measured ablated surface are closely aligned.

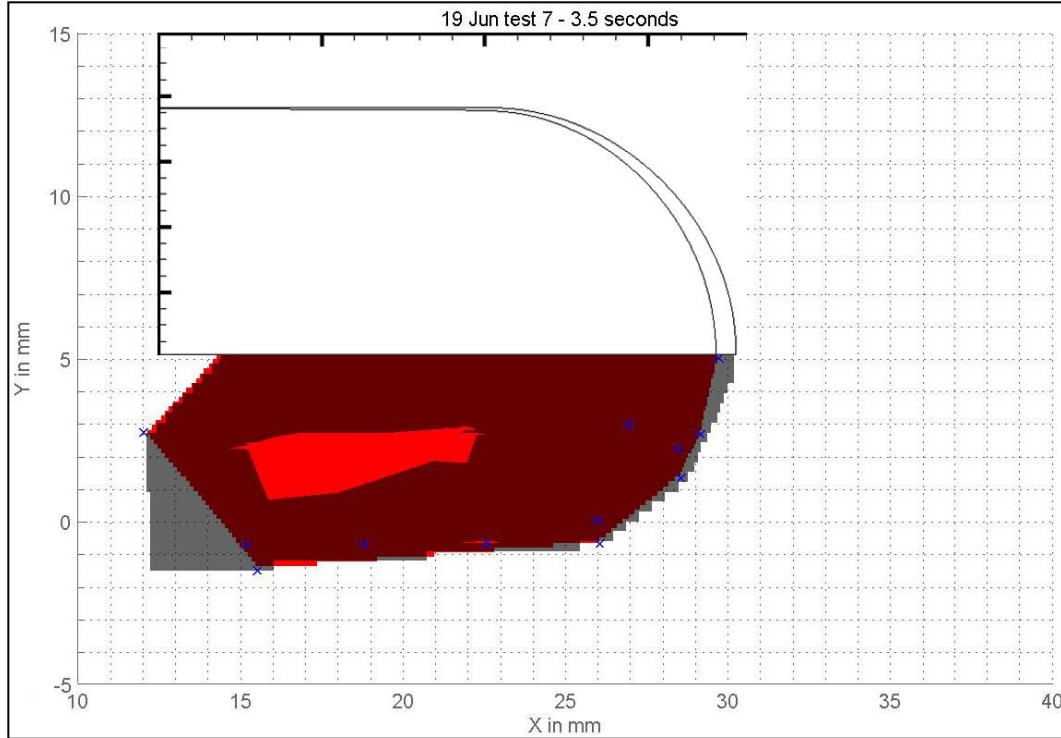


Figure 107: Visual comparison of ACFD to experimental results for spherically blunted cylinder at 19.5 psia stagnation pressure after 3.5 seconds

5.2.3 Spherically Blunted Cylinder at 0 Angle of Attack, $P_o = 37.9$ psia

A comparison of the ACFD and experimental nose recession rates for a spherically blunted cylinder at zero angle of attack and nominally $P_o = 37.9$ psia is compared in Figure 108. The ACFD result is shown in red, and the experimental results are represented by tests 19 Jun Test 2 and 19 Jun Test 3. The average recession rate of each test was determined by a least squares best fit curve and is compared with the ACFD projected result in Table 32. As mentioned in Section 3.2.4, the higher pressure tests

tended to take longer to reach steady state, and the 19 Jun Test 3 test is a good example of this. If the first half second is neglected as tunnel initiation delay, the recession rates match up very well with ACFD results. The largest difference in these cases between experimental results and ACFD predicted results in these test cases was 2.5% in test 19 Jun Test 3, while the 19 Jun Test 2 case's average recession was exceptionally close to the ACFD results.

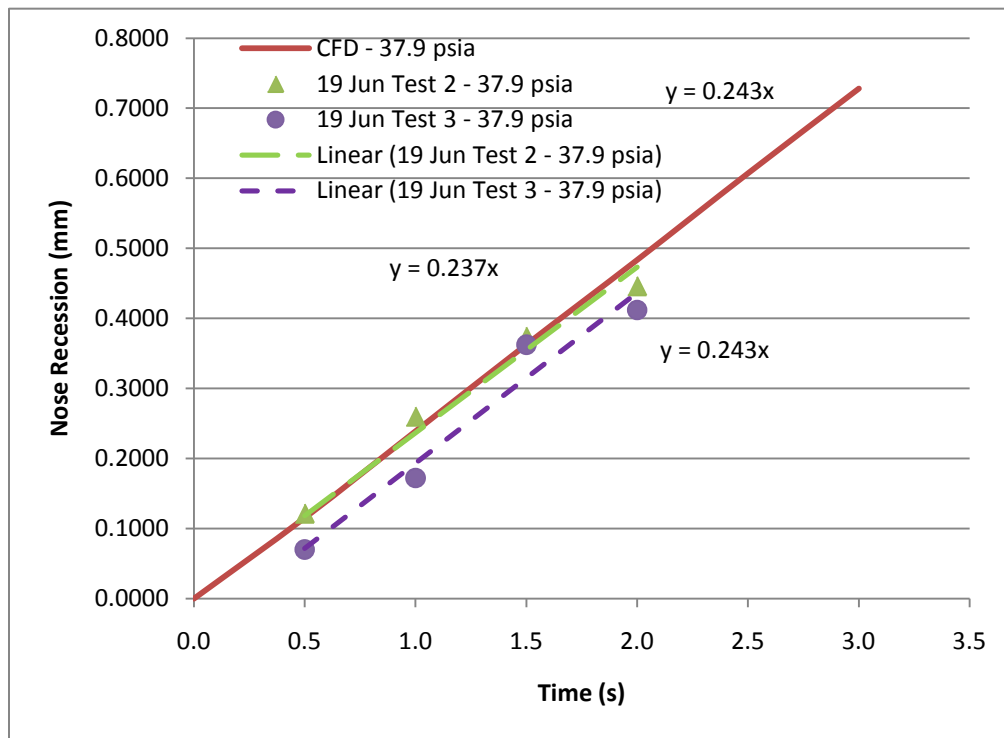


Figure 108: Comparison of ACFD to experimental nose tip recession for a spherically blunted cylinder at $P_0 = 37.9$ psia

Table 32: Average difference comparison between experimental and ACFD results for a spherically blunted cylinder at $P_0 = 37.9$ psia

Test Name	Average Recession Rate (mm/s)	CFD Recession Rate (mm/s)	Comparison with ACFD (% Difference)
19 Jun Test 2	0.237	0.243	2.5
19 Jun Test 3	0.243	0.243	0

5.2.4 Spherically Blunted Cylinder at 0 Angle of Attack, Multiple Stagnation Pressures

The ACFD predicted nose recession rates for a spherically blunted cylinder at zero angle of attack at was compared to the experimental test conditions of tests 19 Jun Test 8 ($P_o = 7.5$ psia), 19 Jun Test 6 ($P_o = 19.5$ psia), and 19 Jun Test 2 ($P_o = 37.9$ psia). The experimental results of these tests were combined with the ACFD results and graphed in Figure 109. Visual inspection shows that all the cases match up well. The average recession rate of each test was determined by a least squares best fit curve and is compared with the ACFD projected result in Table 33.

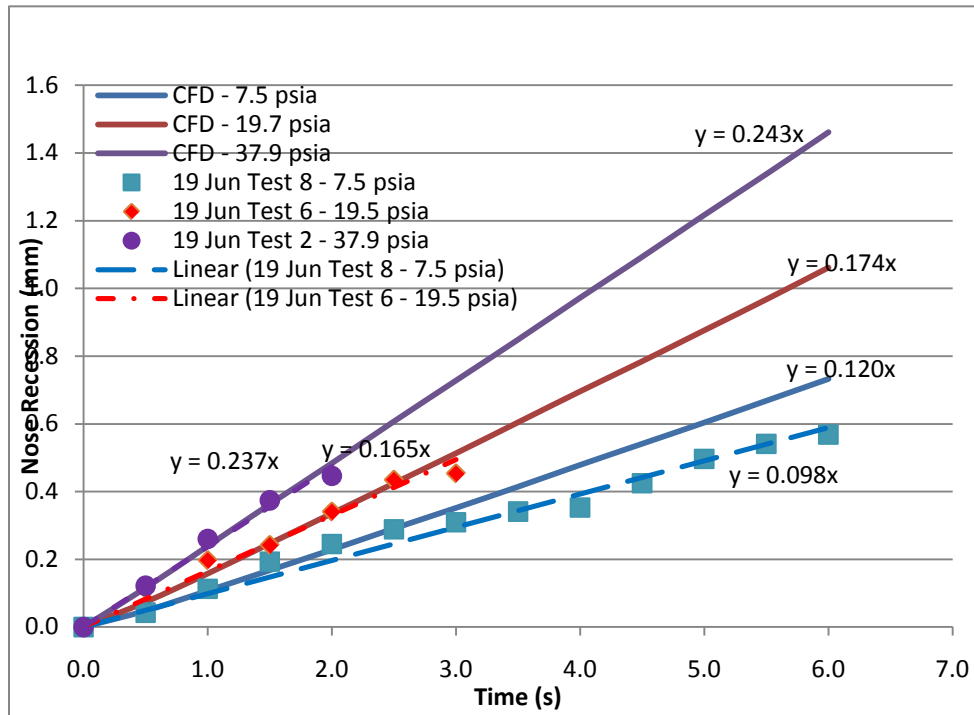


Figure 109: Comparison of ACFD and experimental nose recession for a spherically blunted cylinder at $P_o = 7.5, 19.7, \text{ and } 37.9$ psia

The best agreement was found with the higher pressure $P_o = 37.9$ psia test case which was within 2.5% of the ACFD output. The largest difference between experimental and computational results in these cases was 18.3 % in the $P_o = 7.5$ psia case. However, as previously, a portion of the experimental data, this time the first 2.5 seconds appears visually to parallel the ACFD results. When only these first 2.5 seconds of data are used, the difference with the ACFD output is only 0.8%.

While the level of the agreement is good, one might ask whether this holds true for repeated experiments. To this end, the individual conditions above are separated and compared to multiple runs at similar test conditions.

Table 33: Comparison of nose recession in ACFD and experimental tests of a spherically blunted cylinder at zero angle of attack and $P_o = 7.5, 19.5, 27.9$ and 37.9 psia

Test Name	Average Recession Rate (mm/s)	CFD Recession Rate (mm/s)	Comparison with ACFD (% Difference)
19 Jun Test 8 - 7.5 psia	0.098	0.12	18.3
19 Jun Test 8 – Initial 2.5 seconds	0.119	0.12	0.8
19 Jun Test 6 - 19.5 psia	0.165	0.174	5.2
19 Jun Test 2 - 37.9 psia	0.237	0.243	2.5

5.3 Relation to Real World Effects

An objective of this research is to relate the results of low temperature ablation to more real world conditions. There are some limitations as the flow is only supersonic, not hypersonic, and thus does not have radiative and dissociative processes occurring in the flow. Also, the ablating body is a pure sublimator, without the charring process. Two areas of interest for relating this data are investigated in this section: stagnation point heating relations and a Buckingham Pi analysis.

5.3.1 Stagnation Point Heating

The analytical solution for the convective heat transfer at the stagnation point of a sphere in a hypersonic flow in chemical equilibrium is described by the widely renowned Fay-Riddell correlation. The development of the solution is given by (Bertin, 1994, pp. 247-256). The outcome of this correlation had a profound effect on the progress of spaceflight in that it was demonstrated that the heat transfer was inversely proportional to the nose radius. This finding, which was counter-intuitive to many at the time, led directly to the Apollo capsule design.

Two of the more commonly used stagnation convective heating rate equations stem from simplification of the Fay-Riddell correlation for a sphere flying through the atmosphere. An expression attributed to Scott, *et al*, (Scott, Ried, & Maraia, 1984) is presented in Equation (29) and a second expression was developed by Sutton and Graves (Sutton & Graves, 1971), which is presented in Equation (30). In Equations (29) and (30), R_N is the radius of the nose, ρ_∞ is the free stream density, U_∞ is the free stream

velocity, and q_c is the convective heat-transfer rate (Bertin, 1994, pp. 256-258). For the experiments presented herein the velocity is nominally the same in each test case.

$$\frac{q_c}{\rho V^2} = \frac{C_h}{2} \quad (29)$$

Equation (29) is described by Bertin as an “engineering correlation” and provides an approximate value used for reentry into the Earth’s atmosphere. Equation (30) was developed by Sutton and Graves in order to determine stagnation heating using a general relation for mixtures of arbitrary gases in chemical equilibrium. Sutton and Graves arrive at values for the heat transfer factor, K , based on a relation for gas mixture viscosity which, in turn, is based on calculation of the viscosity of pure gases from first principles of molecular gas dynamics. The parameters used to calculate predictions of K include molecular weight, the maximum energy of attraction, temperature, molecular collision diameter, and the Boltzmann constant.

$$K = \frac{q_w}{\rho V^2} \quad (30)$$

In the stagnation region of a real-world hypersonic vehicle, the heat transfer rate includes the convective value as represented in Equation (29) and Equation (30), radiative heat to and from the vehicle, the thermal conduction into the vehicle, and chemical reactions and phase changes if present. The rate of heat transferred through sublimation can be calculated directly from the recession rate and heat of sublimation (\dot{m}_s as in Equation (31).

(31)

If the assumption is made that the radiation and conduction is negligible, then heat transfer at the stagnation point would all be absorbed in the sublimation point, and K can be found by substituting Equation (31) into Equation (30). This assumption is certainly valid for radiation effects. Using this technique, the spherically blunted cone and spherically blunted cylinder recession rates were used and averaged over multiple runs and pressures to produce the constants shown in Table 34. The tables used to calculate these constants are available in Appendix E.

Table 34: K constants calculated from results and from Sutton and Graves

Shape	Experimental K constant ($\text{kg s}^{-1} \text{m}^{-1.5} \text{Pa}^{-0.5}$)	ACFD K constant ($\text{kg s}^{-1} \text{m}^{-1.5} \text{Pa}^{-0.5}$)	Standard Deviation
Spherically Blunted Cone	2.64E-04	2.52E-04	2.25E-05
Spherically Blunted Cylinder	3.82E-04	3.70E-04	0.81E-05
Universal Shape Result	3.23E-04	3.11E-04	6.49E-05
K Constant For Air (Sutton & Graves, 1971)	3.50E-04		

Also in Table 34 is presented the heat transfer factor, K , from a Sutton and Graves (Sutton & Graves, 1971) produced table for air. This constant is in very good agreement with the constant calculated from both shapes (8%) and the spherically blunted cylinder shape (9%). The spherically blunted cone has a much higher difference (24%), however, the Fay-Ridell correlation which forms a basis for the Sutton and Graves equation is based on a velocity gradient present for Newtonian flow over spheres and sphere cylinders. It is then expected that the spherically blunted cone would lead to a larger discrepancy from the reported values of K . Due to this expected difference, the majority

of the results discussed in the remainder of this section deal with the spherically blunted cylinder.

Figure 110 presents a comparison of the results of Equation (29) to the results of Equation (31) for the spherically blunted cylinder test articles and test conditions. The data is taken from Table 18. It is apparent that Equation (29) predicts a higher heating rate, allowing that the assumptions stated above are correct; however, the general trend is fairly well represented.

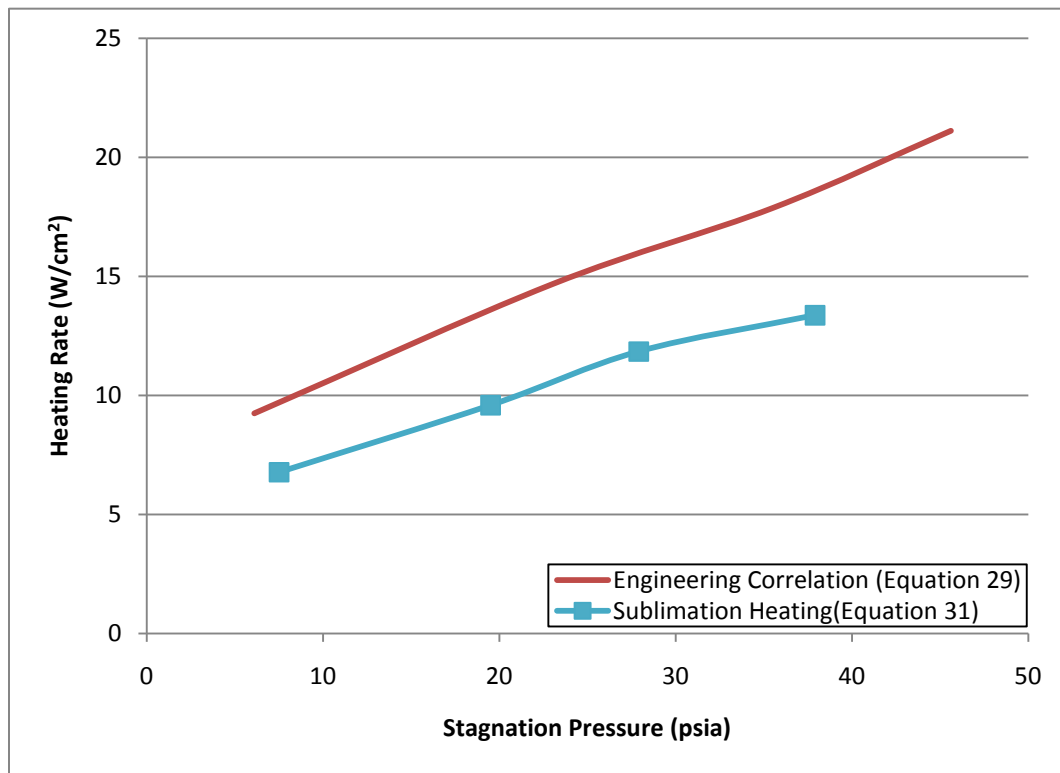


Figure 110: Comparison of Scott, *et al*, and sublimation based heating rates for a spherically blunted cylinder

Since Equation (29) over predicted the experimental results, a constant was calculated to replace the constant of 18,300. Solving in a manner similar to that done for K, the evaluated constants were calculated and were found to be 12,500 for the

spherically blunted cylinder (Equation (32)) and 8,600 for spherically blunted cone models (Equation (33)).

$$\frac{\dot{q}_{\text{rad}}}{\dot{q}_{\text{conv}}} = \frac{1}{2} \left(\frac{1}{\text{Pr}} \right)^{1/4} \left(\frac{1}{\text{Re}} \right)^{1/4} \left(\frac{1}{\text{Ma}} \right)^{1/4} \quad (32)$$

$$\frac{\dot{q}_{\text{rad}}}{\dot{q}_{\text{conv}}} = \frac{1}{2} \left(\frac{1}{\text{Pr}} \right)^{1/4} \left(\frac{1}{\text{Re}} \right)^{1/4} \left(\frac{1}{\text{Ma}} \right)^{1/4} \quad (33)$$

The motivation for posing these two equations was to directly relate the acquired data to a real world application. Following the lead of (Scott, Ried, & Maraia, 1984), all three equations, Equation (29), Equation (32), and Equation (33), were compared against stagnation heating rate data from FIRE II (Cauchon, 1967) as seen in Figure 111.

As stated previously, the conditions of the research presented herein is at too low a Mach number to produce a radiative heating rate from the flow, however, the 11.4 km/s FIRE II has a significant amount of radiative heating. When the radiative heating is taken into account with the FIRE II data (see error bars in Figure 111), the heating rate predicted using the constant found for the spherically blunted cylinder is in reasonably good agreement with experimental results.

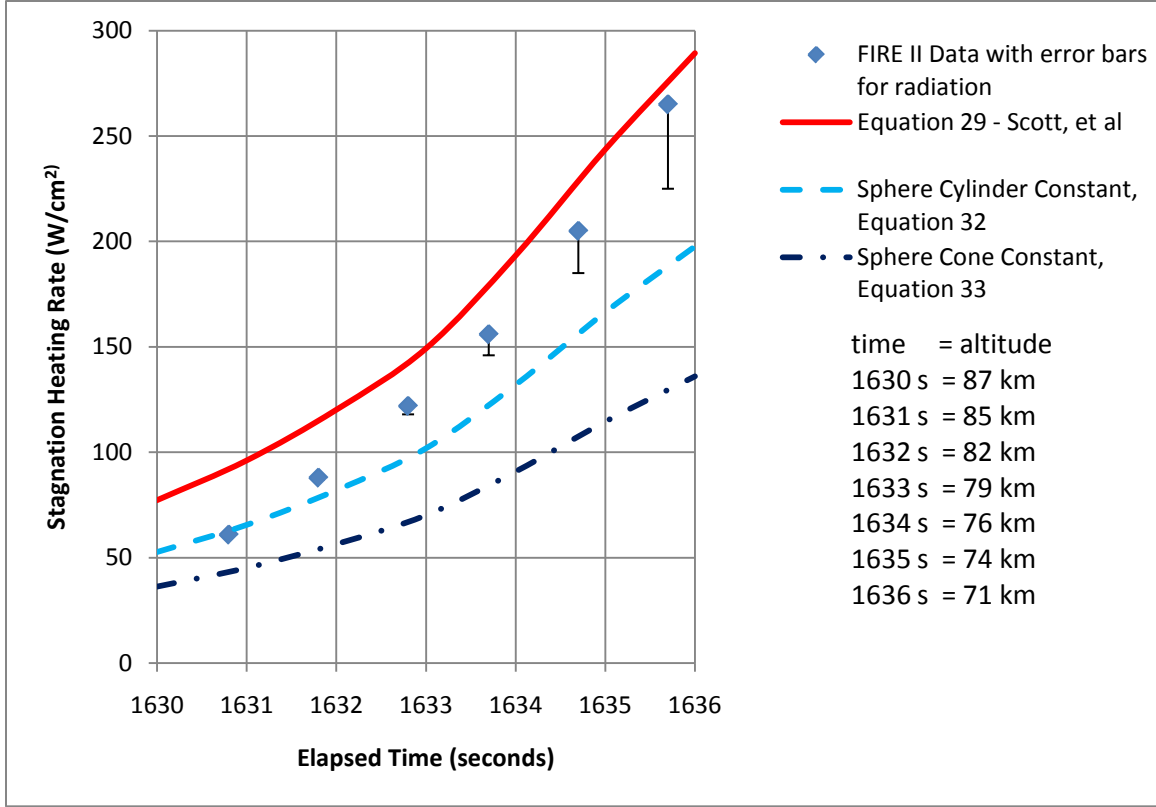


Figure 111: Comparison of Equation 26 to Experimental Projections of FIRE II conditions and FIRE II data points (Cauchon, 1967) (Scott, Ried, & Maraia, 1984)

Another version of Equation (29) is found in (Johnson, 2009) and (Tauber, Menees, & Adelman, 1987) which includes a g_w term which is a ratio of wall enthalpy to total enthalpy. This stagnation point convective heat flux is presented in Equation (34) and assumes an equilibrium flow field where boundary-layer theory is valid.

(34)

For Johnson's work, the g_w term is assumed zero, but in the case of the research presented herein, that assumption cannot be made. Rather g_w varies from 0.59 to 0.65.

Solving Equation (34) for the test conditions of this research produces the curves plotted in Figure 112 and Figure 113. Figure 112 gives a comparison of Equation (34) with actual g_w and $g_w = 0$ to the sublimation determined heating rate of Equation (31), and the modified Scott, *et al*, Equation (33), for the spherically blunted cylinder tests. Equation (34) under predicts the heating rate but has a similar slope and is within the same order of magnitude.

Figure 113 presents a comparison of the Johnson equation with the sublimation determined heating rate of Equation (31), and the modified Scott, *et al*, Equation (32), for the spherically blunted cone tests. In this case, the spherically blunted cone cases match up closer than the spherically blunted cylinder.

These results demonstrate that the heating rates determined from the spherically blunted cylinder case can provide input onto the convective heating rates of real world ablators. The limitation to convective heating rates is only due to the range of wind tunnel operating conditions.

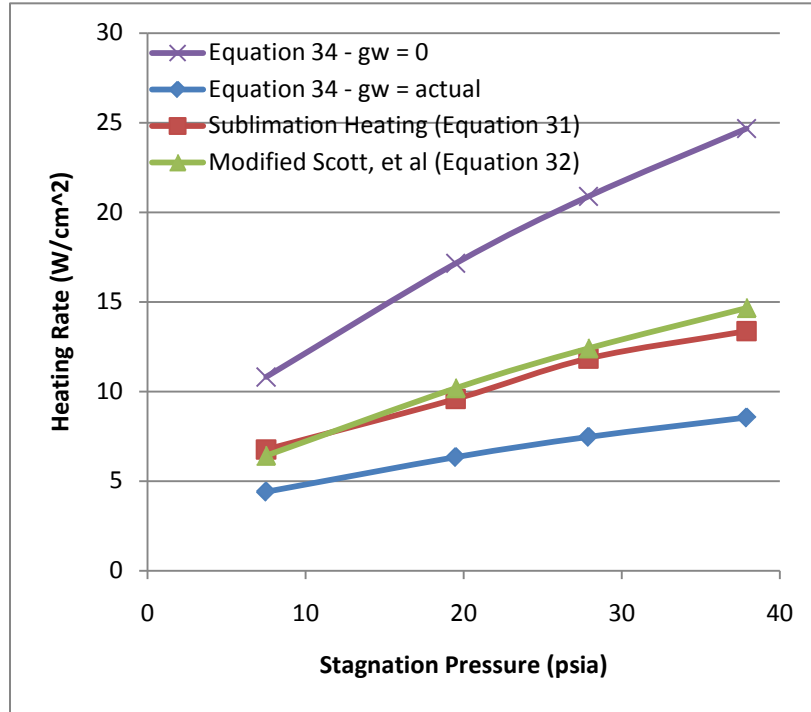


Figure 112: Comparison of heating rates on a spherically blunted cylinder for Johnson, Scott , *et al*, and sublimation based equations

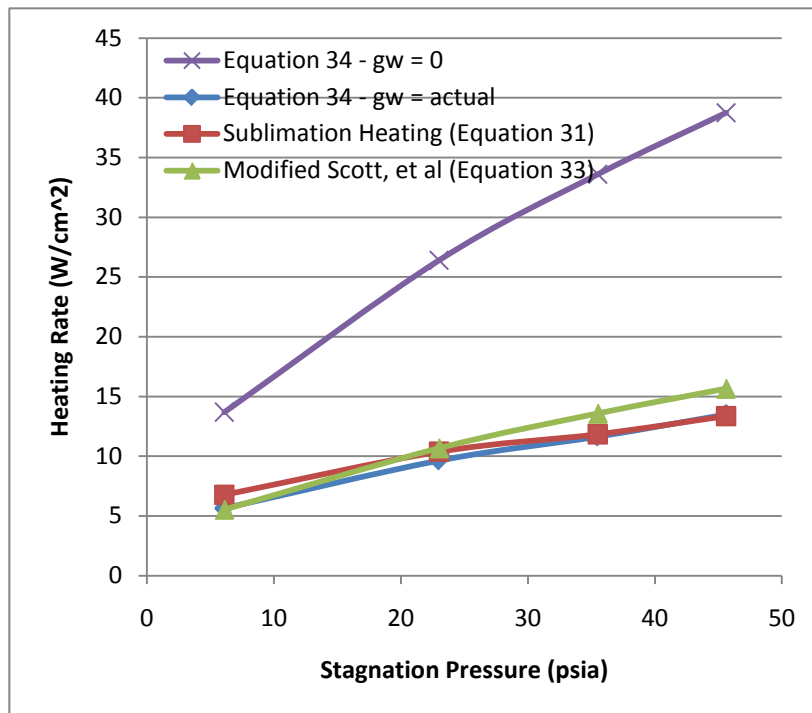


Figure 113: Comparison of heating rates on a spherically blunted cone for Johnson, Scott , *et al*, and sublimation based equations

5.3.2 *Recession Predictions*

Given that the prediction of heating rates at the stagnation point were reasonably close to expectations, it is of interest to use the results presented here in to predict the recession rates for tests of other conditions and materials. In that interest, a formula was determined for the recession rate by solving Equation (30) using the values for K found for the spherically blunted cylinder ($K = 3.82E-4$) and substituting into Equation (31) with the heat of sublimation and density of the subliming material. This approach can be written as presented in Equation (35) where the recession rate is given in m/s.

$$\frac{\dot{m}}{\rho_s A} = \frac{K \sqrt{q_w}}{\rho_s \Delta H_{sub}} \quad (35)$$

Three test cases were considered: a carbon heat shield under sounding rocket flight conditions, a camphor model at Mach 8, and a large scale hypersonic wind tunnel with dry ice. The test conditions and material characteristics of each are presented in Table 35 along with the recession rates predicted. In all three cases, the temperature at the wall, T_w , was found using the vapor pressures of the material as found in (Lide, CRC Handbook of Chemistry and Physics, 2009).

The test conditions for the carbon heat shield were taken from an actual flight test described in (Graves & Witte, 1968). Since the material used for Graves and Witte's test was a carbon based char ablator with a sealant, the recession predicted here under

predicts the true ablation rate, which Graves and Witte reported to be 2.47 mm/s at the stagnation point. This value does not compare well with results predicted by a pure sublimator.

The camphor tests were based upon the results of (Baker, 1972) who conducted tests at Mach 8 on camphor models. The test article in Baker's tests was small ($R_N = 6$ mm) and the recession rates reported in that paper were 0.38 mm/s, or approximately half of the predicted rate. However, in the test the R_N blunted considerably over the approximately one minute of testing. If the R_N is higher, then the prediction found would compare closely with the experimental results at approximately $R_N = 1.4$ inches (35.6 mm).

The scale of dry ice to a large scale hypersonic wind tunnel is warranted for the consideration of future work. The conditions chosen are known capabilities of existing facilities, and therefore of interest. If a model with a nose radius of 4 inches (0.102 m) were used, the predicted recession rate would be 0.76 mm/s. So here ten percent of the nose radius would ablate after approximately 13 seconds. This is a time scale that is reasonable for a blow down tunnel. These results lend credence to the possibility of extending this research to other low temperature ablators and limited collaboration with high temperature ablators.

Table 35: Test conditions for recession rate prediction of carbon based, camphor and dry ice at hypersonic velocities

Ablator Type	Carbon based	Camphor	Camphor (modified R_N)	Dry ice
Mach	10	8	8	8
U (m/s)	3000	1178	1178	1521
(psia)	34000	800	800	2000
(Pa)	7.15E+05	4.68E+04	4.68E+04	1.17E+05
(K)	4550	744	744	1240
(K)	220	54	54	90
(K)	3391	444	444	196
(kg/m ³)	0.089	0.037	0.037	0.055
(kg/m ³)	2270	990	990	1010
(m)	0.110	0.006	0.036	0.102
(J/kg)	5.96E+07	3.52E+05	3.52E+05	5.58E+05
(J/kg)	4.57E+06	7.48E+05	7.48E+05	1.25E+06
(J/kg)	3.41E+06	4.46E+05	4.46E+05	1.97E+05
Predicted Recession (mm/s)	0.01	0.90	0.38	0.76

6. Summary and Conclusions

6.1 Motivation

Since at least the 1960's, researchers have pursued low temperature ablation to simulate ablative heat shields and have desired to use dry ice as their test medium. However, many found problems with fabrication, testing, and imaging. While fabrication techniques improved over the years, most of them were lengthy processes with close to 24 hours needed to produce a test article. If the researchers chose a faster technique, they often reported problems with the models spalling or disintegrating. Even if these problems were overcome, the imaging techniques were often limited to shadowgraph measurements.

The majority of ablation research stopped in the 1970s with the advent of reusable heat shields. This movement away from ablation research caused a gap in development as ablative heat shields now start to make a comeback. This research seeks to close that gap by combining modern techniques and new ideas to facilitate fast and repeatable low temperature ablation data and to use this capability to validate computational models.

6.2 Summary of Research

The research objectives were broken into four incremental tasks. The first goal was to produce reliable and reproducible test articles. A technique was developed and

shown to rapidly produce dry ice test articles with satisfactory repeatability. The technique opens the possibility for rapidly producing many test articles for a variety of research.

The second objective was to capture of ablation recession in three-dimensions. The data from this research showed conclusively that laser dot-projection is an effective method for collecting three-dimensional ablation recession data. High-speed Schlieren imaging was used to complement the laser dot-projection for a qualitative assessment. The laser dot-projection technique proved to have sub millimeter accuracy and was usable on a homogenous surface.

Research objective three was to compare the collected recession data to the ACFD model and validate the computational model under limited conditions. As Chapter 5 demonstrated, the recession data gathered during this research matched the ACFD projections with excellent agreement.

Objective four was to relate the gathered data to real world applications. Several avenues were investigated for scaling the data. The stagnation point recession data correlated well when all heat from the flow was assumed to lead to phase change via sublimation. Lastly, an approach was taken to predict ablation rates for three cases under varying conditions.

6.3 Conclusions and Contributions to the Hypersonics Community

The development of the acquisition technique of this data is an accomplishment which is critical to the missions of NASA and the United States Air Force because of the role ablation plays in hypersonic flight. Although a true hypersonic flow includes chemically reactive gases and can lead to chemical reactions on the surface, a vital aspect of ablation is the coupled relationship between aerodynamic shape change and hypersonic flight conditions. The experimental technique developed herein can be applied at high Mach number, but otherwise benign conditions, to measure aerodynamic shape change, independent of chemical reactions.

A significant achievement of this effort was that three-dimensional recession data were collected for a large number of models and conditions. This achievement was made possible for dry ice ablators, which are essentially uniform in their surface texture, by using laser dot projection in combination with high-speed stereo photogrammetry. While laser dot projection has been used in combination with stereo photogrammetry for other areas of research, to the knowledge of the author, this is the initial effort where the technique has been applied as a non-intrusive ablation recession measurement. The results demonstrated that the approach used to collect ablation data was repeatable and effective. The diagnostic tool developed in the course of this research enabled both qualitative and quantitative analysis of the results. In agreement with the literature, the ablation rate was generally found to be highest at the nose of the test article.

In addition to providing data for ACFD, results were used to predict ablation at the stagnation in potential real world applications. It was found that if one assumed all heat transfer at the stagnation point resulted in the sublimation phase change, a heating rate could be backed out. This heating rate was compared to the results of the Fay-Riddell correlation. Sutton and Graves framed the Fay-Riddell equation in terms of a coefficient, K , which was derived from first principles to get a K of 0.00035 _____ for air (Sutton & Graves, 1971). The experimental results presented herein found a K of 0.00038 _____ for the spherically blunted cylinder and 0.00026 _____ for a spherically blunted cone. Since the Fay-Riddell correlation was developed assuming the shape of a sphere or a sphere cylinder, the difference in the results for the spherically blunted cone is not surprising. The heating rate also compared favorably with the convective heating rate of FIRE II, a real world test conducted at 11 km/s.

The same simple approach yielded a predicted recession rate of the correct order of magnitude for a test using camphor at Mach 8, as described by Baker (Baker, 1972). Furthermore, the same approach yielded a predicted ablation rate for the use of dry ice in a large scale hypersonic wind tunnel that is reasonable for short test times found in blow down tunnels. This is an important finding as it suggests that scaled up tests could lend additional insight into Reynolds and Mach number effects on ablation.

In addition to low temperature ablation, one can use this approach to predict performance of a real world ablators. However, as discussed in the literature, the

approach is limited to a non-reacting flow and pure subliming material absent thermal conduction and radiation effects.

Also of great significance is that the data from this research will be available for validation of other solvers in the future. The ACFD settings were modified several times during the data processing for this research and will continue to be improved. Certainly in the future, other ablation solvers will also be developed, and this data will be available for comparison of those models. In addition, this research effort may lay the foundation for improved methods of generating models and testing methods used to acquire low temperature ablation data on a variety of other, more sophisticated aerodynamic designs.

6.4 Recommendations for Future Work

This research was the initial step towards producing a viable way to simulate ablation with low temperature ablators and capture three-dimensional shape change over time. The groundwork for the idea of low temperature ablators was laid more than fifty years ago, but has had a long hiatus until the recent interest in ablative heat shield technology. During the research, recommendations for future work were taken note of to improve the technique:

- Expand research to hypersonic flow and scale up the experiment.
- Compare Angle of Attack experimental results with ACFD results
- Collaborate with Sandia National Laboratory to compare results.

- Repeat tests with a finer projected laser grid and additional cameras.
- Compare the experimental data collected in this research to future CFD model outputs.

APPENDIX A: Model Diagrams

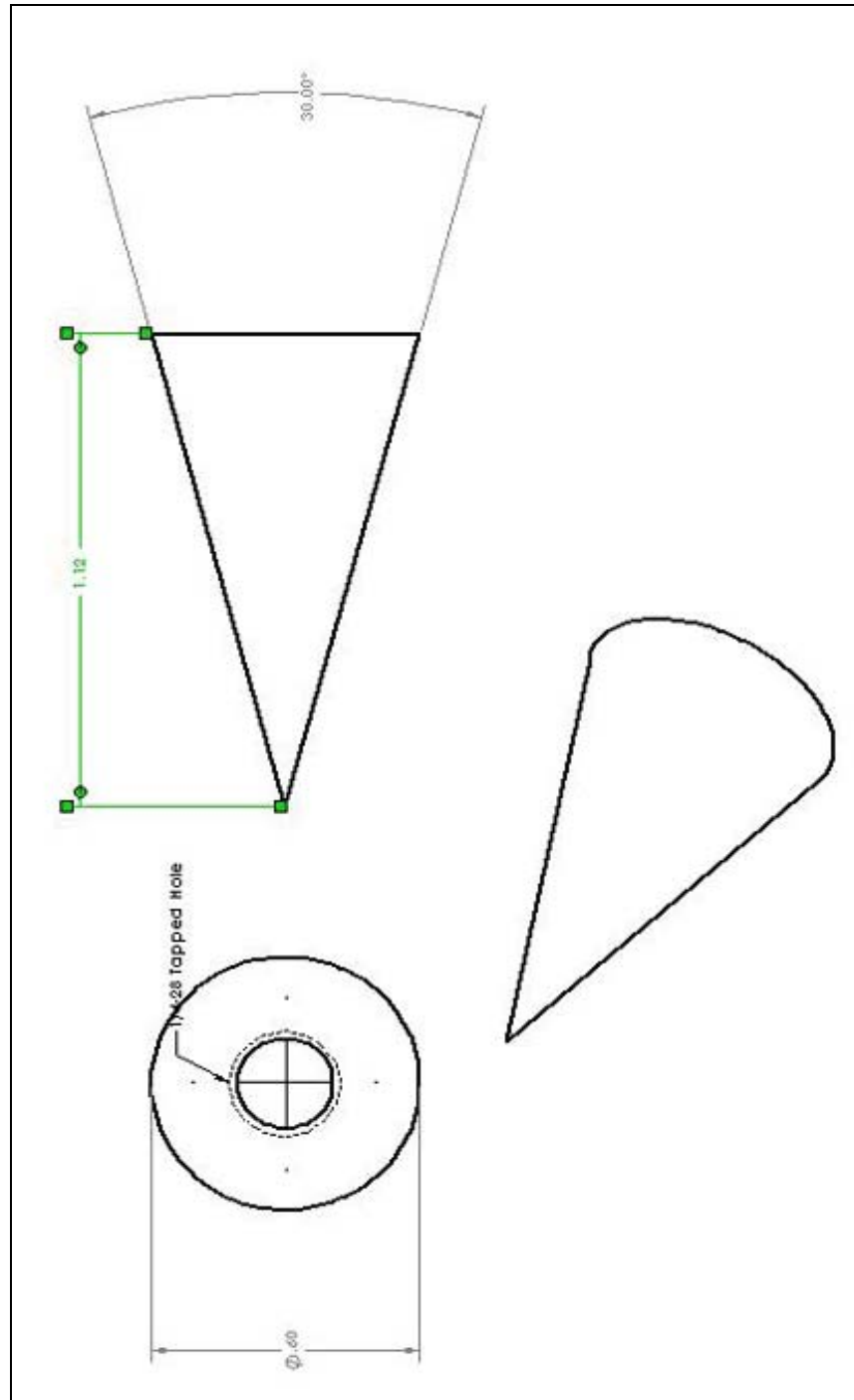


Figure 114: 30 degree cone model on 0.60 inch base

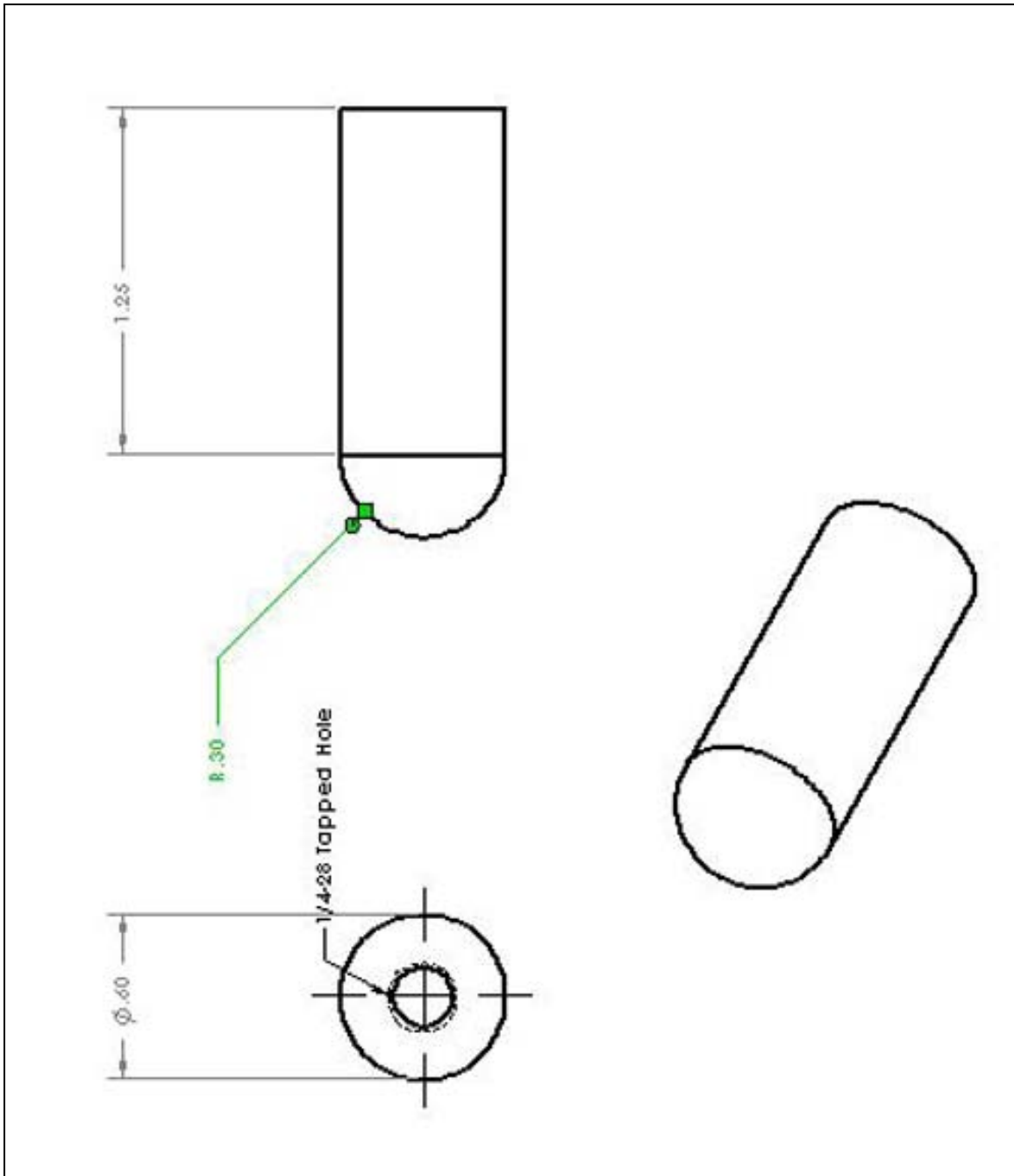


Figure 115: Spherically blunted cylinder on 0.60 inch base

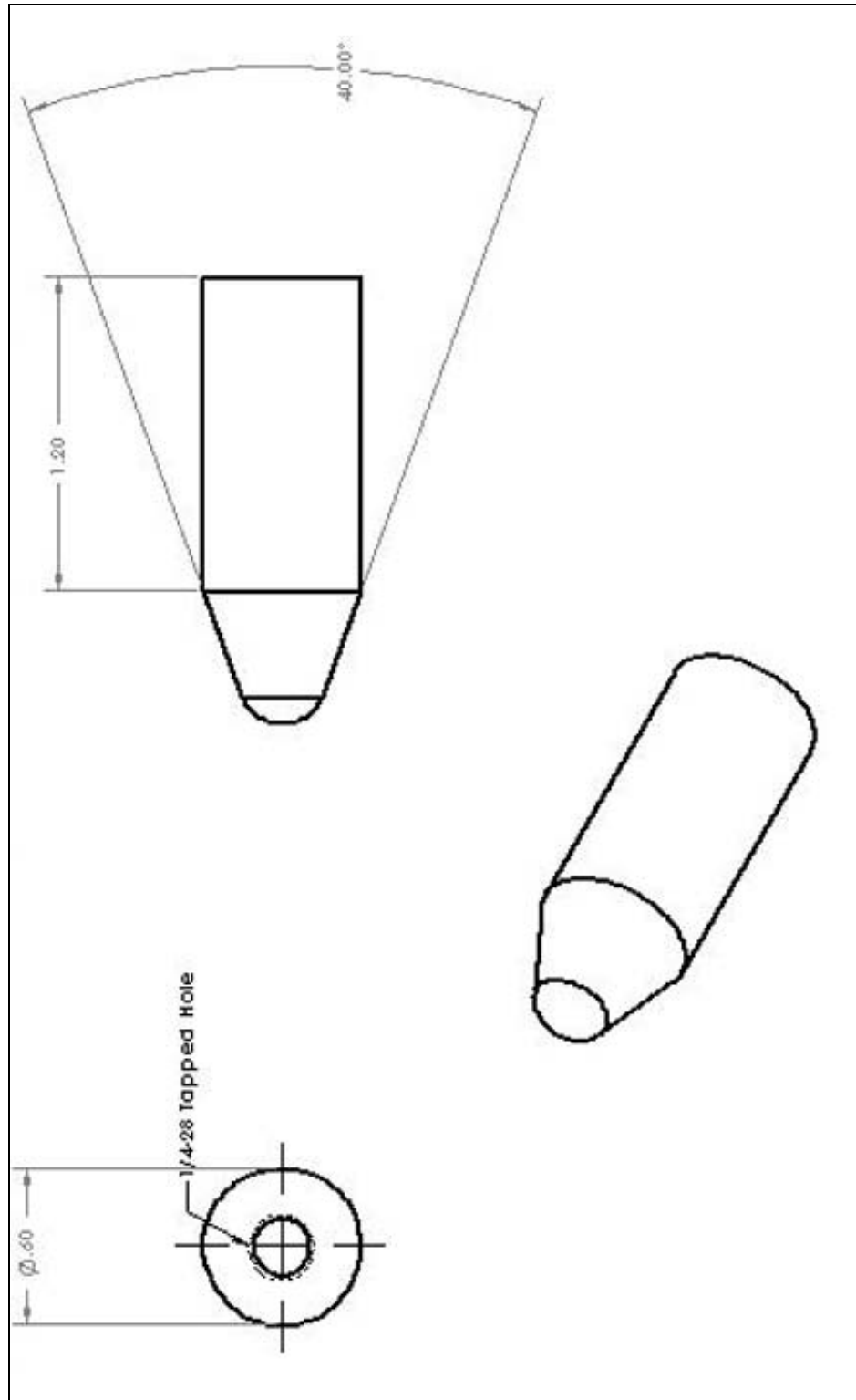


Figure 116: Spherically blunted cone on 0.60 inch base

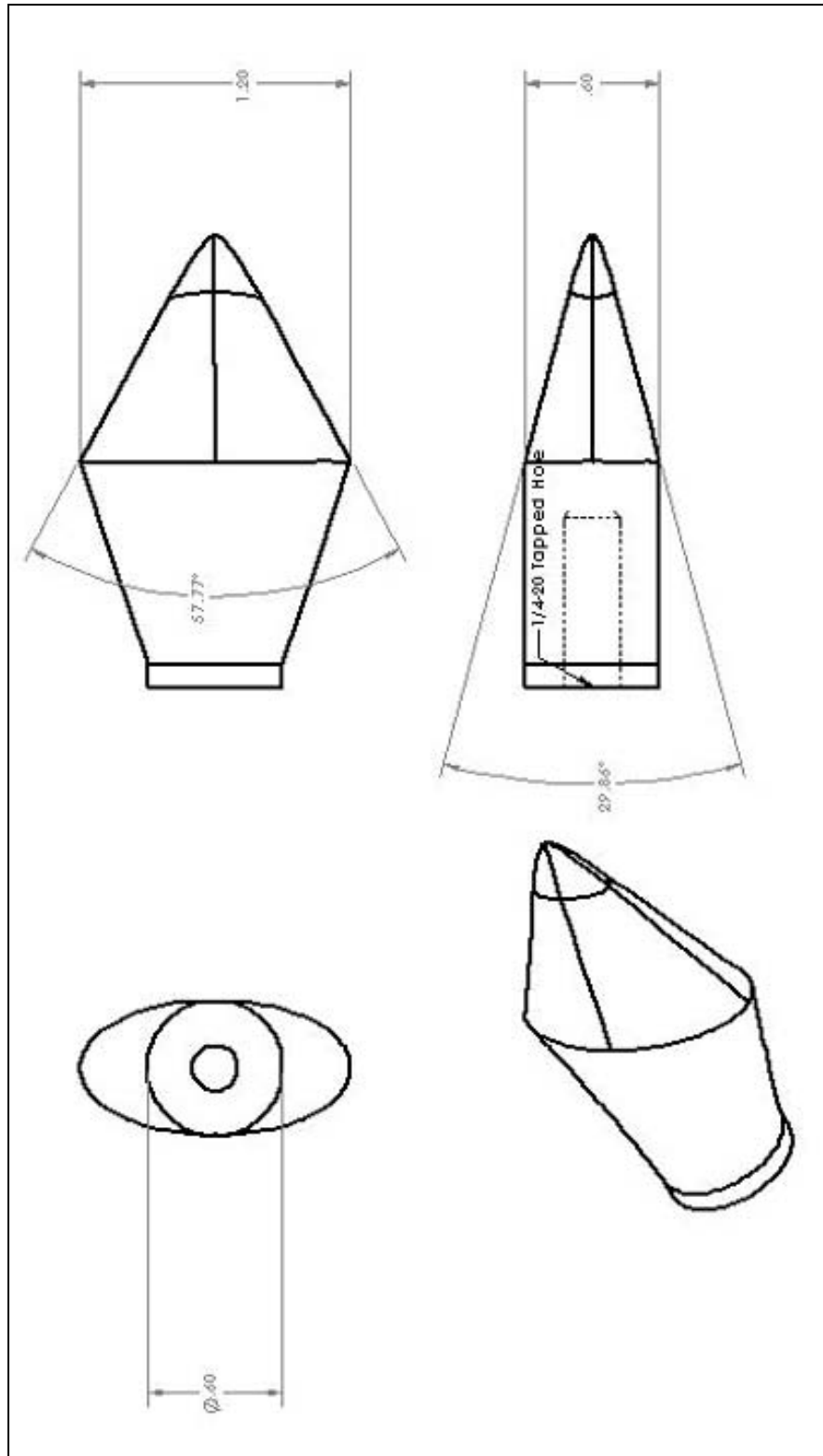


Figure 117: Elliptical shape with wings on 0.60 inch base

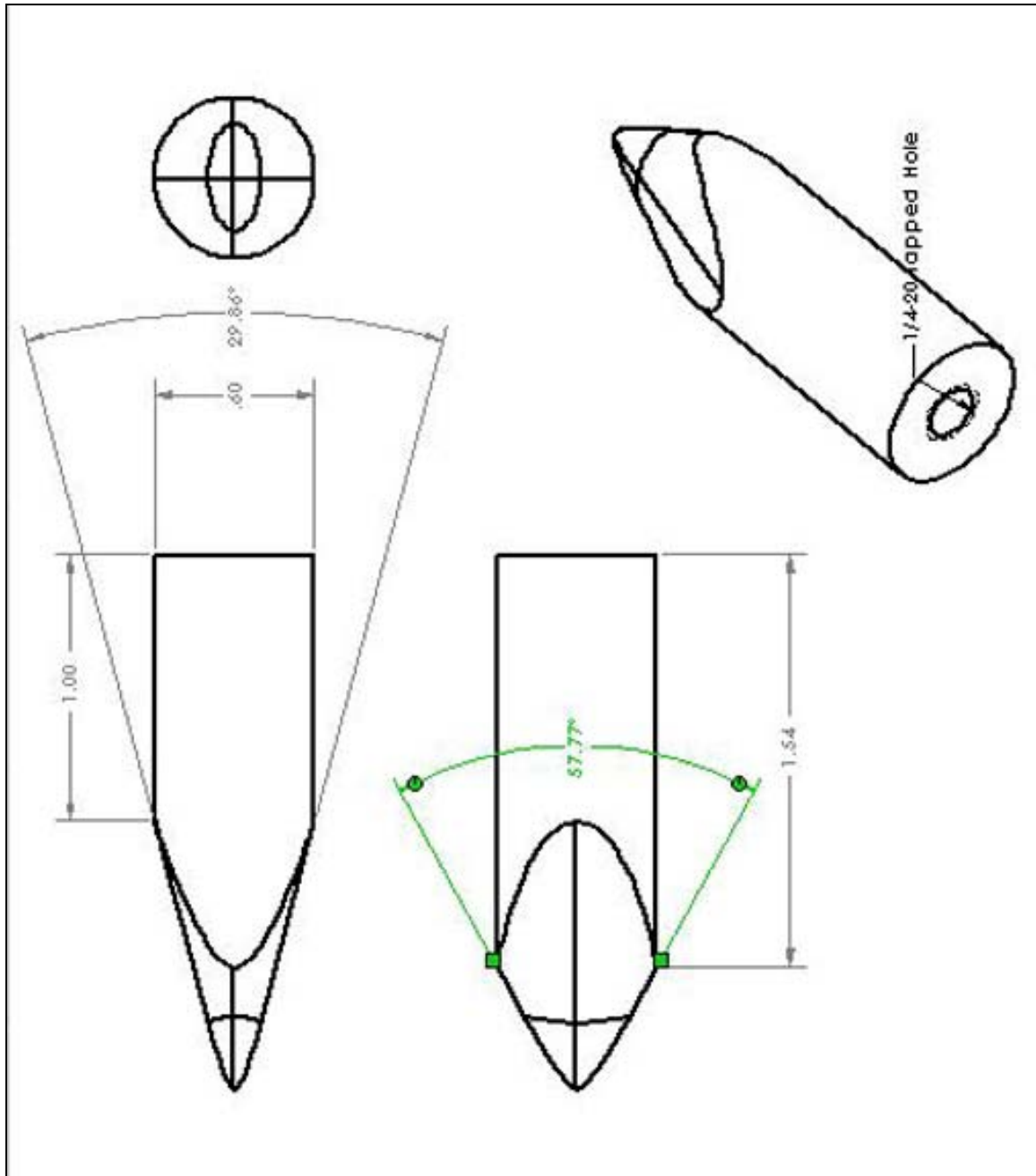


Figure 118: Elliptical nose on 0.60 inch base

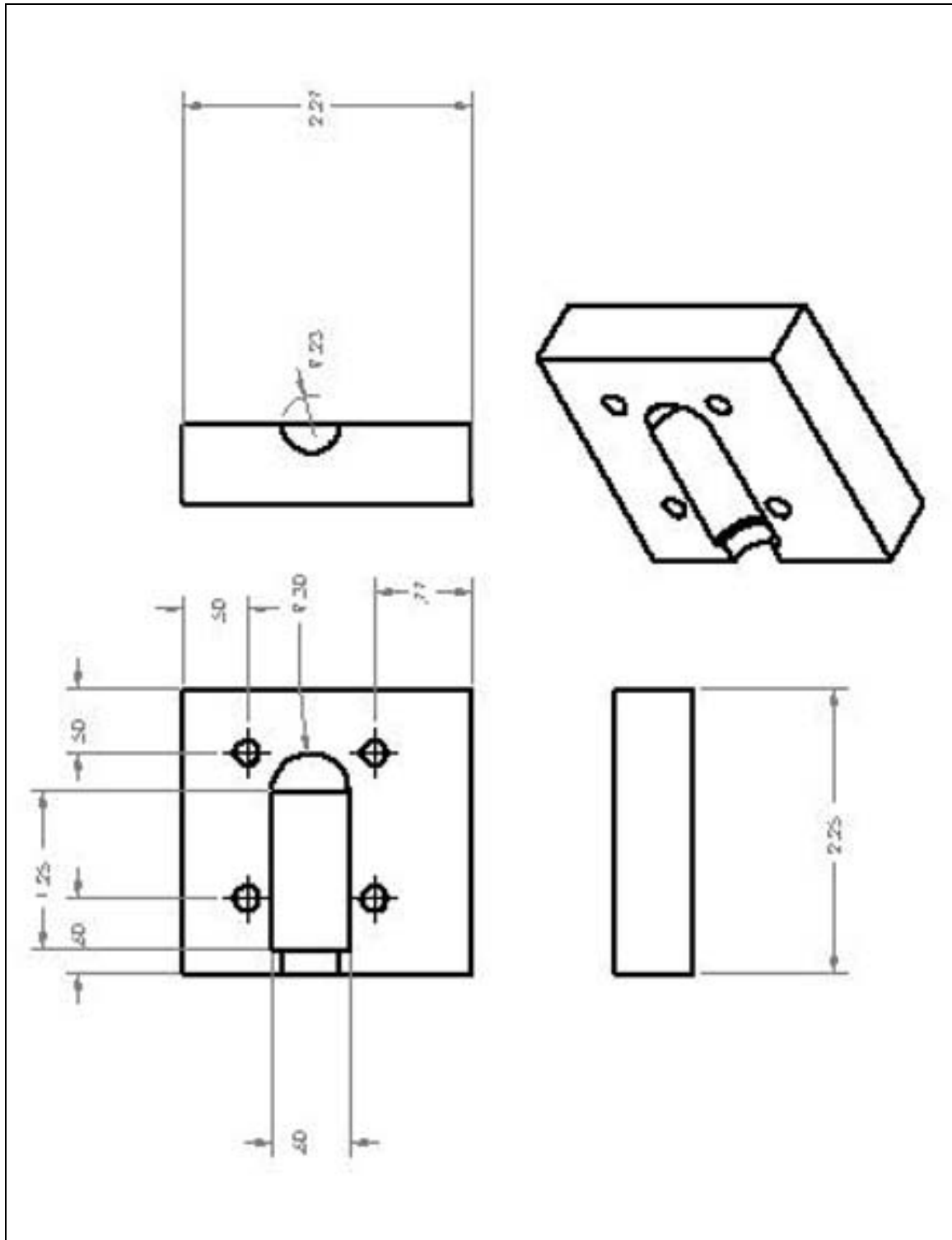


Figure 119: Example of mold for spherically blunted cylinder

APPENDIX B: ACFD Input Parameters

A main input deck controls ACFD. It controls the solution procedure and initialization of the grid domains. The user-accessible variables are:

- `nstop`: the number of time steps to be run
- `iplot`: = 0 for no solution write, = 1 for solution write (default = 1)
- `nplot`: the number of time steps between solution writes
- `iconr`: = 0 for no restart file (start from scratch), = 1 for start from previous solution
- `impl`: = 0 for explicit time integration, = 1 for DPLR time integration, = 2 for FMDP time integration (default = 1)
- `kmax`: number of sub-iterations in implicit method (default = 4)
- `ivisc`: = 0 for inviscid simulation, = 1 for viscous simulation, = -1 for fully turbulent viscous simulation (default = 1)
- `iwall`: = 1 for adiabatic wall, = 2 for isothermal wall (temperature given by `twall`), = 3 for radiative equilibrium wall, = 4 for surface ablation using the model described in Section 3.4
- `itrj`: = 0 for no trajectory (run at input free-stream conditions for entire run), = 1 for trajectory read from `trajectory.dat`.
- `irece`: = 0 for no grid motion / shape change, = 1 for shape change
- `imatl`: = 0 for graphite solid material, = -1 for carbon-carbon, = -2 for aluminum, = 1 for camphor, = 2 for dry ice. For the low-temperature ablators (camphor and dry ice), it is assumed that the flow field will be described by a perfect gas; in these cases, the number of gases in the simulation must be set to 2 and the elemental compositions are not used.
- `imxls`: number of nodes in solid wall-normal lines for grid motion.
- `iorder`: = 1 for first order accurate simulation, = 2 for second order accurate simulation (default = 2)
- `iuem`: = 0 for pure upwind extrapolation, = 1 for MUSCL extrapolation on conserved variables, = 2 for MUSCL extrapolation using primitive variables and Taylor series reconstruction of E (default = 2)
- `kbl`: = number of elements from wall for which the eigenvalue limiter is disabled to prevent corruption of boundary layer (default = 20)
- `iman`: = the number of time steps between calls to the solution manager driven by the `manage.inp` file
- `press`: = free-stream pressure (Pa)
- `Tin`: = free-stream temperature (K)
- `Twall`: = wall temperature (`iwall`=2) and initial solid temperature of simulation (K)
- `vin`: = free-stream velocity (m/s)
- `cfl`: = initial CFL number for computation of time step; if `cfl` is negative, then the time step is taken to be the absolute value of `cfl` in seconds.
- `epsj`: = eigenvalue limiter value (default = 0.3)

- `wdis`: = physical distance (in meters) for which an artificial boundary layer is put in place at initial start (`iconr=0`)
- `direction cosines`: = direction cosines in grid coordinates of free-stream at start-up.

APPENDIX C: Master List of Tests

Zero Angle of Attack Tests					
Date	Test	Model	Processed Frames	Maximum Usable Frames	Stagnation Pressure (PSIA)
2-Jun	1	Spherically Blunted Cone	5	20	12.90
	2	Spherically Blunted Cone	5	20	12.86
	3	Spherically Blunted Cone	5	15	12.48
	4	Spherically Blunted Cone	5	32	12.65
	5	Spherically Blunted Cone	5	10	12.77
	6	Spherically Blunted Cone	15	22	6.14
	7	Spherically Blunted Cone	5	8	6.12
	8	Spherically Blunted Cone	5	32	6.10
	9	Spherically Blunted Cone	5	32	6.16
3-Jun	1	Spherically Blunted Cone	5	5	20.57
	2	Spherically Blunted Cone	6	6	20.54
	3	Spherically Blunted Cone	5	5	16.72
	4	Spherically Blunted Cone	5	5	20.63
	5	Spherically Blunted Cone	6	6	20.59
9-Jun	1	Spherically Blunted Cone	15	15	23.03
	2	Spherically Blunted Cone	5	6	23.10
	3	Spherically Blunted Cone	6	6	29.70
	4	Spherically Blunted Cone	5	5	29.45
10-Jun	1	Spherically Blunted Cone	3	3	22.04
	2	Spherically Blunted Cone	4	4	21.96
	3	Spherically Blunted Cone	5	11	16.95
	4	Spherically Blunted Cone	5	8	20.70
	5	Spherically Blunted Cone	4	4	11.06

Zero Angle of Attack Tests					
Date	Test	Model	Processed Frames	Maximum Usable Frames	Stagnation Pressure (PSIA)
	6	Spherically Blunted Cone	5	5	20.87
	7	Spherically Blunted Cone	0	0	26.76
10-Jun	8	Spherically Blunted Cone	0	0	23.50
11-Jun	1	Spherically Blunted Cone	5	16	23.28
	2	Spherically Blunted Cone	5	11	26.19
	3	Spherically Blunted Cone	5	5	28.16
13-Jun	1	Spherically Blunted Cone	5	5	28.19
	2	Spherically Blunted Cone	5	8	28.25
	3	Spherically Blunted Cone	5	5	31.08
	4	Spherically Blunted Cone	0	0	31.16
	5	Spherically Blunted Cone	0	0	33.22
	6	Spherically Blunted Cone	4	4	33.21
15-Jun	1	Spherically Blunted Cone	6	6	33.26
	2	Spherically Blunted Cone	0	0	35.54
	3	Spherically Blunted Cone	0	0	35.47
	4	Spherically Blunted Cone	5	5	35.45
	5	Spherically Blunted Cone	5	5	37.93
16-Jun	1	Spherically Blunted Cone	4	4	45.70
	2	Spherically Blunted Cone	0	0	38.08
	3	Spherically Blunted Cone	0	0	40.15
	4	Spherically Blunted Cone	0	0	40.14
	5	Spherically Blunted Cone	0	0	41.89

Zero Angle of Attack Tests					
Date	Test	Model	Processed Frames	Maximum Usable Frames	Stagnation Pressure (PSIA)
	6	Spherically Blunted Cone	0	0	42.01
	7	Spherically Blunted Cone	0	0	42.08
	8	Spherically Blunted Cone	0	0	43.88
	9	Spherically Blunted Cone	3	3	43.79
16-Jun	10	Spherically Blunted Cone	0	0	45.70
	11	Spherically Blunted Cone	0	0	45.70
17-Jun	1	Spherically Blunted Cone	0	0	46.81
	2	Spherically Blunted Cone	3	3	46.90
	3	Spherically Blunted Cylinder	4	4	46.90
19-Jun	1	Spherically Blunted Cylinder	0	0	47.15
	2	Spherically Blunted Cylinder	5	5	37.86
	3	Spherically Blunted Cylinder	5	5	37.94
	4	Spherically Blunted Cylinder	5	5	27.86
	5	Spherically Blunted Cylinder	5	5	27.90
	6	Spherically Blunted Cylinder	6	6	19.75
	7	Spherically Blunted Cylinder	7	7	19.75
	8	Spherically Blunted Cylinder	16	16	7.50
	9	Spherically Blunted Cylinder	16	16	7.53
13-Jul	1	Elliptical Nose, Horizontal	6	6	17.40
	2	Elliptical Nose, Horizontal	3	3	17.40
	3	Elliptical Nose, Horizontal	5	5	17.31
	4	Elliptical Nose, Horizontal	0	0	21.99
	5	Elliptical Nose, Horizontal	5	5	22.01

Zero Angle of Attack Tests					
Date	Test	Model	Processed Frames	Maximum Usable Frames	Stagnation Pressure (PSIA)
	6	Elliptical Nose, Horizontal	5	5	21.93
14-Jul	1	Elliptical Nose, Horizontal	5	5	25.80
	2	Elliptical Nose, Horizontal	5	5	25.91
	3	Elliptical Nose, Horizontal	0	0	30.55
	4	Elliptical Nose, Horizontal	0	0	30.54
14-Jul	5	Elliptical Nose, Horizontal	4	4	30.43
	6	Elliptical Nose, Horizontal	0	0	35.88
18-Jul	1	Elliptical Nose, Horizontal	0	0	35.67
	2	Elliptical Nose, Horizontal	0	0	39.19
	3	Elliptical Nose, Horizontal	5	5	39.10
	4	Elliptical Nose, Horizontal	5	5	39.08
	5	Elliptical Nose, Horizontal	5	5	42.18
	6	Elliptical Nose, Horizontal	0	0	42.28
	7	Elliptical Nose, Horizontal	3	3	42.29
	8	Elliptical Nose, Horizontal	4	4	45.79
	9	Elliptical Nose, Horizontal	3	3	46.16
	10	Elliptical Nose, Horizontal	2	2	46.51
21-Jul	1	Elliptical Shape with Wings, Horizontal	0	0	
27-Jul	1	Elliptical Shape with Wings, Horizontal	2	2	45.77
	2	Elliptical Shape with Wings, Horizontal	0	0	45.61
	3	Elliptical Shape with Wings, Horizontal	5	5	37.90

Zero Angle of Attack Tests					
Date	Test	Model	Processed Frames	Maximum Usable Frames	Stagnation Pressure (PSIA)
	4	Elliptical Shape with Wings, Horizontal	3	3	38.08
1-Aug	1	Elliptical Shape with Wings, Horizontal	0	0	28.88
	2	Elliptical Shape with Wings, Horizontal	3	3	28.94
	3	Elliptical Shape with Wings, Horizontal	3	3	28.98
	4	Elliptical Shape with Wings, Horizontal	0	0	18.49
	5	Elliptical Shape with Wings, Horizontal	3	3	20.91
5-Aug	1	Elliptical Nose, Vertical	3	3	46.60
	2	Elliptical Nose, Vertical	2	2	46.93
	3	Elliptical Nose, Vertical	2	2	39.48
	4	Elliptical Nose, Vertical	0	0	39.48
6-Aug	1	Elliptical Nose, Vertical	0	0	39.59
	2	Elliptical Nose, Vertical	0	0	28.67
	3	Elliptical Nose, Vertical	0	0	28.57
	4	Elliptical Nose, Vertical	0	0	23.14
	5	Elliptical Nose, Vertical	0	0	23.07
	6	Elliptical Nose, Vertical	3	3	19.18
Solid Models					
3-Aug	1	Spherically Blunted Cone			20.85
	2	Spherically Blunted Cone			26.44
	3	Spherically Blunted Cone			31.22
	4	Spherically Blunted Cone			18.56

Zero Angle of Attack Tests					
Date	Test	Model	Processed Frames	Maximum Usable Frames	Stagnation Pressure (PSIA)
	5	Spherically Blunted Cone			26.73
	6	Spherically Blunted Cone			33.35
	7	Spherically Blunted Cone			38.67
	8	Spherically Blunted Cone			42.99
	9	Spherically Blunted Cone			45.62

5 Degree Angle of Attack Tests					
Date	Test	Model	Processed Frames	Maximum Usable Frames	Stagnation Pressure (PSIA)
28-Aug	1	Spherically Blunted Cone	5	9	20.68
	2	Spherically Blunted Cone	0	0	20.77
	3	Spherically Blunted Cylinder	0	0	20.81
	4	Spherically Blunted Cylinder	5	12	20.80
	5	Elliptical Nose, Vertical	0	0	20.79
	6	Spherically Blunted Cylinder	0	0	45.54
29-Aug	1	Spherically Blunted Cone	0	0	46.17
	2	Spherically Blunted Cone	0	0	45.84
	3	Spherically Blunted Cylinder	4	4	45.74
	4	Spherically Blunted Cylinder	4	5	45.80
	5	Spherically Blunted Cone	0	0	39.85
	6	Spherically Blunted Cone	5	5	39.91
	7	Spherically Blunted Cone	0	0	40.03
	8	Spherically Blunted Cone	0	0	27.12
	9	Spherically Blunted Cone	5	5	27.24
	10	Spherically Blunted Cone	0	0	27.19
	11	Solid Sph Cone			27.22
	12	Solid Sph Cone			16.53
	13	Solid Sph Cone			40.66
	14	Solid Sph Cone			47.15

10 Degree Angle of Attack Tests					
Date	Test	Model	Processed Frames	Maximum Usable Frames	Stagnation Pressure (PSIA)
14-Aug	A	Elliptical Nose, Vertical	0	0	
	1	Elliptical Nose, Vertical	0	0	19.31
	2	Elliptical Nose, Vertical	0	0	19.18
18-Aug	1	Elliptical Nose, Vertical	5	10	19.22
	2	Elliptical Nose, Vertical	0	0	19.22
	3	Elliptical Nose, Vertical	0	0	19.27
	4	Elliptical Nose, Vertical	0	0	19.17
	5	Spherically Blunted Cone	0	0	19.23
	6	Spherically Blunted Cone	5	16	19.22
21-Aug	1	Spherically Blunted Cone	5	9	19.14
	2	Spherically Blunted Cone	5	9	19.08
	3	Spherically Blunted Cylinder	5	7	19.24
	4	Spherically Blunted Cylinder	5	11	19.13
	5	Spherically Blunted Cylinder	0	0	19.15
	6	Spherically Blunted Cylinder	4	4	46.22
	7	Spherically Blunted Cylinder	0	0	46.01
24-Aug	1	Spherically Blunted Cylinder	5	5	42.18
	2	Elliptical Nose, Vertical	0	0	42.67
	3	Spherically Blunted Cone	5	7	42.84
	4	Spherically Blunted Cone	0	0	42.36
25-Aug	1	Spherically Blunted Cone	0	0	36.23
	2	Elliptical Nose, Vertical	0	0	36.23
	3	Elliptical Nose, Vertical	0	0	36.23

10 Degree Angle of Attack Tests					
Date	Test	Model	Processed Frames	Maximum Usable Frames	Stagnation Pressure (PSIA)
26-Aug	1	Elliptical Nose, Vertical	5	4	36.37
	2	Elliptical Nose, Vertical	0	1	36.48
	3	Elliptical Nose, Vertical	0	0	46.62
	4	Spherically Blunted Cone	5	9	36.77
	5	Spherically Blunted Cone	5	6	36.88
	6	Spherically Blunted Cylinder	5	9	36.68
27-Aug	1	Spherically Blunted Cylinder	5	7	36.69
	2	Spherically Blunted Cylinder	5	11	27.41
	3	Spherically Blunted Cylinder	5	8	30.85
	4	Spherically Blunted Cone	5	6	30.73
	5	Spherically Blunted Cone	5	11	30.78
	6	Elliptical Nose, Vertical	0	0	30.82
	7	Elliptical Nose, Vertical	0	0	30.77
	8	Solid Sph Cone			30.75
	9	Solid Sph Cone			42.19
	10	Solid Sph Cone			47.66
	11	Solid Sph Cone			20.64

APPENDIX D: 2 Jun Test 6 data at 0.5 second intervals

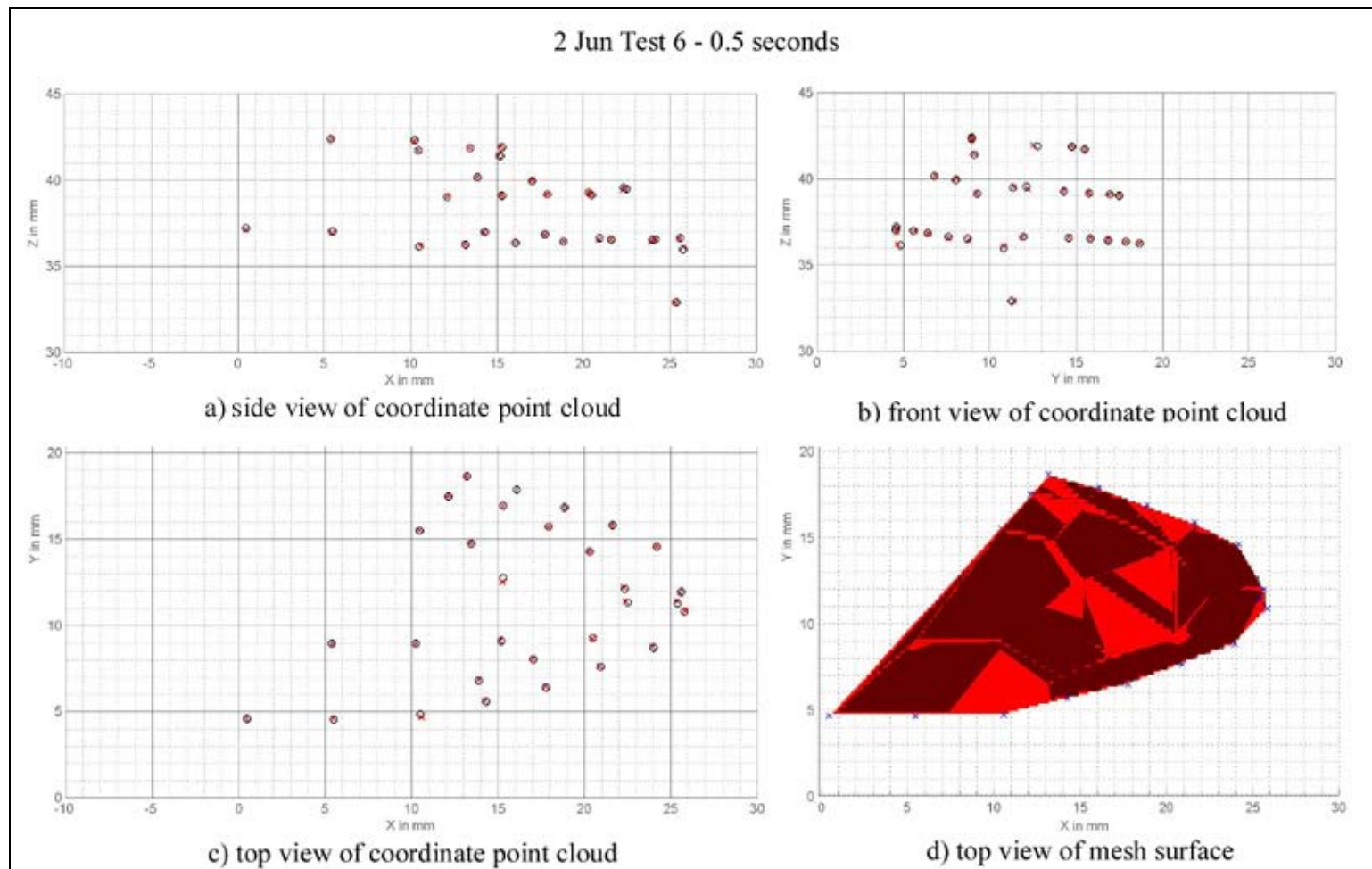


Figure 120: Spherically blunted cone at a stagnation pressure of 6.1 psia and time = 0.5 seconds

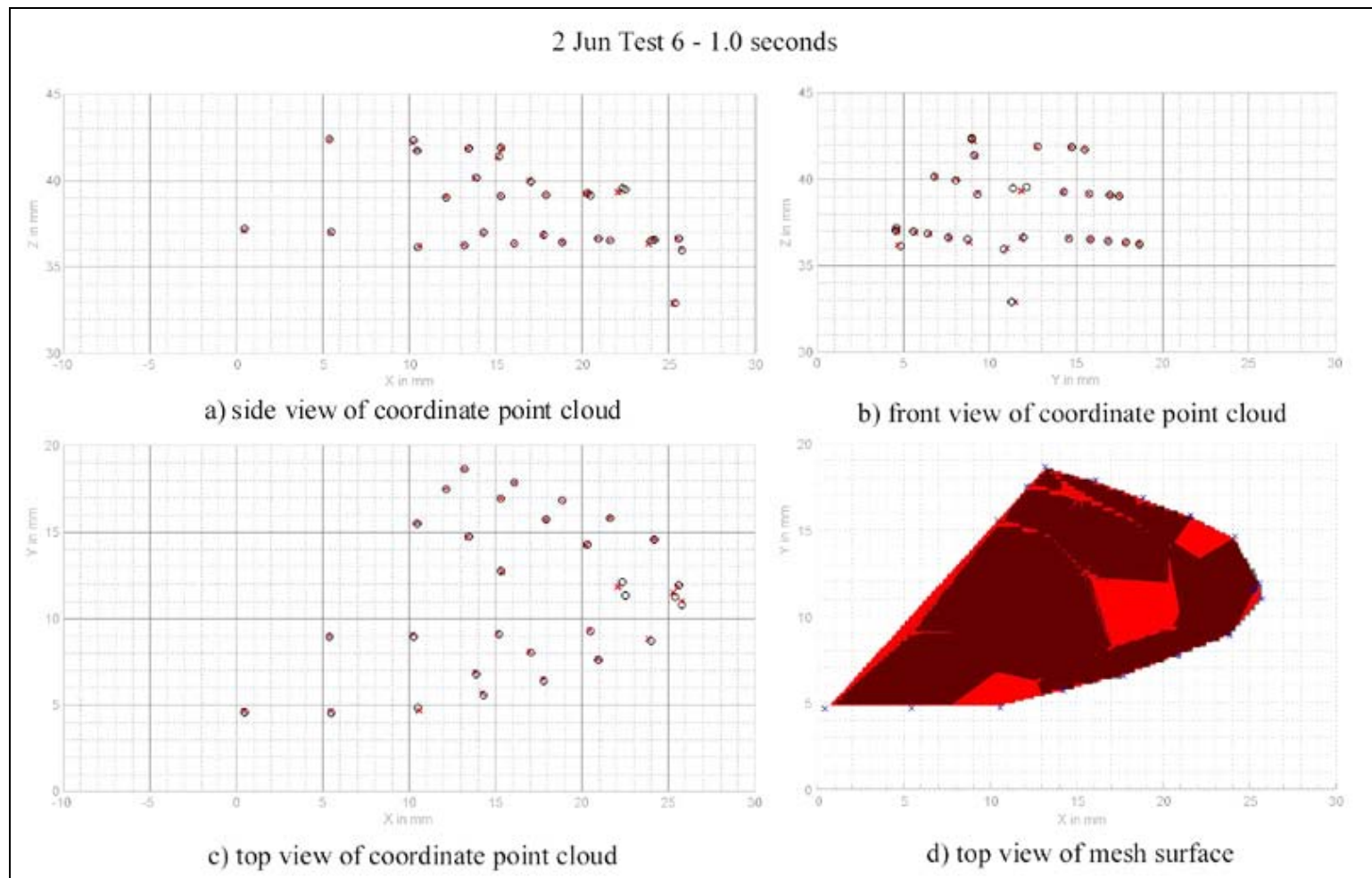


Figure 121: Spherically blunted cone at a stagnation pressure of 6.1 psia and time = 1.0 seconds

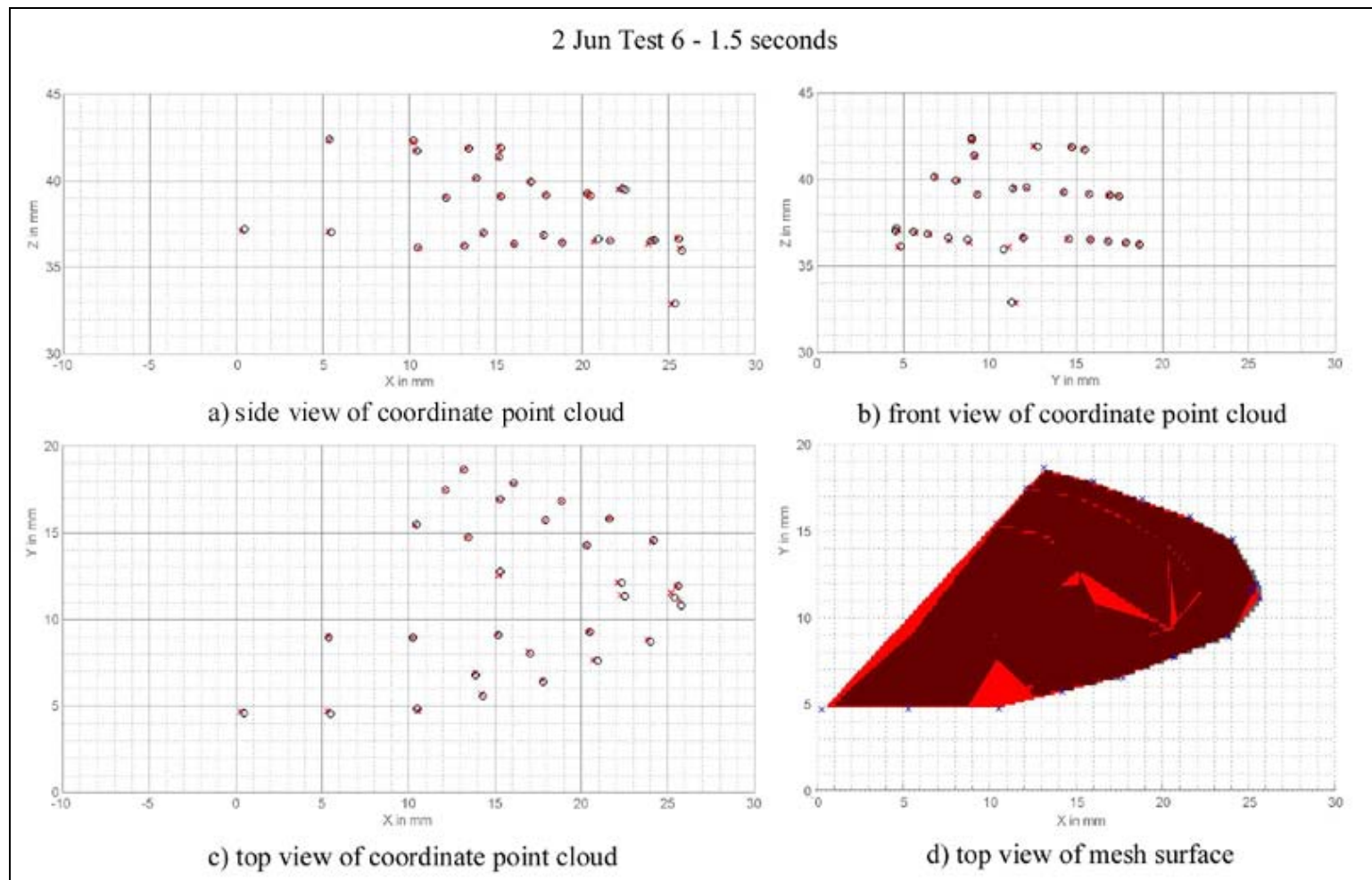


Figure 122: Spherically blunted cone at a stagnation pressure of 6.1 psia and time = 1.5 seconds

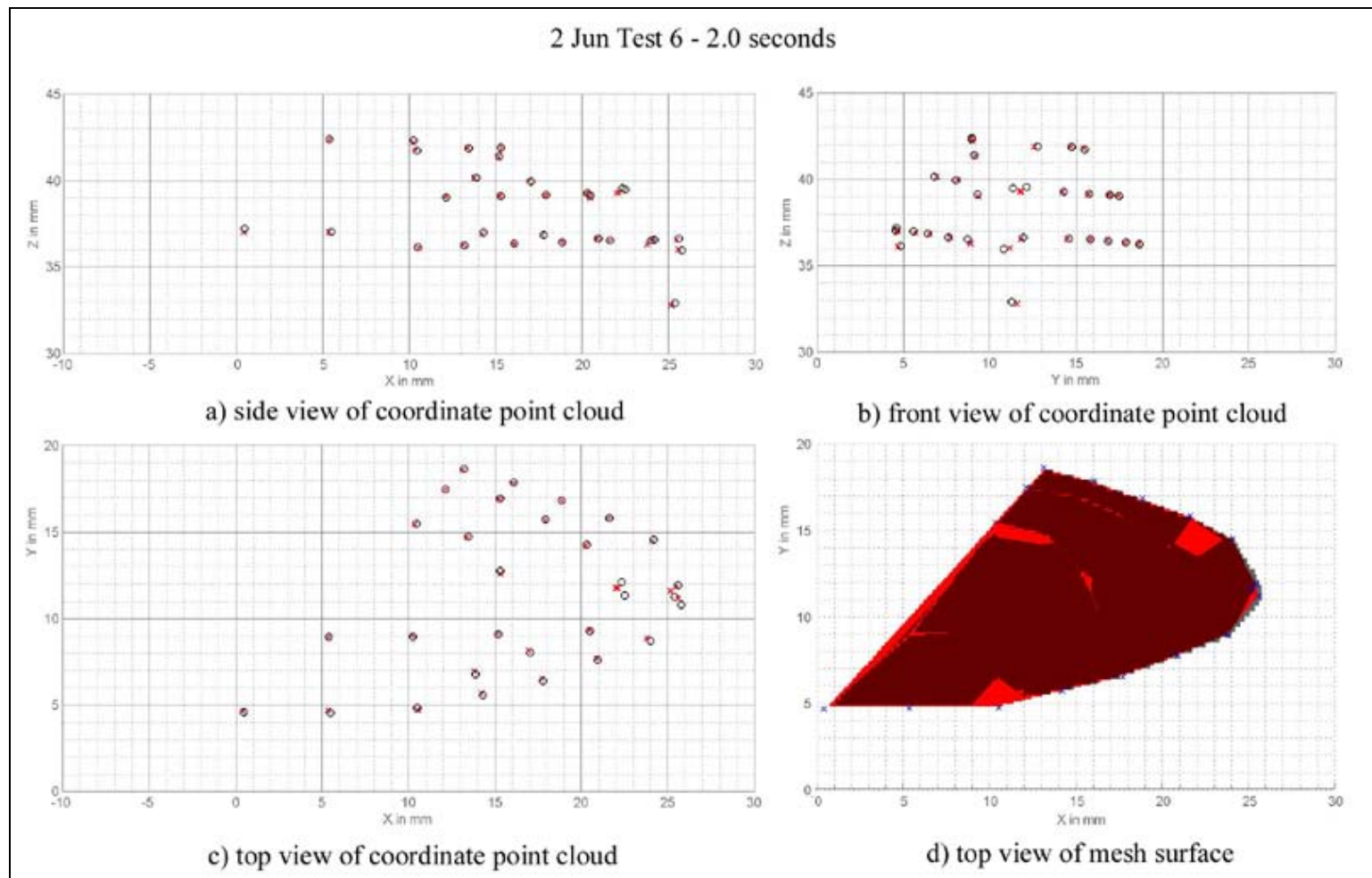


Figure 123: Spherically blunted cone at a stagnation pressure of 6.1 psia and time = 2.0 seconds

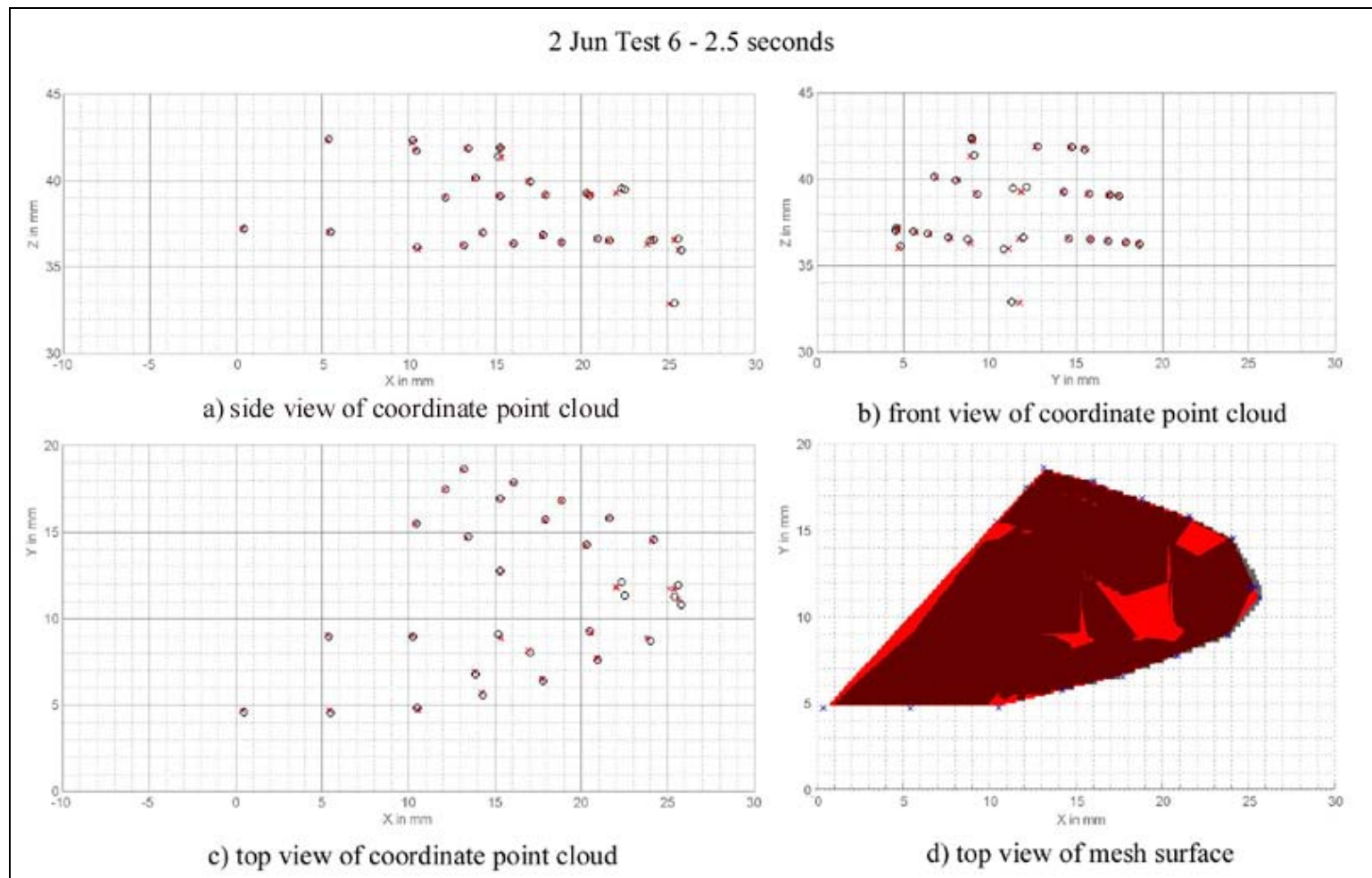


Figure 124: Spherically blunted cone at a stagnation pressure of 6.1 psia and time = 2.5 seconds

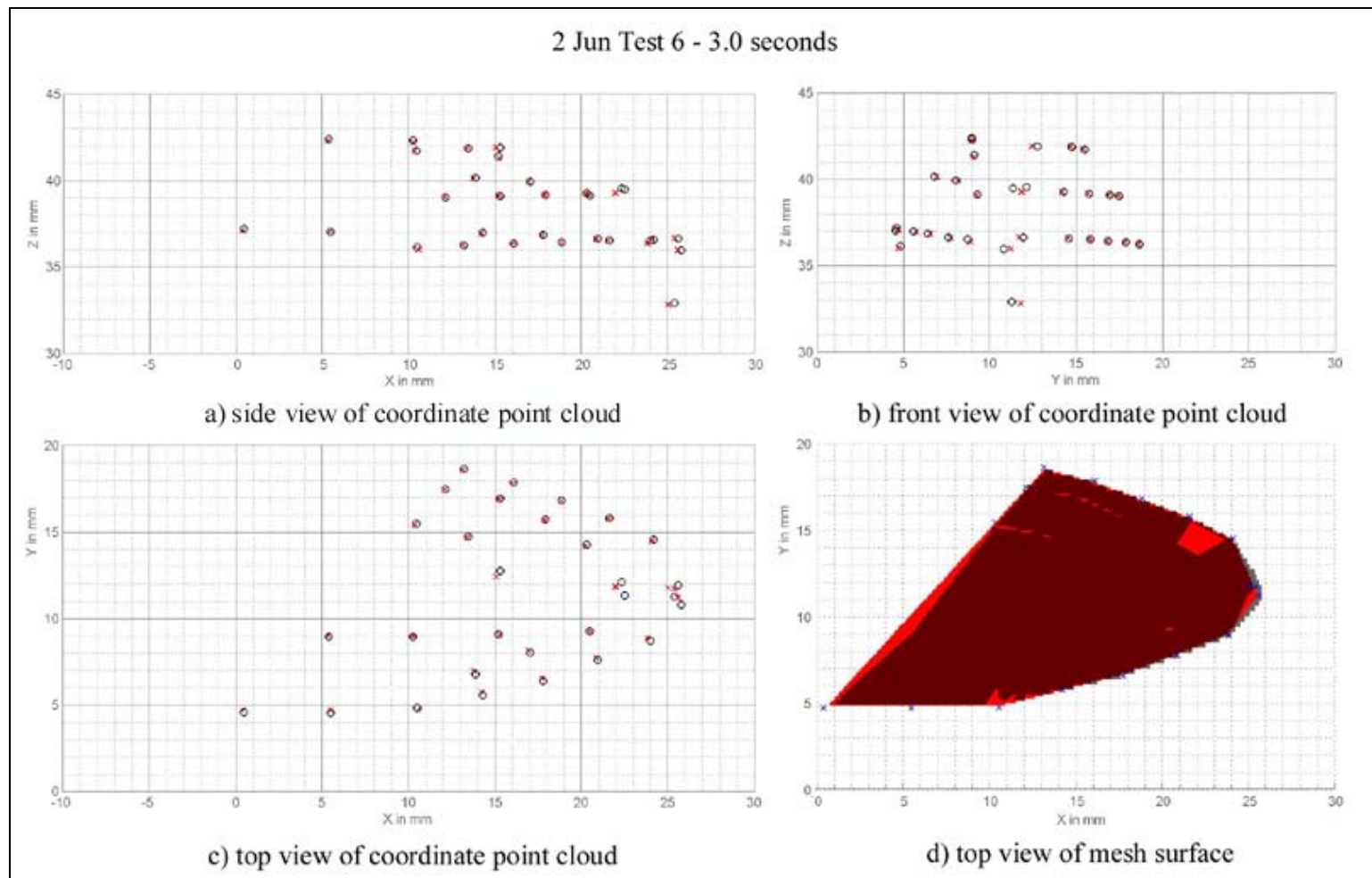


Figure 125: Spherically blunted cone at a stagnation pressure of 6.1 psia and time = 3.0 seconds

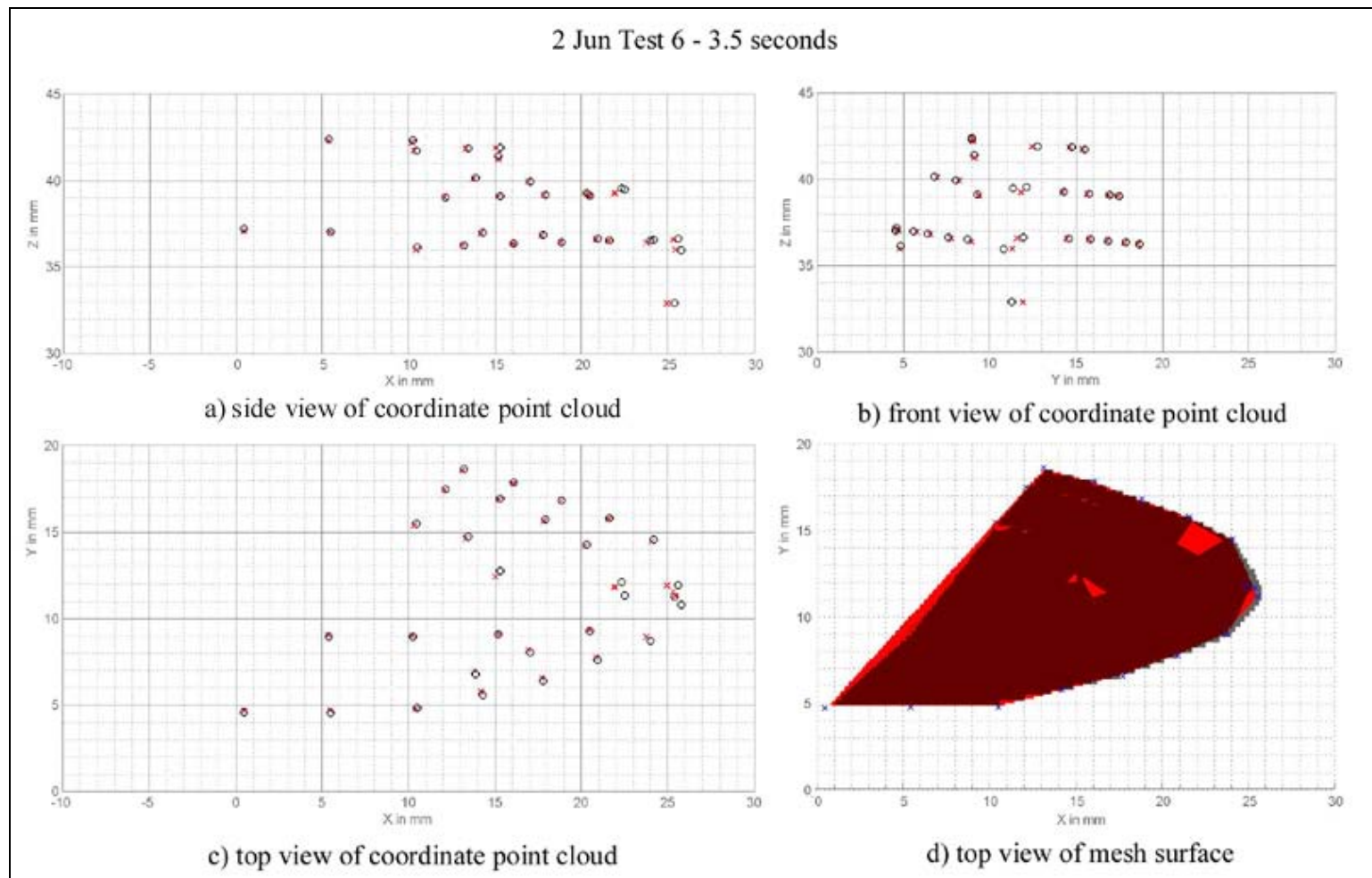


Figure 126: Spherically blunted cone at a stagnation pressure of 6.1 psia and time = 3.5 seconds

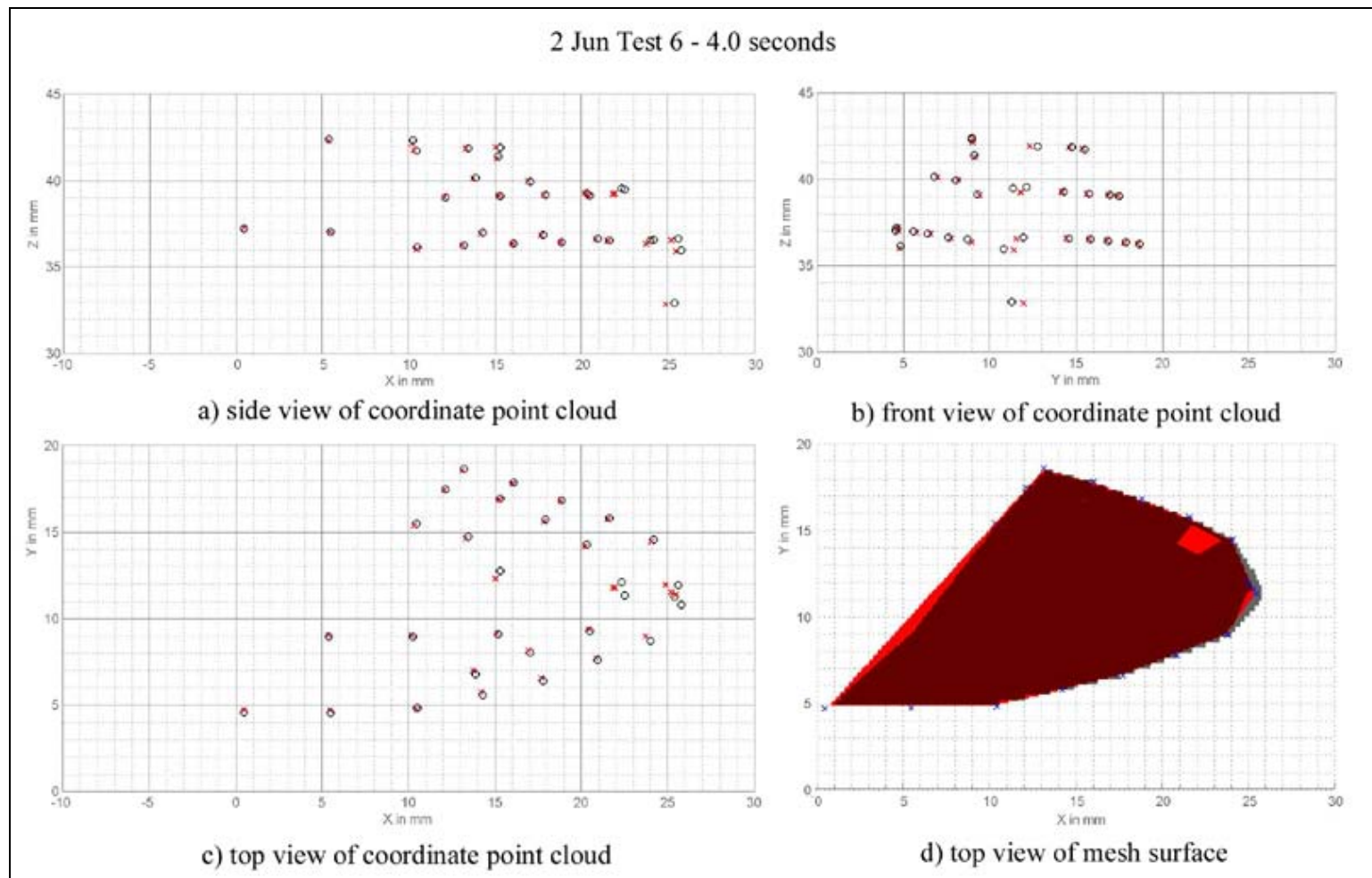


Figure 127: Spherically blunted cone at a stagnation pressure of 6.1 psia and time = 4.0 seconds

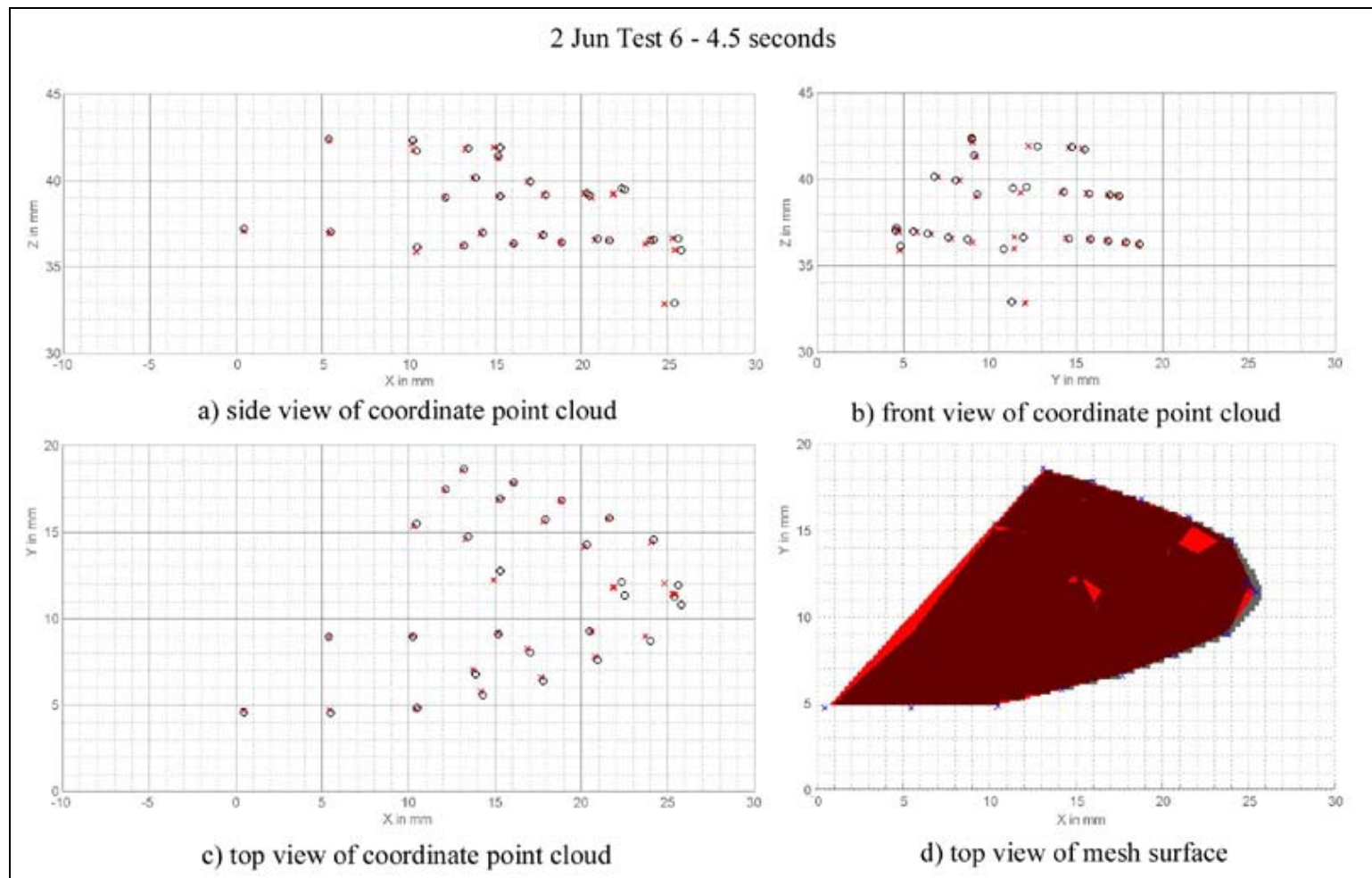


Figure 128: Spherically blunted cone at a stagnation pressure of 6.1 psia and time = 4.5 seconds

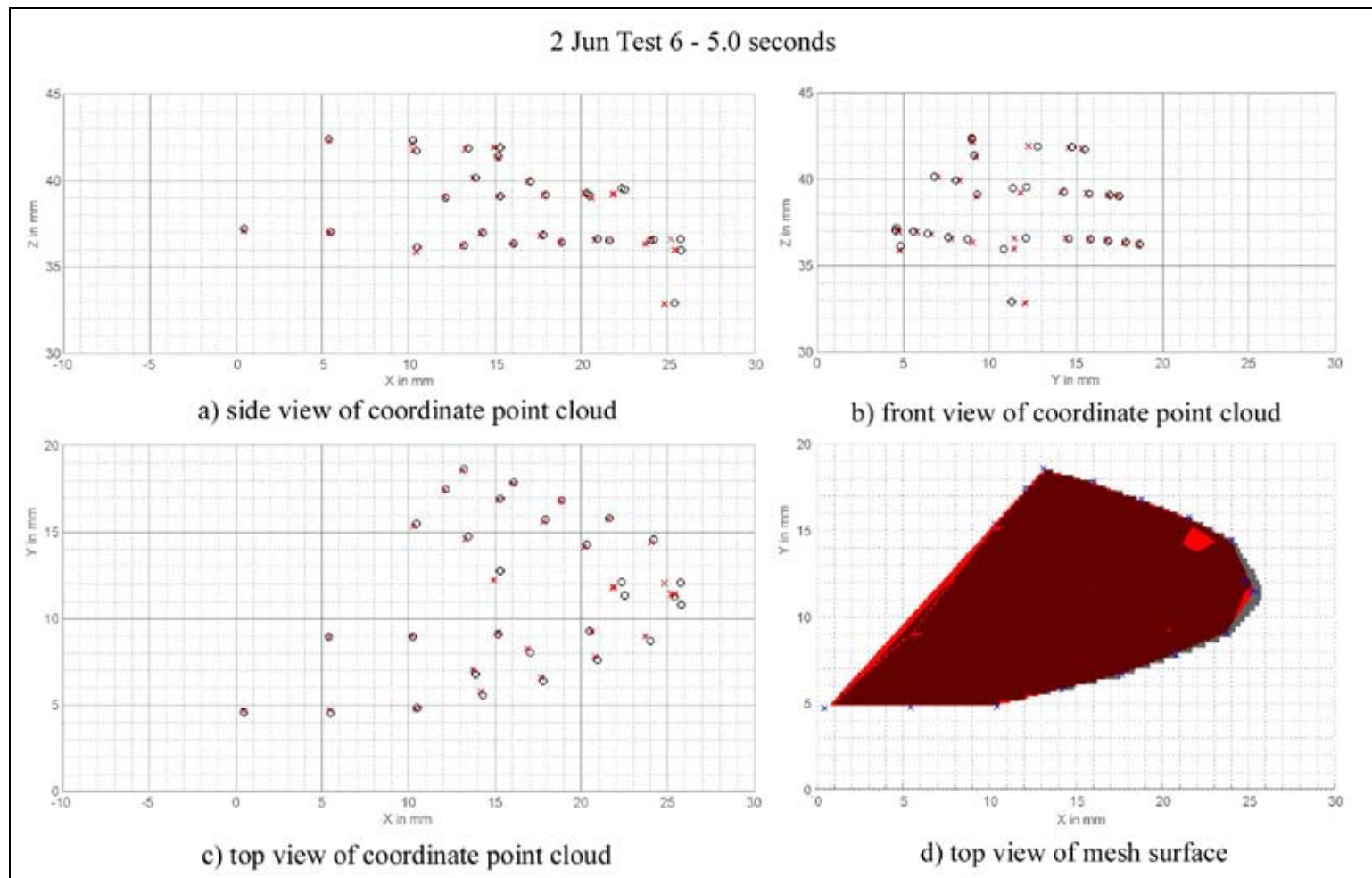


Figure 129: Spherically blunted cone at a stagnation pressure of 6.1 psia and time = 5.0 seconds

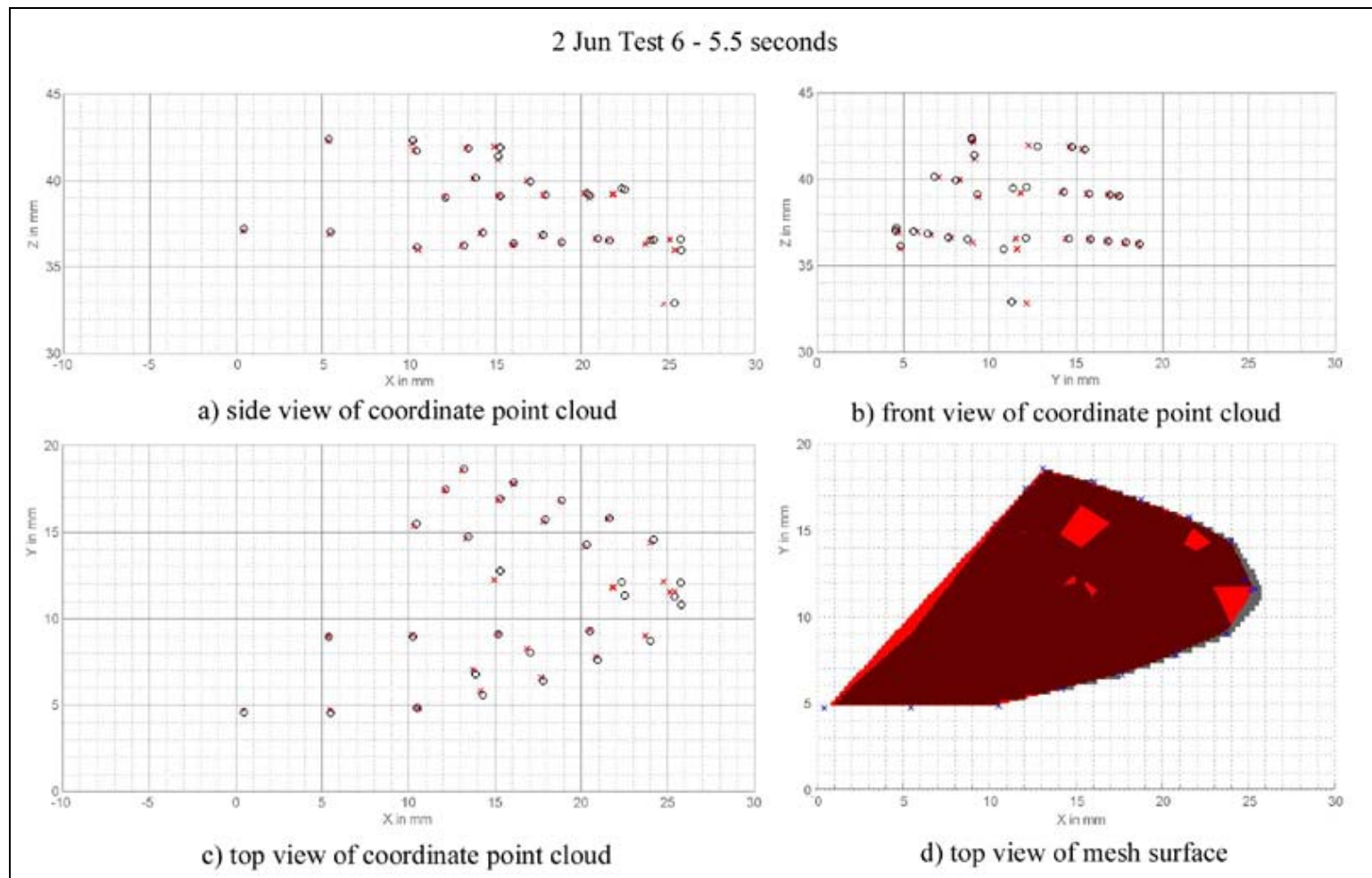


Figure 130: Spherically blunted cone at a stagnation pressure of 6.1 psia and time = 5.5 seconds

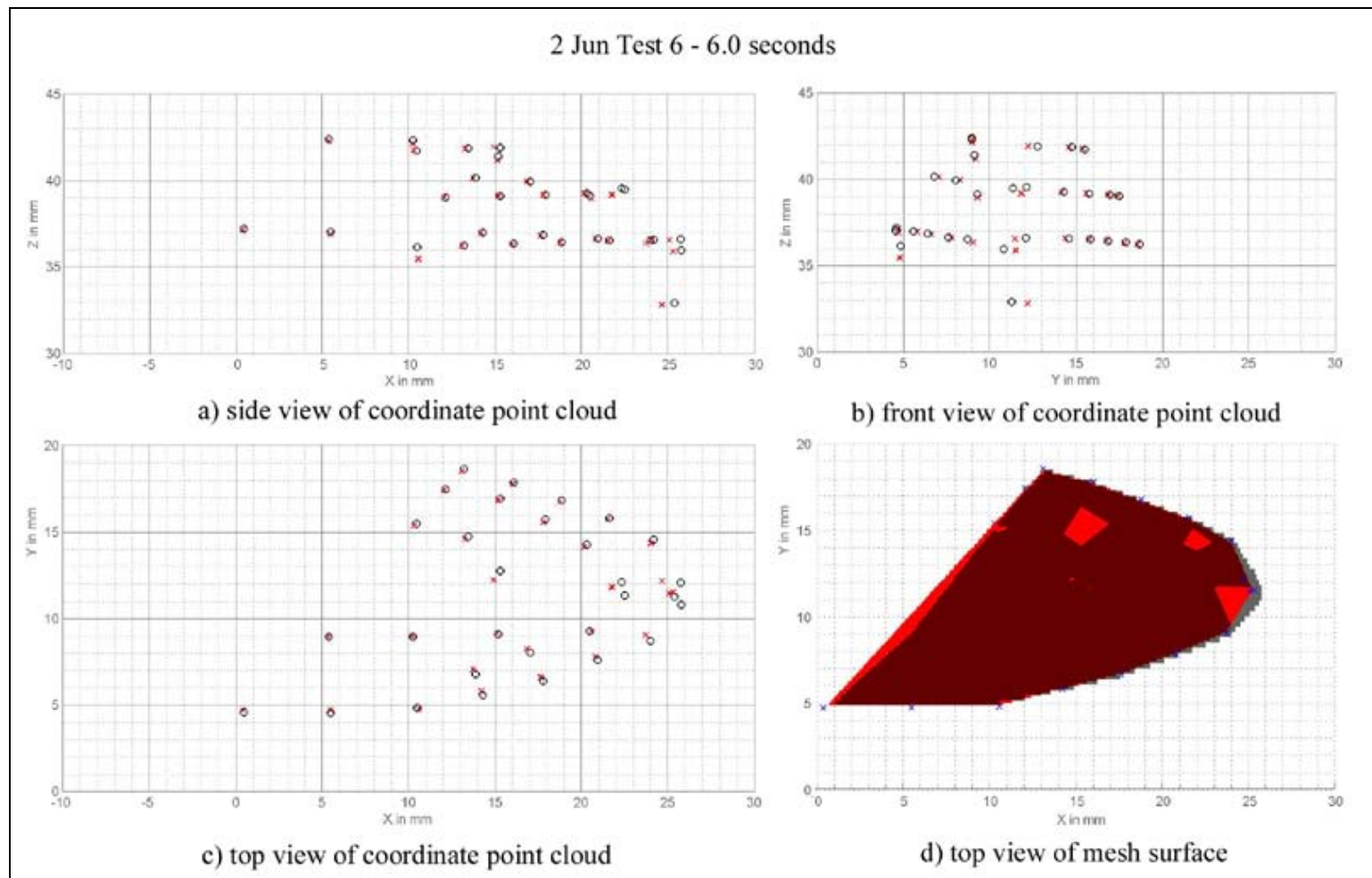


Figure 131: Spherically blunted cone at a stagnation pressure of 6.1 psia and time = 6.0 seconds

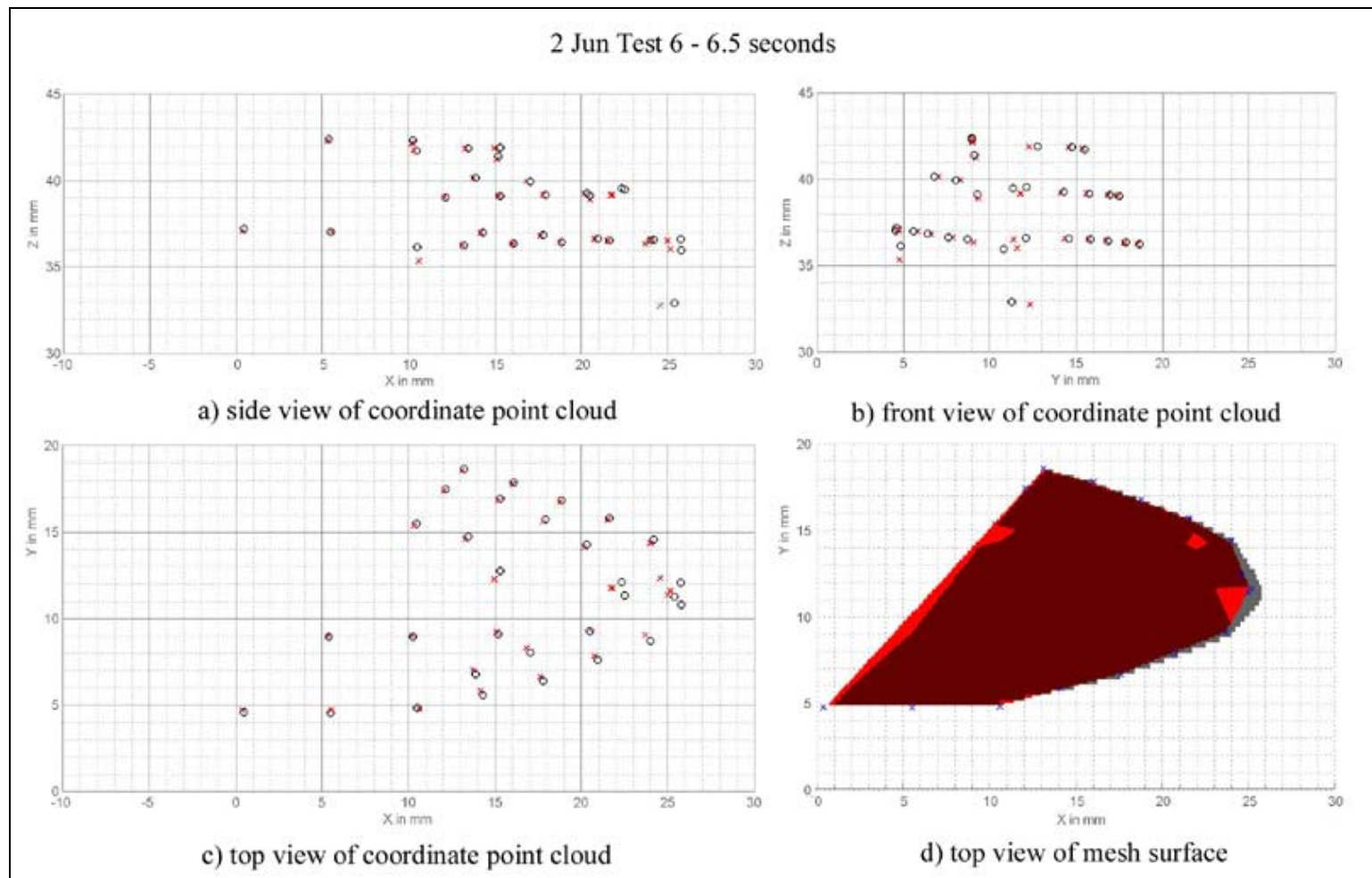


Figure 132: Spherically blunted cone at a stagnation pressure of 6.1 psia and time = 6.5 seconds

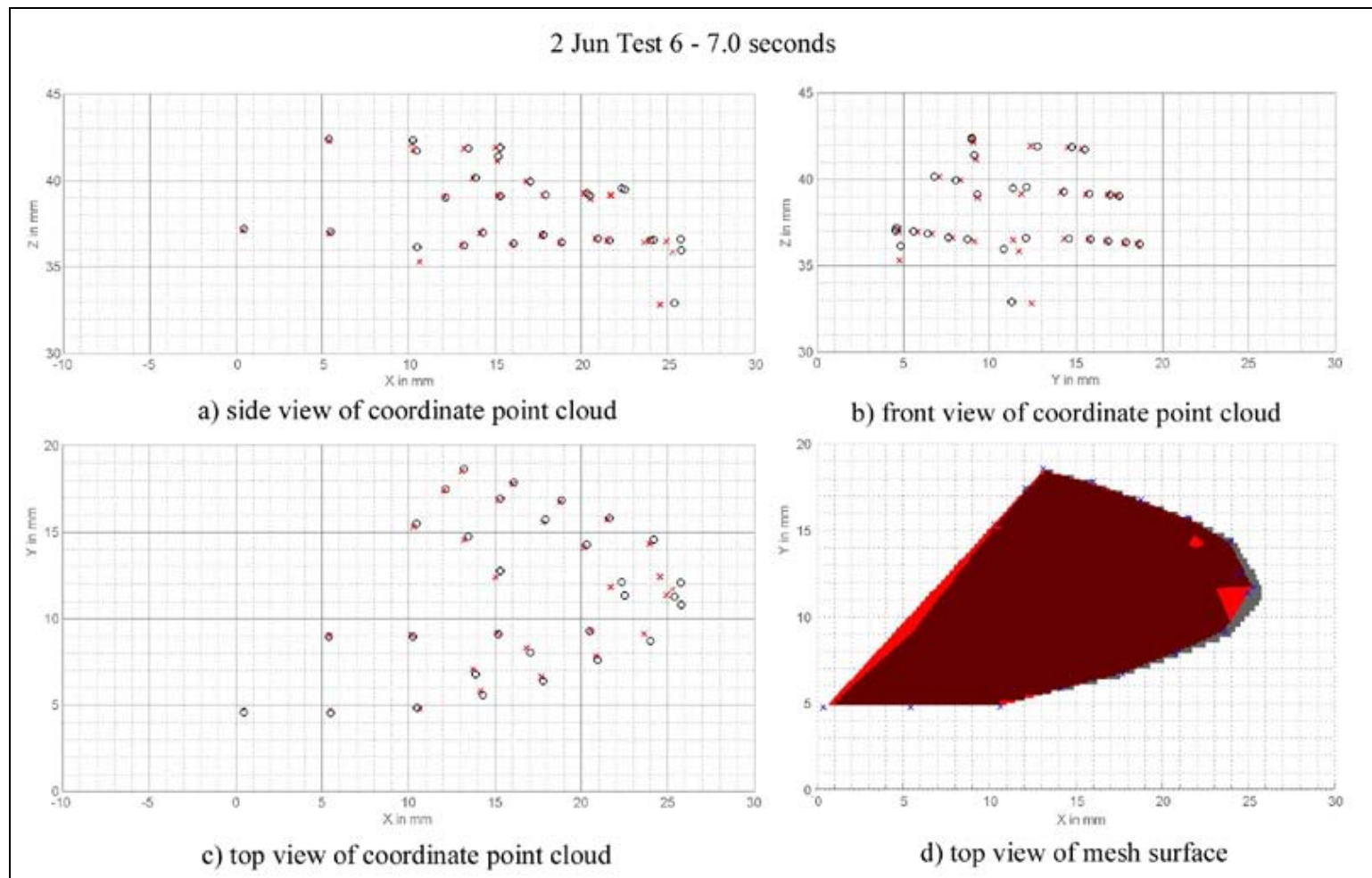


Figure 133: Spherically blunted cone at a stagnation pressure of 6.1 psia and time = 7.0 seconds

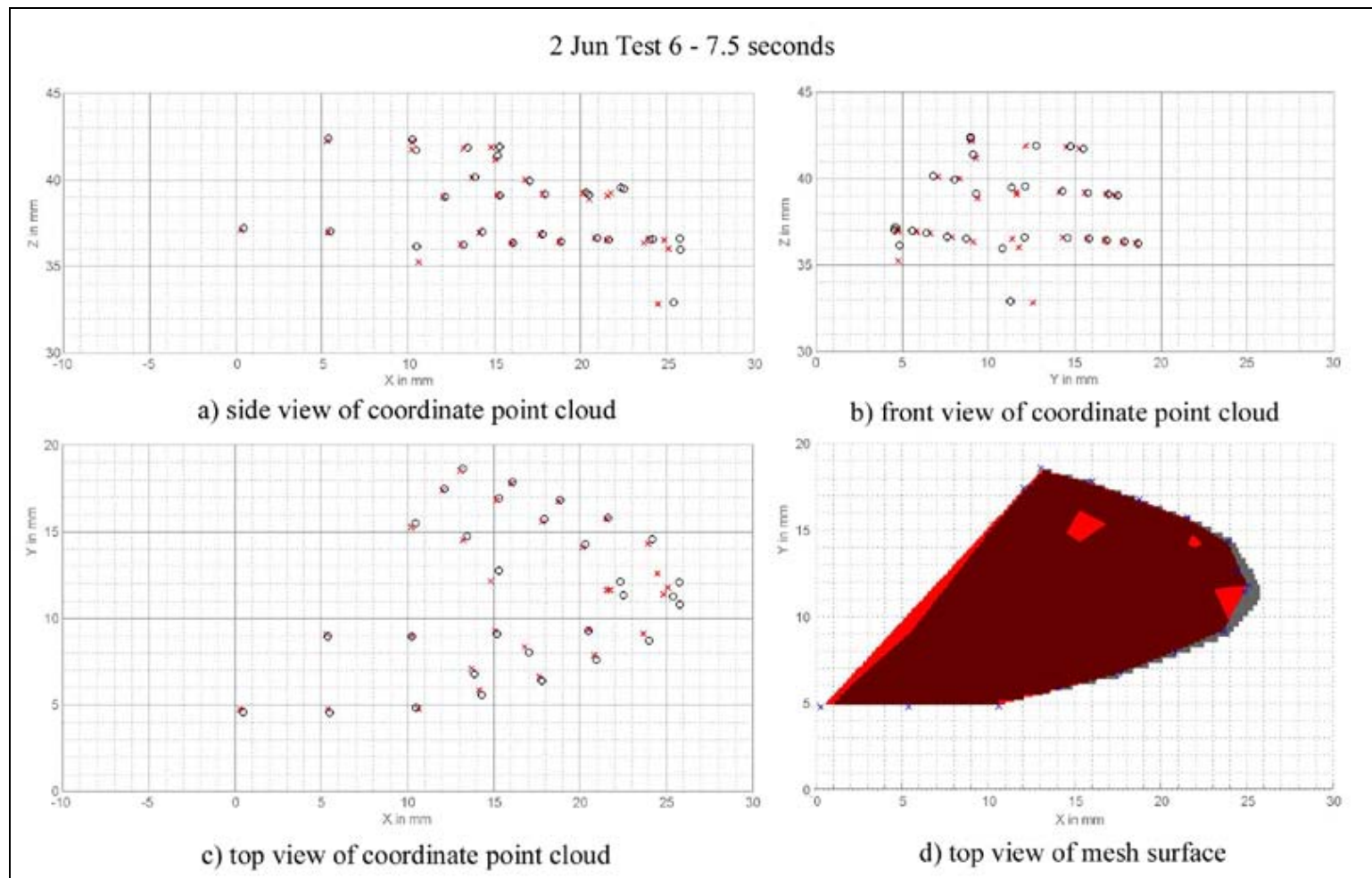


Figure 134: Spherically blunted cone at a stagnation pressure of 6.1 psia and time = 7.5 seconds

APPENDIX E: Table Calculations of Constants for Section 5.2.4

Shape	Test Name	Po psia	P _∞ (Pa)	T1 (K)	ρ _∞ (kg/m ³)	recession rate (m/s)	ρ _{CO2} (kg/m ³)	H _{sub} (J/kg)	^{sub} (W/ m ²)
Sph Cone	2 Jun T 9	6.10E+00	1.25E+03	1.07E+02	4.09E-02	1.20E-04	1.01E+03	5.58E+05	6.77E+04
	9 Jun T1	2.30E+01	4.63E+03	1.08E+02	1.50E-01	1.84E-04	1.01E+03	5.58E+05	1.04E+05
	15 Jun T4 after 0.5	3.55E+01	7.43E+03	1.08E+02	2.40E-01	2.10E-04	1.01E+03	5.58E+05	1.18E+05
	16 Jun T1	4.56E+01	9.76E+03	1.08E+02	3.17E-01	2.37E-04	1.01E+03	5.58E+05	1.34E+05
Sph Cyl	19 Jun T8	7.50E+00	1.55E+03	1.07E+02	5.04E-02	1.20E-04	1.01E+03	5.58E+05	6.77E+04
	19 Jun T6	1.95E+01	3.88E+03	1.08E+02	1.26E-01	1.70E-04	1.01E+03	5.58E+05	9.58E+04
	19 Jun T5	2.79E+01	5.74E+03	1.08E+02	1.85E-01	2.10E-04	1.01E+03	5.58E+05	1.18E+05
	19 Jun T2	3.79E+01	7.95E+03	1.08E+02	2.56E-01	2.37E-04	1.01E+03	5.58E+05	1.34E+05

Shape	Test Name	Pt2/P1	Pt2 (Pa)	RN (m)	Tt2 (K)	Ht2 (J/kg)	Tw (K)	hw,t (J/kg)
Sph Cone	2 Jun T 9	1.17E+01	1.47E+04	3.82E-03	2.93E+02	2.94E+05	1.72E+02	1.73E+05
	9 Jun T1	1.17E+01	5.41E+04	3.82E-03	2.95E+02	2.96E+05	1.87E+02	1.88E+05
	15 Jun T4 after 0.5	1.17E+01	8.68E+04	3.82E-03	2.95E+02	2.97E+05	1.93E+02	1.94E+05
	16 Jun T1	1.17E+01	1.14E+05	3.82E-03	2.96E+02	2.98E+05	1.93E+02	1.94E+05
Sph Cyl	19 Jun T8	1.17E+01	1.81E+04	7.63E-03	2.94E+02	2.95E+05	1.74E+02	1.75E+05
	19 Jun T6	1.17E+01	4.53E+04	7.63E-03	2.95E+02	2.97E+05	1.86E+02	1.87E+05
	19 Jun T5	1.17E+01	6.70E+04	7.63E-03	2.96E+02	2.97E+05	1.90E+02	1.91E+05
	19 Jun T2	1.17E+01	9.28E+04	7.63E-03	2.97E+02	2.98E+05	1.94E+02	1.95E+05

Shape	Test Name	(Equation 27 without K) (W/m ²)	K (kg / (s m ^{1.5} Pa ^{0.5}))	Velocity (m/s)	(Equation 26 without const) (W/cm ²)	constant
Sph Cone	2 Jun T 9	2.38E+08	2.84E-04	611	6.50E-04	1.04E+04
	9 Jun T1	4.07E+08	2.55E-04	613	1.25E-03	8.27E+03
	15 Jun T4 after 0.5	4.91E+08	2.41E-04	614	1.60E-03	7.41E+03
	16 Jun T1	5.67E+08	2.36E-04	615	1.84E-03	7.26E+03
		Average K for Spherically Blunted Cone	2.54E-04		Average Constant for Spherically Blunted Cone	8.33E+03
		Standard Deviation	2.16E-05		Standard Deviation	1.45E+03
Sph Cyl	19 Jun T8	1.86E+08	3.64E-04	613	5.14E-04	1.32E+04
	19 Jun T6	2.67E+08	3.59E-04	614	8.15E-04	1.18E+04
	19 Jun T5	3.15E+08	3.76E-04	614	9.93E-04	1.19E+04
	19 Jun T2	3.60E+08	3.71E-04	615	1.17E-03	1.14E+04
		Average K for Spherically Blunted Cylinder	3.67E-04		Average Constant for Spherically Blunted Cylinder	1.21E+04
		Standard Deviation	7.80E-06		Standard Deviation	7.73E+02
		Average K for both shapes	3.00E-04		Average Constant for both shapes	1.02E+04
		Standard Deviation	6.61E-05		Standard Deviation	2.42E+03

Works Cited

- Ackerman, K., & Ackerman, E. C. (2009). *Manufacturing*. Retrieved Nov 2, 2009, from Dry Ice Info.Com: <http://www.dryiceinfo.com>
- Anderson, D. E. (1960). *Investigation of Ablation of Ice Bodies in Hypersonic Flows*. Thesis, California Institute of Technology, Aeronautical Engineering Department, Pasadena, CA.
- Anderson, J. D. (2001). *Fundamentals of Aerodynamics, Third Edition*. New York: McGraw Hill.
- Anderson, J. D. (2000). *Hypersonic and High Temperature Gas Dynamics*. Reston, VA: AIAA.
- Anderson, J. D. (2003). *Modern Compressible Flow with Historical Perspective* (3rd Edition ed.). Boston: McGraw-Hill.
- Antón, P. S., Johnson, D. J., Block, M., Brown, M., Drezner, J., Dryden, J., et al. (2004). *Wind Tunnel and Propulsion Test Facilities: Supporting Analyses to an Assessment of NASA's Capabilities to Serve National Needs*. Santa Monica, CA: RAND TR134.
- Ayasoufi, A., Rahmani, R., Cheng, G., Koomullil, R., & Neroorkar, K. (2006). Numerical Simulation of Ablation for Reentry Vehicles. *9th AIAA/ASME Joint Thermophysics and Heat Transfer Conference*. San Francisco: AIAA 2006-2903.
- Baker, R. (1972). Low Temperature Ablator Nosetip Shape Change at Angle of Attack. *AIAA 72-90*.
- Barnhardt, M., & Candler, G. (2008). Detached Eddy Simulation of the Reentry-F Flight Experiment. *46th AIAA Aerospace Sciences Meeting and Exhibit*. Reno, NV: AIAA 2008-625.
- Barron, J., & Van Moorhem, W. (1998). A Novel Investigation of the Oscillatory Field Over a Transpiring Surface. *2nd Theoretical Fluid Mechanics Meeting*. Albuquerque, NM: AIAA 1998-2694.
- Barrows, D. A. (2007). Videogrammetric Model Deformation Measurement Technique for Wind Tunnel Applications. *45th AIAA Aerospace Sciences Meeting and Exhibit* (p. 12). Reno, NV: AIAA 2007-1163.
- Beresh, S. J. (n.d.). Retrieved July 10, 2008, from Sandia National Laboratories: http://www.sandia.gov/bus-ops/partnerships/tech-access/facilities/docs/tunnel_overview.pdf

Bertin, J. J. (1994). *Hypersonic Aerothermodynamics*. Washington, DC: American Institute of Aeronautics and Astronautics, Inc.

Bjorge, S., Reeder, M., Subramanian, C., Crafton, J., & Fonov, S. (2005). Flow Around an Object Projected from a Cavity into a Supersonic Freestream. *AIAA Journal* , 43 (7), 1465-1475.

Black, J., Pitcher, N., Reeder, M., & Maple, R. (2010). Videogrammetry Dynamics Measurements of a Lightweight. *Journal of Aircraft* , Vol 47, No 1, 172-180.

Callaway, D. W., Reeder, M. F., & Greendyke, R. B. (2008). Experimental Studies of Low Temperature Ablation Using Dry Ice. *15th AIAA International Space Planes and Hypersonic Systems and Technologies Conference* (p. 9). Dayton, OH: AIAA 2008-2554.

Candler, G., & MacCormack, R. (1991). The Computation of Hypersonic Ionized Flows in Chemical and Thermal Nonequilibrium. *Journal of Thermophysics and Heat Transfer* , 5 (3), 266-273.

Candler, G., & Nompelis, I. (2007). Ablation CFD Code User's Manual.

Cauchon, D. (1967). *Radiative Heating Results From the Fire II Flight Experiment at a Reentry Velocity of 11.4 Kilometers per Second*. Washington, D.C.: NASA TM X-1402.

Charwat, A. (1968). *Exploratory Studies on the Sublimation of Slender Camphor and Naphthalene Models in a Supersonic Wind-Tunnel*. RAND Corporation, RM-5506-ARPA.

Chen, C. J. (1978). Low Temperature Simulation of Subliming Boundary-Layer Flow in Jupiter Atmosphere. *AIAA Journal* , 259-267.

Chen, Y., & Milos, F. (2005). Navier–Stokes Solutions with Finite Rate Ablation. *Journal of Spacecraft and Rockets* , 42 (6), 961-970.

Chen, Y., & Milos, F. (2005). Three-Dimensional Ablation and Thermal Response Simulation System. *38th AIAA Thermophysics Conference*. Toronto: AIAA 2005-5064.

Chhabra, R., & Richardson, J. (2008). *Non-Newtonian Flow and Applied Rheology: Engineering Applications*. Butterworth-Heinemann.

Conti, R., & MacCormack, R. (1991). Inexpensive Navier-Stokes Computation of Hypersonic Flows. *26th Thermophysics Conference*. Honolulu, HI: AIAA 1991-1391.

Damon, T. D. (2001). *Introduction to Space: The Science of Spaceflight, 3rd Edition*. Malabar, FL: Krieger Publishing Company.

Day, D. A. (2003). *Shuttle Thermal Protection System (TPS)*. Retrieved July 31, 2010, from U.S. Centennial of Flight Commission: http://www.centennialofflight.gov/essay/Evolution_of_Technology/TPS/Tech41.htm

Eos Systems Inc. (2007, Jan). PhotoModeler 6 User Guide. Eos Systems Inc.

Fleming, G. A., Bartram, S. M., Waszak, M. R., & Jenkins, L. N. (2001). Projection Moiré Interferometry Measurements of. *SPIE conference on Optical Diagnostics for Fluids, Solids, and Combustion* (p. 13). San Diego, CA: SPIE.

Gordon, S., & McBride, B. (1994, Oct). Computer Program for Calculation of Complex Chemical Equilibrium and Applications: I. Analysis. *NASA Reference Publication 1311* . NASA.

Gosse, R., Callaway, D. W., Reeder, M. F., Nompelis, I., & Candler, G. (2009). Validation of an Equilibrium Ablation CFD Solver with Low Temperature Ablation Experiments Using Dry Ice. *4th Symposium on Integrating CFD and Experiments in Aerodynamics*. Rhode-Saint-Genese,Belgium: von Karman Institute.

Graves, J. R., & Witte, W. (1968). *Flight-Test Analysis of Apollo Heat-Shield Material Using the Pacemaker Vehicle System*. Washington, D.C.: NASA Technical Note D-4713.

Hankey, W. L. (1988). *Re-Entry Aerodynamics*. Washington, DC: American Institute of Aeronautics and Astronautics, Inc.

Hogan, R., Blackwell, B., & Cochran, R. (1996). Application of Moving Grid Control Volume Finite Element Method to Ablation Problems. *Journal of Thermophysics and Heat Transfer* , 10 (2).

Houghton Mifflin Company. *The American Heritage Dictionary of the English Language* (4th Edition ed.). 2003: Houghton Mifflin Company.

Inger, G., & Zee, S. (1971). Transonic Shockwave/Turbulent-Boundary-Layer Interaction with Suction or Blowing. *Journal of Aircraft* , 15 (11), 750-754.

Integrated Design Tools, Inc. (2008, June). Motion Studio Cross-Platform User Manual. Integrated Design Tools, Inc.

Johnson, J. (2009). *Aerothermodynamic Optimization of Earth Entry Blunt-Body Heat Shields for Lunar and Mars Return*. University of Maryland, Dissertation.

Jones, T., & Pappa, R. (2002). Dot Projection Photogrammetric Technique for Shape Measurements of Aerospace Test Articles. *40th AIAA Applied Aerodynamics Conference* (p. 11). Reno: AIAA 2002-0532.

Jumper, G. Y. (1975). *Thermomechanical Ablation*. AFIT Dissertation, ADA021275.

Jumper, G. Y., & Hitchcock, J. E. (1988). Ablation with a Large Fraction of Solid Removal. *Journal of Thermophysics and Heat Transfer*, 2 (3), 264-270, AIAA 0887-8722.

Jung, T. P., Reeder, M. F., Maple, R. C., & Crafton, J. (2006). Wind Tunnel Study of Interference Effects Relating to Aft Supersonic Ejection of a Store. *36th AIAA Fluid Dynamics Conference and Exhibit* (p. 18). San Francisco: AIAA-2006-3363.

Kaga, K., Matsu-ura, T., & Fujiwara, T. (2002). Experimental Study of Ablation Gas Jet Opposing to Hypersonic Flow. *40th AIAA Aerospace Sciences Meeting & Exhibit* (p. 10). Reno, NV: AIAA 2002-297.

Keenan, J., & Candler, G. (1993). Simulation of Ablation in Earth Atmospheric Entry. *28th AIAA Thermophysics Conference*. Orlando: AIAA 93-2789.

Kerley, G. I., & Chhabildas, L. (2001). *Multicomponent-Multiphase Equilibrium Multiphase Equation of State for Carbon*. Albuquerque: Sandia National Laboratories (SAND2001-2619).

Kohlman, D. L., & Richardson, R. W. (1969). Experiments on the Use of Dry Ice Ablating Wind-Tunnel Models. *Journal of Spacecraft and Rockets*, 6 (9).

Koo, J. H., Ho, D. W., & Ezekoye, O. A. (2006). A Review of Numerical and Experimental Characterization of Thermal Protection Materials - Part I. Numerical Modeling. *42nd AIAA/ASME/SAE/ASEE Joint Propulsion Conference & Exhibit*. Sacramento: AIAA 2006-4936.

Kuntz, D. (2007). *Low Temperature Ablators for Simulating Carbon-Carbon Ablation on Boost-Glide Vehicles*. Sandia National Laboratories SAND 2007-3428P (FOR OFFICIAL USE ONLY).

Larson, H. K., & Nachtsheim, P. R. (1970). *Crosshatching*. Retrieved from http://ntrs.nasa.gov/archive/nasa/casi.ntrs.nasa.gov/19700001135_1970001135.pdf

Lide, D. R. (Ed.). (2009). *CRC Handbook of Chemistry and Physics* (90th ed.). New York: CRC Press.

Lide, D. R., & Haynes, W. M. (2009). *CRC Handbook of Chemistry and Physics* (90th Edition ed.). New York: CRC Press.

Lipfert, F., & Genovese, J. (1971). An Experimental Study of the Boundary Layers on Low-Temperature Subliming Ablators. *AIAA Journal*, 1330-1337.

Ma, Y., Van Moorhem, W., & Shorthill, R. (1990). An Experimental Investigation of Velocity Coupling in Combustion Instability. *28th Aerospace Sciences Meeting*. Reno: AIAA 1990-38.

MacCormack, R. (1985). Current Status of Numerical Solutions of the Navier-Stokes Equations. *23rd Aerospace Sciences meeting*. Reno, NV: AIAA 1985-32.

McBride, B., & Gordon, S. (1996, June). Computer Program for Calculation of Complex Chemical Equilibrium Compositions and Applications: II. Users Manual and Program Description. *NASA Reference Publication 1311*. NASA.

Micol, J. (1998). Langley Aerothermodynamic Facilities Complex: Enhancements and Testing Capabilities. *36th Aerospace Sciences Meeting and Exhibit* (p. 27). Reno: AIAA 1998-147.

Moster, G. E., Callaway, D., & Bhungalia, A. (2005). Thermal-Based Comparison Between Rocket Boost-Back and Jet Fly-Back Booster Recovery Approaches. *Thermal & Fluids Analysis Workshop*. Orlando: NASA.

Moyer, C. B., & Rindal, R. A. (1968). *Finite Difference Solution for the In-Depth Response of Charring Materials Considering Surface Chemical and Energy Balances*. NASA CR-1061.

Mullenix, N., Povitsky, A., & Goitonde, D. (2008). Modeling of Local Intense Ablation in Hypersonic Flight. *15th AIAA International Space Planes and Hypersonic Systems and Technologies Conference* (p. 16). Dayton, OH: AIAA 2008-2555.

NASA. (2000, August 28). *Orbiter Thermal Protection Systems*. Retrieved July 10, 2008, from John F. Kennedy Space Center: <http://www-pao.ksc.nasa.gov/nasafact/tps.htm>

Nompelis, I., Drayna, T., & Candler, G. (2005). A Parallel Unstructured Implicit Solver for Hypersonic Reacting Flow Simulation. *17th AIAA Computational Fluid Dynamics Conference*. Toronto, Ontario: AIAA 2005-4867.

Pappa, R., Black, J., Blandino, J., Jones, T., Danehy, P., & Dorrington, A. (2003). Dot-Projection Photogrammetry and Videogrammetry of Gossamer Space Structures. *Journal of Spacecraft and Rockets*, 40 (6), 858-867.

Peltier III, D. W. (2007). Performing Particle Image Velocimetry in a Supersonic Wind Tunnel Using Carbon Dioxide as the Seeding Material. *AFIT-GAE-ENY-07-J17 (Thesis)*. Wright-Patterson AFB: Air Force Institute of Technology.

Potter, W., & Grossman, L. (1971). The Conductivity of a Medium Interrupted by Voids. *Zeitschrift Fur Angewandte Mathematik und Physik (ZAMP)*, Vol. 22, No. 3, pp. 621-629.

Quinn, E. L., & Jones, C. L. (1936). *Carbon Dioxide*. New York: Reinhold Publishing Corporation.

Reuther, J. J., Prabhu, D. K., Brown, J. L., Wright, M. J., & Saunders, D. A. (2004). Computational Fluid Dynamics for Winged Re-entry Vehicles at Hypersonic Conditions. *34th AIAA Fluid Dynamics Conference and Exhibit*. Portland: AIAA 2004-2537.

Schairer, E. T., & Heineck, J. T. (2007). Photogrammetric Recession Measurements of Ablative Materials during Arcjet Testing. *45th AIAA Aerospace Sciences Meeting and Exhibit*. Reno: AIAA 2007-1158.

Scott, C., Ried, R., & Maraia, R. (1984). An AOTV Aeroheating and Thermal Protection Study. *Thermal Design of Aeroassisted Orbital Transfer Vehicles*, Vol 96, pp 309-337.

Shakhashiri, B. Z. (2008). *Chemical of the Week: Carbon Dioxide*. Retrieved Oct 2009, from Science is Fun in theLab of Shakhashiri: <http://www.scifun.org>

Sherman, M. (1968). *Entry Thermal Protection*. NASA SP-8014.

Sherrouse, P., Sheeley, J., Mansfield, J., & Rotach, D. (2003). Design and Testing of a Zero-Focus Shadowgraph System for Ablation Measurement During Arc Jet Testing. *36th AIAA Thermophysics Conference* (p. 8). Orlando: AIAA 2003-4046.

Silton, S. I., & Goldstein, D. B. (2000). Ablation Onset in Unsteady Hypersonic Flow About Nose Tip with Cavity. *Journal of Thermophysics and Heat Transfer*, 14 (3), 421-434.

Silton, S. I., & Goldstein, D. B. (2003). Optimization of an Axial Nose-Tip Cavity for Delaying Ablation Onset in Hypersonic Flow. *41st Aerospace Sciences Meeting and Exhibit*. Reno, NV: AIAA 2003-152.

Sumarokov, V., Stachowiak, P., & Jezowski, A. (2007). The Peculiarities of Heat Transfer in CO₂ and N₂O Solids at Low Temperatures. *Low Temperature Physics*, Vol. 33, No. 6-7.

Sutton, G. W. (1982). The Initial Development of Ablation Heat Protection, An Historical Perspective. *Journal of Spacecraft*, Vol 19, No 1, JAN-FEB 1982, 3-8.

Sutton, K., & Graves, R. (1971). *A General Stagnation-Point Convective-Heating Equation For Arbitrary Gas Mixtures*. Washington, D.C.: NASA TR R-376.

Svanberg, C., Reeder, M., Curtis, D., & Cobb, R. (2009). Flapping Wing Micro Air Vehicle Bench Test Set-up. *47th AIAA Aerospace Sciences Meeting*. Orlando: AIAA.

Swenson, J. L., Grimwood, J. M., & Alexander, C. C. (1989). *This New Ocean: A History of Project Mercury. NASA History Series* .

Tannehill, J. C., Anderson, D., & Pletcher, R. (1997). *Computational Fluid Mechanics and Heat Transfer* (2nd Edition ed.). Philadelphia: Taylor & Francis.

Tauber, M., Menees, G., & Adelman, H. (1987). Aerothermodynamics of Transatmopsheric Vehicles. *Journal of Aircraft* , vol.24 no.9 (594-602).

Thompson, R., & Gnoffo, P. (2008). Implementation of a Blowing Boundary Condition in the LAURA Code. *46th AIAA Aerospace Sciences Meeting and Exhibit*. Reno, NV: AIAA 2008-1243 .

White, F. M. (2002). *Fluid Mechanics, Fifth Edition*. New York: McGraw-Hill.

White, F. M. (1991). *Viscous Fluid Flow, 2nd Edition*. Boston, MA: McGraw Hill.

Williams, S., Curry, D. M., Bouslog, S. A., & Rochelle, W. C. (1993). Thermal Protection System Design Studies. *AIAA 28th Thermophysics Conference* (p. 9). Orlando: AIAA 93-2843.

Wright, M., Bose, D., & Candler, G. (1998). A Data-Parallel Line Relaxation Method for the Navier-Stokes Equations. *AIAA Journal* , 36 (9), 1603-1609.

Zoby, E., Thompson, R., & Wurster, K. (2004). Aeroheating Design Issues for Reusable Launch Vehicles - A Perspective. *34th AIAA Fluid Dynamics Conference and Exhibit*. Portland, OR: AIAA 2004-2535.

VITA

David “Walker” Callaway was raised in La Feria, Texas and graduated from La Feria High School in 1995. He attended Embry-Riddle Aeronautical University in Daytona Beach, Florida on an Air Force ROTC scholarship, earning a Bachelor of Science in Engineering Physics in 2000. Commissioned in the United States Air Force, he attended undergraduate pilot training at Laughlin AFB, Texas in 2001. After an injury sidelined his flying career, David Callaway continued his Air Force career as an aeronautical engineer, earning a Master of Science in Aeronautical Engineering from the Air Force Institute of Technology in 2004. In September 2006, he entered the Graduate School of Engineering and Management at the Air Force Institute of Technology. David Callaway retired from the Air Force in February 2011.

REPORT DOCUMENTATION PAGE			Form Approved OMB No. 0704-0188		
<p>The public reporting burden for this collection of information is estimated to average 1 hour per response, including the time for reviewing instructions, searching existing data sources, gathering and maintaining the data needed, and completing and reviewing the collection of information. Send comments regarding this burden estimate or any other aspect of this collection of information, including suggestions for reducing this burden to Department of Defense, Washington Headquarters Services, Directorate for Information Operations and Reports (0704-0188), 1215 Jefferson Davis Highway, Suite 1204, Arlington, VA 22202-4302. Respondents should be aware that notwithstanding any other provision of law, no person shall be subject to any penalty for failing to comply with a collection of information if it does not display a currently valid OMB control number. PLEASE DO NOT RETURN YOUR FORM TO THE ABOVE ADDRESS.</p>					
1. REPORT DATE (DD-MM-YYYY) 16-06-2011		2. REPORT TYPE Doctoral Dissertation		3. DATES COVERED (From — To) Sep 2006 – Jun 2011	
4. TITLE AND SUBTITLE Photogrammetric Measurement of Recession Rates of Low Temperature Ablators Subjected to High Speed Flow			5a. CONTRACT NUMBER		
			5b. GRANT NUMBER		
			5c. PROGRAM ELEMENT NUMBER		
6. AUTHOR(S) David W. Callaway, Maj, USAF, Retired			5d. PROJECT NUMBER		
			5e. TASK NUMBER		
			5f. WORK UNIT NUMBER		
7. PERFORMING ORGANIZATION NAME(S) AND ADDRESS(ES) Air Force Institute of Technology Graduate School of Engineering and Management (AFIT/ENY) 2950 Hobson Way WPAFB OH 45433-7765			8. PERFORMING ORGANIZATION REPORT NUMBER AFIT/DS/ENY/11-03		
9. SPONSORING / MONITORING AGENCY NAME(S) AND ADDRESS(ES) Dr. Ryan Gosse Ryan.Gosse@wpafb.af.mil 1950 Fifth Street Air Force Research Laboratory, Air Vehicles Directorate Wright Patterson AFB, OH 45433 937-904-4024			10. SPONSOR/MONITOR'S ACRONYM(S) AFRL/RBAC		
			11. SPONSOR/MONITOR'S REPORT NUMBER(S)		
12. DISTRIBUTION / AVAILABILITY STATEMENT APPROVED FOR PUBLIC RELEASE; DISTRIBUTION UNLIMITED					
13. SUPPLEMENTARY NOTES This material is declared a work of the U.S. Government and is not subject to copyright protection in the United States.					
14. ABSTRACT This research advances a technique to simulate high temperature/high speed effects in a high speed/low temperature environment and to capture recession of the test article in three-dimensions. A method of fabricating dry ice test articles was developed, and the AFIT Mach 3 pressure-vacuum wind tunnel was used in combination with the dry ice test articles to collect three-dimensional ablation data for models of different shapes at stagnation pressures ranging from approximately 0.4 atm to 3 atm and stagnation temperatures equivalent to room temperature. High speed Schlieren photography was used for visualization, and the three dimensional shape change was quantified with sub-millimeter accuracy using laser dot photogrammetry. Experimental results for multiple shapes were compared to those computed using a computational model called ACFD. The ACFD model employed a finite-volume approach to solving the (3-D) Navier-Stokes equations with the gas assumed to be at equilibrium while employing an implicit solver accounting for the material response. By and large, the computational approach was validated for the conditions tested herein. Measurement of ablation rates at the stagnation point yielded approximate values of convective heat transfer rate when conduction through the solid is assumed negligible. The results of this analysis compared favorably to a variety of extensions of the Fay-Riddell correlation given in the literature. Paths for further research were selected and discussed.					
15. SUBJECT TERMS LTA, Low Temperature Ablator, Ablation, Supersonic, Photogrammetry, Recession, Stagnation Point, Convective Heat Transfer, Dry Ice, High Speed Flow					
16. SECURITY CLASSIFICATION OF:			17. LIMITATION OF ABSTRACT UU	18. NUMBER OF PAGES 289	19a. NAME OF RESPONSIBLE PERSON Dr. Mark Reeder, AFIT/ENY
a. REPORT U	b. ABSTRACT U	c. THIS PAGE U			19b. TELEPHONE NUMBER (Include Area Code) (937)255-3636, ext 4530

Prescribed by ANSI Std. Z39.